Recovery of metals from spent lithium-ion batteries through adsorption processes using waste materials

Melina Roshanfar

Under the Supervision of

Professor Majid Sartaj, Ph.D., P.Eng.

Thesis submitted to the University of Ottawa in partial Fulfillment of the requirements for the Doctorate in Philosophy degree in Environmental Engineering at the University of Ottawa

Department of Civil Engineering
Faculty of Engineering
University of Ottawa
Ottawa, ON, Canada

*****The Doctor of Philosophy in Environmental Engineering is a Joint Program with Carleton University, administered by the Ottawa-Carleton Institute for Environmental Engineering

ABSTRACT

The rapid growth in the use of lithium-ion batteries in electric vehicles and portable electronics has made their recycling a pressing global concern. The primary challenge is developing a universal, sustainable process capable of effectively treating diverse cathode chemistries, such as $LiCoO_2$ (LCO), $LiMn_2O_4$ (LMO), and $LiNi_xCo_\gamma Mn_{1-x-\gamma}O_2$ (NMC). This study has developed an integrated, environmentally friendly recycling method that incorporates thermal pretreatment, selective leaching, bio-based adsorption, and lithium recovery, making it suitable for all major cathode materials. Thermal treatment at 570 °C in air for 2 hours effectively removed the PVDF binder and organic residues, without forming unwanted cobalt oxides or metallic alloys, resulting in clean, reactive powders. Optimized leaching using a mixed citric–sulfuric acid system achieved almost complete metal recovery (Li, 99%; Co, 98%; Ni, 90%; Mn, 92%) under mild conditions, with citric acid acting as both a complexing and reducing agent, thereby eliminating the need for external reductants. The adsorption process was preferred over traditional separation methods because of its simplicity, low cost, high selectivity, and minimal secondary waste. Chitosan powder, a by-product derived from marine waste, exhibited strong affinity for Co(II), Mn(II), and Ni(II), while leaving lithium in solution. Crosslinking with 1 wt.% L-cystine produced stable CS1%CYS with increased porosity and mechanical strength, reaching adsorption uptake capacities of 153 mg/g for Co(II), 15.6 mg/g for Ni(II), and 7.7 mg/g for Mn(II), and maintaining over 92% recovery after multiple regeneration cycles with 0.1 M EDTA. Additionally, a greener version of chitosan was synthesized using the protic ionic liquid [Eth][Ac], showing similar adsorption performance to commercial powder while lessening environmental impact. Advancing toward practical application, fixed-bed column experiments demonstrated the scalability and stability of the beads under continuous-flow operation, with Co(II) and Ni(II) exhibiting strong retention and predictable breakthrough behavior. The residual Mn(II) was effectively removed (>86%) by $KMnO_4$ oxidation or pH adjustment, while Li can be recovered as Li_2CO_3 from the solution by reacting with saturated Na_2CO_3 at 90 °C. Comprehensive characterization techniques, including XRD, SEM-EDS, FT-IR, TGA, and BET, supported the results of each stage, confirming the complete removal of the binder, successful metal coordination through amine and hydroxyl groups, and an increased surface area of the modified chitosan. Overall, this study presents a universal, scalable, and sustainable methodology for the selective recovery of critical metals and

battery-grade lithium carbonate from spent lithium-ion batteries, representing a significant advancement toward circular, low-carbon battery recycling.

Dedication

To my beloved husband, **Misagh**, whose unwavering love, patience, and encouragement have been my greatest source of strength.

To my wonderful family (**Masoud**, **Elahe**, and **Melika**) for their endless support, sacrifices, and belief in me throughout this journey.

This achievement is just as much yours as it is mine.

Acknowledgements

This journey has truly been one of the most challenging yet rewarding experiences of my life, filled with valuable lessons, personal growth, and inspiration from many incredible individuals. I would like to express my deepest gratitude to my supervisor, Professor Majid Sartaj, for his invaluable guidance, encouragement, and ongoing support throughout this research. His mentorship, patience, and insights have been crucial in developing my academic and professional development.

I also extend my sincere appreciation to my thesis committee members for their valuable time, insightful feedback, and constructive comments, which significantly improved the quality of this research and guided me through the final stages of my doctoral journey.

My sincere thanks go to our laboratory technicians, Ms. Tram Nguyen and Dr. Patrick D'Aoust, for their technical expertise, patience, and dedication that significantly supported my experimental work. I am also grateful to all members of our research group, especially Dr. Fatemeh Saadat Ghareh Bagh, for her collaboration, insightful discussions, and friendship that made this journey both productive and enjoyable.

I would like to thank ERS International for their industrial collaboration and support. My sincere appreciation goes to Dr. Sam Kazemeini and Mr. Nick Fonceca for their technical advice, encouragement, and trust in my work. I also thank the Ontario Centre of Innovation (OCI) for its ongoing support of research.

Special thanks to my student, Ayaz Mohammad Saad Nayeck, for his dedication, enthusiasm, and valuable assistance in the laboratory.

I gratefully acknowledge the Solid Waste Association of North America (SWANA, Ontario Chapter) for awarding me the SWANA Scholarship, and the Ontario Graduate Scholarship (OGS) program for their generous financial support, which greatly contributed to the success of this work.

Finally, I am profoundly grateful to my family (Misagh, Masoud, Elahe, and Melika) for their unconditional love, patience, and faith in me. Their continual encouragement and support have been my most significant source of strength throughout this journey.

Table of Contents

Table of Figures

List of Tables

ABBREVIATIONS

1 wt.% L-cystine crosslinked chitosan beads	CS1%CYS
1,3-Dioctyl imidazolium 2-hydroxybenzoate	[DOIM][OHB]
1,3-dioctyl imidazolium 2-hydroxybenzoate	[DOIM][OHB]
2-Ethylhexyl phosphonic acid-mono-2-ethylhexyl ester	PC88A
4-methyl-2-pentanol	MIBC
Acetic acid	AA
Acorga M5640, 2-ethylhexylphosphonic acid mono-2-ethylhexyl ester	PC-88A
Activated Carbon	AC
Aluminum	Al
Amino	$-NH_2$
Atomic Absorption Spectroscopy	AAS
Bis(trifluoromethanesylfonyl) imide	$Li(SO_2CF_3)_2$
Bis-(2, 4, 4-trimethylpentyl) phosphonic acid	Cyanex 272
Bis(2,4,4-trimethyl pentyl)phosphinic acid	Cynex 272
Black mass	BM
Box-Behnken design	BBD
Brunauer, Emmett, and Teller analysis	BET
Carbon	C
Carbon Nanotubes	CNT
Carboxyl	COOH
Carboxymethylcellulose	CMC
Chitosan	CS
Chitosan beads	CBs
Chloride ions	Cl-
Citric acid	Cit

Citric monohydrate	$C_6H_8O_7.H_2O$
Cobalt	Co
Cobalt oxide	Co_3O_2
Compound Annual Growth Rate	GAGR
Copper	Cu
Copper oxide	CuO
Deep Eutectic Solvents	DES
Degree of Acetylation	DA
Degree of Deacetylation	DD
Demineralization	DM
Deproteinization	DP
Di-2-Ethylhexyl phosphoric acid	D2EHPA
Diisopropylethylammonium acetate	[Dipea][Ac]
Diisopropylethylammonium propanoate	[Dipea][P]
Dimethyl acetamide	DMAC
Dimethyl sulfoxide	DMSO
Dimethylbutylammonium acetate	[Dmba][Ac]
Dimethylformamide	DMF
Electric Vehicle	EV
Ethanolammonium acetate	(Eth][Ac]
Ethylene glycol	EG
Ethylenediaminetetraacetic acid	EDTA
Fatty acid methyl esters	FAME
Fourier Transform Infrared Spectroscopy	FT-IR
Graphene oxide	GO
Graphene oxide–chitosan	GOCS
hard and soft (Lewis) acids and bases	HSAB
HSAB theory	Hard and Soft (Lewis) Acids and Bases

Hydrochloric acid	HCl
Hydrogen Bond Acceptor	HBA
Hydrogen Bond Donor	HBD
Hydrogen peroxide	H_2O_2
Hydroxyl	-OH
Inductively Coupled Plasma Spectroscopy	ICP
Internet of things	IoT
Ion exchange	IX
Ionic Liquid	IL
Ionic Liquids	ILs
Iron oxide	Fe_2O_3
L-arginine	Arg
L-cystine	Cys
$LiNiCoAlO_2$	NCA
Lithium	Li
Lithium Carbonate	Li_2CO_3
lithium cobalt oxide	LCO
Lithium hexafluoro arsenate	$LiAsF_6$
Lithium hexafluorophosphate	$LiPF_6$
Lithium iron phosphate	LFP
Lithium manganese oxide	LMO
Lithium nickel manganese cobalt oxide	NMC
Lithium perchlorate	$LiClO_4$
Lithium tetrafluoroborate	$LiBF_4$
Lithium titanium oxide	LTO
Lithium triflate	$LiCF_3SO_3$
Lithium-ion batteries	LIBs
Magnesium	Mn

Magnesium	Mg
Manganese oxide	Mn_3O_4
Mean Squared Error	MSE
N-methyl-2-pyrrolidone	NMP
N-methyl-N, N, N-trioctylammonium chloride	Aliquat 336
N-methyl-N, N, N-trioctylammonium chloride	Aliquat 336
Nickel	Ni
Nickel–metal hydride battery	NiMH
Nitric acid	HNO_3
Organic Acid	Org
Phosphoric acid	H_3PO_4
Phosphoric acid	H_3PO_4
Phytolacca Americana branch	PA
Poly(vinylidene fluoride)	PVDF
Polyethylene	PE
Polyethylene terephthalate	PET
Polypropylene	PP
Polytetrafluoroethylene	PTFE
Polythiosemicarbazide	PTSC
Potassium	K
Potassium Permanganate	$KMnO_4$
Protic Ionic Liquids	PILs
Pyrite	FeS_2
Quality control and Quality assurance	QC/QA
Response surface methodology	RSM
Scanning Electron Microscope coupled with Energy Dispersive X-ray Spectroscopy	SEM-EDS
Shrimp Shells	SS

Sodium	Na
Sodium Carbonate	Na_2CO_3
Sodium hydroxide	NaOH
Sodium Phosphate	Na_3PO_4
Sodium sulfate	$NaSO_4$
Sodium tripolyphosphate (STPP)	$Na_5P_3O_{10}$
Solid-to-liquid ratio	S/L
Solvent Extraction	SX
Stainless-Steel Foil	SSF
Standard Deviation	SD
Sulfuric acid (SA)	H_2SO_4
Sum of Squares of Residuals	SSR
Thermogravimetric analysis	TGA
Thiocyanate	SCN^-
Tin oxide	SnO_2
Tioctylamine	TOA
Tributyl tetradecyl phosphonium chloride	$[P_{44414}]Cl$
Triethylammonium acetate	[Tea][Ac]
Triethylenetetrammonium acetate	[Teta][Ac]
Tris-2-methylhexanamine	TEHA
Vinylidene fluoride	CH_2-CF_2
X-ray photoelectron spectroscopy	XPS
X-ray powder Diffraction Analysis	XRD

Chapter 1 INTRODUCTION

1.1. Background and Statement of Problem

Lithium-ion batteries (LIBs) are widely used globally and are employed in electric vehicles (EVs), electronic devices, and the Internet of Things (IoT). Compared to other batteries, such as NiMH and lead-acid batteries, LIBs offer more promising features, including a longer lifespan, compact design, lower environmental risks, higher resistance to self-discharge, higher voltage outputs, and greater temperature tolerance (Golmohammadzadeh et al., 2022; Velázquez-Martínez et al., 2019; Windisch-Kern et al., 2022).

The rapid adoption of EVs is driving unprecedented growth in the global lithium-ion battery (LIB) market. By 2030, the number of EVs on the road is projected to reach 253 million, with battery demand rising from 340 GWh in 2024 to more than 3500 GWh (Paul and Shrotriya, 2025). In 2023 alone, nearly 14 million new EVs were registered worldwide, representing a 35% increase from the previous year. In North America, existing and announced gigafactories were estimated to collectively supply over 1 TWh of annual battery capacity, while in China, the generation of spent LIBs is anticipated to exceed 500,000 tons (Ma et al., 2025). LIBs are central to the transition toward net-zero emissions, as their use in EVs significantly reduces greenhouse gas emissions compared to conventional vehicles and supports the Paris Agreement's decarbonization targets. The global LIB market has expanded sharply, growing from USD 12 billion in 2011 to USD 50 billion in 2020, and is expected to reach USD 116.6 billion by 2030. Similarly, the EV battery sector alone is projected to contribute more than USD 15 billion by 2025, with global sales surpassing USD 90 billion (Cheng et al., 2021).

This exponential growth highlights the growing strain on the supply of critical metals, including lithium (Li), cobalt (Co), nickel (Ni), copper (Cu), aluminum (Al), and manganese (Mn). These metals are essential for clean energy technologies. Yet, their demand is projected to rise steeply: by 2025, the demand for Li, Ni, and Co is expected to increase by 26%, 39%, and 25%, respectively, with annual consumption of Ni and Co projected to reach 1.1 and 0.3 million tons by 2030. Currently, approximately 35% of global Li and 25% of global Co production are consumed

solely by the LIB industry, a share that is expected to rise significantly soon (Baudino et al., 2022; Wilkinson and Champagne, 2022; Kader et al., 2021).

The rapid growth in LIB production inevitably leads to an increasing volume of spent batteries. In 2017, approximately 250,000 tons of waste LIBs were generated, rising to 500,000 tons/year by 2019. Projections indicate that by 2040, this figure could reach 8 million tons (Baudino et al., 2022; Sethurajan and Gaydardzhiev, 2021). Managing such massive waste streams poses a serious challenge, as conventional disposal methods such as landfilling and incineration are unsustainable. LIBs are classified as hazardous waste; in landfills, leaking electrolytes can react with water to emit toxic gases such as hydrogen fluoride, while acid-producing microorganisms can leach metals into soil and groundwater, causing contamination and health risks (Baum et al., 2022; Golmohammadzadeh et al., 2022; Kader et al., 2021). Incineration, on the other hand, releases harmful gases into the atmosphere, adding to the already existing environmental burdens.

Beyond environmental concerns, the growing demand for LIB metals also raises questions about long-term resource availability, as the mining of critical elements such as Li, Co, and Ni struggles to keep pace with industrial consumption (Sommerville et al., 2020). A sustainable alternative is to recover and recycle these valuable materials, thereby returning them to the production-consumption cycle (Baum et al., 2022; Gaines, 2018; Kader et al., 2021). LIBs contain 6-7% Li on a weight basis, which is higher than that of natural sources (Golmohammadzadeh et al., 2022; C. Liu et al., 2019). Recycling not only conserves resources but is also economically attractive; for example, processing 500,000 tons of spent LIBs could yield 60,000 tons of Co and 75,000 tons of Li for reuse (Baudino et al., 2022).

However, current recycling technologies remain limited. Pyrometallurgical and hydrometallurgical methods, although widely used, are energy-intensive, generate hazardous emissions, and produce by-products that require further treatment. Consequently, the global recycling rate of LIBs remains below 4%, despite forecasts that around 11 million tons will need to be recycled annually by 2030 (Velázquez-Martínez et al., 2019). Given these challenges, advancing efficient and sustainable LIB recycling has become a pressing research and industrial priority.

1.2. Research Hypotheses and Objectives

This research is based on the hypothesis that critical metals, namely lithium (Li), cobalt (Co), manganese (Mn), and nickel (Ni), can be selectively recovered from spent LIB cathode materials through an integrated hydrometallurgical process consisting of pretreatment, greener leaching, and selective adsorption using waste-derived adsorbents. It is hypothesized that certain waste-derived materials, particularly chitosan and other bio-based adsorbents, can adsorb transition metals such as Co, Ni, and Mn, while lithium remains in solution for subsequent recovery. Furthermore, modification of chitosan and its production using greener extraction methods are expected to improve adsorption performance and enable applications in continuous systems, thereby supporting process scalability.

To test this hypothesis, the main objective of this research is to develop an environmentally friendly and efficient process for the selective recovery of critical metals from spent LIBs using waste-derived adsorbents. The specific objectives of this study are as follows:

- Characterization of raw spent LIB materials and pretreatment of the collected materials through thermal treatment to remove impurities such as collectors, binders, separators, and casing materials.
- Investigation and optimization of a novel greener leaching process using statistical analysis and response surface methodology (RSM).
- Evaluation of the feasibility of selective metal separation through adsorption using different waste-derived adsorbents, including chitosan (CS), coconut shell activated carbon (AC), graphene oxide (GO), and modified flax fiber, and selection of the most efficient adsorbent.
- Characterization of the selected adsorbent and evaluation of adsorption performance through isotherm, kinetic, and thermodynamic studies.
- Modification of the selected adsorbent (chitosan) to improve adsorption performance and physical properties and to enable its application in larger-scale systems (e.g., bead production).
- Investigation of desorption processes and evaluation of adsorbent reusability.
- Production of chitosan from waste shrimp shells using a greener extraction method based on protic ionic liquids.

- Assessment of the scalability of the process from batch experiments to a continuous fixed-bed column system to evaluate practical applicability.

The different phases of the proposed research are summarized in Figure 1.1.

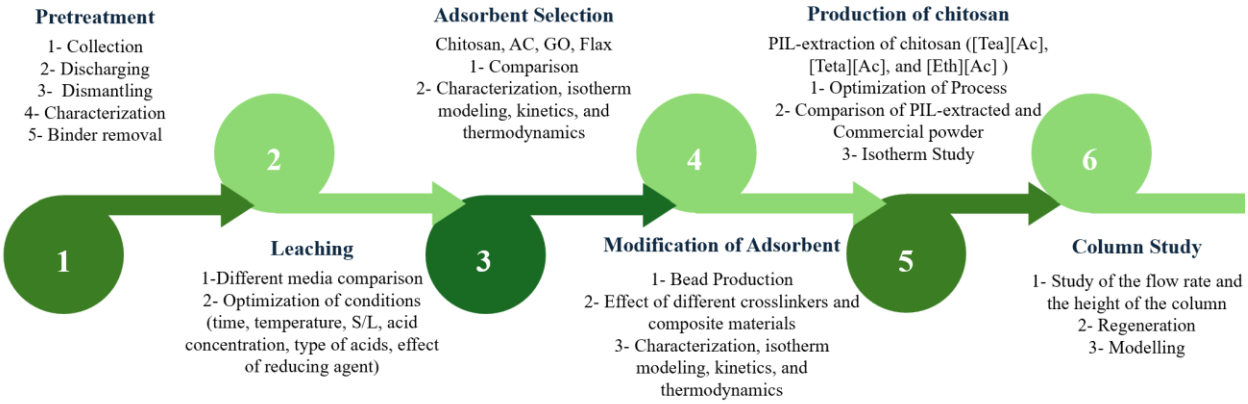

Figure 1.1. The flowchart of the objectives and different phases of the study.

1.3. Methodology

As shown in Figure 1.1, several stages are involved, including the characterization of raw materials, LIBs' cathode materials, thermal treatments (to decompose binders), assessment and optimization of leaching media, comparison of different adsorbents to separate metals, selection of the best adsorbent, modification of the adsorbent, optimization of the separation process, production of chitosan using a greener method, and column studies. Here is a summary of the stages:

- Collection of spent batteries and discharging are the first steps.
- Dismantling and disassembly of the spent batteries to separate cathode materials from anode materials and the other parts of the batteries.
- Thermogravimetric analysis (TGA), X-ray powder Diffraction Analysis (XRD), Scanning Electron Microscope (SEM) coupled with Energy Dispersive X-ray Spectroscopy (EDS), Fourier Transform Infrared Spectroscopy (FT-IR), Brunauer–Emmett–Teller (BET), Inductively Coupled Plasma Spectroscopy (ICP), and Atomic Absorption Spectroscopy (AAS), are employed to determine the thermal behavior of cathode materials, the material

phases, the material surface, analyze the functional groups, the specific surface area, and measure metal concentrations, respectively.

- As an essential pretreatment stage, the binder materials should be removed using thermal treatment to increase efficiency. Different furnace atmospheres (air and inert), process times, and temperatures were examined to optimize thermal treatment. The optimal condition is selected and applied in subsequent steps.

- Leaching parameters should be optimized in terms of acid type and concentration, time, temperature, solid-to-liquid ratio (S/L), and the effect of adding a reducing agent at a specific dosage. Design of experiments is used to plan and statistically analyze experiments.

- Different waste materials, such as chitosan, activated carbon produced from coconut shells, graphene oxide, and flax fiber, have been investigated to assess and compare their performance in adsorbing metals, and the most effective adsorbent is selected for modification. Thermodynamics, kinetics, and isotherms will be investigated.

- Chitosan is selected as the best adsorbent for selectively separating Co, Mn, and Ni, while leaving Li in the solution. The effect of different parameters (initial concentration, pH, and dosage) was investigated. Isotherm models, kinetics, and thermodynamics were studied. Desorption of the critical metals was also investigated.

- Beads are produced with various crosslinkers and composite materials, and the selected one is evaluated through adsorption parameters, isotherms, kinetics, and thermodynamic analyses, along with desorption studies.

- Chitosan production via a greener route using a protic ionic liquid is investigated and optimized through the design of experiments. Its performance is compared with that of a commercial powder, and isotherm modeling was also conducted.

- The feasibility of scaling up is assessed through column studies to explore the continuous process. The effects of flow rate and bed height are examined, column modeling is performed, and the results are compared with those of batch experiments.

1.4. Novelty

As noted, Li-ion battery recycling is of paramount importance in today's world, where demand for portable electronic devices and electric vehicles is rapidly increasing. These batteries, although efficient and long-lasting, pose significant environmental challenges if not managed properly. However, conventional methods for recycling LIBs are energy-intensive or require harsh conditions for metal recovery, which could pose environmental risks. In addition, there is a need to explore more efficient, environmentally compatible metal separation methods, such as selective extraction and the use of waste materials, to enhance current practices.

This study presented a novel, environmentally friendly integrated leaching-and-sorption process for battery recycling, significantly advancing research in the field. It proposes a novel, essential method for recovering critical metals from spent Li-ion batteries, addressing the need for sustainable battery management. By recovering valuable materials in a greener environment and using waste as an adsorbent, the process not only reduces environmental impact but also conserves energy resources. Furthermore, using waste can bring about the "circular economy" and “waste-to-treat-waste” concepts and promote "sustainability".

1.5. Research Outline

This dissertation is composed of 10 chapters. In the first chapter, the background and importance of recycling LIBs from an environmental and economic perspective are discussed. Also, a summary of the methodology is discussed. In the second chapter, a comprehensive literature review is presented, covering battery structures, conventional methods for recycling LIBs, and gaps and research opportunities. The advantages and disadvantages of conventional methods are investigated, and the adsorption process is introduced as a novel method for recycling LIBs. In Chapter Three, the detailed materials and methods for the completed steps are discussed. In chapters four to eight, the achieved results are presented as five scientific publications. Chapter nine integrates the findings and conclusions from all phases, providing a summary overview

organized into broader categories. Chapter ten summarizes the conclusions derived from this research. Recommendations for future work are then presented, highlighting areas with potential for development and improvement. Chapter eleven provides the complete citations for all references used in the thesis. It was decided to compile all references in a single chapter rather than placing them at the end of each chapter to prevent repetition. Also, the appendix provides detailed results on pretreatment and additional data from stages. This chapter also provide data that previously presented at international conferences on adsorbent selection (*Sustainable Recovery of Critical Metals from Spent Lithium-Ion Batteries Using Adsorption*, International Conference on Energy, Resources, Environment, and Sustainable Development, China, 2024) and the selection of a crosslinker for bead production (*Eco-Friendly Beads for Sustainable Recycling: Functionalized Chitosan for Critical Metal Recovery from Spent Lithium-Ion Batteries*, Recycling and Waste Management, Italy, 2025).

Chapter 2 LITERATURE REVIEW

2.1. Lithium-ion battery structure

As shown in Figure 2.1, LIBs consist of two electrodes, positive and negative, electrolyte, collectors, and separators (Baum et al., 2022; Gaines, 2018; Kader et al., 2021). Generally, batteries consist of 66 wt.%, 17 wt.%, 4 wt.%, 3 wt.%, and 10 wt.% of cells, housing, electronics, cables, and other components, respectively (Windisch-Kern et al., 2022). Each part, which has a specific task, is produced from materials that may be both valuable and hazardous. For instance, 60% of cell materials are cathode, anode, and binder materials. Figure 2.2 shows the typical composition of LIBs.

There are different types of cathode materials in LIBs, including lithium cobalt oxide (LCO), lithium iron phosphate (LFP), lithium manganese oxide (LMO), lithium titanium oxide (LTO), lithium nickel cobalt aluminum oxide (NCA), and lithium nickel manganese cobalt oxide (NMC), each serving a specific application (Paul and Shrotriya, 2025). LMO and NMC batteries are primarily used in portable electronic devices and automotive applications, such as the Chevy Volt, BMW i3, and Nissan models. However, LMO is less stable and dense than other types, which limits its use. Many companies, such as BMW, BYD Auto, Renault, Tesla, and Volkswagen, to name a few, are utilizing NMC and NCA batteries due to their higher energy density compared to other battery types (Ciez and Whitacre, 2019; Windisch-Kern et al., 2022). LFP batteries are usually employed in electric buses (Ciez and Whitacre, 2019).

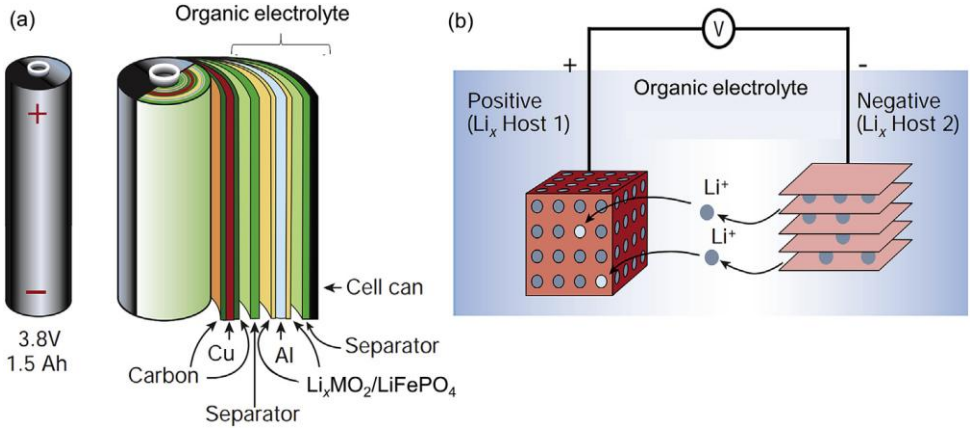

Figure 2.1. Different parts of a) a cylindrical LIB, and b) the operation mechanism of LIBs (C. Liu et al., 2019).

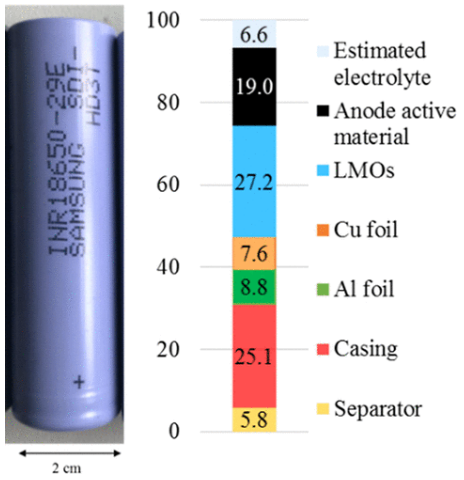

Figure 2.2. Li-ion battery composition (Vanderbruggen et al., 2022) .

2.1.1. Cathode

The cathode, the positive electrode, has been made from various lithium-based metal oxides. As mentioned, the common cathode materials are lithium cobalt oxide, lithium iron phosphate, lithium manganese oxide, lithium nickel cobalt aluminum oxide, and lithium nickel manganese cobalt oxide. NMC batteries' composition has been changing since 2000 from 1:1:1 ($LiNi_{1/3}Mn_{1/3}Co_{1/3}O_2$) to 6:2:2 ($LiNi_{0.6}Mn_{0.2}Co_{0.2}O_2$) and 8:1:1 ($LiNi_{0.8}Mn_{0.1}Co_{0.1}O_2$) (Windisch-Kern et al., 2022). Cathode materials are attached to the aluminum surface, i.e., collectors (Golmohammadzadeh et al., 2022; Kader et al., 2021).

2.1.2. Anode

The negative electrode, also known as the anode, is typically made from carbon-based materials. Other oxide materials, such as tin oxide (SnO_2), iron oxide (Fe_2O_3), manganese oxide (Mn_3O_4), copper oxide (CuO), lithium titanium oxide (LTO), and cobalt oxide (Co_3O_4), have been used; however, they are not commercially available. Graphite is the most common carbon-based material used for LIB anodes. LTO is the only anode material, other than graphite, used to date. Generally, anode materials are attached to a collector made from a copper sheet (Golmohammadzadeh et al., 2022; Kader et al., 2021; Piątek et al., 2021).

2.1.3. Electrolyte, Binders, and Separator

Electrolytes, binders, and separators in LIBs are typically composed of organic compounds. The electrolyte is a lithium salt dissolved in an organic solvent, a mixture of ethylene carbonate and dimethyl carbonate. The common salts are lithium hexafluorophosphate ($LiPF_6$), lithium hexafluoroarsenate ($LiAsF_6$), lithium perchlorate ($LiClO_4$), lithium triflate ($LiCF_3SO_3$), bis (trifluoromethanesulfonate) imide ($Li(SO_2CF_3)_2$), and lithium tetrafluoroborate ($LiBF_4$). The electrolyte is liquid, with high permittivity and low viscosity. Binder, which binds separators to the electrode materials, is made of Poly(vinylidene fluoride) (PVDF), polytetrafluoroethylene (PTFE), and carboxymethylcellulose (CMC). To separate the cathode and anode, separators are utilized. Typically, the separator is made of polyethylene (PE) or polypropylene (PP) and provides ionic conductivity for the electrolyte, preventing short-circuiting. All materials are wrapped in an iron, aluminum, or plastic casing (Golmohammadzadeh et al., 2022; Kader et al., 2021).

2.2. Recycling Method

Conventional methods for recycling LIBs include pyrometallurgy and hydrometallurgy. Direct recycling is also another option for recycling LIBs (Dobó et al., 2023; Sommerville et al., 2020). Each method has advantages and disadvantages, which are presented in the following sections.

2.2.1. Direct recycling

The direct recycling method is a non-destructive and selective method for regenerating cathode materials. In addition to being cost-effective, the process is energy-efficient and is completed in just a few steps. In this method, all materials are recycled and used to manufacture new batteries. The process, however, is highly dependent on several factors, including the type of battery, the battery's sorting, extensive pretreatment, the accumulation of defects and impurities in the active materials, and the battery's health state. For example, LFP-type LIBs can be recycled using this method (Sloop et al., 2020). The olivine-structured $LiFePO_4$ experiences an irreversible phase transformation over extended cycling, primarily caused by Fe(II) migration and hindered Li ion diffusion. Thus, the central challenge in the direct recycling of spent LFP lies in stabilizing Fe atoms within the crystal lattice to enhance Li-ion migration and overall electrochemical performance (Han et al., 2025). Moreover, disassembly should be done manually (Baum et al.,

2022). Therefore, the process has limitations and is not economical from an industrial perspective (Gaines, 2018). Cathode-to-cathode recycling, mechanical recycling, electrochemical recycling, and cathode-healing recycling all fall under direct recycling. In each method, the cathode particle is recovered without decomposing into the individual metals (Sloop et al., 2020).

2.2.2. Pyrometallurgy

Pyrometallurgical processes require a high temperature to recover metals. At such high temperatures (1200-1800 °C), plastics, electrolytes, and carbon-based materials decompose, forming a mixed-metal alloy as the final product. The process is simple and adaptable, with rapid kinetics. Furthermore, owing to the high values of Ni and Co, pyrometallurgical processes may be suitable for high-Co and Ni-content batteries (Sommerville et al., 2020). However, pyrometallurgical recycling of spent LIBs is energy-intensive, often results in losses of Li and aluminum to slag, and generates significant emissions that require complex off-gas treatment. Smelting and reduction are the two principal pyrometallurgical processes in which graphite can be used as a reductant (Kader et al., 2021). Reduction roasting is suitable for LIB recycling because it is simple and effective. In this process, graphite, hydrogen, or biomass can act as reducing agents, though carbon is most commonly used. During high-temperature treatment (typically 600–1000 °C), the cathode materials are reduced to lithium oxides, lithium carbonate, and transition-metal oxides or metals. These products can then be readily separated and recovered via water or mild-acid leaching, enabling selective extraction of valuable metals from spent lithium-ion batteries (Han et al., 2025). Despite its simplicity, the reduction roasting process suffers from several drawbacks, including high energy consumption, CO_2 emissions, poor lithium recovery, and complex downstream separation, making it less suitable for sustainable, large-scale LIB recycling.

2.2.3. Hydrometallurgy

As an alternative to pyrometallurgy for recycling LIBs, low-temperature hydrometallurgical methods can be employed. The maximum temperature is 150°C, and the process comprises several stages: leaching, separation, and purification. Although the process raises some environmental concerns that should be considered, its impacts, such as dioxin emissions and the environmental effects of chloride compounds, are significantly less severe than those of pyrometallurgical

processes (Gaines, 2018; Kader et al., 2021). Hydrometallurgy can be applied to different types of LIBs and requires low energy. The process has high capacity, is cost-effective, and yields high-purity final products (Gaines, 2018; Kader et al., 2021). The process typically involves using strong acids, both organic and inorganic, to dissolve LIB materials, which makes it complex (Gaines, 2018). Prior to leaching, several pretreatment steps, such as sorting, dismantling, shredding, and physical separation, should be performed to improve process efficiency. Using appropriate pretreatment processes, Cu and Al collectors can be separated immediately (Gaines, 2018; Han et al., 2025).

2.2.3.1. Pretreatment

Pretreatment processes play a crucial role in battery recycling by enhancing recovery efficiency and reducing costs. They can be classified into two main categories, physical separation and chemical separation. Physical separation processes in which there is no significant change in the material compositions are sorting, discharging, dismantling, crushing, sieving, flotation, magnetic separation, and air separation. Sorting is a crucial stage for improving recycling efficiency (Wang et al., 2019). Chemical separation processes are thermal treatments such as pyrolysis, incineration, calcination, and roasting (Golmohammadzadeh et al., 2022; Mansur et al., 2021; Sommerville et al., 2020). The following are descriptions of pretreatment processes used to remove or recycle materials and metals from LIBs.

a) Discharging and disassembling

Discharging is the first step of dismantling and is considered a safety process to prevent battery explosions. Discharging can be carried out in a conductive solution, such as sodium chloride (NaCl) or sodium sulfate (Na_2SO_4), e.g., 10% NaCl or 0.8 mol/L NaCl + 0.8 mol/L $FeSO_4$, to discharge LIBs (Zhang et al., 2022). The common solution for discharging batteries is a NaCl solution at 5-20 wt.% concentration, with a discharge time of 12-72 hours. Then, the batteries should rest for another 24 hours before being dismantled. Another way to discharge batteries is to cool them in liquid nitrogen at -175 to -200 °C (P. Li et al., 2024). The other method is short-circuit discharge, which connects the positive and negative terminals of spent LIBs to an external resistor, allowing the residual energy to be dissipated as heat. It is mainly suitable for small

batteries, as rapid discharge in larger ones can cause excessive heat buildup and potential safety issues, such as ignition. Among the common discharging methods, the salt solution method is popular because of its low cost and quick discharge rate, although it produces toxic gases and large amounts of wastewater; the short-circuit method offers fast discharge but generates excessive heat and risks of explosion; while the cryogenic method is the safest and most environmentally friendly option, but requires specialized equipment and high operational costs (P. Li et al., 2024).

After discharging, the casing can be separated, and the feed goes through sieving and shredding processes (Golmohammadzadeh et al., 2022; Windisch-Kern et al., 2022). It is necessary to dismantle the whole battery to enhance recovery efficiency (Baum et al., 2022). However, the discharging step is time-consuming, expensive, and requires a large facility. For this reason, the industry bypasses the discharging process, classifies batteries by cathode composition, and shreds each battery stream separately. By doing so, the risk of explosion is minimized, and the area is considered safe. However, metal oxide and graphite agglomerations may have resulted in this manner. Hence, some steps need to be taken before or during the shredding process, as well as to ensure that LIBs are recycled effectively (Golmohammadzadeh et al., 2022). After this step, the product, known as a black mass (BM), contains cathode materials, anode materials, binders, casing, plastics, and collectors.

b) Crushing or shredding

Initially, the batteries are shredded and broken into smaller components to facilitate separation in subsequent stages. Then, future crushing can be applied to reduce the particle size to increase its surface area (Golmohammadzadeh et al., 2022). Hammer crushing, shear crushing, impact crushing, and cutting milling are some technologies to crush BM. Also, there are two types of crushing, wet and dry. Although wet crushing can achieve finer particles than dry crushing, it may cause agglomeration, allowing water to pass most particles through the mesh. Therefore, the next step, sieving, cannot be done properly.

In contrast, dry crushing yields a more uniform particle-size distribution. Hence, dry crushing is preferable (Zhang et al., 2022, 2013). At an industrial scale, however, the crushing stage can be combined with the discharge step to save time, reduce costs, and eliminate the need for additional facilities. To prevent thermal runaway, an exothermic reaction within the batteries, crushing or

shredding can be carried out in an inert atmosphere (CO_2, N_2, or Ar) (Peschel et al., 2022). Water spray can help reduce temperature during the crushing/shredding process, thereby reducing the risk of explosions. Shredding can also be done while immersing LIBs in water (Sommerville et al., 2020). Cryogenic crushing is an effective technique for simultaneously crushing and discharging batteries. LIBs are cooled down by liquid N_2 or dry ice. At low temperatures (-175 °C to -195 °C), batteries become brittle and inactive, thereby allowing them to be safely crushed (Windisch-Kern et al., 2022; Zhong et al., 2020b, 2020a). Alternatively, crushing can be performed at high temperatures. LIBs should be heated to 300 °C for discharge; therefore, binders and electrolytes can also be removed from the BM. However, it requires additional equipment to capture and recycle hazardous gases (Mansur et al., 2021). Alternatively, in laboratory environments where only a small number of LIBs need disassembly, manual disassembly is usually employed (Han et al., 2025).

c) Sieving

A sieving stage is a crucial step in particle size classification. Collectors such as aluminum and copper are separated by sieving because they have larger particle sizes. LIB's materials are separated into two categories: course and fine. Black mass (cathode and anode materials) tends to be in the fine fraction, while collectors, casing, and plastic are accumulated in the coarse fraction. Sieving can be implemented in various configurations, including cyclones, air separation, zigzags, and vibration, among others (Golmohammadzadeh et al., 2022). Sieving can be performed using either a dry or a wet method, depending on the crushing approach. When comparing the distribution of crushed products across three particle size ranges (<0.25 mm, 0.25–2 mm, and >2 mm) under various crushing conditions, wet sieving was found to be more effective at producing fine-grained fractions. Subsequently, the metal content within each particle-size range was analyzed to assess separation efficiency (Han et al., 2025). Instead of sieving, pneumatic separation can be utilized to separate black mass from collectors and electrolytes. It separates light metals from heavy metals using sufficient airflow. However, it requires a volatilization step (e.g., at 130 °C) as a pretreatment to remove certain carbon-based materials, such as binders (Zhong et al., 2020b, 2020a).

d) Magnetic separation

The magnetic separation of the magnetic components of LIBs, such as Al alloy and steel casing, can be carried out to separate these parts from other materials (Golmohammadzadeh et al., 2022; Han et al., 2025). Nevertheless, it is an unnecessary step that can be omitted. Due to the differences in conductivity between Cu and Al, eddy currents are utilized as a method of magnetic separation for removing Cu and Al from non-ferrous parts of LIBs (Zhang et al., 2022). In an eddy current separator, nonferrous metals are separated from input waste by using a powerful magnetic field, and separation is achieved using eddy currents.

e) Thermal treatment

Thermal treatment can be used to decompose binder materials. Thermal treatments at temperatures ranging from 350 to 850 °C have been reported to remove binders, electrolytes, separators, and carbon-based materials (Golmohammadzadeh et al., 2022). Heat not only decomposes carbon materials but also improves the electrode surface quality, thereby enhancing flotation and leaching efficiency (Dobó et al., 2023; H. Huang et al., 2022). Different reactions may occur at high temperatures, including volatilization, decomposition, and oxidation. Therefore, it is necessary to optimize the temperature (H. Huang et al., 2022). For example, it has been reported that PVDF may decompose at approximately 350°C, while other materials remain unaffected (Mansur et al., 2021). Another study reported that the maximum temperature for this stage is 550 °C, above which graphite decomposes, an undesirable outcome. In another study, the optimal condition for removing the binder and electrolyte was reported to be 500 °C for 15 min (Zhang et al., 2022).

The pyrolysis temperature can be optimized using thermogravimetric analysis (TGA). The results for LIB cathode materials typically show three stages: decomposition of residual electrolytes, decomposition of binders, and carbothermal reactions. The first mass reduction is for the volatilization of residue electrolytes and adsorbed water (30-400 °C). Binder decomposition occurs in the second stage around a temperature of 450-600 °C. During the last mass reduction above 650 °C, carbothermal reactions and the creation of metal alloys may occur (Zhang et al., 2021).

Additionally, at temperatures above 600 °C, the Al layers become brittle, which hinders the proper separation of the active metal powders (Dobó et al., 2023). The pyrolysis process can be carried out under either an inert or an air atmosphere. Despite the effectiveness of aerobic pyrolysis in

removing binder materials, the emission of hazardous gases may cause environmental concerns. On the other hand, in anaerobic pyrolysis, utilizing an exhaust gas collection system, the pyrolysis gases can be captured and recycled in a step-by-step process (Zhang et al., 2021).

In summary, pyrolysis is an essential step for decomposing binders to separate collectors from cathode and anode materials and can enhance subsequent steps, namely flotation and leaching. However, because of the emission of hazardous gases, such as hydrogen fluoride, scrubbers are required to remove these contaminants. Additionally, to prevent the oxidation of Al, this stage should be performed under a vacuum or in an inert atmosphere. Using furnaces with controlled atmospheres can also promote gas recycling. By doing so, the production of secondary pollution would be minimized (Dobó et al., 2023; Windisch-Kern et al., 2022).

The removal of binders can also be achieved using cryogenic grinding to overcome concerns associated with high temperatures. Binders are removed at an extremely low temperature. Using liquid N_2, batteries are cooled to the glass transition temperatures of the binders and electrolytes. As a result, battery materials become brittle, and the peel-off efficiency of the electrode materials improves. At such temperatures, Cu and Al exhibit different behaviors and become stronger. Therefore, during grinding, the Cu and Al collectors are separated from the active materials. Unfortunately, the technology has not been well developed and is costly; as a result, large-scale implementation would not be feasible. The outputs of this stage are the separated active materials, the Cu and Al collectors, the binders, and the electrolytes. Because of the separation of binders from graphite, the next step, flotation, is done more efficiently (Liu et al., 2020; Wang et al., 2019; Yu et al., 2021; Zhang et al., 2022).

f) Chemical Dissociation

In some cases, chemical processes may be preferred over thermal treatment to remove impurities or to separate LIB materials. Using sodium hydroxide (NaOH) as a leaching solution enables the separation of the remaining Al foil (Mansur et al., 2021). Additionally, sonification facilitates binder removal via dissolution in organic solvents. N-methyl-2-pyrrolidone (NMP), Dimethylformamide (DMF), dimethyl acetamide (DMAC), dimethyl sulfoxide (DMSO), and acetone have been used to remove binders from spent LIBs. Cathode materials are soaked in solvents at 100 °C for 1 h. The ultrasonic process can accelerate the separation of collectors that

adhere firmly to cathode/anode materials and cannot be separated by crushing and sieving (Mansur et al., 2021). However, this process is time-consuming, expensive, and requires a large facility. Moreover, it produces hazardous gases and secondary pollution and requires additional cleaning equipment. Such solvents are hazardous, toxic, and irritating.

g) Flotation

Flotation can be used to separate cathode and anode materials (graphite). Separating graphite offers two main benefits. First, it can reduce excessive acid consumption, and second, it helps prevent a future shortage of graphite. Therefore, recycling provides an important opportunity to reuse it (Y. Wang et al., 2022). This method is an efficient means of separating materials based on differences in surface hydrophilicity. The process may, however, be hindered by organic materials, such as binders and residual electrolytes, which reduce the floatability difference between graphite and cathode materials (P. Li et al., 2024; Y. Wang et al., 2022). These carbonaceous materials must be removed prior to the flotation step.

Froth flotation has been used, both in the industrial and laboratory scales, to separate graphite from cathode materials (Gaines, 2018). This process is quick, but it consumes a considerable amount of water, which can be recycled (Salces et al., 2022). Salces et al. (2022) found that using recycled water did not significantly affect flotation efficiency. Some Li accumulations have been detected in the process water, which should be removed. Binder materials can reduce flotation efficiency. Therefore, pretreatment methods should be used to improve flotation efficiency (Salces et al., 2022; Vanderbruggen et al., 2022). First, binder materials are removed by cryogenic grinding, heat treatment, and chemical dissolution. To further enhance efficiency, residual organic materials are removed using attrition and ultrasonic cleaning (Salces et al., 2022). In froth flotation, collectors and frothers are used (Golmohammadzadeh et al., 2022; Salces et al., 2022; Y. Wang et al., 2022). Common frothing agents used to produce bubbles for separating graphite from metal oxides including pine oil, alcohols, and cyclic carbonates.

2.2.3.2. Leaching

Following pretreatment, a leaching step should be performed to dissolve metals in a specified solution. Media and conditions for leaching are selected according to the pretreatment steps that

batteries undergo (Mansur et al., 2021). Acidic or basic media can be used under different conditions to dissolve various materials. Also, selective leaching can be achieved using a determined medium. In general, however, leaching selectivity is low, particularly with strong acids. If the selected medium is acidic solutions, metals can be dissolved in inorganic acids such as sulfuric acid (H_2SO_4), hydrochloric acid (HCl), phosphoric acid (H_3PO_4), and nitric acid (HNO_3) or organic acids such as citric acid, acetic acid, lactic acid, malic acid, and gluconic acid. When metals dissolve in solution, oxidation or reduction reactions occur due to charge transfer. Temperature, pH, acid/base concentration, solid-to-liquid ratio (S/L), time, and reducing agent dosage should be optimized based on the target metals and initial conditions (Golmohammadzadeh et al., 2022; He et al., 2024; Paul and Shrotriya, 2025). As the acid concentration increases, the metal recovery rate generally increases; however, there is a limit to this improvement, and efficiency decreases beyond a certain point. The S/L ratio has a limitation. A high S/L ratio hinders recovery. Leaching rates can also be improved by increasing both temperature and time. Stirring speed typically has a minimal impact on the process.

a) Inorganic acids

Some studies have examined the leaching of LIBs using inorganic acids. The industry prefers inorganic acids for leaching feed materials because they dissolve all metals and achieve high recovery rates. Hydrochloric acid, sulfuric acid, phosphoric acid, and nitric acid are examples of inorganic acids (Zeng et al., 2021). The efficiencies of the inorganic acids to leach Li and Co are in order of H_2SO_4 ~ HCl > HNO_3 > H_2SO_3 (Mansur et al., 2021). Reagents such as hydrogen peroxide (H_2O_2) can improve the leaching efficiency. The most commonly used acid is H_2SO_4, with or without the addition of H_2O_2 (Mansur et al., 2021). The leaching efficiency with inorganic acids is high and can be rapid. Conversely, the use of inorganic acids has some disadvantages, including the production of hazardous gases such as SO_3, Cl_2, and NO_x, as well as the transport of hazardous residues from untreated discharges or dumped residues into the soil and groundwater, which pose a threat to health and the environment (Roshanfar et al., 2019; Zeng et al., 2021). For example, the reactions of LCO cathode materials with sulfuric acid, nitric acid, and hydrochloric acid are as follows (Mansur et al., 2021):

$$3H_2SO_4 + 2LiCo_2 + H_2O_2 \rightarrow Li_2SO_4 + 2CoSO_4 + 5H_2O + 1.5O_2 \quad (2\text{-}1)$$

$$3HNO_3 + LiCo_2 \rightarrow LiNO_3 + Co(NO_3)_2 + 1.5H_2O + 0.25O_2 \quad (2\text{-}2)$$

$$3HCl + LiCo_2 \rightarrow LiCl + CoCl_2 + 1.5H_2O + 0.25O_2 \quad (2\text{-}3)$$

The optimum conditions were reported as follows: an S/L ratio of 20-60 g/L, a temperature of 40-95 °C, an acid concentration of 1-6 M, a reagent concentration (H_2O_2) of 0.25-5% v/v, and a reaction time of 60-240 min. The leaching recovery of the metals can reach more than 95% for all types of batteries (Mansur et al., 2021).

It has been reported that phosphoric acid can dissolve Li and precipitate Co as $Co_3(PO_4)_2$. In this regard, Li can be separated from other metals in a single step (Chen et al., 2017). Chen et al. (2017) investigated the leaching efficiency of phosphoric acid to leach LCO cathode materials. The results showed that at 40 °C for 60 min, with an S/L ratio of 0.05 g/mL and an acid concentration of 0.7 M, using 4 vol.% H_2O_2, 99% of Co was precipitated. Chen et al. (2018a) reported that a mild phosphoric acid solution (0.8 M) can selectively leach Li from all types of batteries within 1 h. Their results demonstrated that nearly 100% of Li leached selectively across all battery types. Another study has shown that 4 M HCl in 60 minutes at 80 °C and an S/L of 20 g/L leached NMC111 ($LiNi_{0.33}Co_{0.33}Mn_{0.33}O_2$) (Chen et al., 2017). Porvali et al. (2020) investigated the use of a low concentration of sulfuric acid (0.5M) with Cu-Fe^{2+} as a reductant to leach LCO. The results showed that 92% of Co recovered at 30 °C within 2 h.

b) Organic acids

Organic acids are environmentally friendly, efficient, less corrosive, and biodegradable compared to inorganic acids. In recent years, the use of organic acids for leaching LIBs has attracted increasing attention due to their superior safety and reduced environmental impact. However, organic acids are more expensive than inorganic acids and generate more stable complexes (Golmohammadzadeh et al., 2022; Punt et al., 2021; Zeng et al., 2021). Organic acids, such as oxalic acid, acetic acid, citric acid, tartaric acid, ascorbic acid, lactic acid, and gluconic acid, have been employed to leach metals with lower concentrations of acids compared to inorganic acids over a wide range of pH values (Golmohammadzadeh et al., 2022). To leach metals efficiently, organic acids still require the presence of reducing agents. Previously used reducing agents include

H_2O_2, Na_2SO_3, $Na_2S_2O_3$, $NaHSO_3$, tea waste, and Phytolacca Americana branch powders. The most common reducing agent still is H_2O_2 (Golmohammadzadeh et al., 2022).

Parameters, including S/L (g/L), T (°C), time (min), acid concentration (M), and reagent concentration (% v/v), should be optimized. As organic acid concentrations increase, metal recovery rates generally increase. However, there is a limit to the improvement in recovery, and efficiency begins to decline after a certain point. In the leaching solution, a higher H^+ concentration is associated with higher acid concentrations, resulting in a more acidic environment. The rate at which metals are leached depends on the concentration of H^+. Thus, as the acid concentration increases, the rate of recovery increases. However, some chelates form at lower pH, resulting in reduced metal recovery. The S/L ratio has limitations; a high S/L ratio hinders recovery because it is associated with a lower volume-to-area ratio, which impairs metal recovery. Furthermore, leaching rates can be increased by increasing temperature and time, as higher temperatures and longer contact times facilitate the dissociation of organic acids. Stirring speed typically has a minimal impact on the process (Roshanfar et al., 2019).

Among the organic acids mentioned, citric acid is the most widely used. Citric acid, a weak acid with high solubility in water, is capable of dissolving cathode materials effectively. The leaching mechanism involves the diffusion of citric acid into the cathode surface, thereby promoting metal dissolution. During the diffusion process, citric acid dissociates and provides three hydrogen ions as follows (Chaudhary et al., 2023):

$$C_6H_8O_7 \rightarrow C_6H_5O_7{}^{3-} + 3H^+ \qquad pK_{a1} = 3.11 \qquad (2\text{-}4)$$

Citrate ions form a complex with Li, Co, Ni, and Mn. Figure 2.3 shows dimeric complexes and monomeric complexes of metals with citric acid. Complexation and recovery can be accelerated by increasing the temperature and acid concentration, and by reducing the dosage of the reducing agent. Although the recovery rate can be enhanced by increasing the acid concentration to 2 M, it decreases beyond this concentration (Chaudhary et al., 2023). For example, 2 M citric acid, along with 3.0% v/v H_2O_2, a solid-to-liquid ratio of 20 g/L, a temperature of 80 °C, and a time of 90 min, can leach $LiCoO_2$ cathode materials to 100% Co and Li (Mansur et al., 2021). Another study showed that a 1.25 M citric acid solution, 2 vol% H_2O_2, a 20 g/L S/L ratio, and a temperature of

90 °C for 30 min can recover 99% of Co and Li (Chaudhary et al., 2023). Ethylene glycol (EG) and citric acid (Cit) have been used to leach $LiNi_{1/3}Co_{1/3}Mn_{1/3}O_2$ cathode materials. At optimum conditions, 99.1% Li, 96.2% Co, 97.6% Ni, and 98.3% Mn have been leached. In this system, Al foil can be separated because Al leaching was inhibited by citric acid. The conditions were an EG/CA ratio of 2.5:1, an S/L of 15 g/L, and a temperature of 95 °C in 10 h (Zeng et al., 2021).

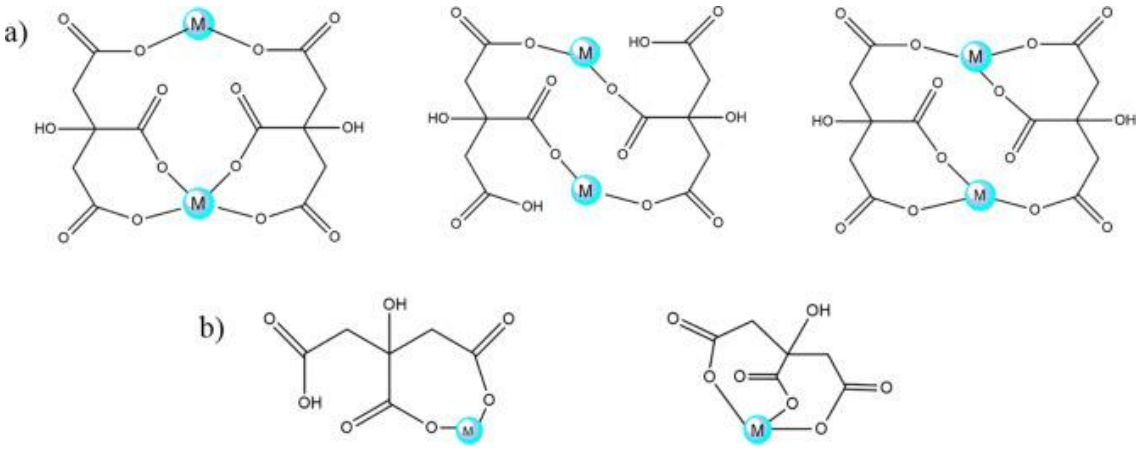

Figure 2.3. Different geometries of citric acid coordination with metals (a and b show dimeric and monomeric complexes, respectively) (Zabiszak et al., 2018).

Acetic acid, also known as vinegar, is another cost-effective and efficient organic acid for recovering metals from LIBs. During dissociation, acetic acid releases one hydrogen. The dissociation reaction is as follows (Chaudhary et al., 2023):

$$CH_3COOH \rightarrow CH_3COO^- + H^+ \qquad PK_a = 4.75 \tag{2-5}$$

In the same manner as citric acid, temperature is the most effective factor in the recovery of metals using acetic acid. However, it has been reported that increasing temperature enhances Li recovery while reducing Co recovery. This can result from the nature of Li-Co reactions with acetate ions. Co and acetate chelation is an exothermic reaction, whereas Li and acetate chelation is an endothermic reaction. Interestingly, all metals except aluminum were reported to be leached by acetic acid. Prior to the separation process, it can be used to reduce impurities (Chaudhary et al.,

2023). Pinna et al. (2021) has used acetate media to recover Li and Co, with recoveries approaching 100%. Afterward, 90% of Co and 92% of Li were separated as Co-oxalate and Li-carbonate, respectively. It was reported that, at 80 °C for 60 min, with an acid concentration of 1.7 M, an H_2O_2 concentration of 6% v/v, and an S/L of 8 g/L, the recovery was optimized. The rate of recovery was also unaffected by stirring speed (Pinna et al., 2021).

Spent LIBs can be leached by ascorbic acid, also known as vitamin C, a naturally occurring organic acid. It can act as both a leaching and a reducing agent. The dissociation reaction is as follows:

$$C_6H_8O_6 \rightarrow C_6H_6O_6^- + 2H^+ \qquad PK_a = 4.1 \tag{2-6}$$

Spinach, beets, and other plants contain oxalic acid, a natural acid (Yang et al., 2022a). Oxalic acid has been used as a precipitation and leaching agent in many studies. Oxalic acid leaches Li but precipitates Co, Ni, and Mn. A previous study showed that 1 M oxalic acid at 80 °C, with an S/L of 50 g/L, recovered more than 98% of Li and Co as leachate and precipitate, respectively, within 120 min. Additionally, increasing the oxalic acid concentration helps improve the recovery rate (Gao et al., 2022).

Unfortunately, the weak acidity of organic acids reduces their dissociation and production of hydrogen ions. In this regard, it is necessary to use high temperatures, a high solid-to-liquid ratio, and large quantities of acid and reagents to improve metal recovery rates (Yang et al., 2022a). Additionally, organic acids are expensive and have low leaching capacity per unit volume. As a result, they are limited in their ability to scale up (Gao et al., 2022). Therefore, the synergistic effects of inorganic and organic acids have been investigated to overcome the limitations and disadvantages mentioned above. For example, Yang et al. (2022) examined the synergic effect of sulfuric and oxalic acids. As both a leaching and a reducing agent, oxalic acid can eliminate the need for additional reductants, providing lower production costs. In this research, the optimized condition was 2.5 mg/L of sulfuric acid, 20 g/L of oxalic acid, the S/L ratio of 1/10 g/L, and a temperature of 85 °C in 100 min, and the recovery of Li, Ni, Co, and Mn were 99.3%, 98.4%, 96.9%, and 97.5%, respectively (Yang et al., 2022a). The proposed reaction is as follows:

$$LiNi_{0.8}Co_{0.1}Mn_{0.1}O_2 + H_2SO_4 + H_2C_2O_4 \rightarrow Li_2SO_4 + NiSO_4 + CoSO_4 + MnSO_4 + H_2O + CO_2 \uparrow \tag{2-7}$$

Malonic acid ($C_3H_4O_4$) is another organic acid that is a decent candidate for use as a lixiviant to recover metals. As the strongest organic acid, malonic acid is used in various applications, including spice production, resin additives, adhesives, and pharmaceuticals. In addition, it is more soluble in water than other organic acids. Furthermore, malonic acid acts as a complexing agent in the leaching solution. A study investigated the synergistic effect of malonic and sulfuric acids on the leaching of NMC cathode materials. The results showed that 0.93 M of sulfuric acid and 0.85 M of malonic acid in the S/L ratio of 61 g/L, a temperature of 70 °C, and 5 vol.% of H_2O_2 with a purity of 30% can recover 99.79%, 99.46%, 97.24%, and 96.88% of Li, Ni, Co, and Mn, respectively (Li et al., 2022).

The synergistic effect of phosphoric acid and citric acid has also been examined in the leaching of NMC cathode materials ($LiNi_{0.5}Co_{0.2}Mn_{0.3}O_2$). A low concentration of phosphoric acid (0.2 M) combined with 0.4 M of citric acid at 90 °C with an S/L ratio of 20 g/L in 30 min was able to recover 100% of Li, 93.38% of Ni, 91.63% of Co, and 92.00% of Mn (Gao et al., 2022). A formic acid–acetic acid (FA–AA) synergistic leaching system achieved 96.81% selective lithium recovery from spent NMC cathodes while minimizing transition metal dissolution and enabling acid recyclability up to 90.5% (Zhang et al., 2024). However, large-scale implementation may be constrained by the efficiency of solvent recovery and the need for precise control of reaction conditions.

c) Basic media

Basic media are typically used to selectively leach Cu and Al. N-methyl pyrrolidone (NMP), ammonia, and sodium hydroxide are examples of basic media (Gaye et al., 2019). Gaye et. al (2019) studied the leaching of spent LIBs using NaOH. Results showed an Al recovery efficiency of approximately 59.31%. A slight leaching of Li (about 9%) was also reported. The leaching efficiency of other metals, however, was insignificant. Other studies reported that 5% and 15% NaOH solutions can recover 99% and 58% of Al, respectively (Gao et al., 2022).

By adjusting pH, ammonia can recover Cu, Ni, and Co. The results showed that a medium containing ammonium sulfate as a leaching reagent and sodium sulfate as a reductant is capable of recovering Ni, Co, and Li by more than 98.6% (Gao et al., 2022). The use of $(NH_4)_2SO_4$-

$(NH_4)_2SO_3$ for selective leaching has also been reported. Ni, Li, Mn, and Co recovered in 98%, 98%, 92%, and 81%, respectively, in different precipitated salts (Gao et al., 2022).

d) Selective leaching

Simultaneous leaching of all metals could result in a complex solution that is difficult to separate. Using selective leaching, the target metals are dissolved while the other metals remain in the residue. Alternatively, the process may be referred to as multi-stage leaching, as it involves a second leaching step following the initial selective leaching to dissolve the remaining metals. Li is usually the target metal of a selective leaching process. For example, Li can be selectively leached by oxalic and phosphoric acids. At a given pH and acid concentration, the other metals form strong complexes with oxalate and phosphate ions, thereby precipitating them and complicating subsequent leaching.

As an alternative, roasting reduction may be combined with water leaching to selectively recover Li. In reduction roasting, oxygen is removed from a component using carbonaceous materials. A black mass is first mixed with a carbon-based material, such as carbon black, and then heated at around 550°C for 30 min to 6 h (C. Liu et al., 2019; P. Liu et al., 2019). Li is then selectively leached from the roasted materials using water. The Li recovery rate would exceed 85%, potentially reaching 95%. Another study has reported that after heat treatment of the black mass with 19.9% lignite as a reductant at 650 °C for 30 min, Li was leached by carbonated water, yielding a recovery rate of 84.7% (Hu et al., 2017). Subsequently, other metals were leached with sulfuric acid under the optimum conditions of 3.5 M H_2SO_4 at an S/L ratio of 200 g/L at 85 °C for 3 h.

e) Reducing agents

As spent LIBs contain metals in higher oxidation states, such as Co and Mn (Co(III) and Mn(III)), these metals are difficult to leach. Therefore, an additional reagent is necessary to enhance recovery rates. The term 'reducing agent' or ‘reductant’ refers to chemicals that can donate electrons to electron acceptors. Ideally, the metal reduction potential should exceed that of the reductant to achieve the highest recovery rate. The metal reduction reactions are:

$$Co^{3+} + e^- \leftrightarrow Co^{2+} \qquad E^0(V) = 1.92 \tag{2-8}$$

$$Fe^{3+} + e^- \leftrightarrow Fe^{2+} \qquad E^0(V) = 0.77 \tag{2-9}$$

$$Mn^{3+} + e^- \leftrightarrow Mn^{2+} \qquad E^0(V) = 1.5 \tag{2-10}$$

Reducing agents are hydrogen peroxide (H_2O_2), sodium sulfite (Na_2SO_3), ascorbic acid, iron powder, glucose, lactose, tea waste, vitamins, plant extracts, orange juice, orange peel, sugars, proteins, and agricultural waste (C. Liu et al., 2019; P. Liu et al., 2019). Among them, hydrogen peroxide is widely used in industry and laboratory research because its reduction potential is high enough to donate electrons to metals. The reduction reaction is as follows:

$$O_2 + 2H^+ + 2e^- \leftrightarrow H_2O_2 \qquad E^0(V) = 0.58 \tag{2-11}$$

Hydrogen peroxide does not introduce impurities into the system because the reaction products are oxygen gas and water. It should be noted, however, that because hydrogen peroxide decomposes spontaneously, the gas produced during the reduction reaction may be substantial and could lead to an explosion. Hydrogen peroxide may also act as an oxidizing agent, oxidizing other metals present in the environment (Cu, Al), thereby exceeding the amount needed to be consumed (C. Liu et al., 2019; P. Liu et al., 2019).

$$H_2O_2 + 2H^+ + 2e^- \leftrightarrow 2H_2O. \quad E^0(V) = 1.82 \tag{2-12}$$

Hydrogen peroxide is an extremely reactive chemical, categorized as a hazardous substance (Zeng et al., 2021). Therefore, safer alternative reductants should be considered.

Iron can be used as a reductant, reducing Co and Mn while being oxidized. The reaction for cobalt is:

$$Co^{3+} + Fe^{2+} \leftrightarrow Fe^{3+} + Co^{2+} \tag{2-13}$$

Iron should be in the form of iron sulfate and can be obtained from sources such as iron scrap, pyrite (FeS_2), and LIB casing. Using iron scraps for BMs that already contain Fe is beneficial for improving recovery, as the solution already contains impurities and no additional impurities are introduced. However, if Fe is removed prior to leaching, increasing the impurities is not recommended. Ghessa et al. (2021) have used iron scraps from LIBs' casings in sulfate media. They leached the shells in sulfuric acid and introduced the leachate into the system as the reductant. The recovery rate of Co, Ni, and Li at the optimum conditions of 25 g/L of iron scrap, 10 g/L of S/L, and 150 min of leaching time reached 99.1%, 94.9%, and 90.5%, respectively. Another study has utilized pyrite, the most abundant iron mineral, in conjunction with sulfuric acid. The results showed that the recovery rates of Ni, Co, Mn, and Li exceeded 98% under optimal conditions of 3 M acid, L/S of 40 mL/g, a reductant dosage of 1:0.8, and 80 °C for 2 hours.

Ascorbic acid and salicylic acid are organic acids that can be utilized as reducing agents. In addition to improving recovery rates, ascorbic acid (vitamin C) is a safe, cost-effective organic acid. It has been reported that LIB leaching in sulfuric acid, in the presence of ascorbic acid, can enhance the recovery of Co, Mn, and Li; however, copper remains in the residue. Ascorbic acid is widely used in the production of Cu powder and is capable of reducing Cu-ions to elemental Cu. As a result, the further separation of Cu can be avoided, which is beneficial. Many medicines and cosmetic products contain salicylic acid, which makes it a safe organic acid. It has been demonstrated that the leaching efficiency of spent LIBs in a citrate medium can be improved by adding a small amount of salicylic acid, thereby reducing the utilization of hydrogen peroxide (Xu et al., 2021). The results showed 99.5% and 97% recoveries for Co and Li, respectively, using 1.5 M citric acid, 0.2 M salicylic acid, an S/L ratio of 15 g/L, 6 vol.% H_2O_2, and 90°C for 90 min. In this regard, the use of salicylic acid did not eliminate the need for hydrogen peroxide effectively (Xu et al., 2021).

The application of apple juice, lemon juice, orange juice, and orange peels as reductants has also been investigated. The application of Cu and Al foils as reducing agents has also been investigated. Cu can act more efficiently than Al foil. Adding Cu to the system will prevent future impurities from being added. Cu foils showed promising results in both inorganic and organic acid media. Given the discussion above, further research is required to identify the optimal reductant that is both strong, cost-effective, safe, and environmentally benign. Using waste materials as reducing

agents can contribute to a circular economy and help preserve the environment. Waste is a cost-effective reagent and does not generate secondary pollution.

f) Deep eutectic solvent media

Deep eutectic solvents (DESs) have recently emerged as promising green alternatives to conventional mineral acids for leaching and metal recovery from spent LIBs. DESs are formed by mixing a hydrogen-bond donor (HBD) and a hydrogen-bond acceptor (HBA) in a specific molar ratio, yielding a eutectic mixture with a melting point lower than that of either component (Bhattacharyya et al., 2025; Chongzhi Wang et al., 2024). These solvents can dissolve and bind metal ions via protonation, hydrogen bonding, and coordination interactions, enabling simultaneous leaching and selective separation of critical metals such as Li, Co, Ni, and Mn (R. Liu et al., 2025). Compared with conventional acid leaching, DESs offer advantages such as low volatility, non-flammability, recyclability, and tunable acidity, making them environmentally benign and well-suited for closed-loop recycling systems (Chung et al., 2025).

Liu et al. (2025) demonstrated the potential of DESs by developing a ternary guanidine hydrochloride–ethylene glycol–maleic acid system, which achieved over 99.5% leaching efficiency for Li and Co from $LiCoO_2$ at 100 °C for 9 hours and a liquid–solid ratio of 50:1. The high efficiency was due to the synergistic acidity and coordination of the DES components, which enhanced metal dissolution while allowing solvent reusability for at least three cycles without notable performance loss (Liu et al., 2025). Similarly, C. Wang et al. (2024) used a hydrated choline chloride–citric acid DES and found that adding 25.7 wt% water significantly reduced viscosity and improved metal solubility, achieving 97.6% Co and 100% Li recovery at 120 °C for 4 hours (L/S = 50). However, when the water content exceeded 35 wt%, hydrogen bonding was disrupted, thereby reducing Co extraction efficiency. Chung et al. (2025) reported the use of a choline chloride–oxalic acid dihydrate DES for the leaching of NCM111 cathodes. Under optimized conditions (1:1 molar ratio, 90 °C, 20 g/L solid–liquid ratio, 8 h), more than 95% of Co and Mn were leached, while Ni selectively precipitated as $NiC_2O_4 \cdot 2H_2O$, enabling the sequential recovery of high-purity metal oxides. It was reported that ChCl: EG (1:2) DES systems operated at 180–220 °C for 24 hours recovered approximately 90% Li, 84% Co, and 75% Ni from NMC111 cathodes, demonstrating that DES performance heavily depends on solvent composition, reaction

time, and temperature (Bhattacharyya et al., 2025). Thus, DES-based leaching systems combine acidic dissolution and complexation in a recyclable, environmentally friendly medium, providing high selectivity, reduced chemical waste, and near-complete metal recovery. However, current challenges, such as high viscosity, long reaction times, and sensitivity to solvent composition, still limit their industrial use (Bhattacharyya et al., 2025; Karimi et al., 2025; H. Liu et al., 2024). Further research into ternary, hydrated, and task-specific DES formulations is vital to enhancing leaching rate and scalability, thereby supporting sustainable LIB recycling.

2.2.3.3. Purification

a) Precipitation

Precipitation is a hydrometallurgical process used to recover and separate metals from their aqueous solutions. The process is straightforward. A chemical is added to the leached solution, and by adjusting the pH/Eh, insoluble complexes form between the metals and the precipitants. By doing so, metals can be converted into solid forms. After leaching LCO, oxalic acid can be added to make Li oxalate in aqueous form, as well as Co oxalate precipitate. The following shows the reaction (Verma et al., 2019):

$$4H_2C_2O_4(aq) + 2LiCoO_2(s) \rightarrow Li_2C_2O_4(aq) + 2CoC_2O_4.2H_2O(s) + 2CO_2(aq) \quad (2\text{-}14)$$

However, the process may not be selective and may precipitate all metals. For example, sodium phosphate (Na_3PO_4) can precipitate Li in the form of Li_3PO_4 (Golmohammadzadeh et al., 2022). It is also possible to precipitate metals by altering their oxidation state. For example, ozone and potassium permanganate can be used to change the oxidation stage of Mn and separate it from other metals (Asadi Dalini et al., 2021, 2020; Schaeffer et al., 2020). Ni can be precipitated by dimethylglyoxime and separated from other metals (Asadi Dalini et al., 2021, 2020). To separate metals and recover them, precipitation is generally inefficient and lacks a high metal separation factor (Gao et al., 2022).

b) Solvent Extraction (SX) and Ionic Liquid (IL) Extraction

Solvent extraction (SX) is performed after leaching to recover metals from the pregnant solution. The process involves the extraction of leached metals in aqueous solutions using organic solutions (liquid-liquid separation) (Gao et al., 2022; Golmohammadzadeh et al., 2022; Piątek et al., 2021). In addition to its low energy consumption, SX offers a good separation ratio and simple operating conditions. Di-(2-ethylhexyl) phosphoric acid (D2EHPA), trioctylamine (TOA), acorga M5640, 2-ethylhexylphosphonic acid mono-2-ethylhexyl ester (PC-88A), and bis-(2, 4, 4-trimethylpentyl) phosphonic acid (Cyanex 272) are examples of solvent extractants (Gao et al., 2022).

The extraction mechanism can be ion exchange or chelation. In ion exchange, solvent functional groups can be replaced by cations or anions. In other words, by changing pH, metals or metal complexes can be replaced or chelated by the functional groups of solvents (Golmohammadzadeh et al., 2022; Piątek et al., 2021). In this process, a specific metal can be separated selectively. It is typically necessary to perform multiple stages of extraction to effectively recover metals (Gaines, 2018; Golmohammadzadeh et al., 2022; Piątek et al., 2021). Multistage extraction processes include cross-current batch extraction, continuous countercurrent extraction, and countercurrent batch extraction (Golmohammadzadeh et al., 2022).

In leached LIB solutions, metals, particularly divalent metals, exhibit similar chemical properties, which makes separation difficult. Considering that Co and Ni are very close in the periodic table, their ionic radii are similar, and their properties are also similar (Gaines, 2018). As a result, the separation process warrants further investigation. Some studies have focused on the separation of Co and Ni using chloride ions (Cl^-). Different types of complexes can be formed between chloride and Co and Ni. Co-chloride has a negative charge, whereas Ni-chloride has a positive charge. Thus, using an ionic solvent extractant separates them from one another. Among the cationic solvent extractants, Aliquat 336 (N-methyl-N, N, N-trioctylammonium chloride) contains ammonium, which explains why it is capable of extracting ionic complexes such as Co-chloride (Nguyen et al., 2021). Likewise, other solvents, such as D2EHPA (di-2-ethylhexyl phosphoric acid), PC88A (2-ethylhexyl phosphonic acid-mono-2-ethylhexyl ester), and Cynex 272 (bis(2,4,4-trimethyl pentyl) phosphinic acid), have been employed to extract metals from a leached LIB solution (Liu et al., 2015).

It is also worth noting that Co and Ni can form complexes with thiocyanate (SCN^-). According to the HSAB (hard and soft (Lewis) acids and bases) theory, Co is an intermediate acid and makes an ionic complex with SCN^-. In contrast, Ni, a soft acid, has a low affinity for thiocyanate. In this regard, they can be easily separated using a solvent extractant (Nguyen et al., 2021; Nguyen and Lee, 2020). Nguyen et al. (2021) employed tris(2-methylhexanamine) (TEHA) with fatty acid methyl esters (FAME) derived from catfish oil to separate Co from Li. The results showed that 97% of Co was recovered from the HCl-leached solution of spent LIBs.

Metals can be selectively extracted from spent LIBs using a synergistic solvent extraction process that employs two or more solvent extractants. For instance, the synergistic effect of D2EHPA and PC-88A has been investigated for the recovery of Co from a solution containing Co, Ni, Mn, and Cu. At pH 2.6 and 2.7, Cu and Mn were extracted with D2EHPA. Subsequently, at pH 4.2, Co and Ni were extracted using PC-88A. Furthermore, using oxalic acid precipitated Co as CoC_2O_4. Previous studies have demonstrated satisfactory recovery rates and purity for SX. However, it is important to note that SX is expensive (Gao et al., 2022).

Researchers have also used ionic liquids (ILs) to separate metals. An IL is a type of extractant with a melting point below 100 °C (Paul and Shrotriya, 2025). It is non-volatile and highly thermally stable. For example, tributyltetradecylphosphonium chloride ($[P_{44414}]Cl$) in combination with $NiCl_2$ has been used to recover Co from a solution containing Ni, Co, and Mn. First, Mn was precipitated by ozone. Then, Co was separated from Ni using the IL (Schaeffer et al., 2020). Muhammad et al. (Muhammad et al., 2022) have utilized a water-IL biphasic solvent extraction system to separate Co from Fe and Ni. At room temperature, 1,3-dioctyl imidazolium 2-hydroxybenzoate [DOIM][OHB] extracts Co within 5 minutes, with Co and Fe recovery rates exceeding 90% and 70%, respectively. Then, Fe ions are also extracted after Co. However, the extraction efficiency of Ni was insignificant (Muhammad et al., 2022). For large-scale implementation, cost considerations, particularly the high cost of ionic liquid, must be carefully addressed. Notably, up to 98.9% of the ionic liquid can be recovered and reused, which significantly enhances the economic viability and sustainability of the process (Paul and Shrotriya, 2025).

c) Ion-exchange resins

As an alternative separation method, the liquid-solid extraction method, ion exchange (IX), has been employed. The process involves loading metal ions on functionalized polymeric resin beads. Ion-exchange resins, which offer higher selectivity and lower operating costs than solvent extractants, can be used to extract and separate metals from spent LIB solutions. Metals can also be extracted by resins over a wide pH range (Strauss et al., 2021; Vaughan et al., 2016). Functionalizing beads, however, is a time-consuming and complex procedure. Therefore, the application is limited in this field (Vaughan et al., 2016). Dowex M4195, which is an amine-based ion exchanger, was used to separate Ni from Co, Mn, and Li in spent LIB solutions. After two stages of separation, 99% of Ni and 98.5% of Co have recovered with a high separation factor (Ni/Co) of 2170 (Strauss et al., 2021). Lei et al. (2025) investigated the selective adsorption of lithium from spent LIBs using a D113 cation-exchange resin, achieving a separation factor of 127 over the temperature range 298-328 K, thereby demonstrating high-purity lithium recovery and cathode material regeneration.

d) Adsorption

One promising extraction method for recovering metals from aqueous media is adsorption, which is cost-effective, simple, efficient, and environmentally friendly (Orooji et al., 2022; Purnomo et al., 2018; Sethurajan and Gaydardzhiev, 2021). The adsorption process involves extracting metals using a solid-liquid interface. There are two types of adsorption processes, chemical and physical. In chemical adsorption, metals are bonded to the adsorbent via chemical interactions, complicating separation. In physical adsorption, adsorbents come into contact with solute molecules in solution (Dąbrowski, 2001). As a result of the Van Der Waals force and electrostatic force, physical adsorption occurs between molecules of the adsorbate and the atoms from the adsorbent surface. The surface area and polarity of adsorbents are important characteristic parameters in adsorption (Suzuki and Suzuki, 1990). Although this method is more efficient and easier than solvent extraction, it has not been used in industrial applications due to the lack of efficient, cost-effective adsorbents (Orooji et al., 2022). Furthermore, most adsorbents are in powder form, which can limit the process due to pressure drops and increased energy consumption. To overcome this issue, various methods, including beading, foaming, granulation, fiber formation, magnetization, and

membranes, have been employed. It is also important to consider reusability as a factor that may hinder commercialization (Liang et al., 2020).

Various adsorbents, such as ion sieves and metal-organic frameworks, have been developed to date for adsorbing metals from spent LIBs. Nevertheless, it is crucial to select adsorbents that can efficiently recover and separate metals without harming the environment. In addition, adsorbents are not always selective, and metals can be adsorbed simultaneously. To improve selectivity, a method must be employed; one such method is surface ion imprinting. A surface-ion-imprinted adsorbent can selectively recover the target metal (Y. Huang et al., 2022). An adsorbent's surface is characterized by specific holes, sized according to the target ion to be extracted and selectively separated. Additionally, certain functional groups that tend to form complexes with the target metals may be employed. For example, a crown ether, a large-ring ether, has been used to selectively separate Li from brine. The most widely used crown ether to date is 12-crown-4, which can extract Li and separate it from potassium (K), magnesium (Mg), and sodium (Na). A strong electrostatic interaction force will be formed between Li and the crown ether oxygen as soon as Li enters the hole of the ligand (Gao et al., 2022; Zhang et al., 2023). Huang et al. (2022) employed a magnetic ion-imprinted adsorbent functionalized with a crown ether to recover Li from brine. Due to their magnetic properties, the adsorbents were readily separated from the solution, and Li was readily separated from other metals during extraction. Lithium was separated from Na, K, and Mg by OS@FeSi@CE-OH[1] with separation factors of 7.74, 2.75, and 2.98, respectively.

As part of efforts towards sustainability and the circular economy, there has been recent research interest in using waste materials as adsorbents. In other words, waste can be used to treat other waste, thereby minimizing future waste production. Modified waste materials, such as chitosan, spent battery materials, recycled graphene oxide, and carbon-based materials (e.g., activated carbon and biochar produced from waste materials), are capable of adsorbing metals in LIBs (Purnomo et al., 2018; Sethurajan and Gaydardzhiev, 2021).

[1] OS@FeSi@CE-OH is an ion-imprinted magnetic adsorbent, consisting of the oxygen and sulfur bond (OS), FeSi, and dibenzo-14 crown-4 with an OH bond.

i. Carbon-Based Adsorbents

Carbon-based materials exhibit remarkable potential for the selective recovery of metals owing to their high porosity, tunable surface chemistry, and cost-effectiveness. Among these, activated carbon (AC) is the most commonly used, due to its large surface area, well-developed pore structure, and strong chemical and mechanical stability (Mariana et al., 2021; Naz et al., 2025; Park et al., 2025). Conventional AC is produced from coal, wood, peat, bamboo, or coconut. Meanwhile, recent advances have focused on utilizing low-cost biomass and industrial waste sources, such as polyethylene terephthalate (PET) and agricultural residues, to reduce costs and enhance sustainability (Mwanat et al., 2024; Naz et al., 2025). For example, PET-derived activated carbon effectively removed Fe(II) and Mn(II) from cobalt-rich raffinates, achieving efficiencies of 62.14% and 68.43%, respectively, indicating that chemisorption is the dominant process (Mwanat et al., 2024). The adsorption performance of AC depends on its surface area, surface functionality, and acidity, while chemical activation methods (e.g., KOH activation) are preferred for producing highly porous materials enriched with oxygen-containing functional groups that enhance electrostatic attraction toward cationic species. Adsorption happens through various mechanisms, including physical adsorption (Van Der Waals forces), electrostatic attraction, ion exchange, surface complexation, and redox or co-precipitation processes (Mariana et al., 2021).

To further improve cost efficiency, biomass-derived carbons, such as those from sawdust, rice husk, walnut shells, or fruit peels, have been widely used. For example, pomegranate peel-based activated carbon (PPAC) achieved 90% removal efficiency and ~85 mg/g Co(II) uptake, illustrating the potential of agro-waste precursors for wastewater treatment (Sushma et al., 2025). Similarly, acid- and steam-activated sawdust carbons demonstrated enhanced mesoporosity (BET $\approx 226\ m^2\ g^{-1}$) and high arsenic adsorption (Naz et al., 2025). Beyond conventional AC, biochar, GO, and carbon nanotubes (CNTs) have emerged as promising carbonaceous adsorbents owing to their high surface areas, diverse functionalities, and excellent structural stability. Their adsorption mechanisms typically involve cation-π bonding, surface complexation, and electrostatic interactions, which are governed by the type and density of functional groups, such as –COOH, –OH, and $–NH_2$ (Yang et al., 2019).

Composite and functionalized carbons have proven highly effective in the selective recovery of metals. For example, TEDA-modified AC pellets achieved 99.1% and 93.4% removal of Co(II) through coordination of the C–N amine group, even after pelletization (Park et al., 2025). In another study, xanthate-functionalized wood flour with a 3D macroporous carbon network demonstrated over 99% selective recovery of Co(II) and Ni(II) from a $LiNiCoAlO_2$ (NCA) cathode, whereas Li remained in solution. Subsequently, the solution was recovered as 99.2% pure Li_2CO_3 via precipitation with sodium carbonate (Na_2CO_3). The functional groups –O–C(=S)–SNa, –OH, and –COOH offered strong chelation and ion-exchange sites, ensuring efficient metal adsorption and easy regeneration (Lin et al., 2025a). Purnomo et al. (2018) also investigated the removal of Li, Co(II), Mn(II), and Ni(II) from spent LIBs using AC produced from coconut shell charcoal. Co(II), Mn(II), and Ni(II) were removed simultaneously by adsorption, whereas Li remained in solution. Therefore, carbon-based adsorbents, especially activated carbon, biochar, GO, CNTs, and biomass-derived composites, can provide a sustainable, efficient, and regenerable platform for metal recovery. Advances in surface modification and waste-to-resource synthesis continue to improve their selectivity, capacity, and economic feasibility for large-scale hydrometallurgical recycling of critical metals from spent materials batteries.

ii. Chitosan

Chitosan (CS), a natural polysaccharide derived from the deacetylation of chitin, is primarily sourced from the exoskeletons of crustaceans, such as shrimp, crab, and lobster, as well as from fungal sources (Babakhani and Sartaj, 2025; Rostami and Khodaei, 2024). Structurally, chitosan consists of β-(1→4)-2-amino-2-deoxy-D-glucose and β-(1→4)-2-acetamido-D-glucose units. Its physicochemical properties, such as molecular weight, crystallinity, and degree of deacetylation (DD), strongly influence its solubility, charge density, and adsorption performance (Rostami and Khodaei, 2024; Syeda et al., 2024). When the DD exceeds approximately 55%, chitosan becomes soluble in dilute acids, forming a polycationic, semicrystalline, hydrophobic polymer. (Rostami and Khodaei, 2024).

Due to its biocompatibility, biodegradability, non-toxicity, and natural abundance, chitosan has gained increasing interest as a green adsorbent for wastewater treatment and critical-metal

recovery (Babakhani and Sartaj, 2025; Das et al., 2022; Hamza et al., 2022; Liu et al., 2022; Saheed et al., 2021; Syeda et al., 2024). Its adsorption ability mainly comes from the presence of amino (-NH_2) and hydroxyl (-OH) groups on the glucosidic backbone, which serve as coordination and chelation sites for binding metal ions (Babakhani and Sartaj, 2025; Rostami and Khodaei, 2024). These reactive sites facilitate chelation, ion exchange, and electrostatic interactions, usually forming 1:1 coordination complexes with divalent metal ions (Das et al., 2022; Hamza et al., 2022). Chitosan's strong affinity for metal ions has been shown in many studies. For example, sulfonated chitosan selectively extracted Li^+ from spent LIB leachates (7 M HCl) with an adsorption capacity of 20 mmol/g and Li/Co/Mn/Ni selectivity factors of 26-85 (Hamza et al., 2022). Ion-imprinted chitosan microfibers also achieved a Li uptake of 100 mg/g from coin-cell leachates (Das et al., 2022). EDTA-modified chitosan effectively adsorbed Mg(II) from Li/Mg binary solutions, enriching Li in the liquid phase (Dagdeviren et al., 2025). Chitosan was also able to uptake Cu from printed circuit boards (Manickasundaram et al., 2024). Cheng et al. (2021) proposed a chitosan nanofiber membrane as a Li-adsorbent from brine. Li is also efficiently extracted from brine using modified waste, $Ni_{0.01}$-MnO_2/biochar nanocomposite (Kamran and Park, 2022). In addition, Ofudje et al. (2021) used fish scale-derived nano-rod hydroxyapatite (FSDNHA) to recover Ni from an aqueous solution, achieving a maximum adsorption capacity of 283.3 mg/g.

Although effective, pristine chitosan has limitations, including low mechanical strength, high solubility in acidic media, a small surface area, and water-induced swelling, which limit its reusability and scalability in industry (Babakhani and Sartaj, 2025; Promkatkaew et al., 2025). To overcome these issues, chitosan is often processed into beads, membranes, or hydrogels, improving mechanical stability, diffusion pathways, and reusability (Promkatkaew et al., 2025). To form beads, crosslinking is commonly used to improve the physicochemical durability of chitosan. Crosslinking agents (e.g., glutaraldehyde, epichlorohydrin, or eco-friendly ionic liquids) form intermolecular bridges between polymer chains, reducing solubility and increasing rigidity (Babakhani and Sartaj, 2025). However, this may partially block amino groups, reducing the number of active adsorption sites. Therefore, the crosslinker should be carefully selected to avoid significantly reducing chitosan's adsorption efficiency. Ideally, it should either form beads via different functional groups or add additional active sites to improve its metal-binding capacity. Environmentally friendly crosslinkers are increasingly preferred to support green chemistry and

reduce secondary pollution (Babakhani and Sartaj, 2025). For example, hybrid systems, such as graphene oxide-chitosan (GOCS) composites, have been developed to enhance both structural stability and surface reactivity. The GOCS biosorbent demonstrated excellent adsorption efficiencies (99.98% for Cu(II), 92.55% for Co(II), and 72.36% for Ni(II)), highlighting that incorporating carbon-based materials can enhance chitosan's performance while preserving its environmental advantages (Promkatkaew et al., 2025). Therefore, chitosan's unique chemical structure, abundance of reactive groups, and adjustable modification potential make it an excellent platform for creating sustainable, high-performance adsorbents. With optimized crosslinking and beading, chitosan can achieve the mechanical strength, chemical stability, and selectivity required for large-scale, environmentally friendly applications.

Batch adsorption is a widely used approach for evaluating adsorption capacity, isotherms, and kinetic mechanisms in laboratory-scale research. It offers simplicity and cost-effectiveness, making it suitable for small-scale testing and optimization (Patel, 2022; Patel and In, 2021). However, batch systems are inherently constrained by mass-transfer resistance, equilibrium time, and scalability limitations, as they require multiple operational cycles to treat large volumes of wastewater. These limitations restrict their industrial applicability due to adsorbent saturation, non-uniform mixing, and downtime between adsorption and regeneration cycles (Khanam et al., 2025; Patel, 2022). To overcome these challenges, continuous fixed-bed (column) adsorption systems have been increasingly adopted as efficient and scalable alternatives. In a column setup, the adsorbate solution continuously flows through a packed bed of adsorbent, enabling steady-state operation and enhanced contact efficiency between the adsorbate and the solid phase (Abbasi et al., 2021; Callura et al., 2021; Patel and In, 2021). Such systems offer higher throughput, improved mass-transfer kinetics, and easier automation, making them well-suited for industrial water and metal recovery processes.

Recent studies have shown the superiority of continuous systems across various materials and target metals. Khanam et al. (2025) developed a lignin-based hydrogel–composite dual-layer packed column that achieved a cumulative adsorption capacity of 476.75 mg/g for Pb(II) during continuous operation, outperforming batch adsorption due to enhanced flow distribution and extended operation at pH 6–8. Similarly, Baskar et al. (2025) reported the efficient removal of Ni(II) from simulated wastewater using a multi-port packed bed column filled with powdered

clamshell waste. The system achieved 87.68% removal efficiency at a flow rate of 8 mL/min and a bed height of 25 cm. Modeling with the Thomas and BDST models provided valuable insights for scaling up. The multi-port configuration enhanced bed utilization and lowered pressure drop, ensuring uniform adsorption throughout the column. In advanced applications, Aburabie et al. (2025) employed a chelation-based packed-bed column using polythiosemicarbazide (PTSC) polymer for the dynamic adsorption of trace metals, such as Ni, Zn, Cu, Ag, and Co, from seawater and brine. The system achieved over 98% silver recovery and 99% copper recovery under optimized flow and pH conditions, and the column was regenerable with 0.1 M thiourea, enabling sustainable reuse. Similarly, Syeda et al. (2025) demonstrated the continuous adsorption of heavy metals on regenerable biopolymeric aerogels in a fixed-bed reactor, confirming consistent removal over multiple adsorption–desorption cycles.

These findings align with recent studies that show that column and continuous-flow systems offer superior removal efficiency, lower adsorbent loss, and stable performance over extended operating periods (Robeck and Horn, 2024a; Romal et al., 2025; Z. Wang et al., 2025). In contrast, batch systems often exhibit uneven diffusion zones and inefficient regeneration, disrupting process continuity. Transitioning from batch to continuous adsorption systems is crucial for developing scalable, energy-efficient, and sustainable methods for metal recovery. Continuous fixed-bed columns offer real-time control and regeneration capabilities and more accurately mimic industrial conditions, enabling the integration of adsorption into circular recovery loops for wastewater treatment and battery recycling processes (Aburabie et al., 2025; Baskar et al., 2025; Khanam et al., 2025; Robeck and Horn, 2024a; Syeda et al., 2025). Although there is growing attention to the use of waste-derived adsorbents for the selective recovery of critical metals (Li, Co, Ni, and Mn) from spent lithium-ion batteries, further efforts are required to develop practical technologies, evaluate their performance under real-world conditions, and scale up processes for industrial implementation.

2.3. Chitosan Production

Chitin, the second most abundant natural polysaccharide after cellulose, is primarily extracted from crustacean shells, such as shrimp, crab, and lobster, via acid–base chemical processing (Campalani et al., 2024a; Mohan et al., 2022). The traditional extraction involves three main steps:

demineralization (DM) with acids such as HCl, HNO_3, or H_2SO_4 to dissolve calcium carbonate; deproteinization (DP) using alkaline solutions such as NaOH or KOH at 65-100 °C for several hours to remove proteins; and decolorization with oxidants or organic solvents such as acetone, ethanol, or H_2O_2 to remove pigments. While effective, this method often causes polymer degradation, resulting in a lower molecular weight and a decreased degree of acetylation (DA), along with environmental issues due to the production of highly saline wastewater and CO_2 release from acid–carbonate reactions (Campalani et al., 2024a; Mohan et al., 2022). For instance, demineralizing 100 g of crab shell waste requires approximately 1 L of concentrated HCl, producing about 220 g CO_2 and large volumes of acidic effluent (Campalani et al., 2024a; Mohan et al., 2022). Furthermore, the process consumes significant energy, and the recovered proteins and minerals are often unsuitable for reuse due to contamination (Mohan et al., 2022). Despite these challenges, chemical extraction remains the primary industrial method due to its simplicity and high yield. However, it is unsustainable for large-scale circular bioeconomy applications because it generates significant waste and alters chitin's molecular structure, resulting in brittle chitosan with reduced adsorption efficiency.

To address the environmental and efficiency drawbacks of the chemical route, greener solvent-based approaches have recently gained attention, particularly ionic liquids (ILs), DESs, and protic ionic liquids (PILs) (Khajavian et al., 2022; Sulthan et al., 2023; Y. Wang et al., 2025). These solvents can extract chitin by disrupting its hydrogen-bonding network while also removing protein and mineral fractions, thereby enabling a one-pot demineralization–deproteinization process. As noted previously, DESs are mixtures of an HBA, such as choline chloride, and an HBD, such as an organic acid (lactic, malonic, or citric) or urea. The hydrogen-bond network among these components creates a low-melting-point eutectic phase capable of dissolving biopolymers (Khajavian et al., 2022). Compared to traditional solvents, DESs are non-toxic, biodegradable, affordable, and recyclable. For instance, choline chloride–lactic acid and choline chloride–malonic acid systems effectively demineralized and deproteinized shrimp and lobster shells, producing chitin with up to 95% purity and a 93% degree of acetylation while shortening process time and removing hazardous waste (Alhamad et al., 2024; Khajavian et al., 2022). Furthermore, DESs can be adjusted by changing the HBA/HBD molar ratio to control acidity and extraction selectivity. However, DES-based extraction still faces certain challenges. The viscosity of DESs can slow down mass transfer, especially at low temperatures, and recycling efficiency

may decline after multiple extraction cycles due to the buildup of organic residues (Khajavian et al., 2022; Mohan et al., 2022). Additionally, the energy requirements for heating (usually 80–100 °C) and the need for solvent regeneration remain hurdles for industrial-scale up. Despite these issues, DESs have proven highly effective for sustainable chitin recovery and nanostructure formation (nanocrystals and nanofibers), with enhanced purity, crystallinity, and mechanical strength, and have the potential to produce bio-adsorbents and films (Alhamad et al., 2024; Khajavian et al., 2022; Sulthan et al., 2023).

More recently, PILs have been developed as advanced green solvents for the selective extraction and modification of chitin. PILs are produced through proton transfer between a Brønsted acid and a Brønsted base, resulting in adjustable acidity, high ionic conductivity, and low viscosity compared to traditional ILs (C. Wang et al., 2025). They combine the strong solvation capacity of ILs with the gentle, biodegradable nature of DESs, enabling simultaneous deproteinization, demineralization, and partial deacetylation in a single step. Y. Wang et al. (2025) demonstrated that chelating amine-based PILs, such as triethanolamine formate, effectively dissolved crustacean shell biowaste under mild conditions, yielding high-molecular-weight chitin with a degree of acetylation above 94%. The process used less energy, avoided harsh acids, and produced chitin that was comparable to or superior to commercial-grade materials. Furthermore, PILs are recyclable, have low vapor pressure, and can be tailored to target specific interactions, such as coordination with Ca(II) or protein residues, thereby boosting selectivity. Compared with conventional ILs, PILs offer several distinct advantages, including lower toxicity and higher biodegradability; adjustable acidity and chelating ability for the controlled removal of proteins and minerals; reduced viscosity for improved mass transfer and scalability; and compatibility with water, facilitating easy product separation and solvent recovery. However, the design of PILs still needs careful optimization to balance solvation ability and polymer stability, as overly acidic PILs may hydrolyze glycosidic bonds. In contrast, weakly basic ones may lead to incomplete extraction of the reaction products.

Adopting DESs and PILs for chitin and chitosan extraction represents a shift toward sustainable biorefinery practices that address both environmental and process-efficiency concerns. These methods reduce hazardous waste generation by replacing strong mineral acids and alkalis with biodegradable solvents, lowering energy and water use through single-step processes, and

improving chitin quality by maintaining molecular integrity and acetylation level. They also allow solvent recycling and the use of by-products, such as proteins and pigments. While acid–base extraction remains the primary method used in industry, the emergence of DES- and PIL-based systems has shifted chitin and chitosan production toward more environmentally friendly, safer, and more efficient processes. PILs combine tunability, low viscosity, and recyclability, representing a promising bridge between laboratory-scale innovation and industrial implementation (Campalani et al., 2024a; Khajavian et al., 2022; Mohan et al., 2022; Sulthan et al., 2023; Y. Wang et al., 2025).

2.4. Research Gaps and Possibilities

Considering the discussion above, there is an urgent need to recover critical metals from spent LIB waste to meet the rapidly growing demand for net-zero energy consumption. However, conventional methods are insufficient for industrial-scale recycling of LIBs and require modification and development to become practical. Due to the disadvantages of pyrometallurgical processes, including high energy consumption and low efficiency, the industry is turning to hydrometallurgical methods. Most previous studies on hydrometallurgy have focused on recovering metals from synthetic LIB solutions but have not addressed actual spent LIB waste. Conventional hydrometallurgical recycling methods also employ harsh conditions, such as strong acids or bases, to dissolve metals, posing risks to the environment and human health. Current metal separation methods are not highly efficient, and metals are often recovered simultaneously without clear selectivity. Further research is essential to address these issues comprehensively. Additionally, solvents used in the separation stage are typically discarded after a few extraction cycles, resulting in secondary pollution. Therefore, developing a new, environmentally friendly method is crucial to overcoming these challenges.

Limited research has also been conducted on the scaling up and development of continuous adsorption systems using biosorbents to recover critical metals from spent LIBs, despite their potential for sustainable recycling. Developing such continuous, scalable systems is crucial and urgent for the rapid commercialization of battery-recycling technologies, particularly given the industry's rapid global growth. Furthermore, the concept of “waste-to-treat-waste,” which addresses the circular economy, remains underexplored. This concept involves directly converting

natural biowaste materials, such as shrimp shells, into chitosan-based adsorbents for recovering metals from spent LIBs. Exploring this pathway could mark a significant step toward fully circular and sustainable recycling processes. Consequently, this study aims to address these gaps by employing bio-based adsorption within a continuous-system framework, enabling the efficient, selective, and environmentally friendly recovery of valuable metals from LIB waste.

Chapter 3 RESEARCH METHODOLOGY

A detailed description of the materials used, the methods employed, and the analyses performed will be provided in this section. Figure 3.1 shows the proposed stages of experimental work.

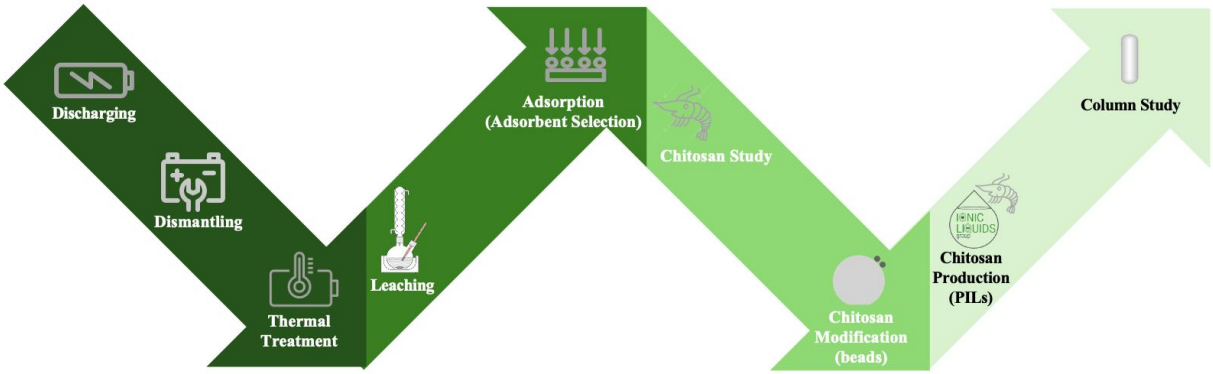

Figure 3.1. Schematic flowchart of the experimental study.

3.1. Sample Collection

Spent LIBs, including laptops, cellphones, and Li-polymer batteries, have been collected from a recycling facility in Toronto, Canada. The facility regularly receives electronic waste and spent or discarded batteries. Currently, the facility only performs physical separation of waste, and only limited physical treatment is applied to large waste streams. Meanwhile, other wastes, including spent LIBs, are stored or shipped to other companies. Consequently, to meet circular-economy, sustainability, and waste-management goals, they must be able to recycle spent LIBs efficiently and in an environmentally friendly manner. To conduct the study, approximately 28 kg of spent batteries from various brands, including LG, Samsung, TechTrex Inc., and Motorola, were collected and transported to the University of Ottawa. Figure 3.2 shows the Li-ion batteries collected.

Figure 3.2. The collected Li-ion batteries (Left-hand side: laptop batteries, middle: Li-polymer batteries, right-hand side: cellphone batteries).

3.2. Discharging

Discharging collected LIBs is the first step in the study. For safety reasons, discharges must be conducted to prevent fires or explosions. Discharging has been done in anticorrosion plastic buckets containing a 10% sodium chloride (NaCl) solution under a fume hood for 24 h (Li et al., 2016.; Shaw-Stewart et al., 2019). To prevent short circuits and fires, batteries were kept separate from one another. Then, samples were removed from the solution and allowed to rest for an additional 24 hours. A multimeter was then used to measure each battery's voltage to determine the remaining voltage. Almost all battery voltages were approximately 2.5V. Over-discharged batteries have voltages between 0 and 2.5V. Over-discharging is undesirable, as it leads to the release of hazardous gases and electrolyte leakage (Li et al., 2016; Shaw-Stewart et al., 2019). As there was no evidence of leakage, the process was deemed successful.

3.3. Dismantling

Dismantling batteries and separating cathodes from anodes, as well as other materials such as separators, plastics, and casings, was performed manually in the University of Ottawa laboratory. To disassemble each battery, various tools and methods were employed. The case of the cellphone batteries was made of thin stainless-steel foil. Therefore, a pair of pliers capable of cutting SS was used. Both ends of the batteries were cut, and the anodes and cathodes were separated manually. The casings of Li-polymer batteries are made of plastic and can be easily cut with standard pliers. The process was the same with the cellphone batteries. The laptop batteries have two shells, one of hard plastic and one of stainless steel. A screwdriver and a hammer have been used to break the

plastic. Then, both ends of the cylindrical stainless-steel shell were cut by a stainless-steel tubing cutter. A hacksaw was used to cut the stainless-steel line and open the batteries. To proceed to the next steps, all cathode materials were cut into 2 cm × 2 cm squares. All cathodes were separated from the anodes and other materials and stored in separate buckets. To characterize batteries separately, they were stored separately. To conduct the leaching process, mixed batteries were examined. Figure 3.3 illustrates the various components of batteries after disassembly. Figure 3.4 illustrates the cathode, anode, and other components of the battery.

a)

b)

c)

Figure 3.3. Different parts of batteries: a) laptop, b) cellphone, and c) Li-polymer batteries.

a) b) c)

Figure 3.4. Different parts of a typical Li-ion battery: a) cathode, b) anode, c) separators, and casing.

3.4. Characterization

3.4.1. Weights and Mass Balance

Following the dismantling of the LIBs, the components were weighed to determine the weight percentages of the cathode, anode, and other materials for each LIB type. A two-decimal balance (Mettler Toledo, Model PL3002, Canada) has been used to weigh all parts.

3.4.2. Thermogravimetric analysis (TGA)

TGA was performed to characterize the thermal behavior of the materials and to determine an appropriate temperature for binder decomposition (PVDF). A sample was taken from each cathode material and ground together. Al foils are flexible and cannot be ground into particles that are too fine. Thus, large particles, such as Al foils, were separated by sieving through mesh No. 45. The sample (black powder) was then sent for analysis. Generally, a certain amount of material is placed in a controlled-atmosphere furnace (either inert or air atmosphere), and the temperature rises from ambient to 800-900 °C. A computer-controlled balance is used to measure changes in mass. In this study, samples were sent to the Materials Research and Analysis Platform (PRAM) (Sherbrooke University, Quebec, Canada), and the determined amounts were placed in a controlled-atmosphere furnace (Setaram Setsys 24 equipped with a TG-DTA 1600 °C rod). The conditions were a heating rate of 2.5°C/min and a flow rate of 1.5 L/h (approximately 24 mL/min) in an Al_2O_3 crucible under an argon atmosphere (20% oxygen + 80% argon) from 25 to 800 °C, simulating both inert and air environments.

3.4.3. X-ray diffraction (XRD)

To determine the phase of the materials and identify the most effective heat treatment to remove binders and separate aluminum, samples were sent to an X-ray core facility (STEM building, University of Ottawa, Canada). X-ray diffraction data were collected on a Bruker D8 Endeavor XRD equipped with a sealed-tube Cu Kα source (λ= 1.54184 Å) operating at 40 kV and 25 mA, and a LynxEye XE-T 1-D Si strip detector. The powdered sample was prepared in a 25 mm-diameter front-loading sample holder and rotated at 15 rpm during data collection. Determination of crystalline phases was performed using DIFFRAC.EVA software (Bruker) in conjunction with the 2023 PDF-4+ database (ICDD). Raw materials (LIB cathode materials) and heat-treated samples were sent for XRD analysis, which will be conducted under optimal conditions at each step.

3.4.4. Inductively Coupled Plasma (ICP) and Atomic Absorption Spectroscopy (AAS)

To measure metal concentrations in the cathode materials, inductively coupled plasma (ICP; Agilent 5110 ICP-ES) was used. Samples were sent to Geochemistry Laboratories (ARC building, University of Ottawa, Canada). 100 mg of the samples, raw materials, and heat-treated materials were accurately weighed into a vial and digested overnight at 120 °C on a hotplate with aqua regia (HNO_3:HCl = 1:3). Additionally, Atomic Absorption Spectroscopy (AAS, PinAAcle 500, PerkinElmer, Environmental Laboratory, University of Ottawa) was used to measure metal concentrations during the experiments. The instrument was calibrated using a nonlinear method with zero intercept. Each sample underwent 3-5 readings, and the average was used for subsequent calculations. The pH of the solution was measured using a HACH pH Meter (HQ40D).

3.4.5. Scanning electron microscope (SEM)

The surface morphologies and elemental composition were characterized using a scanning electron microscope (SEM) equipped with energy-dispersive X-ray spectroscopy (EDS). Cathode materials were analyzed in the Electron Microprobe Laboratory (ARC, University of Ottawa, Canada). SEM (JEOL 6610LV) was operated in low vacuum mode with a chamber pressure of 30 Pa of nitrogen. The accelerating voltage was 20 kV, and the beam current was ~1 nA. The EDS detector (Oxford XMax) used to detect surface materials is a 20 mm^2 solid-state detector, and data were collected

using Oxford Inca software. Chitosan samples were also analyzed at the Department of Bioscience at the University of Ottawa, Canada, using Scanning Electron Microscopy (Field Emission SEM, JEOL JSM-7500F) and Energy-Dispersive X-ray Spectroscopy (EDS, Oxford detector at 30 kV), with INCA software.

3.4.6. Fourier Transform Infrared Spectroscopy (FT-IR)

Fourier Transform Infrared Spectroscopy (FT-IR; Thermo Scientific IS50 FT-IR) was used in the 4000–500 cm^{-1} range to analyze the functional groups present on chitosan before and after adsorption.

3.4.7. Brunauer–Emmett–Teller (BET)

The specific surface area was measured using Brunauer–Emmett–Teller (BET) N_2 isotherms collected on a Micromeritics 3Flex adsorption analyzer (Micromeritics Instruments Inc.) at 77 K (liquid N_2 bath) at the University of Ottawa, or on a Quantachrome instrument at McGill University. Prior to measurement, samples were activated under high vacuum at 50 °C for 7 hours, followed by 10 hours at 100 °C (Sing, 1985).

3.5. Pyrolysis

Different parameters, such as time (30 min-6 h), temperature (570–650 °C), and furnace atmosphere (air and Ar), have been studied for optimization of the pyrolysis process (Portia Makwarimba et al., 2022; G. Zhang et al., 2021. A muffle furnace (Thermolyne, Model 62700, USA) and a muffle/atmosphere-controlled furnace (Thermo Scientific, Model F6000, USA) have been utilized to analyze air and inert atmospheres. First, a certain amount of cathode material was placed in the furnace to examine the effect of the parameters. After optimizing the process, 10 g of cathode material per crucible was placed in the furnace to treat all cathode materials and prepare them for subsequent stages.

3.6. Leaching

3-6-1- Design of Experiments and Analytical Method

Using Design-Expert 12 (State-Ease Inc., Minneapolis, MN, USA), experiments were designed, and metal recoveries were statistically analyzed. The design consisted of two stages: screening and modification. Screening tests were conducted to optimize acid types (sulfuric acid + citric acid and sulfuric acid + acetic acid) and acid concentrations (inorganic and organic acids at 0.5-2 M and 0.1-1 M, respectively). Other parameters were kept constant at 90 °C, 2 h, an S/L of 50 g/L, and a hydrogen peroxide dosage of 5 vol.%. Because the purpose of this stage is to achieve precise predictions of acid types and concentrations, the I-optimal response surface methodology (RSM) was employed (Byran Smucker et al., 2018). The optimum condition was repeated without hydrogen peroxide addition to examine the effect of H_2O_2 on efficiency.

Subsequently, the optimal conditions identified during the screening stage are applied during the modification stage. The modification stage was conducted to optimize temperature (40-90 °C), time (30-180 min), and S/L ratio (50-200 g/L). A D-optimal response surface methodology (RSM) was implemented to investigate the effect of parameters and obtain accurate results (Smucker et al., 2018). The recovery of each element was determined using the following equation:

$$\text{Recovery (\%)} = \frac{\text{Extracted metal in Leaching solution } (\frac{\text{mg}}{\text{L}})}{\text{Total metal concentration in initial sample } (\frac{\text{mg}}{\text{L}})} \quad (3\text{-}1)$$

3.6.2. Experimental Procedure

Sulfuric acid (H_2SO_4, Fisher Chemical, USA), Citric monohydrate ($C_6H_8O_7 \cdot H_2O$, Fisher Chemical, USA), and acetic acid (CH_3COOH, Fisher Chemical, USA) with a purity of 98%, 99%, and 99.7%, respectively, were used in the leaching step. Also, Hydrogen peroxide (H_2O_2) with 30% purity (Acros, USA) was used as a reducing agent. All solutions were prepared using deionized water. Unless otherwise stated, all materials are analytically grade. In all experiments, a 50 mL solution was placed in a 250 mL, three-neck, round-bottom flask. To maintain a constant temperature, the flask was placed in a water bath. Water evaporation was minimized by attaching a glass condenser to the flask. The solution was heated and mixed using a magnetic stirrer. A thermometer was used to measure the temperature within a range of ±5 °C.

Finally, a filter paper (125 mm, medium-flow, Labasics, USA) was used to filter the leachates. Figure 3.5 illustrates the leaching setup.

Figure 3.5. Leaching setup.

3.7. Adsorption

3.7.1. Materials

Chitosan with a deacetylation degree (DD) of 85%, sodium hydroxide (NaOH), sodium chloride (NaCl), and sodium hydroxide (NaOH) were acquired from Fisher Scientific Co., Canada. L-arginine (98%), L-cystine (99%), and Ethylenediaminetetraacetic acid (EDTA, disodium salt dihydrate) were purchased from Thermo Scientific, Canada. Sodium tripolyphosphate ($Na_5P_3O_{10}$) was purchased from Sigma, Canada. Triethylamine, triethylenetetramine, and ethanolamine, with purities greater than 98%, 60%, and 99.5%, respectively, were purchased from Sigma-Aldrich, USA. Activated carbon (AC) derived from coconut shells was obtained from Calgon Carbon Co. (Pennsylvania, USA). Grafoid Inc. (Canada) provided GO. Fiber flax (supplied by Biolin Research Inc., Canada) modification was performed in two stages. After manually removing husk remnants, the fibers underwent a two-step pre-treatment. First, they are boiled in acetone to remove surface impurities, such as fats and waxes, thereby exposing them to subsequent treatment. Then, they are soaked in a 5% NaOH solution for 2 hours to remove lignin and hemicellulose, enhancing their

readiness for oxidation. The fibers are rinsed in neutral pH water and dried overnight at 50 °C. To oxidize fiber flax and improve its interaction with adsorbates, hydroxyl groups in the fibers are converted to carboxyl groups through oxidation. A TEMPO solution is prepared by mixing sodium bromide, sodium chloride, and TEMPO oxidizer in de-ionized water, adjusting the pH to 10. Fibers are oxidized in 0.5 g bundles for 60 s, rinsed, and dried overnight at 50 °C. All solutions were prepared using deionized water (DI). Unless otherwise specified, all materials used were of analytical grade.

3.7.2. Adsorbent Selection

To select the most effective adsorbents, various waste materials, including chitosan, coconut-shell activated carbon, graphene oxide, and chemically modified flax, were compared, and their adsorption capacities were evaluated. The effect of pH was examined to select the best adsorbent. Batch adsorption experiments were conducted in 125 mL Erlenmeyer flasks with 50 mL of diluted, leached BM to investigate the impact of different adsorbents on the adsorption of Li, Co(II), Mn(II), and Ni(II). Each flask contained 0.5 g of adsorbent (10 g/L), except for GO, which was 3.5 g/L (0.1764 g), and was agitated at 150 rpm for 24 hours at room temperature. At this stage, initial concentrations were adjusted by a factor of 100 at pH 7, with pH adjusted within the range 4 to 7. After equilibrium, metal concentrations were measured using AAS. Adsorption capacity and rates were calculated from duplicate experiments using the following equations:

$$q_e = \frac{(C_0 - C_e) \times V}{W} \tag{3-2}$$

$$Adsorption\ rate\ (\%) = 100 - (\frac{C_e}{C_0}) \tag{3-3}$$

where C_0 (mg/L) stands for the initial concentration, and C_e (mg/L) represents the equilibrium concentration of adsorbate in the solution. V (L) denotes the volume of the solution, and W (g) indicates the weight of the dry adsorbent. The adsorbents in the solution are shown in Figure 3.6 (the detailed results are provided in the appendix).

Figure 3.6. Solution containing the adsorbent.

3.7.3. Adsorption Study on the Selected Adsorbent (Chitosan)

Batch adsorption experiments were conducted in 125 mL Erlenmeyer flasks containing 50 mL of leachate to investigate the impact of initial metal concentration, pH, and adsorbent dosage on the removal of Li, Co(II), Mn(II), and Ni(II). The solutions were agitated at 150 rpm for 24 h at room temperature. Initial concentrations were varied by dilution (100-20×), while the influence of pH was examined under both unadjusted and adjusted conditions (pH 4-8) using 10 wt.% NaOH and 1% (v/v) H_2SO_4. Adsorbent dosage varied from 0.1 to 5 g (2-100 g/L). After filtration, equilibrium concentrations were measured by AAS. Figure 3.7 shows the appearance of the leachate after pH adjustment.

3.7.3.1. Adsorption isotherm modeling

Langmuir, Freundlich, Temkin, and Toth isotherm models were applied to describe the adsorption behavior (Al-Ghouti and Da'ana, 2020; Babakhani and Sartaj, 2023, 2022a; Piccin et al., 2017). The best-fitting model was determined using the coefficient of determination (R^2), Sum of Squares of Residuals (SSR), and Mean Squared Error (MSE), where lower SSR and MSE values indicate higher predictive accuracy (Anderson and Whitcomb, 2017).

3.7.3.2.Kinetics and Thermodynamics

The effect of contact time on Li, Co(II), Mn(II), and Ni(II) adsorption was studied using 10 g/L chitosan in 50 mL of leachate (dilution factor 40, pH 4) agitated at 150 rpm for 5–2880 min. After

filtration (a 0.45 µm pore size membrane filter (EZFlow Membrane)), adsorption data were fitted to pseudo-first- and pseudo-second-order models. Thermodynamic studies were conducted at 4 °C and 22 °C under identical conditions, using 0.5 g of chitosan for 24 h, to evaluate the effects of temperature.

3.7.3.3. Desorption Study

After adsorption of Co(II), Mn(II), and Ni(II) from a leachate (dilution factor 40, pH 4), the chitosan was filtered, rinsed, and air-dried. Desorption was then performed in DI water, 0.1 M HCl, 1 M NaCl, and 0.01–0.1 M H_2SO_4 for 72 h. The desorbed metal concentrations were measured by AAS, and desorption efficiency was calculated as the average of duplicate tests. The desorption percentage was calculated using the following equation:

$$Desorption\ (\%) = \frac{Amount\ of\ metal\ ions\ desorbed\ (mg)}{Amount\ of\ metal\ ions\ adsorbed\ (mg)} \times 100 \qquad (3\text{-}4)$$

Figure 3.7. Solutions after pH adjustment.

3.7.4. Chitosan Bead Modification

Chitosan beads (CBs) were synthesized as follows. Initially, 3.2 g of chitosan powder was dissolved in 80 mL of a 5% (v/v) acetic acid solution at 30 °C, and the mixture was stirred continuously for 24 hours. Next, varying amounts of crosslinkers (L-arginine and L-cystine) at different dosages (1 wt.%, 5 wt.%, 10 wt.%, 12.5 wt.%, 25 wt.%, and 100 wt.%), Triethylamine, Tri-octylamine, Pyrazine at 100 wt.%, and sodium tripolyphosphate (STPP, 2.92 wt.%), relative to the chitosan powder, were added to the solution. After 3 hours of mixing, the mixture was slowly dropped into a precipitation bath containing 0.60 M NaOH and left overnight to form spherical chitosan beads. The beads were then thoroughly rinsed with DI water to remove residual NaOH from their surface. Finally, the beads were air-dried to remove moisture from within their structure. Also, the effect of compositing with AC (AC: CS= 0.25, 0.5, and 0.75 to 1) and iron (II, III) oxide (Fe_3O_4, magnetic CB) (Magnet: CS= 0.25, 0.5, and 1 to 1) was investigated. Magnetic beads were produced according to the two-pot method. Ferric and ferrous chlorides (2:1) were co-precipitated with NH_4OH under N_2 at 25 °C (pH ~10), and the precipitate was heated (80 °C, 30 min), washed, and dried (70 °C) (Chang and Chen, 2005). The resulting magnetic iron oxide was then added to a chitosan solution to form magnetic beads. Figure 3.8 illustrates bead formation under different conditions (a, b), the produced beads (c), beads after adsorption (d, f), and the adsorption process (e) (the detailed results of some crosslinkers and composite materials are provided in the appendix).

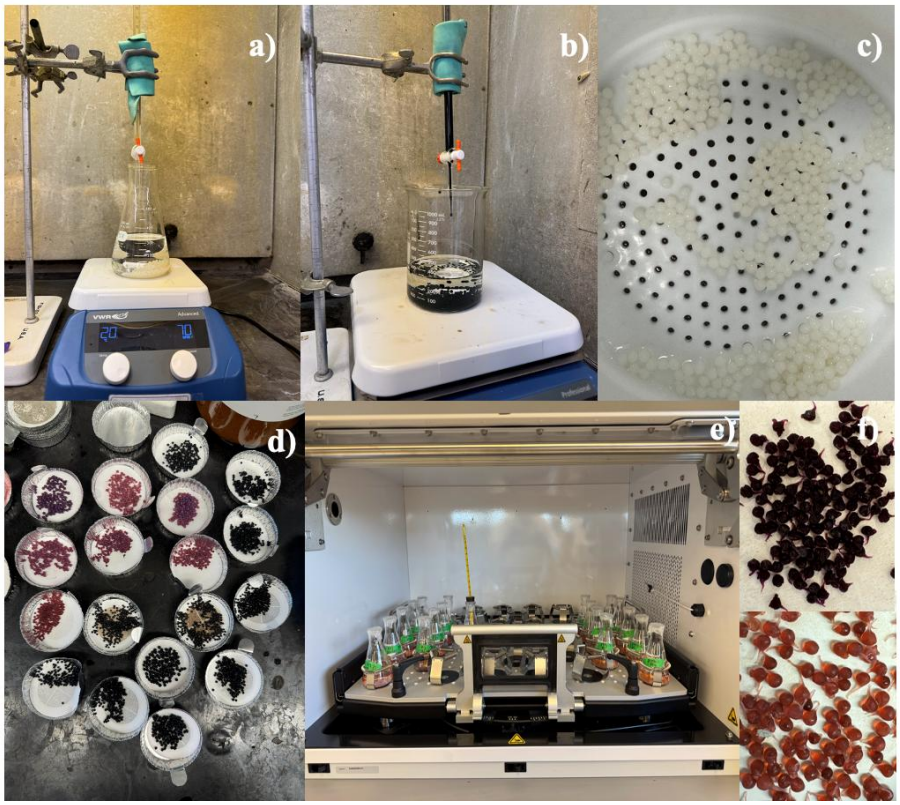

Figure 3.8. Bead formation (a–b), produced beads (c), beads after adsorption (d, f), and the adsorption process (e).

3.7.4.1. Batch Adsorption and Isotherm Study on the Synthesized Bead

Batch adsorption tests were performed in 125 mL flasks containing 50 mL of pregnant solution and 0.5 g of crosslinked CBs, with agitation at 150 rpm at room temperature for 24 h. Metal concentrations were varied using dilution factors of 10–50, followed by pH studies at natural (~2), 4, and 5 (adjusted with 10 wt.% NaOH or 1% v/v H_2SO_4). pH above 8 was avoided to prevent precipitation. After filtration, equilibrium concentrations were analyzed by AAS, and adsorption uptake and efficiency were calculated. Isotherm data were modeled using the Langmuir, Freundlich, and Toth equations, and R^2, SSR, and MSE were used to assess model fit.

3.7.4.2. Kinetics and Thermodynamic Study

The effect of contact time on adsorption was examined under optimal conditions at room temperature for 5–1800 min. Kinetic data were fitted to pseudo-first- and pseudo-second-order models. Thermodynamic studies were then conducted using 50 mL of pregnant solution (dilution factor 30, pH 4) with 0.5 g of crosslinked CBs at 4 °C and 22 °C for 24 h. $\Delta G°$, $\Delta H°$, and $\Delta S°$ were calculated to assess spontaneity, disorder, and the nature of adsorption.

3.7.4.3. Desorption Study

After completing the adsorption tests, the optimized crosslinked beads (CS1%CYS) were separated via vacuum filtration, rinsed with DI water, and dried at room temperature. Desorption tests were subsequently conducted in 50 mL of DI water, 0.01 M H_2SO_4, and 0.1 and 0.5 M EDTA solutions. The final metal concentrations were then determined using AAS.

3.7.5. Chitosan Production from shrimp shell (SS) using Protic Ionic Liquids (PILs)

3.7.5.1. Protic Ionic Liquid Synthesis

The PILs (Triethylammonium acetate ([Tea][Ac]), Triethylenetetrammonium acetate ([Teta][Ac]), and Ethanolammonium acetate ([Eth][Ac])) were synthesized via acid–base neutralization. Equimolar amounts of amines (TEA, TETA, or ETH) and acetic acid were stirred in a 250 mL flask, with the acid added dropwise in an ice bath, and the mixture was then stirred for 24 h at room temperature. To maintain a controlled reaction temperature, the flask was immersed in a shallow ice-water bath throughout the mixing process. After the addition was complete, stirring continued at room temperature for 24 hours to ensure complete reaction. The product was heated to 80 °C to remove unreacted components, yielding clear or yellow liquids with a purity of greater than 95%. Figure 3.9 shows the produced PILs.

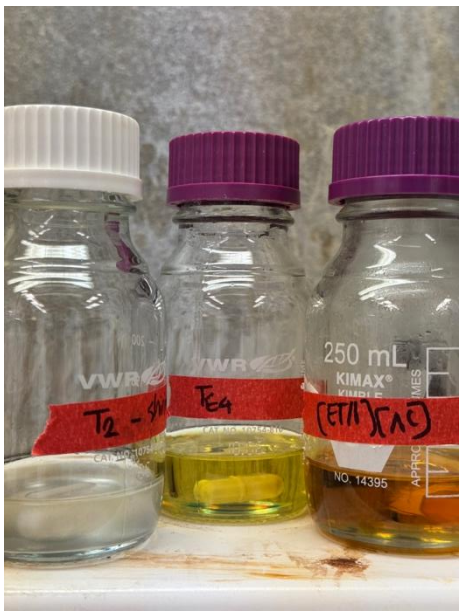

Figure 3.9. Produced PILs.

3.7.5.2. Isolation of Chitin from Shrimp Shells and Deacetylation

Chitin was extracted from shrimp shells (SS). Clean, dried shells (2 g) were ground and mixed with 30 g of the synthesized ionic liquid at a controlled temperature for a specified time. After extraction, the mixture was centrifuged, and the supernatant was treated with 2.4% citric acid for 5 h to remove minerals. The precipitate was collected, dried at 60 °C, and converted to chitosan by treating with 50 wt.% NaOH (S/L = 1:15) at 100 °C for 6 h. The product was rinsed, filtered, and oven-dried at 60 °C for 12 h.

3.7.5.3. Design of Experiment (DOE) and Extraction Optimization Study

Statistical analysis was performed using Design-Expert 12 (State-Ease Inc., USA) for QA/QC and process optimization. The study included two stages: screening and optimization. Screening identified the best PIL ([Eth][Ac], [Tea][Ac], or [Teta][Ac]) under fixed conditions (24 h, 90 °C, L/S = 15 g/g). The chitin extraction was then optimized using a Box–Behnken design (BBD) with three variables (time (18–36 h), temperature (70–120 °C), and L/S ratio (10–20 g/g)) following RSM principles (Smucker et al., 2018; Roshanfar et al., 2019).

3.7.5.4. Batch Adsorption and Isotherm Study

Batch adsorption tests were conducted in 125 mL flasks with 25 mL of leachate to assess the chitosan extraction efficiency and the effect of initial concentration (dilution factors 50–20). Samples were agitated at 180 rpm for 24 h at room temperature and pH 4 (adjusted with 10 wt.% NaOH or 1% H_2SO_4). After filtration, the concentrations of Li, Co(II), Mn(II), and Ni(II) were analyzed by AAS. All tests were duplicated, and average values were used. Adsorption data were fitted to the Langmuir and Freundlich models, and R^2, SSR, and MSE were used to determine the best fit.

3.7.6. Column Study

Column experiments were conducted in a 100 cm glass column (2.2 cm i.d., ACE Glass, NJ) packed with crosslinked chitosan beads (CS1%CYS). A glass disk ensured uniform flow, and a bottom filter prevented bead loss. A diluted leachate (30×) containing 964 mg/L Co, 133 mg/L Li, 46 mg/L Mn, and 60 mg/L Ni was fed downward at a constant rate using a peristaltic pump. Effluent samples were collected periodically and analyzed by AAS. The bed saturation time (t_s) was defined as the time at which the effluent reached 95% of the inlet concentration. Metal uptake was determined from breakthrough curves using a mass-balance approach, and the total adsorption capacity (Q, mg/g) was calculated. Figure 3.10 illustrates the experimental setup of the column study.

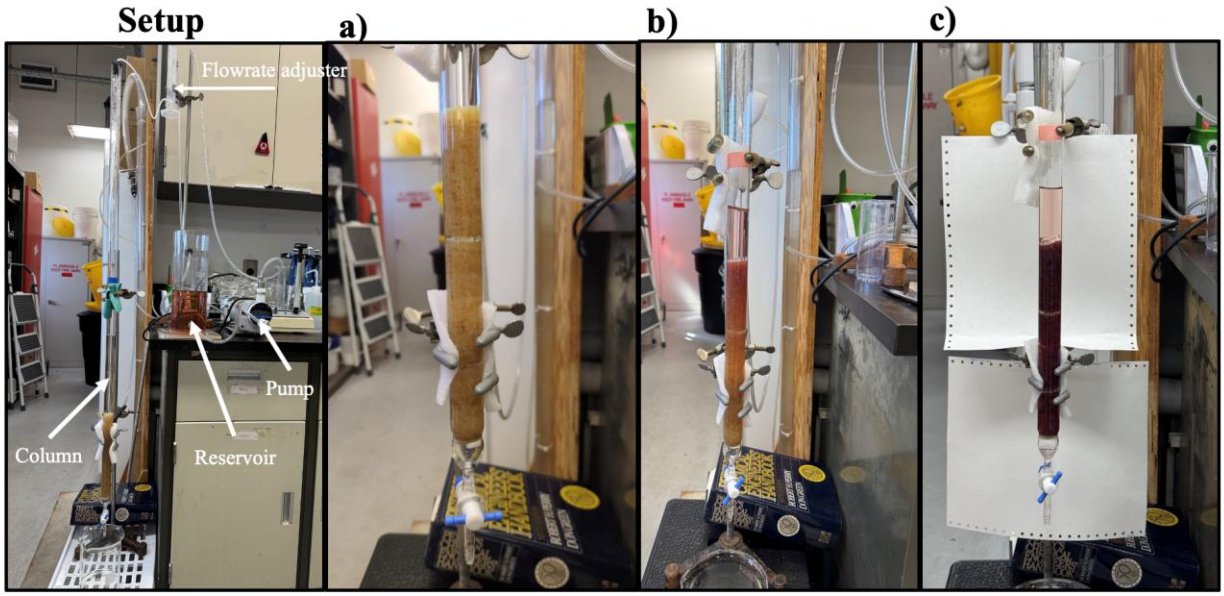

Figure 3.10. Setup of the column study and adsorption stages from a) fresh beads, b) mass transfer zone, and c) saturation.

3.7.6.1. Column Regeneration Experiments

After the initial loading at 4.3 mL/min, the column was regenerated with 0.5 M EDTA in downflow mode (2.4 mL/min). In the second cycle, 1.0 M EDTA (pH 9.5) was used at a flow rate of 2.13 mL/min for enhanced desorption. Loading continued until the effluent reached 95% of the influent concentration, and desorption continued until the residual metal content fell below 5%. Figure 3.11 depicts the experimental adsorption and desorption processes.

Adsorption:

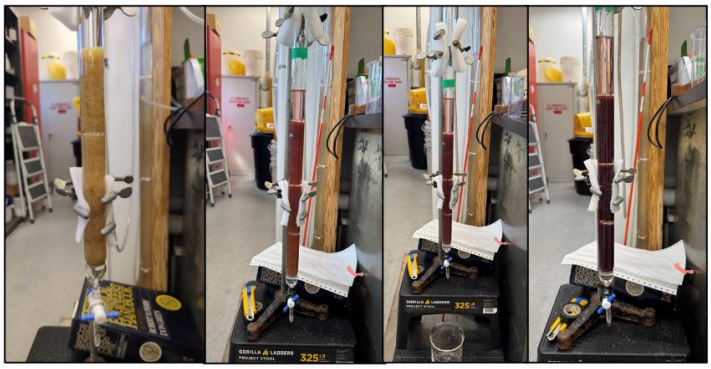

Desorption:

Figure 3.11. The experimental processes of adsorption and desorption.

3.7.6.2. Mathematical Models for Continuous Column Adsorption

Two models, Thomas and Yoon-Nelson (Malbenia John et al., 2024; Patel and In, 2021; Rahman et al., 2025b, 2025a), were employed to describe fixed-bed adsorption behavior due to their simplicity, accuracy, and scalability. The Thomas model assumes Langmuir kinetics and no axial dispersion, enabling the joint assessment of kinetic and equilibrium parameters for column optimization. The Yoon-Nelson model offers a simpler, fewer-parameter approach that effectively predicts breakthrough time at 50% and overall adsorption behavior (See Section 8.3.5 for more details).

Chapter 4 A GREENER METHOD TO RECOVER CRITICAL METALS FROM SPENT LITHIUM-ION BATTERIES: SYNERGISTIC LEACHING WITHOUT REDUCING AGENTS

Published as a research article in Journal of Environmental Management, Vol. 366, Page 121886, August 2024, https://doi.org/10.1016/j.jenvman.2024.121862.

4.1. Abstract

Efficient recycling of critical metals from spent lithium-ion batteries is vital for clean energy and sustainable industry growth. Conventional methods often fail to manage large waste volumes, leading to hazardous gas emissions and dangerous materials. This study investigates innovative methods for recovering critical metals from spent LIBs using synergistic leaching. The first step optimized thermal treatment conditions (570 °C for 2 hours in air) to remove binder materials while maintaining cathode material crystallinity, confirmed by X-ray diffraction (XRD) analysis. Next, response surface methodology (RSM), I-optimal, was used to examine the synergistic effects of sulfuric acid (SA) and organic acids (Org, citric and acetic acids) and their concentrations (SA: 0.5-2M and Org: 0.1-2M) on metal leaching for an eco-friendlier process. Results showed that adding citric acid to SA was more effective, especially at lower concentrations, than using acetic acid. The medium was tested to evaluate the impact of reductant addition. Remarkably, it was discovered that the optimized leaching mixture (1.25M SA and 0.55M citric acid) efficiently extracted metals without the need for any reductant like H_2O_2, highlighting its potential for a simpler and more eco-friendly recycling process. Further optimization identified the ideal solid-to-liquid ratio (62.5 g/L) to minimize acid use. Finally, RSM (D-optimal) was used to investigate the effects of time and temperature on leaching, achieving remarkable recovery efficiencies of 99% ± 0.7 for Li, 98% ± 0.0 for Co, 90% ± 6.6 for Ni, and 92% ± 0.4 for Mn under optimized conditions at 189 minutes and 95°C. Chemical cost analysis revealed this method is about 25% more cost-effective than conventional methods.

Keywords: Li-ion batteries (LIBs); Critical Metals Recovery; Sustainable Waste Management; Synergistic Leaching.

4.2. Introduction

As the world shifts towards clean and low-carbon energy production, the supply of critical metals is of utmost importance. Critical metals play a crucial role in the success of global efforts to transition towards low-carbon energy sources and achieve climate change adaptation goals such as "carbon neutrality", which can help reduce greenhouse gas emissions, aligning with the goals of the Paris Agreement (Cheng et al., 2021; Han et al., 2023; Purnomo et al., 2018; Sethurajan and Gaydardzhiev, 2021). Critical metals, namely, lithium (Li), cobalt (Co), and nickel (Ni), are the main constituents in the functionality of lithium-ion batteries (LIBs). Thus, there is a continuous and growing need to ensure a stable and reliable supply of these elements to facilitate the sustainable growth of the electric vehicle (EVs) and energy storage industries (Jonathan Wilkinson and François-Philippe Champagne, 2022). However, due to significantly increasing demands, it is expected that soon, there will be a supply shortage of elements such as Li and Co (Han et al., 2023).

In the coming years, traditional metal production, like mining, may struggle to match the growing demand for Li, Co, and Ni (Sommerville et al., 2020). This surge, along with the increase in LIB production, is expected to generate around 11 million tons of spent LIBs by 2030 (Xu et al., 2020). This presents significant environmental challenges as conventional waste management may struggle with the vast quantities of waste LIBs. Moreover, metals from discarded LIBs can leach into the environment over time, posing risks of soil and groundwater contamination and various adverse environmental impacts (Baum et al., 2022; Golmohammadzadeh et al., 2022; Kader et al., 2021; Metwally et al., 2013).

Recycling the critical materials would be an environmentally responsible and sustainable approach, reintegrating them into consumption and production processes (Baum et al., 2022; Gaines, 2018; Kader et al., 2021). It is worth noting that spent LIBs contain 6-7 wt.% Li, which is even higher than the levels in its natural sources (Golmohammadzadeh et al., 2022; C. Liu et al., 2019). Conventional recycling methods are pyrometallurgy and hydrometallurgy. Pyrometallurgy, though capable of handling various battery types (C. Yang et al., 2022), is energy-intensive, inefficient, emits greenhouse gases, and results in the loss of valuable materials such as Li and aluminum (Al) in oxide form to slag, which generates harmful by-products that require additional treatment (Gaines, 2018; Golmohammadzadeh et al., 2022; Kader et al., 2021). In contrast,

hydrometallurgical processes can treat LIB waste at a low temperature with high capacity and high recovery rates. The processes usually require low energy, are cost-effective, and final products could have a high purity (Gaines, 2018; Kader et al., 2021).

For LIB recycling via hydrometallurgy, collected batteries are discharged, disassembled, and undergo several preliminary processes: crushing, sieving, magnetic separation, and thermal treatment (350-850°C) to reduce impurities. Thermal treatment decomposes binder materials (usually polyvinylidene fluoride (PVDF)) and enhances electrode surface quality, improving leaching and flotation efficiency (Golmohammadzadeh et al., 2022; H. Huang et al., 2022). Following the removal of binder materials, leaching is conducted to dissolve metals using specific media and conditions tailored to the battery's pre-treatment (Mansur et al., 2021). Leaching processes are primarily affected by factors such as acid concentration and type, temperature, solid-to-liquid ratio (S/L), time, and the presence of reducing agents such as hydrogen peroxide (H_2O_2), which can enhance leaching efficiency. Metals can be leached out using inorganic acids such as sulfuric acid (H_2SO_4) (Guimarães et al., 2022), hydrochloric acid (HCl) (Aaltonen et al., 2017), phosphoric acid (H_3PO_4) (L. Yang et al., 2022), and nitric acid (HNO_3) (Chen et al., 2021) or organic acids such as citric acid (CA), acetic acid (AA), oxalic acid (Golmohammadzadeh et al., 2022, 2017), lactic acid (LA), and gluconic acid (GA) (Roshanfar et al., 2019). Inorganic acids are industry-preferred for their ability to dissolve all metals rapidly, yielding high recovery rates (Zeng et al., 2021). Among them, H_2SO_4 is widely used due to its cost-effectiveness and efficient leaching (Mansur et al., 2021). However, inorganic acids have some drawbacks, including the potential generation of harmful gases (SO_3, Cl_2, NO_x) and hazardous residues, which could result in soil and groundwater contamination and pose health and environmental risks (Roshanfar et al., 2019; Wang et al., 2022; Zeng et al., 2021). Organic acids are eco-friendly, efficient, less corrosive, biodegradable, and comparable in efficiency to inorganic acids. Their use in LIBs waste processing has gained attention for safety and reduced environmental impacts. However, organic acids are more expensive than inorganic acids and form more stable complexes, posing challenges for subsequent metal separation steps (Golmohammadzadeh et al., 2022; Punt et al., 2021; Zeng et al., 2021). While organic acids efficiently leach metals, reducing agents may still be needed (Golmohammadzadeh et al., 2022).

Among organic acids, citric and acetic acids have been employed for the recovery of valuable metals from spent LIBs. Citric acid is highly soluble in water and dissolves cathode materials well, and acetic acid (vinegar) is cost-effective for recovering metals from LIBs (Chaudhary et al., 2023; Mansur et al., 2021). It is worth noting that due to their higher cost and lower leaching capacity per unit volume compared to inorganic acids, organic acids face constraints on their scalability and industrial applicability (Gao et al., 2022; Hossain and Sahajwalla, 2022). To overcome the limitations of individual acid types and leverage their benefits, there is growing interest in studying the synergistic effects of combining inorganic and organic acids. For example, Yang et al. (2022) examined the synergistic effect of sulfuric and oxalic acids. As both leaching and reducing agents, oxalic acid eliminated the need to use additional reductants and resulted in lower operational costs. In another study, the synergistic effect of malonic and sulfuric acid was also investigated to leach nickel manganese cobalt oxide (NMC) cathode materials (Li et al., 2022).

Reducing agents are essential for efficient leaching of cathode materials. While H_2O_2 is clean and doesn't introduce impurities, it poses risks due to its self-decomposing nature. This can lead to potentially dangerous gas production and can oxidize other metals, surpassing the required consumption levels (C. Liu et al., 2019). Hence, exploring safer alternatives or minimizing their use is imperative.

To our knowledge, few studies have explored synergistic leaching involving sulfuric acid (an inorganic acid) alongside organic acids like citric and acetic acids. Similarly, limited research exists on leaching mixed cathode materials—lithium cobalt oxide (LCO), NMC, and lithium manganese oxide (LMO)—which are the main inputs for recycling plants. This study aims to assess synergistic leaching of waste LIBs (comprising mixed cathode materials) using sulfuric acid (SA) and organic acids (citric and acetic acid), with a focus on potentially eliminating the need for a reducing agent like H_2O_2. Furthermore, influential operational parameters such as solid-to-liquid ratio (S/L), time, and temperature were optimized using statistical analysis. Notably, thermal treatment is essential for binder material removal and improved leaching efficiency; thus, thermal treatment conditions (time, temperature, and furnace atmosphere) were optimized before the leaching process in this study.

4.3. Materials and Methods

4.3.1. Materials and Reagents

About 30 kg of spent LIBs, including laptops, cellphones, and Li-polymer batteries, from different brands, such as LG, Samsung, TechTrex Inc., Motorola, etc., and with different sizes, were collected from a recycling facility in Toronto, Canada. Sulfuric acid (H_2SO_4, Fisher Chemical, USA), citric monohydrate ($C_6H_8O_7.H_2O$, Fisher Chemical, USA), and acetic acid (CH_3COOH, Fisher Chemical, USA) with a purity of 98%, 99%, and 99.7%, respectively, were used in this study. Hydrogen peroxide (H_2O_2) of 30% purity (Acros, USA) was used as a reducing agent. All solutions were prepared using deionized water. Unless otherwise stated, all materials are analytically graded.

4.3.2. Sample Preparation

Discharging of collected batteries was done in anticorrosion plastic buckets (High-Density Polyethylene (HDPE), Pro-Western Plastics) containing a 10% sodium chloride (NaCl) solution under a fume hood for 24 hours (Li et al., 2019.; Mishra et al., 2022; Shaw-Stewart et al., 2019). To prevent short circuits and reduce the risk of fires, the batteries were kept separated from each other within the buckets. Then, samples were taken out of the solution and rested for another 24 hours. All batteries were subsequently tested with a multimeter to ensure that they had discharged completely. Batteries were disassembled, and cathodes were manually separated from anodes using pliers, a stainless-steel tube cutter, a screwdriver, and a hammer. Afterward, all cathode materials (cathode materials + Al foils) were cut into squares of 2×2 cm^2. Following the separation of cathode materials from Al foils, using heat treatment, powder samples were used for subsequent analyses and experiments.

4.3.3. Characterization

Different parts of the dismantled waste LIBs were weighed to determine the weight percentages of the cathode, anode, and other materials using a two-decimal balance (Mettler Toledo, Model PL3002). X-ray diffraction (Bruker D8 Endeavor XRD equipped with a sealed-tube Cu K_α source (λ= 1.54184 Å) was conducted to determine the type of cathode materials and crystallinity, to investigate the efficiency of pre-treatment and to examine the separation of Al from cathode

materials (or black mass (BM)). Crystalline phases were determined using DIFFRAC.EVA software in conjunction with the 2023 PDF-4+ database (ICDD).

The concentration of metals in the cathode materials was measured using inductively coupled plasma (ICP, Agilent 5110 ICP-ES) after digesting the samples using aqua regia (HNO_3: HCl= 1:3) and a temperature of 120 °C overnight.

The cathode material surface morphologies were identified using a scanning electron microscope (SEM, JEOL 6610LV) in combination with energy-dispersive X-ray spectroscopy (EDS, Oxford XMax). A 1:1:1 ratio of cellphone, lithium-polymer, and laptop batteries was used for the experiments. For the main experiments, Atomic Absorption Spectroscopy (AAS, PinAAcle 500, PerkinElmer) was used to measure metal concentrations. The device was calibrated using a nonlinear calibration method with a zero intercept. The AAS machine was calibrated prior to each use to ensure accurate measurements. The samples underwent five readings, and the average of these readings was employed in subsequent calculations. Samples were analyzed immediately following the experiments; if immediate analysis was not possible, they were stored in amber glass containers at room temperature in a dark cabinet.

4.3.4. Thermal Treatment

This stage was conducted to remove binder materials to increase leaching efficiency and separate Al from BM. First, samples were characterized by thermogravimetric analysis (TGA) to determine the optimum range of temperature using a controlled atmosphere furnace (Setaram Setsys 24 equipped with a TG-DTA 1600C rod). The conditions were a heating rate of 2.5 °C/min and flow rate of 1.5 L/h (=24 mL/min) in an Al_2O_3 crucible under argon (inert) and 20% oxygen + 80% argon (simulated air) atmospheres from 25-800 °C. Second, other parameters, including time duration (30 min-6 h) and furnace atmosphere (air and Ar), were studied and optimized (Portia Makwarimba et al., 2022; Zhang et al., n.d.). A muffle furnace (Thermolyne, Model 62700, USA) and a muffle/atmosphere-controlled furnace (Thermo Scientific, Model F6000, USA) were utilized to perform experiments under air and inert atmospheres.

4.3.5. Design of Experiments (DOE) and Leaching Experiments

Statistical analysis serves as a complementary tool to quality control and quality assurance (QA/QC), enhancing process reliability and ensuring consistent and accurate outcomes. Therefore, leaching experiments were designed using Design Expert 12 (State-Ease Inc., Minneapolis, MN, USA), and metal recoveries were analyzed statistically. The design included two stages, i.e., screening and optimization. Screening tests were conducted to optimize acid types (sulfuric acid + citric acid and sulfuric acid + acetic acid) and acid concentrations (sulfuric acid concentration (0.5-2 M) and organic acid concentrations (0.1-1 M)). Other parameters were kept constant at the temperature of 90 °C, time of 2 h, a solid-liquid ratio (S/L) of 50 g/L, and the H_2O_2 dosage of 5 vol.% according to the previous studies (Chen et al., 2021; Guimarães et al., 2022; Roshanfar et al., 2019; Wu et al., 2020). Since the purpose of this stage was to determine optimum conditions for acid types and concentrations, the I-optimal response surface methodology (RSM) was used (Smucker et al., 2018). The optimum condition was repeated without hydrogen peroxide addition to examine the possibility of eliminating H_2O_2 on metal recovery rates.

The optimum conditions of the screening stage were then used in the next stage (optimization) to optimize the S/L ratio (25-150 g/L), temperature (40-95 °C), and time duration (30-240 min). Because the S/L ratio is a key factor in acid usage, it was optimized initially using the one-factor-at-a-time method. The S/L ratio was tested at 25 g/L, 50 g/L, 62.5 g/L, 75 g/L 100 g/L, and 150 g/L while other parameters remained constant (Temperature of 90 °C and 2 h). Afterward, a D-optimal response surface methodology (RSM) was implemented to investigate the effect of time and temperature (Smucker et al., 2018).

The recovery of each element was determined using the following equation:

$$\text{Recovery}\ (\%) = \frac{\text{Extracted metal in Leaching solution}\ (\frac{\text{mg}}{\text{L}})}{\text{Total metal concentration in initial sample}\ (\frac{\text{mg}}{\text{L}})} \times 100 \qquad (4\text{-}1)$$

In all experiments, a 50 mL solution was placed in a three-neck, round-bottom flask with a capacity of 250 mL. The flask was placed in a water bath to maintain a constant temperature. Water evaporation was minimized by attaching a glass condenser to the flask. The solution was also heated and mixed using a magnetic stirrer. A thermometer was used to measure the temperature

within a range of ±2°C. Finally, a glass funnel, volumetric flask, and filter paper (125 mm, medium flow, Labasics, USA) were used to filter the leached solutions.

4.4. Results and Discussions

4.4.1. Characterization of the Cathode Materials in Spent LIBs

Table 4.1 shows the weights of different parts of each battery type (Li-polymer, cellphone, and laptop batteries) and mixed batteries (Li-polymer: cellphone: laptop= 1:1:1) after dismantling. As can be seen, the batteries contained an average of 36 wt.% of cathode materials, which is within the range reported by previous studies (Vanderbruggen et al., 2022). Figure 4.1 (a-c) shows the XRD patterns of untreated cathode materials of different types of batteries, namely cellphone, Li-polymer, and laptop batteries. It can be seen that LCO was detected in all of the batteries as the primary cathode material in batteries (Nancharaiah et al., 2016). LMO was detected in Li-polymer batteries as it is employed in portable electronic devices (Ciez and Whitacre, 2019). In the batteries of cellphones and laptops, NMC was detected due to the fact that NMC cathode materials have a higher energy density (Windisch-Kern et al., 2022).

Table 4.1. The weights of different parts of the LIBs

	Li-Polymer	**Cellphone**	**Laptop**	
	%	%	%	without plastic case (%)
Other	22.9	39.2	56.36	42.9
Cathode	42.5	35.7	29.38	38.4
Anode	34.6	25.1	14.26	18.7

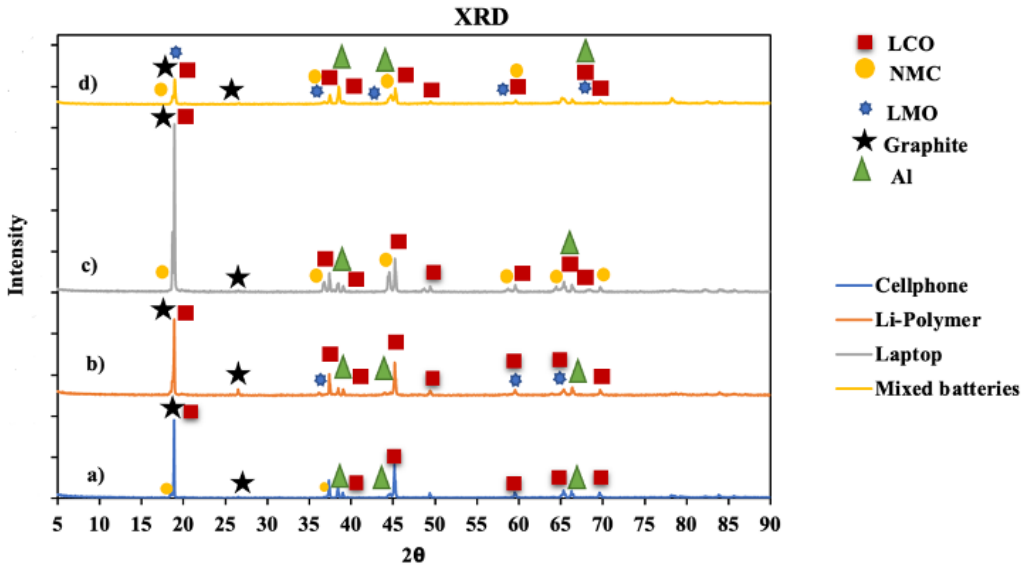

Figure 4.1. XRD results of untreated a) cellphone, b) Li-polymer, c) laptop batteries, and d) mixed batteries (a ratio of 1:1:1).

Table 4.2 shows the metal concentration in the mixed cathode materials (1:1:1 cellphone: Li-polymer: laptop). There was approximately 44 wt.% of Co in the samples, along with 6 wt.% of Li, 3 wt.% of Ni, and 4 wt.% of Mn, respectively. Figure 4.2 illustrates the SEM-EDS image of the mixture of cellphones, laptops, and Li-polymer, which confirms that Co, Li, Ni, and Mn were present on the surface of cathode materials. Carbon (C) was also detected, which can be attributed to the binder materials.

Table 4.2. ICP results of mixed cathode materials of three types before and after Al separation

	Al	Co	Cr	Cu	Fe	Li	Mn	Na	Ni	V	Zn
Mixed batteries with Al foils (wt.%)	7.9	44.5	0.0	0.2	0.1	5.7	3.7	0.1	2.9	0.0	0..0
Mixed batteries after removing Al foils (wt.%)	0.3	50.1	0.0	0.0	0.0	6.3	8.0	0.2	2.8	0.0	0.0

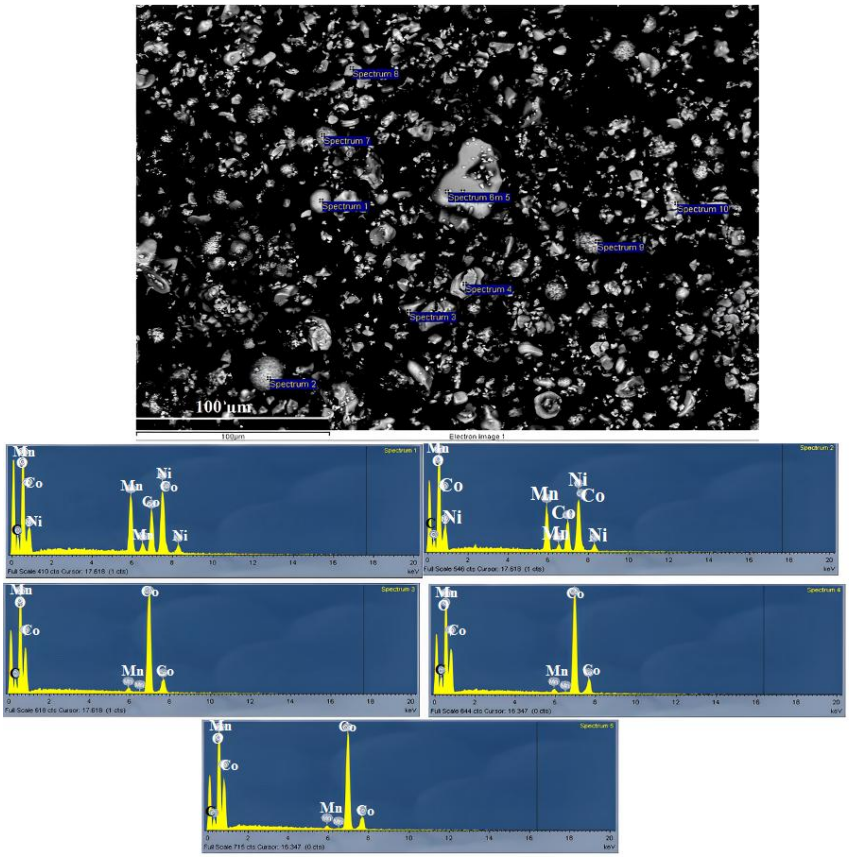

Figure 4.2. SEM-EDS image of cathode materials (a mixture of cellphones, laptops, and Li-polymer).

4.4.2. Thermal Treatment Results

Binder materials, usually PVDF and present on the surface of cathode materials, could significantly reduce metal recovery and need to be removed as a pretreatment step (Golmohammadzadeh et al., 2023). Various methods can be used to remove binder materials, including cryogenic grinding, chemical dissolutions, and thermal treatments (decomposition of the binder materials) (Mansur et al., 2021). Among the various methods, the thermal treatment stands out as the most environmentally sustainable option and is suitable for industrial use. (Liu et al., 2023). Additionally, it can facilitate the separation of aluminum foil from cathode materials. The objective of this phase was to optimize the thermal treatment of the samples and determine the temperature, time duration, and atmosphere type (air or inert) to be used before the leaching stage.

This is important because high temperatures can trigger various reactions, such as volatilization, decomposition, and oxidation.

As a first step, thermal gravimetric analysis (TGA) was used to evaluate the thermal behavior of a mixture of cathode materials. Figure 4.3 shows the results of TG (%) and DTG (%min) for the mixed batteries in argon (a) and simulated air (b) atmospheres in a range of 25-800°C. TGA typically in both air and inert atmospheres reveals three stages: the first stage involves the volatilization of residue electrolytes and adsorbed water (30-400 °C), followed by binder decomposition (450-600 °C), and finally, carbothermal reactions and metal alloy formation (above 650 °C) (H. Huang et al., 2022; Liu et al., 2023; Yuan et al., 2023.; Zhang et al., 2023.). In the present study, both atmospheres showed three stages, with the second stage being attributed to the decomposition of the binder. In the argon atmosphere, stage 2 was from 177 °C to 571 °C, which is binder decomposition (Liu et al., 2023). The stages 1, 2, and 3 exhibited reductions in mass of 3.4%, 3.0%, and 4.8%, respectively. In the case of air atmosphere, the first stage was from 42 °C to 220 °C (a mass reduction of 3.5%), the second stage was between 220 °C to 570 °C (a mass reduction of 4.7%), and the third stage was from 570 °C to 818 °C, with a mass reduction of 3.7%. The results indicate that, interestingly, the binder materials decompose in both atmospheres at approximately the same temperature. Accordingly, 570 °C was selected as the optimum temperature for both atmospheres, which is in accordance with previous studies (Liu et al., 2023; Salces et al., 2022; Vanderbruggen et al., 2022).

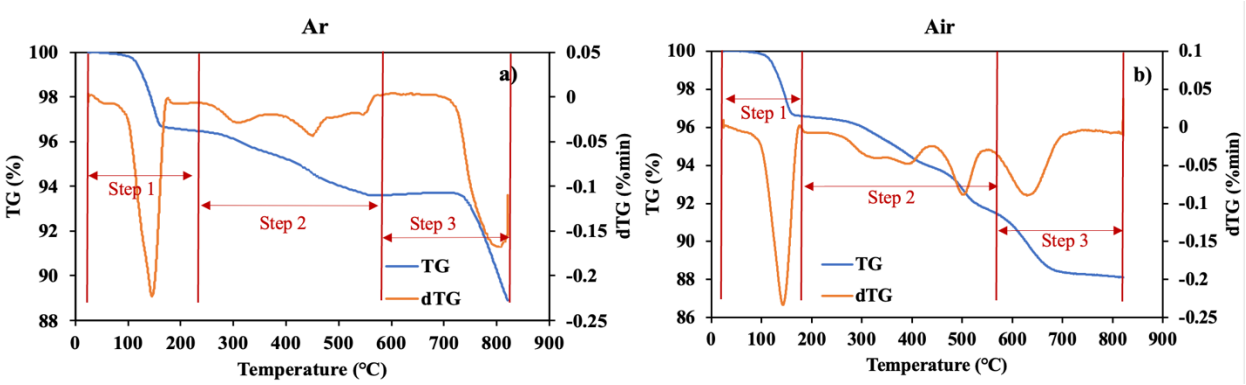

Figure 4.3. TG and dTG results of mixed battery in a) argon (inert) b) 20% oxygen and 80% argon (simulated air) in a range of 25-800 °C.

The optimum time duration of the thermal treatment was determined by conducting experiments at 30 minutes to 240 minutes and comparing the XRD results. As can be seen in Figure 4.4, (a) and (b), for the 30-minute duration of thermal treatment in both atmospheres the Al foil was separated from the cathode materials (in comparison with Figure 4.1 (d)). Moreover, these results demonstrated that both furnace atmospheres did not change the crystallinity of the cathode materials during thermal treatment. Low amounts of cobalt oxide (Co_3O_4) were detected in samples treated in both atmospheres, which was inevitable. Hence, both atmospheres yielded the same results. Thus, considering operational costs, the air atmosphere was selected as the optimal furnace environment for this study.

As shown in Figures 4.4 (c) and (d), binder materials were completely removed after 2 and 4 hours. However, this was not the case for the 30-minute duration, as the binder materials are shown as graphite. The optimal time for thermal treatment of the samples was therefore determined to be two hours. It was also confirmed by the SEM-EDS image of the thermal treatment (Figure 4.5) that there was no carbon detected on the surface after the treatment was carried out for two hours. As a result, the optimal condition for this stage was determined to be subjecting the cathode materials to 2 hours of thermal treatment at a temperature of 570 °C under an air atmosphere.

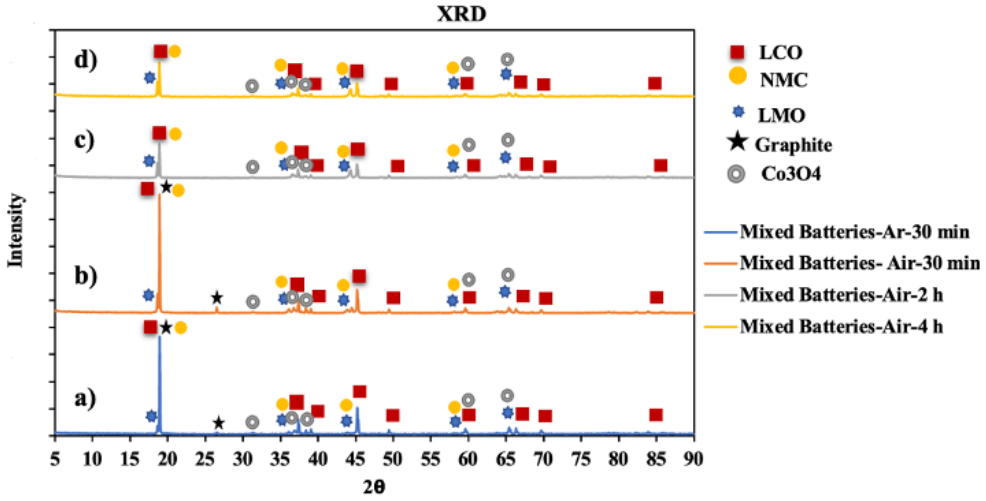

Figure 4.4. XRD results of heat-treated mixture batteries at 570 °C a) under Ar in 30 min, b) under Air in 30 min, c) under Air in 2 h, and d) under Air in 4 h.

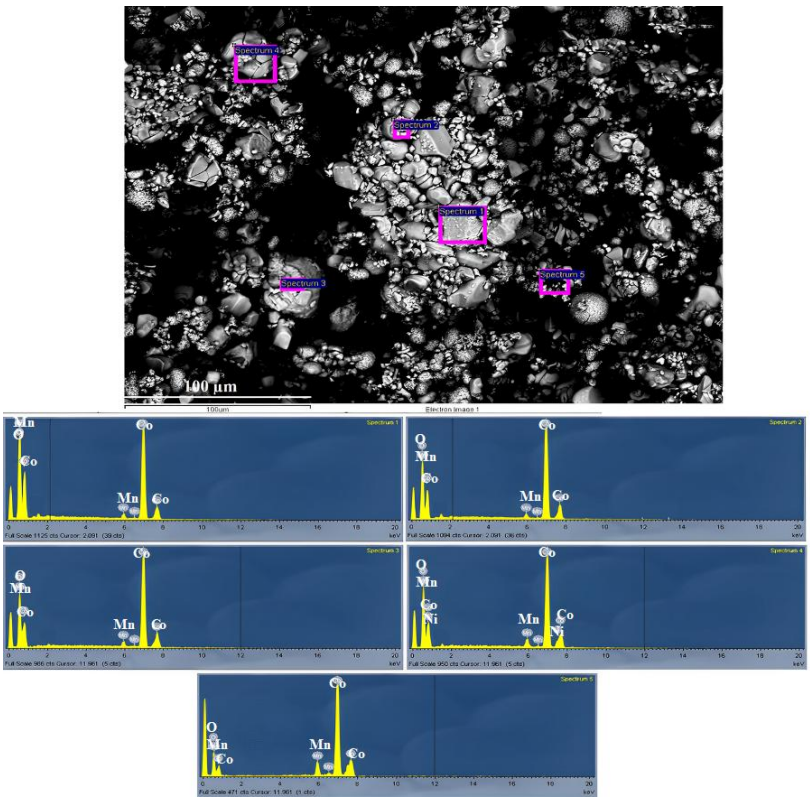

Figure 4.5. SEM-EDS image of heat-treated cathode materials at 570 °C (a mixture of cellphones, laptops, and Li-polymer) after 2 h under air atmosphere.

4.4.3. Leaching Stage Results

The experiments were designed into three phases: screening, optimization of the solid-to-liquid ratio (S/L), and optimization of time and temperature. During the screening experiments, the concentrations of acids in the acid mixture and the type of organic acid (citric acid (CA) and acetic acid (AA)) in the mixture were fine-tuned. Given that the S/L ratio significantly impacts acid usage, it was optimized as the second phase. Following this, the impact of time and temperature was investigated. It is important to highlight that following the screening phase, the need for adding a reducing agent was examined.

4.4.3.1. Screening Results

The mixed cathode materials (cellphones, laptops, and Li-polymers = 1:1:1) were used for the leaching stage after they had been thermally treated under the optimal conditions determined in the previous step (570 °C in 2 h under an air atmosphere). Based on the previous studies (Chen et al., 2015; Li et al., 2022; Peng et al., 2018; Urias et al., 2020; Yang et al., 2022a; Zhang et al., 2013), screening experiments were conducted using sulfuric acid with concentrations ranging from 0.5-2 M, organic acids with concentrations ranging from 0.1-1 M, and two types of organic acids (acetic acid (AA) and citric acid (CA)). To design the experiments, an I-optimal design was modified with additional center points (RSM). Table 4.3 summarizes the results of 25 experiments that were conducted in this stage. Temperature, time, S/L ratio, and hydrogen peroxide dosage were kept constant in all experiments at 90 °C, 2h, 50 g/L, and 5 vol.%, respectively (Chen et al., 2020, 2015; Meng et al., 2020; Peng et al., 2018; Roshanfar et al., 2019). The results showed that both organic acids along with sulfuric acid were effective in recovering metals. However, citric acid was more effective at a lower concentration. For instance, in experiments labeled 13 (1.25M of SA and 0.55M of AA) compared to 19 (1.25M of SA and 0.55M of CA), the recovery rates for Li, Co, Ni, and Mn were 97.3%, 88.8%, 100.0%, and 99.5%, respectively, as opposed to 99.9%, 98.7%, 100%, and 100% for Li, Co, Ni, and Mn.

Table 4.3. The metal recovery in the screening stage

Run	Sulfuric acid concentration (SA, M)	Organic acid concentration (Org, M)	Type of acid	Li Recovery (%)	Co Recovery (%)	Ni Recovery (%)	Mn Recovery (%)
1	0.5	1	Acetic	92.6	93.2	95.7	95.7
2	2	1	Acetic	95.4	92.7	99.3	100.0
3	2	0.79	Citric	90.3	93.6	93.9	94.1
4	2	0.1	Acetic	100.0	98.7	100.0	100.0
5	2	1	Acetic	96.3	90.3	99.9	98.4
6	1.25	0.55	Acetic	96.7	90.7	100.0	100.0
7	2	0.1	Citric	94.5	89.9	95.3	95.6
8	1.17	1	Citric	94.0	85.5	96.5	96.1

9	1.41	0.19	Citric	93.0	93.2	93.9	96.5
10	2	0.55	Acetic	99.0	95.9	100.0	99.4
11	0.5	0.61	Citric	98.6	92.0	100.0	100.0
12	2	0.79	Citric	92.4	94.4	95.4	94.3
13	1.25	0.55	Acetic	97.4	88.8	100.0	99.5
14	1.25	0.1	Acetic	90.0	87.5	93.7	92.4
15	0.5	0.1	Acetic	81.7	64.6	99.6	100.0
16	0.5	0.55	Acetic	85.5	70.3	100.0	100.0
17	0.5	1	Acetic	93.5	94.0	95.9	95.9
18	0.5	0.61	Citric	100.0	92.9	100.0	100.0
19	1.25	0.55	Citric	99.9	98.7	100.0	100.0
20	0.5	1	Citric	97.8	89.2	100.0	100.0
21	0.83	0.1	Citric	95.0	94.8	99.6	100.0
22	1.25	0.55	Citric	97.7	99.5	100.0	99.7
23	1.17	1	Citric	95.3	85.1	97.9	99.2
24	1.25	0.55	Citric	98.9	98.9	100.0	100.0
25	1.25	0.55	Acetic	94.1	88.2	97.3	97.1

As stated, the RSM I-optimal model of Design Expert was employed to analyze the recovery rates. As an example, the proposed model for the Li recovery rate at this stage is as follows:

$$\boldsymbol{Li\ recovery} = 96.72 + 1.55\,SA + 0.9727\,Org + 0.8835\,AT - 3.44\,SA * Org - 3.98\,SA * AT - 1.28\,Org * AT - 1.41\,SA^2 - 2.69\,Org^2 \quad (4\text{-}2)$$

where SA, Org, and AT represent the coded values of sulfuric acid concentration, organic acid concentration, and acid type (acetic acid and citric acid), respectively. R-squared, P-values, and F-values are shown in Table 4.4. P-values indicate whether a model is significant, and if it is less than 0.05 (95% confidence), then the model is significant (Anderson and Whitcomb, 2017). Based on Table 4.4, the predicted models are significant and within 95% confidence. F value refers to a value on the F distribution. As F-values increase, the model becomes more confident, and it is less likely that the data are due to chance (Anderson and Whitcomb, 2017). The correlation coefficient

(R-squared) amounts are close to one, which indicates that the predicted models can be fitted to the experimental data (Anderson and Whitcomb, 2017; Roshanfar et al., 2019).

Table 4.4. R-squared data for metal recoveries

Metal	Li	Co	Ni	Mn
Screening				
R^2	0.89	0.99	0.95	0.95
P-Value	<0.0001	<0.0001	0.0006	0.0004
F-value	0.0067	120.49	1047	11.32
Optimization				
R^2	0.94	0.98	0.96	0.97
P-Value	<0.0001	<0.0001	< 0.0001	< 0.0001
F-value	63.97	97.29	154.79	73.1

Based on the experiments and statistical results, and to enhance the clarity of the findings, a detailed discussion of Li, the most critical metal in batteries, is presented as follows. However, it is important to note that the results apply to all metals, which follow the same trend. Figure 4.6 shows the effect of the parameters (concentration of acids and organic acid type) on the Li recovery rate at the optimum conditions. According to the results, both organic acids, in combination with sulfuric acid, showed high potential and were effective at leaching metals (Figure 4.6 (c)). The application of organic acid helped reduce the use and concentration of sulfuric acid. However, citric acid is slightly more effective than acetic acid and achieves higher efficiency at lower concentrations, especially for Li (about 98% for CA compared to about 95% for AA) and Co (about 100% for CA compared to 98% for AA). This is because citric acid has a greater capacity to complex metals than acetic acid. Therefore, citric acid was selected as the optimum organic acid. Also, CA is a strong organic acid and chelating agent that releases three hydrogen ions (H^+) during dissociation reactions (pKa_1 = 3.28, pKa_2 = 4.71, and pKa_3 = 6.39) (Asadi Dalini et al., 2020). Acetic acid, on the other hand, is a weak acid with a pKa value of 4.75, which releases one hydrogen ion upon reaction.

The recovery of Li was reduced when the concentration of sulfuric acid was increased in the case of citric acid being used (Figure 4.6 (a)). As for citric acid concentration, Li recovery had an optimum concentration (0.55M), after which it began to decline (Figure 4.6 (b)). It could be because an increase in acid concentrations results in a greater concentration of H^+ in the media, delaying the formation of chelates. The formation of chelate occurs at higher pH levels, and an increase in acidity may delay this process (Golmohammadzadeh et al., 2017; Musariri et al., 2019; Roshanfar et al., 2019). According to Figure 4.6 (d), there is an interaction between sulfuric acid (SA) concentration and organic acid concentration, and the optimum point was 1.25 M and 0.55 M of sulfuric acid and citric acid, respectively. As far as Co, Ni, and Mn are concerned, increasing both sulfuric acid and citric acid concentrations to 1.25 M and 0.55 M enhanced the recovery rate. Thereafter, the recovery of metals began to decrease as the SA and CA concentrations increased to around 1.7 M and 0.9 M, respectively, before increasing again. Accordingly, concentrations of 1.25 M and 0.55 M sulfuric and citric acids were selected to achieve optimal results. The optimum conditions (SA: 1.25 M and CA: 0.55M) were repeated two times, and the results for the recovery of Li, Co, Ni, and Mn were 98%, 99%, 100%, and 100%, respectively.

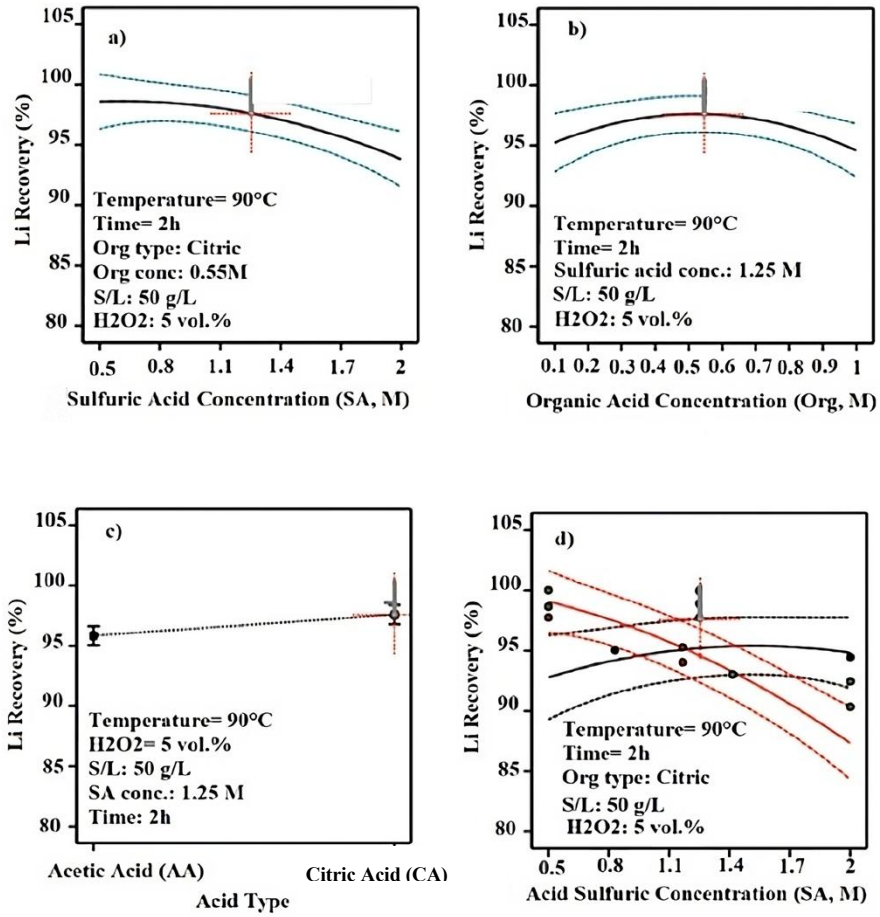

Figure 4.6. Main effect plots based on I-optimal-RSM design, a) the effect of sulfuric acid concentration (SA, M), b) the effect of organic concentration (Org, M), c) the effect of organic acid type, and d) the interaction of sulfuric acid and organic acid content.

4.4.3.2. Effect of Reducing Agent Addition

Citric acid has the capacity to also function as a reducing agent, converting Co (III) and Mn (III) into Co (II) and Mn (II), respectively, and it may not be necessary to add a reducing agent to the obtained optimum condition (SA:1.25 M and CA: 0.55 M) (Zhuang et al., 2019). This is not the case for acetic acid. Thus, it is advantageous to use CA and eliminate the reducing agent, i.e., H_2O_2, which is also hazardous. This could also reduce operating costs and offset the higher cost of citric acid (which is more expensive than acetic acid). To investigate the effect of H_2O_2 on recovery rates, the optimized conditions (SA: 1.25 M and CA: 0.55 M) were repeated three times without adding H_2O_2 at 90 °C for 2 h, and the results were compared with those from H_2O_2-added

solutions. The recovery rates (±SD) were achieved at 96% ± 1.1, 96% ± 2.4, 98% ± 0.9, and 97% ± 0.8 for Li, Co, Ni, and Mn as compared to 98%, 99%, 100%, and 100% for Li, Co, Ni, and Mn, respectively, which were comparable to those for solutions containing H_2O_2. Given that the metals can leach into the medium without hydrogen peroxide, it is unnecessary to add hydrogen peroxide to the solution. It may be because citric acid, in addition to its primary function as a lixiviant, can also act as a reducing agent. When citric acid is used as a reducing agent, it can be oxidized into carbon dioxide and water (Zhuang et al., 2019). Joulié et al. (2017) also reported that adding citric acid to a strong acid, such as sulfuric acid, can enhance metal recoveries.

4.4.3.3. Optimization Results

In addition to the concentration and types of acids, various factors, such as solid-to-liquid ratios, time, and temperature, significantly influence the leaching process and require careful optimization. Generally, excessive solid-to-liquid ratios impede recovery, whereas elevated temperatures and prolonged durations can enhance leaching rates. Stirring speed generally has been reported to have minimal impact (Golmohammadzadeh et al., 2017; Roshanfar et al., 2019).

a) Effect of Solid-to-Liquid ratio (S/L)

Since the S/L ratio has the greatest impact on acid consumption, it was studied first. Typically, increased cathode material usage results in greater acid demand during leaching. Consequently, it was anticipated that higher leaching efficiencies would be achieved by introducing larger quantities of acid. The results of S/L ratios on metal recovery rates are shown in Table 4.5. Time, temperature, and acid concentrations were 1.25 M of SA and 0.55 M of CA in 2 h at 90 °C, respectively. According to the results, increasing the S/L ratio reduces the recovery rate, consistent with previous studies. In general, a high S/L ratio hinders the recovery process because a high S/L ratio is ascribed to the less available volume-to-area ratio, interrupting metal recoveries (P. Li et al., 2022a; Roshanfar et al., 2019; C. Yang et al., 2022; Zhuang et al., 2019). While 25 g/L appeared to offer optimal efficiency, it increased acid consumption during the process. However, raising the S/L ratio to 62.5 g/L shows that the average recovery rates for all metals consistently exceed 95%, with reduced acid consumption. This indicates that optimizing the S/L ratio within this range is crucial for maintaining high recovery rates across diverse metals while minimizing acid

consumption during leaching. Given the high metal recovery rates achieved, a concentration of 62.5 g/L was selected as optimal, balancing economic and environmental considerations.

Table 4.5. Results of changing the ratio of S/L on metal recovery rates (average of two samples)

S/L (g/L)	Co Recovery (%)	Li Recovery (%)	Mn Recovery (%)	Ni Recovery (%)	Average (%)
25	95.3±4.0	97.8±0.8	100.0±0.0	99.1±1.3	98
50	94.8±3.0	96.7±1.4	97.8±0.6	98.5±0.9	97
62.5	97.9±0.7	98.3±1.1	91.3±1.0	88.5±0.5	95
75	87.9±3.4	90.3±3.5	83.9±1.3	87.3±8.4	87
100	80.2±1.1	84.4±1.9	82.4±1.0	80.6±0.7	82
125	62.4±0.9	79.4±1.7	81.2±1.0	79.9±0.6	76
150	53.4±0.8	73.4±1.6	80.4±1.0	78.4±0.4	71

b) Effect of Time and Temperature

The effects of time (30-240 min) and temperature (40-95 °C) were examined using the D-optimal response surface methodology in Design Expert, aiming to explore potential interactions between these variables. Other parameters were kept constant at the optimized conditions (SA and CA concentrations of 1.25 M and 0.55 M and an S/L of 62.5 g/L). Table 4.6 shows the experimental design and results. According to the results, increasing time and temperature enhanced the metal recovery rates. According to previous research findings, it has been consistently observed that increasing both temperature and time leads to notable improvements in leaching rates (Musariri et al., 2019). This phenomenon is attributed to the fact that higher temperatures and prolonged durations effectively stimulate the dissolution process of acids, thereby facilitating enhanced extraction efficiencies (Roshanfar et al., 2019).

Table 4.6. Effects of changing time and temperature on metals recovery

Run	Time (min)	Temperature (°C)	Li Recovery (%)	Co Recovery (%)	Ni Recovery (%)	Mn Recovery (%)
1	30	95	84.8	73.5	86.6	79.0
2	104	93	98.1	89.8	93.4	87.1
3	240	40	77.0	31.8	66.7	57.2
4	30	59	77.3	48.2	70.0	54.1
5	240	78	95.1	81.45	95.9	73.4
6	240	40	74.5	31.6	68.3	53.2
7	178	95	95.1	98.3	94.0	91.7
8	30	95	90.4	65.1	92.0	77.5
9	240	78	96.5	82.1	94.3	75.7
10	120	64	82.5	71.3	78.0	66.9
11	178	95	99.6	97.0	97.3	91.8
12	30	40	72.9	30.7	61.5	48.0
13	30	40	68.8	27.6	51.9	43.9
14	140	40	70.3	29.2	60.5	53.7
15	64.65	77	80.8	65.0	83.3	65.3
16	200	60	84.4	68.8	80.0	72.8

Regarding the statistical analysis, RSM D-Optimal was used in this stage. Table 4.4 shows the R-squared, P-values, and F-values for the proposed models for Li, Co, Ni, and Mn. These results indicate that the models are well-suited to the experimental results. The model for Li, as an example, is as follows:

$$Li\ recovery = 84.34 + 5.27 \times Time + 11.58\ \times Temp + 2.7\ Time \times Temp \quad (4\text{-}2)$$

where Time and Temp represent the coded values of time and temperature, respectively. It can be concluded that temperature has a greater effect than time based on the coefficients for temperature and time for all metals.

Figure 4.7 shows the contour (2D surfaces) of recovery rates as a function of time, temperature, and their interaction, as well as the optimum region for all metals. As shown, increasing both time and temperature improves leaching recovery for all metals. Using lithium (Li) as an example, a 150-minute duration at 80 °C yields a recovery rate of approximately 90%. Extending the duration to 240 minutes and raising the temperature to around 90 °C can increase Li recovery to around 100%. In this study, to streamline the process and conserve energy, a duration of 189 minutes (approximately 3 hours) was chosen at 95 °C. Based on the RSM results, a time of 189 min and a temperature of 95 °C was determined as the optimum point, which is comparable with the literature review (Chen et al., 2018b; Musariri et al., 2019). The recommended condition was repeated twice, and the results for Li, Co, Ni, and Mn were achieved 99% ± 0.7, 98% ± 0.0, 90% ± 6.6, and 92% ± 0.5, respectively, which are comparable with the suggested recovery rates of the metals from software (100%, 98%, 99%, 91% for Li, Co, Ni, and Mn, respectively).

Finally, the optimal conditions for synergistic leaching were selected as 189 min at 95 °C, with sulfuric and citric acid concentrations of 1.25 M and 0.55 M, respectively, and no reducing agent.

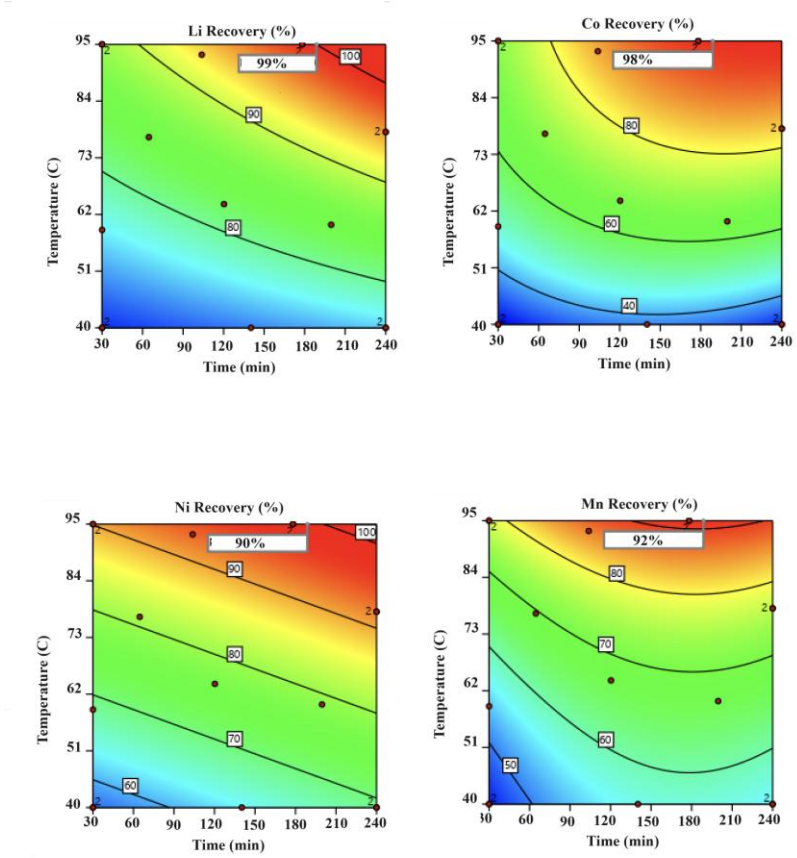

Figure 4.7. The contour of interaction between time and temperature on recovery rates.

Table 4.7 presents a comparison of results between the literature and the current study. While all studies yielded promising results, the current study stands out for the following reasons: Unlike studies employing sulfuric acid (Chernyaev et al., 2021; Kong et al., 2023; Su et al., 2023; C. Yang et al., 2022), this study achieved a reduction in sulfuric acid concentration by employing citric acid. This is important because using a lower SA concentration reduces acid consumption and creates a safer environment. Moreover, it is evident that numerous prior studies incorporated a reducing agent, notably H_2O_2, which may pose environmental hazards (Kong et al., 2023; P. Li et al., 2022; Song et al., 2022). However, this study effectively eliminated the need for a reducing agent through synergistic leaching. From a large-scale perspective, relying solely on high concentrations of organic acids is impractical. In comparison to Song et al. (2022), this study employs a combination of SA and citric acid to reduce the concentrations of both acids, making it feasible for scaling up.

Table 4.7. Literature comparison with the results of this study

Leaching media	Reducing agent	Conditions		Results		Reference
Sulfuric acid and Malonic acid	H_2O_2 (5 vol % of 30%)	Concentration S/L Temperature Time	0.93 M H_2SO_4; 0.85 M malonic acid 61 g/L 70 °C 81 min	Li Co Ni Mn	99.8% 97.2% 97.2% 96.9%	(P. Li et al., 2022a)
Sulfuric acid and oxalic acid (OX)	-	Concentration S/L Temperature Time	2.5 M H_2SO_4; 20 g/L OX 100 g/L 85 °C 100 min	Li Co Ni Mn	99.3% 97.0%, 98.4% 97.5%;	(C. Yang et al., 2022)
Sulfuric acid	Cu, Al, and Fe (2 g/L of Fe and 10 g of Cu added)	Concentration S/L Temperature Time	2 M 200 g/L 60 °C 120 min	Co	100%	(Chernyaev et al., 2021)
Sulfuric acid	Pyrite (FeS_2 dosage: 1:0.8)	Concentration S/L Temperature Time	3 M 25 g/L 80 °C 120 min	Li Co Ni Mn	98-99.9% 98-99.9% 98-99.9% 98-99.9%	(Su et al., 2023)
Sulfuric acid	Methanol (10 vol.%)	Concentration S/L Temperature Time	5 M 10 g/L 90 °C 120 min	Li Co	99% 99%	(Kong et al., 2023)
Citric acid	H_2O_2 (5 vol%)	Concentration S/L Temperature Time	1 M 20 g/L 95 °C 120 min	Li Co Ni Mn	88.2% 94.0%, 72.5% 90.5%	(Song et al., 2022)

Phosphoric acid	H_2O_2 (5 vol%)	Concentration S/L Temperature Time	2 M 20 g/L 95 °C 100 min	Li Co Ni Mn	92.9% 94.8% 93.3% 94.3%	
Acetic acid	H_2O_2 (4.0 % (v/v))	Concentration S/L Temperature Time	2 M 20 g/L 70 °C 40 min	Li Co Ni Mn	98.6% 94.6% 96.4% 99.0%	(K. Wang et al., 2022)
Citric acid	Orange peel powder (200 mg)	Concentration S/L Temperature Time	1.5 M 25 g/L 100 °C 240 min	80–99% of Ni, Mn, Co, and Li		(Wu et al., 2020)
Sulfuric acid + Citric acid (this study)	-	Concentration S/L Temperature Time	1.25 M H_2SO_4; 0.55 M of CA 62.5 g/L 95 °C 189 min	Li Co Ni Mn	99% 98% 90% 92%	

4.4.4. Cost Analysis and Chemical Usage Comparison

Cost analysis is crucial for a battery recycling project to ensure economic viability, identify cost-saving opportunities, and support sustainable business practices. The cost of battery recycling includes both fixed costs, such as investments in plant infrastructure, equipment, and facilities, and operational costs, which encompass expenses for labor, energy, chemicals, and other day-to-day needs. In the proposed method, because the parameters for the mixing and heating systems (including time, temperature, and ambient pressure) are comparable to those of the conventional method, the fixed costs and certain operational costs, such as labor and energy, remain consistent. Nevertheless, significant cost savings are achieved through reduced chemical expenditures. The conventional method typically employs sulfuric acid at high concentrations (2-6 M) along with hydrogen peroxide (5-15% v/v). The S/L ratio changes with acid concentration, ranging from 20 g/L to 100 g/L. Higher S/L ratios necessitate higher acid concentrations and more H_2O_2. For comparison purposes between the proposed method and a conventional method, a middle range was chosen (SA concentration of 4 M, the H_2O_2 dosage at 5% v/v, and an S/L of 60 g/L) to compare with the proposed synergistic method (SA of 1.25 M, CA of 0.55 M, the S/L ratio of 62.5 g/L).

Table 4.8 provides the chemical usage comparison and cost analysis (Dorella and Mansur, 2007; Foxworth et al.; Golmohammadzadeh et al., 2017; Shin et al., 2005; Vanitha and Balasubramanian, 2013). The prices were sourced from the current market rates in Canada, as listed on the Bulk Mart and Lab Alley websites. If there is no fee associated with water and Black Mass (BM), and considering only the cost of chemicals, the significant reduction in sulfuric acid concentration during synergistic leaching would reduce the total cost by about 25% compared with the conventional method, which is considerable. Hence, synergistic leaching not only ensures a safer environment but also offers a cost-effective processing approach.

Table 4.8. Cost analysis and comparison of the synergistic and conventional leaching

Proposed Method				**Conventional Method**			
Input		**Price (per Kg)**	**Price (per ton of BM)**	**Input**		**Price (per Kg)**	**Price (per ton of BM)**
BM (Kg)	1000	0	0	BM (Kg)	1000	0	0
SA (Kg)	1961.6	$2.9	$5,669	SA (Kg)	6538.6	$2.9	$18,897
CA (Kg)	1849.2	$5.6	$10,377	H_2O_2 (Kg)	1208.3	$2.2	$2,704
		Total	$16,046			Total	$21,601

4.5. Conclusions

The present study aimed to investigate the recovery of critical metals (Li, Co, Ni, and Mn) from the cathode materials of spent LIBs (a mixture of different cathode types) through synergistic leaching and its stage-wise optimization. The study's primary findings are as follows:

- The optimum conditions for thermal treatment to remove binder material were 570 °C in 2 h under an air atmosphere. Thermal treatment in air, as opposed to argon, yielded similar results without affecting cathode crystallinity and proved superior because it is more cost-effective.

- The synergistic leaching of critical metals (Li, Co, Ni, and Mn) was effective in reducing the usage of sulfuric acid (SA) using organic acids (citric acid (CA)). It was concluded that CA performed better than acetic acid at lower concentrations. The optimal concentrations of sulfuric acid and citric acid were determined to be 1.25 M and 0.55 M, respectively.
- Utilizing citric acid eliminated the requirement for an additional reducing agent, as citric acid serves both as a lixiviant and a reductant. In contrast, acetic acid lacks this dual functionality.
- The optimized solid-to-liquid ratio, time duration, and temperature for the leaching stage were 62.5 g/L, 189 min, and 95 °C, respectively.
- Statistical models indicated that temperature has a greater impact on critical metal recovery than time.
- A cost analysis of the chemicals revealed that this method is about 25% more economical compared to conventional methods.

4.6. Acknowledgment

The authors express their gratitude to the Ontario Center of Innovation and ERS-International Company for financial support for this project (Application number: OCI 34919).

4.7. References

The references are merged with those of the other chapters and listed at the end of the thesis.

Chapter 5 SUSTAINABLE RECOVERY OF CRITICAL METALS FROM SPENT LITHIUM-ION BATTERIES USING CHITOSAN AS BIOSORBENT IN CITRATE-SULFATE MEDIA: A COMPREHENSIVE ISOTHERM, KINETIC, AND THERMODYNAMIC ANALYSIS

Published as a research article in Journal of Environmental Management, Vol. 375, Page 124400, February 2025, https://doi.org/10.1016/j.jenvman.2025.124400.

5.1. Abstract

This study showcases the ability of chitosan powder to selectively adsorb Co(II), Mn(II), and Ni(II) from spent lithium-ion batteries within a sulfate-citrate medium while effectively maintaining Li in solution. Characterization using BET, FT-IR, and TGA revealed that amine and hydroxyl groups are key contributors to adsorption. Considerably high adsorption rates for Co(II) and Ni(II), exceeding 80%, underscore chitosan's potential for robust metal-ion removal. Notably, chitosan exhibits negligible adsorption capacity for Li, thereby keeping it predominantly in solution and enabling selective separation and recovery. Optimum parameters were determined to be a dilution factor of 40, a pH of 4, and an adsorbent dosage of 10 g/L. While pH variations minimally affected Co(II) and Ni(II) recovery, Mn(II) removal efficiencies increased with pH. Using the Langmuir isotherm model, adsorption capacities for Co(II) and Ni(II) were estimated at 1.86 mmol/g (or 110 mg/g) and 0.37 mmol/g (or 20 mg/g), respectively. Mn followed the Freundlich isotherm model, and its adsorption uptake was 0.02 mmol/g (1.10 mg/g) at an equilibrium concentration of 0.47 mmol/L. Kinetic studies highlighted rapid Co(II) and Ni(II) adsorption within 5 minutes, confirming that surface reaction is the rate-limiting step, while thermodynamic analysis revealed favorable Co(II) and Ni(II) adsorption relative to unfavorable Mn(II) adsorption. Optimal desorption was achieved with 0.01 M sulfuric acid, achieving complete desorption for Co(II) and Ni(II) and over 82% for Mn(II). These findings underscore chitosan powder's potential as a sustainable and efficient green adsorbent for the selective recovery of metal ions in battery recycling, addressing crucial environmental and resource conservation concerns.

Keywords: Li-ion Batteries; Recycling; Critical Metal ions; Adsorption; Chitosan.

5.2. Introduction

In recent years, the proliferation of electronic devices has led to a surge in demand for Li-ion batteries (LIBs), driving concerns about their environmental impacts and the sustainability of their materials (Pei et al., 2024). The demand for LIBs in electric vehicles is surging due to their capacity to curb greenhouse gas emissions and contribute to the decarbonization objectives outlined in the Paris Agreement (Yu et al., 2023). LIBs contain critical metals such as lithium (Li), cobalt (Co), nickel (Ni), copper (Cu), aluminum (Al), and manganese (Mn), all categorized as critical metals. The attainment of a net-zero future for North America hinges on ensuring the accessibility of these metals, given their pivotal role in various burgeoning clean energy technologies (Jonathan Wilkinson and François-Philippe Champagne, 2022). Battery applications accounted for 65% of the global lithium supply in 2019, marking a 30% increase from 2015, driven by the popularity of portable electronics and the growing demand for EVs and renewable energy technologies (Zeng et al., 2022). However, market analysis suggests an impending lithium supply deficit, with estimates indicating 1.1 million tons by 2030. Similarly, the supply of Co and Ni is also facing challenges, with projections suggesting potential shortages as early as 2027 for Ni and between 2030 and 2050 for Co due to the increasing demand from the EV market (Qu et al., 2023; Zeng et al., 2022).

With rising demand for energy storage, battery recycling is key to a circular economy. Spent LIBs contain high concentrations of critical metals, often surpassing natural ores, and recycling reduces emissions, provides a domestic supply, addresses raw material shortages, and mitigates environmental risks from hazardous substances (Ding et al., 2024; Qu et al., 2023; Zanoletti et al., 2024).

Recovering valuable metals from spent battery cathodes (lithium cobalt oxide (LCO), lithium nickel cobalt manganese oxide (NMC), lithium manganese oxide (LMO), and lithium iron phosphate (LFP)) offers significant value, cost efficiency, and environmental benefits. Among these metals, Li stands out for its versatility and widespread applications. The global lithium battery market was projected to reach approximately $100 billion by 2025, with an expected annual growth rate of 14.3% between 2018 and 2025. Alternative recovery methods are essential to meet this growing demand (Das et al., 2022; Natarajan et al., 2019). Despite global reserves of about 4 million tonnes, traditional mining is costly and resource-intensive, making the extraction of Li

from discarded electronics and batteries essential for efficient resource use and environmental protection (Das et al., 2022).

There are various approaches to recycling LIBs, including hydrometallurgy, pyrometallurgy, and direct recycling (Ding et al., 2024; Yang et al., 2024). Among these, hydrometallurgy has been reported to be the most promising option in terms of environmental impact, cost-effectiveness, and scalability. A typical hydrometallurgical process involves leaching, separation, and purification stages (Gaines, 2018; Kader et al., 2021; S. Li et al., 2024). Prior to leaching, several pre-treatment processes, such as sorting, dismantling, shredding, and physical separation, are required to enhance process efficiency. With appropriate pre-treatment processes, copper (Cu) and aluminum (Al) collectors can be separated early in the process (Gaines, 2018). However, conventional methods are insufficient for large-scale LIB recycling and require modification and further development for practical implementation (Solberg et al., 2024). Additionally, solvents used in the separation stage, usually via solvent extraction (SX), must be disposed of after several extraction cycles, resulting in secondary pollution. Ion exchange resins (IX) have also been used for metal ion separation, including in processes for recovering valuable materials from spent LIBs (Siyu et al., 2024; Wesselborg et al., 2025). These resins function by exchanging specific ions in their structure with those present in the solution. However, ion exchange resins have some disadvantages, including high operating costs and resin fouling. Additionally, the process generates secondary waste after multiple cycles, raising environmental concerns (Ma et al., 2023; Ritcey, 1986).

Alternatively, adsorption processes using waste materials offer a cost-effective, efficient method for recovering metal ions from aqueous solutions, serving as a viable alternative to SX and IX. In addition to affordability and operational simplicity, adsorption offers the advantage of potential regeneration, further enhancing its appeal as a recycling method (Das et al., 2022; Metwally et al., 2013). Utilizing waste as an adsorbent fosters a circular economy and the concept of waste-to-treat-waste. This approach helps eliminate secondary waste by preventing additional waste from entering the environment. For example, activated carbon produced from different waste sources (Mariana et al., 2021; Yang et al., 2019), chitin (Yazidi et al., 2020) and chitosan (Das et al., 2022) derived from fishery waste, natural hemp fibers (Tofan et al., 2013), and carbonaceous materials from LIBs' anode materials (Anh Nguyen and Oh, 2021) have been applied to adsorb different metal ions from water and wastewater.

Implementing adsorption with waste materials in the acidic, metal-rich environment of battery recycling offers a promising method for recovering critical metals from spent LIBs. In this regard, activated carbon derived from coconut shells has been employed to extract Co(II), Ni(II), and Mn(II) from leachate, consisting of a sulfuric acid and hydrogen peroxide solution at a pH of 5.2, from spent lithium-ion batteries (LIBs), while Li remains in the solution (Purnomo et al., 2018). The findings indicated successful separation of Co(II) and Ni(II), while a minor quantity of Mn persisted in the solution and precipitated with Li (as lithium carbonate (Li_2CO_3)). Conte and Gómez (2024) employed activated mesoporous carbons produced from sucrose to remove Co(II), Ni(II), and Mn(II) from the leachate of spent LIBs. They found that activated mesoporous carbons were capable of removing more than 80% of Co(II), Ni(II), and Mn(II), achieving adsorption capacities exceeding 20 mg/g at a pH of around 5. However, the removal of Li was comparatively lower, with only 20% being removed. Robeck and Horn (Robeck and Horn, 2024b) utilized a silica adsorbent functionalized with amino-polycarboxylate derivative ligands, referred to as HSU331, to selectively extract Ni(II) from Co(II) in spent LIBs' solution. Their findings revealed that at higher temperatures (50°C), Ni(II) was selectively separated from Co(II). Li et al. (2025) investigate Li recovery from spent LIBs using Mn- and Al-based adsorbents in HCl media, reporting an adsorption capacity of 4–5 mg/g (=0.58-0.72 mmol/g). However, their study did not examine metal ion competition (Co(II), Mn(II), and Ni(II)) in real solutions. Moreover, their adsorbents were synthesized rather than sourced from waste materials, incurring additional costs. In another study, the separation of Co(II) and Li was studied using a hybrid NaA-based MOFs composite (Na-based type A molecular sieve (NaA)), specifically NaA-MOFs(Al). The reported adsorption capacity was 512.00 mg/g (8.69 mmol/g). The investigation was conducted in HCl media using a synthetic solution containing Co(II) and Li rather than real media with competing metal ions such as Ni(II) and Mn(II). Additionally, their adsorbents were synthetic, not derived from waste materials (Chen et al., 2025).

Among diverse waste materials, chitosan, a biopolymer derived from shellfish waste, is widely recognized for its strong metal ion adsorption capabilities due to its amino ($-NH_2$) and hydroxyl (-OH) groups, which enhance adsorption and extend its usability (Syeda et al., 2024). Its cost-effectiveness, ease of functionalization, stability, and biodegradability make it ideal for environmental remediation applications. Metal ions primarily bind to chitosan through coordination with amino groups, typically in a 1:1 ratio for divalent ions, while its decomposition

in biological environments prevents secondary pollution (Das et al., 2022; Hamza et al., 2022; Liu et al., 2022; Saheed et al., 2021). Hamza et al. (2022) used sulfonated chitosan to selectively extract Li from a spent Li-ion mobile battery (leached in 7 M of hydrochloric acid (HCl)) and reported a maximum adsorption capacity of 20 mmol/g at a pH of 2.2, and separation factors for Li against Co(II), Mn(II), Ni(II) ranging 26-85. Imprinted blended chitosan microfibers, at a pH of 6.1, were also able to selectively extract Li from leachates of spent coin cell cathodes (leached by 2 M HCl) with an adsorption uptake potential of 100 mg/g (=14.41 mmol/g) (Das et al., 2022). However, previous studies involved complex procedures for fabricating adsorbents (e.g., chitosan-based adsorbents), examined harsh conditions using a high concentration of HCl as the leaching medium for spent LIBs, and primarily focused on extracting Li rather than other metal ions.

To the best of the authors' knowledge, prior research has yet to explore the application of chitosan for the recovery of critical metal ions from diverse types of spent LIBs (LCO, NMC, and LMO) in a citrate-sulfate medium. Authors previously demonstrated the application of the sulfate-citrate leaching process as a viable and green method to extract critical metal ions from a mixture of spent LIBs (Roshanfar et al., 2024). This study presents findings that lay the groundwork for a broader research project on the use of chitosan as an effective adsorbent for selective metal-ion removal from sulfate-citrate media, with the aim of developing an eco-friendly technology for LIB recycling.

The study investigates the efficacy of chitosan in adsorbing divalent metal ions (Co(II), Mn(II), and Ni(II)) from a sulfate-citrate leachate solution with very high metal ion concentrations while maintaining Li in solution under acidic conditions, thus developing a selective method for the recovery and separation of Li. The study demonstrates proof of concept, and its experimental design encompasses parameters such as initial metal ion concentrations, pH levels, and adsorbent dosages, with optimization conducted for each. Additionally, the kinetics and thermodynamics of the adsorption process were thoroughly examined. Thermogravimetric Analysis (TGA), Fourier Transform Infrared Spectroscopy (FT-IR), and the Brunauer-Emmett-Teller (BET) method were used to characterize the bio-adsorbent. Through this comprehensive investigation, valuable insights into the potential of chitosan as a sustainable and effective biosorbent for the recovery of metal ions in battery recycling are provided.

5.3. Materials and Methods

5.3.1. Materials

This study utilized spent lithium-ion batteries (LIBs) sourced from various devices like laptops, cellphones, and Li-polymer batteries from different brands such as LG, Samsung, TechTrex Inc., Motorola, etc., obtained from a recycling facility in Toronto, Canada. Sulfuric acid (H_2SO_4) and citric monohydrate ($C_6H_8O_7.H_2O$) with purities of 98% and 99%, respectively, from Fisher Chemical, USA, were employed in the leaching stage. Chitosan with a deacetylation degree (DD) of 85%, sodium chloride (NaCl), and sodium hydroxide (NaOH) were acquired from Fisher Scientific Co., Canada. All solutions were made using deionized water (DI). Unless specified otherwise, all materials used were of analytical grade.

5.3.2. Sample Preparation

The sample preparation followed the detailed method described in our previous study (Roshanfar et al., 2024). Briefly, batteries were discharged in 10% sodium chloride solution for 24 h in anti-corrosion plastic buckets, following protocols from (Li et al., 2022b; Mishra et al., 2022; Shaw-Stewart et al., 2019). After 24 hours, samples were rested, and battery discharge was verified with a multimeter. Batteries were then disassembled manually, and the cathode materials were separated. Following the previous study by the authors, a predetermined quantity of the mixture of cathode materials (referred to as black mass (BM)), comprising a 1:1:1 weight ratio from laptops, cellphones, and Li-polymer batteries, underwent heating in a muffle furnace under an air atmosphere at 570°C to eliminate binder materials. Subsequently, the BM was leached with a synergistic solution of sulfuric acid (1.25 M) and citric acid (0.55 M) at 90 °C in the absence of a reducing agent. The solid-to-liquid (S/L) ratio was set at 62.5 g/L, with a duration of 2 h (called pregnant solution) (Roshanfar et al., 2024).

5.3.3. Characterization

The metal ion concentrations within the cathode materials were assessed using inductively coupled plasma (ICP) with an Agilent 5110 ICP-ES, following sample digestion in aqua regia (HNO_3: HCl= 1:3) overnight at 120°C. Metal ion concentrations for adsorption tests were measured using Atomic Absorption Spectroscopy (AAS; PinAAcle 500, PerkinElmer). The instrument was

calibrated using a nonlinear method with zero intercept. Each sample underwent five readings, and the average of those readings was used in subsequent calculations. The pH of the solution was monitored using the HACH Instrument pH Meter (HQ40D). Fourier Transform Infrared Spectroscopy (FT-IR, IS50 FT-IR, ThermoScientific) was employed in the 500–4000 cm^{-1} range to analyze the functional groups present on chitosan before and after adsorption processes. Thermal Gravimetric Analysis (TGA, SDT650, TA Instruments) was conducted over the temperature range from room temperature to 800 °C at a heating rate of 10° C/min. This analysis aimed to assess the thermal behavior of chitosan over the specified temperature range. The specific surface area was measured using the Brunauer–Emmett–Teller (BET) N_2 isotherms collected on a Micromeritics 3Flex adsorption analyzer, supplied by Micromeritics Instruments Inc, at 77 K (liquid N_2 bath). Prior to measurements, samples were activated using a Micromeritics Smart VacPrep under high vacuum at 50 °C for 7 hours, then at 100 °C for 10 hours (Sing, 1985).

5.3.4. Batch adsorption isotherm studies

Batch adsorption isotherm experiments were conducted in 125 mL Erlenmeyer flasks containing 50 mL of leachate following the procedures in the leaching stage of BM outlined in section 2.2 to investigate the impact of various factors (initial metal ions concentration, pH, and adsorbent dosages) on the adsorption of Li, Co(II), Mn(II), and Ni(II) on chitosan. A predetermined quantity of chitosan was introduced into the solution, which was then agitated at 150 rpm for 24 h at room temperature, unless otherwise specified. Initial concentrations were examined using varying dilution factors (100, 60, 50, 40, 20 times). The influence of initial pH on metal ions adsorption was studied across unadjusted pH conditions and a pH range of 4-8 (monitored by HACH (HQ40D)). pH adjustments were made using sodium hydroxide (10 wt.%) and sulfuric acid solution (1% v/v). The effect of adsorbent dosage was also investigated by varying the adsorbent quantity from 0.1 to 5 g in 50 mL (2-100 g/L). After a filtration step, the equilibrium concentrations of Li, Co(II), Mn(II), and Ni(II) in the solution were analyzed using Atomic Absorption Spectroscopy (PinAAcle 500, Perkin Elmer), and the adsorbed amount per unit mass of adsorbent, qe (mmol/g), was calculated accordingly (Metwally et al., 2017).

$$q_e = \frac{(C_0 - C_e) \times V}{W} \tag{5-1}$$

where C_0 (mmol/L) stands for the initial concentration, and C_e (mmol/L) represents the equilibrium concentration of adsorbate in the solution. V (L) denotes the volume of the solution, and W (g) indicates the dry weight of the adsorbent. Each experiment was conducted in duplicate, and the mean (±Standard Deviation (SD)) was recorded. To ensure quality control, blank samples consisting of chitosan powder and DI water, along with a control test containing only the leached cathode material without any adsorbent, were employed. No metal ion uptake or release was observed in either case. The adsorption efficiency (%±SD) was also determined using the following formula:

$$Adsorption\ efficiency\ (\%) = 100 - \left(\frac{Equilibrium\ concentration\ of\ metals}{Initial\ concentration\ of\ metals}\right) \times\ 100 \qquad (5\text{-}2)$$

5.3.5. Adsorption isotherm modeling

Various isotherm models, including Langmuir, Freundlich, Temkin, and Toth (as outlined in Table 1), were employed to characterize the adsorption isotherm data (Al-Ghouti and Da'ana, 2020; Babakhani and Sartaj, 2023, 2022a; Piccin et al., 2017). The coefficient of determination (R^2) was subsequently calculated to determine the most suitable isotherm model. Also, the Sum of Squares of Residuals (SSR) and Mean Squared Error (MSE) were employed to identify the optimal isotherm. SSR and MSE provide standardized measures of prediction accuracy in regression analysis by quantifying how well a model fits the data; lower values indicate a better fit. MSE, in particular, allows for easy comparison across models and datasets by normalizing the error (Anderson and Whitcomb, 2017).

Table 5.1. The studied isotherm model equation and parameters

Isotherm	Equation	Parameters	
Two-Parameter models			
Langmuir	$q_e = \frac{q_m k_L C_e}{1+k_L C_e}$	q_m	Maximum adsorption capacity (mmol/g)
		k_L	Langmuir constant ((L/mmol)

		C_e	Equilibrium concentration of adsorbate (mmol/L)
Freundlich	$q_e = k_F C_e^{\frac{1}{n_F}}$	k_F	Freundlich constant (mmol/g).(L/mmol)$^{1/n}$)
		n_F	Freundlich constant related to the adsorption intensity
		C_e	Equilibrium concentration of adsorbate (mmol/L)
Temkin	$q_e = \frac{q_m RT}{\Delta Q} Ln(K_T C_e)$	q_m	Maximum adsorption capacity (mmol/g)
		R	Universal gas constant (8.314 J/mol K)
		T	Temperature (K)
		ΔQ	Variation of adsorption energy (J/mol)
Three-Parameter models			
Toth	$q_e = \frac{K_T C_e}{(\alpha_T + C_e)^{\frac{1}{t}}}$	K_T	Toth constant (L/mmol)
		t	System heterogeneity; (t≠ 1, denotes heterogeneity)

5.3.6. Thermodynamics study

To examine the effect of temperature and calculate the thermodynamic parameters, a series of flasks were prepared, each containing 50 mL of leachate solution with a dilution factor of 40 at an initial pH of 4. An amount of 0.5 g of dry chitosan (equivalent to 10 g/L) was added to each flask. These flasks were then placed in an incubator shaker operating at 150 rpm for 24 h. The experiments were conducted at different temperatures, including 4 °C and room temperature (22 °C).

5.3.7. Kinetics study and the effect of contact time

The impact of contact time on the adsorption of Li, Co(II), Mn(II), and Ni(II) onto chitosan was examined by placing 10 g/L of the adsorbent in a series of flasks, each containing 50 mL of solution with a dilution factor of 40 and an initial pH of 4. The mixture was then agitated at 150 rpm and at room temperature for varying durations: 5, 10, 15, 20, 30, 45, 60, 180, 360, 480, 960, 1440, 1800, and 2880 minutes. Subsequently, the samples were filtered through a 0.45 µm membrane

filter (EZFlow Membrane), and the adsorption capacities and efficiencies were determined using the provided equations (Eqs. (5-1) and (5-2)). The adsorption kinetics of the metal ions were studied using pseudo-first-order and pseudo-second-order kinetic models.

5.3.8. Desorption study

Following the adsorption of metal ions (Co(II), Mn(II), and Ni(II)) onto chitosan from a solution with a dilution factor of 40 and an initial pH of 4, the chitosan was separated by filtration. Subsequently, it was rinsed with de-ionized water and air-dried. The dried chitosan was then subjected to desorption in 50 mL of various solutions, including DI water, hydrochloric acid (HCl, 0.1 M), sodium chloride (NaCl, 1 M), and sulfuric acid (H_2SO_4, 0.01-0.1 M) for 72 h. AAS was utilized to quantify the amount of desorbed metal ions. Each experiment was replicated twice, and the average value was calculated. The percentage of desorption was determined using the following equation:

$$Desorption\ (\%) = \frac{Amount\ of\ metal\ ions\ desorbed\ (\frac{mmol}{L})}{Amount\ of\ metal\ ions\ adsorbe\ (\frac{mmol}{L})} \times 100 \qquad (5\text{-}7)$$

Figure 5.1 shows the schematic steps of this study.

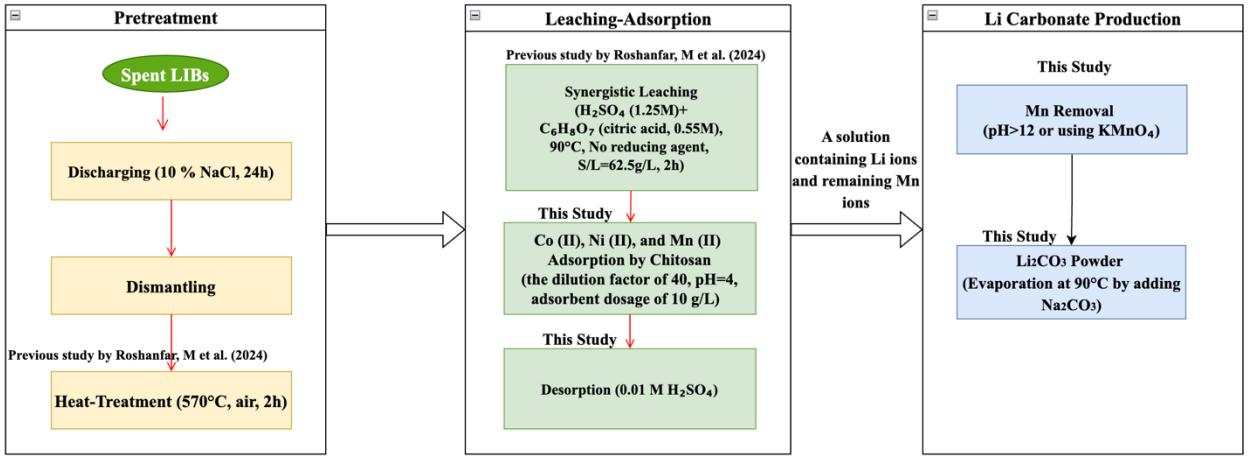

Figure 5.1. The schematic flowchart of this study.

5.4. Results and Discussion

5.4.1. Characterization of chitosan

The corresponding FT-IR and TGA results, which provide insights into the functional groups and bonds as well as thermal stability, are discussed in the following subsections. Additionally, the BET surface area measured as sufficient porosity and surface area is essential for achieving effective adsorption capacity (Metwally et al., 2013). For chitosan powder, the BET surface area (average ± Standard Deviation (SD)) was 7.45±0.28 m^2/g, and the total pore volume was (average ± SD) $7.18\times10^{-3}\pm3.5\times10^{-4}$ cm^3/g. These findings suggest that chitosan has a good BET surface area and total pore volume compared to graphene aerogels derived from spent graphite anodes, which have a reported surface area of 4.59 m^2/g (Zheng et al., 2023). Additionally, biochar produced at 300 °C shows a surface area of 2.04 m^2/g and a pore volume of 5.7×10^{-3} cm^3/g (Elnour et al., 2019).

5.4.1.1. FT-IR analysis

In this study, FT-IR analysis was conducted on chitosan (85% DD) both pre- and post-adsorption, and the findings are depicted in Figure 5.2. The characteristic peaks identified in existing literature are reported in Table 2 (Babakhani and Sartaj, 2022a; Jóźwiak et al., 2017; Mao et al., 2015; Rodrigues et al., 2012; Sharifi et al., 2023). As seen in Figure 5.2, there is a notable decrease in the vibration peaks corresponding to N-H and O-H stretching, as well as C-H symmetric and asymmetric stretching, after adsorption. This reduction may be attributed to the involvement of these bonds in the adsorption process of metal ions (Co(II), Ni(II), and Mn(II)) (Liu et al., 2022; Saheed et al., 2021). The primary reactive sites for metal ion adsorption on the chitosan polymeric chain are reported to be the amine sites, although hydroxyl groups may also play a role. These functional groups interact with metal ions through mechanisms that depend on factors such as the specific metal ions, pH, and the solution matrix. For instance, at pH levels near neutrality, the lone pair on nitrogen can coordinate with metal cations (Guo et al., 2004; Saheed et al., 2021). Additionally, a shift in the vibration peak of the primary amine's N-H group is observed, possibly indicating that N-H bonds contribute to certain reactions in the medium (Hamza et al., 2022). According to the literature, amine groups play a key role in the adsorption of Ni and Co by coordinating with the metal ions through chelation. Similarly, hydroxyl groups contribute to Mn

adsorption by forming hydrogen bonds and engaging in electrostatic interactions with metal ions (Yang et al., 2023, 2018).

Table 5.2. Distinctive spectral bands of chitosan in FT-IR (Babakhani and Sartaj, 2022a)

Wavenumber (cm^{-1})	Functional Groups
3273, 2921, and 2887	N-H and O-H stretching vibration C-H symmetric and asymmetric stretching
1650	C=O of amide group
1590	Bending vibration of N-H of the primary amine
1430	Bending vibration of O-H deformation
1370	Bending vibration of C-H group
1153	C-O-C asymmetric stretching
1066 and 1028	C-O stretching

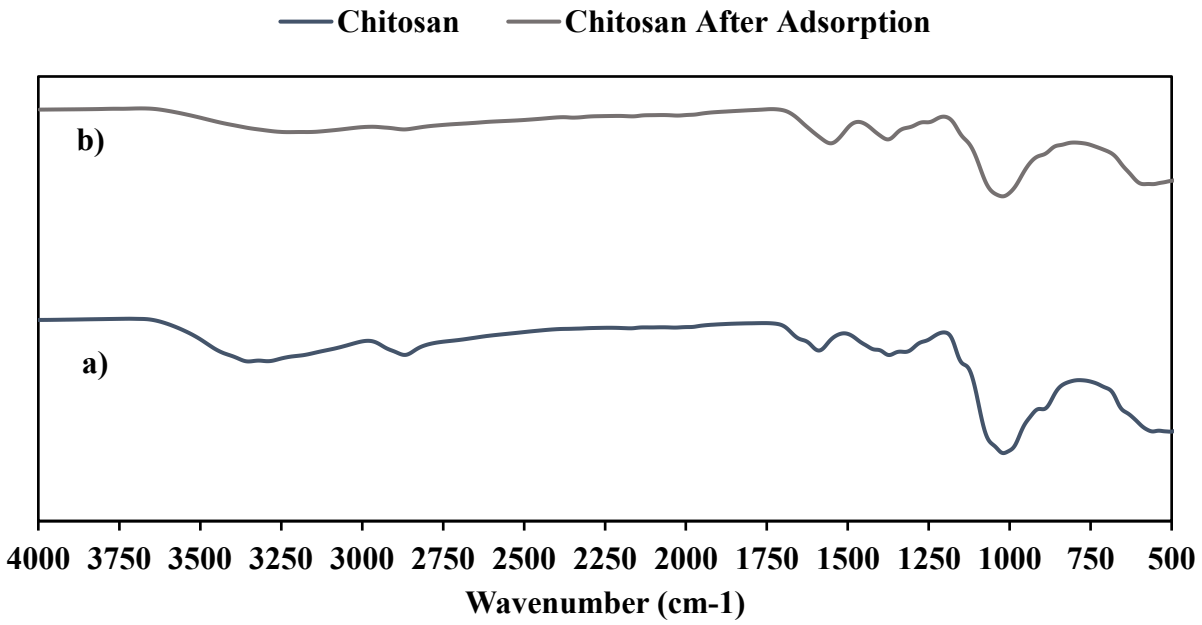

Figure 5.2. FT-IR spectra for chitosan: a) before adsorption and b) after adsorption.

5.4.1.2. TGA analysis

The thermal properties of chitosan were assessed using TGA. The results, depicted in Figure 5.3, revealed a two-step degradation process for chitosan. The initial stage, occurring within the temperature range of 30–125 ℃, exhibited a weight loss of approximately 8-9%, attributed to water (moisture) loss. Subsequently, a second mass loss phase commenced at 250 ℃, constituting around 60% of the total weight loss, which was ascribed to the breakdown of chitosan's glycosidic bonds (Babakhani and Sartaj, 2022a; Sutirman et al., 2016). The result indicated that chitosan remains stable at temperatures up to 125°C.

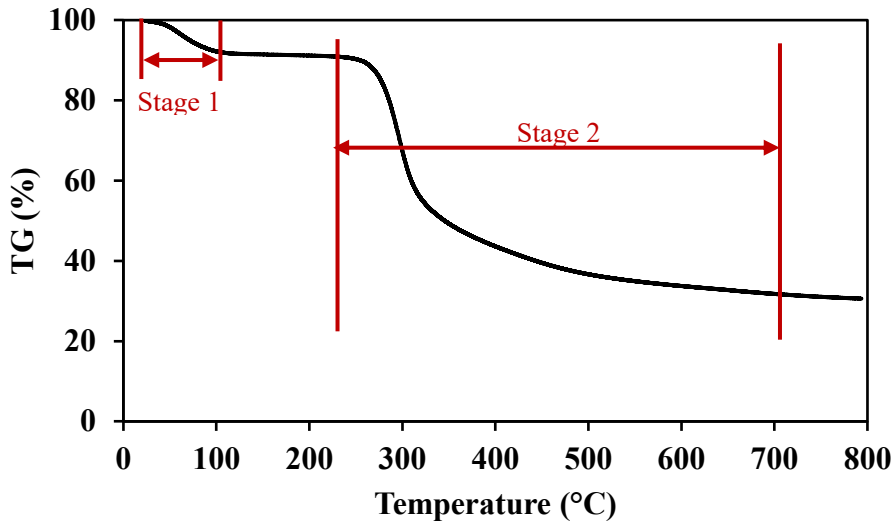

Figure 5.3. Thermal behavior analysis of chitosan powder using TGA.

5.4.2. Batch Adsorption Isotherm Study

Batch experiments were carried out for the adsorption study, using an actual leachate sample (referred to as the pregnant solution) derived from leaching black mass (1.25 M SA and 0.55 M citric acid; solid-to-liquid ratio of 62.5 g/L; temperature of 90 °C; 2 h). The metal ion concentrations in the Black Mass, a mixture of cathode materials (LCO, NMC, and LMO), were 50.06%, 6.28%, 2.36%, and 3.37% for Co, Li, Mn, and Ni. Based on a prior study, recovery rates of approximately (average ± SD) 98 ± 0.1% for Co, 98± 0.7 % for Li, 91±0.4 % for Mn, and 89±6.6% for Ni were attained, and the metal ions concentrations after leaching in the pregnant solution were 509.34±8.49 mmol/L, 576.37±17.72 mmol/L, 24.32±0.40 mmol/L, 36.74±6.61 mmol/L (30000±500 mg/L, 4000±123 mg/L, 1336±22 mg/L, and 2156 ± 388 mg/L) for Co, Li, Mn, and Ni, respectively (Roshanfar et al., 2024). It is worth mentioning that the media consisted of a combination of sulfuric and citric acids (synergistic leaching), distinguishing the process from other previous studies (Conte and Gómez, 2024; Das et al., 2022; Hamza et al., 2022; Purnomo et al., 2018; Robeck and Horn, 2024). The present study's findings reveal a notable trend: chitosan selectively adsorbs Co(II), Mn(II), and Ni(II) across all experiments, while leaving Li predominantly in the liquid phase. Specifically, Li adsorption remained consistently below 1% across all experiments. This suggests the potential for selective separation of Li from the other

heavy metals in solution. This observation might be attributed to the charge characteristics of the metal ions and the propensity of chitosan's functional groups to interact preferentially with metal ions carrying a charge of two, rather than one, such as Li.

5.4.2.1. Effect of dilution factor

The initial concentration of metal ions is a critical factor in the adsorption process, significantly influencing the adsorption uptake. Understanding how metal ion concentration influences adsorption uptake is essential for advancing the applications of adsorbents. Consequently, the initial concentration was varied by altering the dilution factor (×100, ×60, ×50, ×40, and ×20), and the adsorption uptake of metal ions (Li, Co(II), Mn(II), and Ni(II)) onto chitosan was monitored. Optimizing water usage is crucial for sustainability and efficiency in the adsorption process. Given global concerns about water scarcity, responsible water management in battery recycling is paramount. Hence, ensuring the utilization of an optimized dilution factor is of utmost importance in this study. The adsorption experiments were carried out at room temperature for 24 h, with an adsorbent dosage of 10 g/L and an initial pH of 5. To ensure reliability, each test was duplicated, and the mean and standard deviation were calculated and reported. It should be noted that the weight of the chitosan powder was tracked after adsorption, and no decrease in mass was observed. Table 5.3 illustrates the efficiency of metal ions adsorption and the adsorption uptake of Co(II), Mn(II), and Ni(II) on chitosan across different dilution factors (initial metal ions concentrations). It is noteworthy that the Li adsorption efficiency in the experiments was less than 1%. Increasing the dilution factor from 20 to 100 generally enhanced metal ion recovery and decreased metal ion adsorption uptake. Generally, higher initial concentrations (lower dilution factors) lead to decreased adsorption efficiency but increased equilibrium adsorption uptake, indicating heightened occupation of significant binding sites due to greater equilibrium concentrations of metal ions. Adsorption uptake increases notably with rising initial concentration until reaching a maximum, signifying saturation at specific sites on chitosan and the attainment of equilibrium. This underscores the importance of initial concentration in overcoming mass-transfer resistance between the solution and solid phases, thereby enhancing adsorbent uptake (Liu et al., 2022). In this study, there is a slight increase in enhancement after a dilution factor of 40. Therefore, to reduce excessive water consumption, a dilution factor of 40 was selected as the optimal level,

resulting in average concentrations ± SD of 12.98 ±0.83 mmol/L (=765 ±48.79 mg/L) of Co(II), 14.41 ±0.38 mmol/L (=100 ±2.61 mg/L) of Li, 0.67 ±0.05 mmol/L (=36.81 ±2.61 mg/L) of Mn(II), and 0.9 ±0.03 mmol/L (=53 ±1.71 mg/L) of Ni(II). Another interesting finding is the notably high adsorption efficiency observed for Co(II) and Ni(II), surpassing 85% and 83%, respectively, at a dilution factor of 40. Conversely, the adsorption efficiency of Mn(II) was moderate, at 38%. This trend may be attributed to the inherent tendency of chitosan functional groups, such as amine and hydroxyl groups, to exhibit a stronger affinity for Co(II) and Ni(II) than for Mn(II) (Bakshi et al., 2020).

Table 5.3. Metal ions adsorption efficiency (%±SD) and the adsorption uptake (mmol/g ±SD) in different dilution factors (different initial concentrations) at room temperature for 24 h, with an adsorbent dosage of 10 g/L and an initial pH of 5

Dilution factor/	Adsorption efficiency(%) (Adsorption Uptake (mmol/g))	Co	Mn	Ni
×100		89.12±0.60	36.62±2.79	83.96±1.08
		(0.45±0.00)	(0.01±0.00)	(0.03±0.00)
×60		86.15±0.67	36.31±01.22	83.18±1.93
		(0.73±0.01)	(0.02±0.01)	(0.05±0.00)
×50		86.76±0.00	40.74±0.00	85.48±0.28
		(0.87±0.00)	(0.02±0.00)	(0.06±0.00)
×40		85.76±0.04	38.69±0.10	83.64±1.93
		(1.07±0.00)	(0.02±0.00)	(0.08±0.00)
×20		71.88±0.59	34.51±0.31	34.51±3.47
		(1.80±0.01)	(0.04±0.00)	(0.14±0.01)

5.4.2.2. Effect of pH

One of the critical factors affecting metal ion adsorption at solid-water interfaces is the pH of the aqueous solution. Varied pH levels influence both the availability of metal ions in solution and the metal-ion binding sites on the adsorbent surface. Previous literature indicates that Co(II), Mn (II), and Ni(II) tend to precipitate as hydroxides at pH values above 8 (Conte and Gómez, 2024).

Consequently, pH ranges up to 8 were chosen for this investigation. Using the optimal dilution factor of x40 determined in the prior study, experiments were conducted at room temperature for 24 h with an adsorbent dosage of 10 g/L. Adsorption experiments were performed at the initial pHs of unadjusted (2.38), 4, 5, and 8. Figure 5.4 illustrates the adsorption uptake of Co(II), Mn(II), and Ni II) at various initial pH levels. Increasing the pH from 2.38 to 4 enhances the adsorption uptake from 0.49 to 1.02 mmol/g for Co(II), 0 to 0.02 mmol/g for Mn(II), and 0.06 to 0.08 mmol/g for Ni(II). However, for Co(II) and Ni(II), further increases in pH do not significantly enhance adsorption uptake. Conversely, elevating the pH increases the adsorption uptake of Mn(II) up to 0.03 mmol/g and about 47%, respectively. Nevertheless, in the current media (a combination of sulfuric acid and citric acid), metal ion precipitation also commences beyond pH 8. Therefore, to ensure recovery occurs solely through adsorption and to prevent precipitation, higher pH levels are not advisable.

It is worth noting that when chitosan is introduced into the solution, the pH increases considerably, approaching neutral levels. This alleviates concerns about the protonation of chitosan's amino groups, which could otherwise hinder the interaction between metal ions and binding sites. Hence, the unbound lone pair of electrons on the nitrogen atoms of chitosan's amino groups serve as active adsorption sites, exhibiting a strong affinity for the adsorption of metal ions (Babakhani and Sartaj, 2022a). In other words, at a moderate pH, the H^+ concentration is reduced, thereby enhancing the likelihood of metal ion capture at the adsorption site. Conversely, at lower pH levels, a majority of the adsorption sites are occupied by H^+ ions, rendering it more challenging for metal ions to adsorb. Additionally, high competition among ions restricts the adsorption of particular ions (Liu et al., 2022). The increase in pH observed upon the addition of chitosan alleviates concerns related to its point of zero charge (pH_{PZC}), which generally falls within the range of pH 4 to 5. The pH_{PZC} indicates when the surface charge of an adsorbent becomes neutral. For optimal adsorption, the pH should ideally exceed 5 (Babakhani and Sartaj, 2023). For initial pH values of 2.38, 4, 5, and 8, the final pH measurements were 6.38, 7.16, 7.43, and 8.03, respectively. Correspondingly, recovery efficiencies improved from 40% ±5 to 88% ±0.2 for Co(II), from 0% to 47% ±2.6 for Mn(II), and from 60% ±3.7 to 84%±2.8 for Ni(II) (as shown in Table 4). Considering the lack of significant increases in adsorption uptake beyond an initial pH of 4 (with the final pH of 7.16) and the importance of maintaining the final pH below 7.5 during adsorption, pH 4 was selected as the optimal initial pH.

Additionally, it lowers the cost of using chemicals to raise pH. At this stage, the weights of the chitosan powder were also monitored after the experiments, and no decrease in mass was observed. Regarding the selection of dilution factors and pH, it should also be noted that, by combining the pH results with the effects of dilution factors, the investigated dilution factor was kept at a minimum of 20 to avoid excessive chemical consumption for pH adjustment. As the results indicated, the pH needed to be adjusted because the adsorbent was ineffective at capturing metal ions at the leachate's natural pH (2.18). This was confirmed by experiments conducted with a dilution factor of 20 and without pH adjustment, in which no adsorption occurred (0% for Co(II), 2.04% and 1.69% for Mn(II), and 0.18% and 2.80% for Ni(II)).

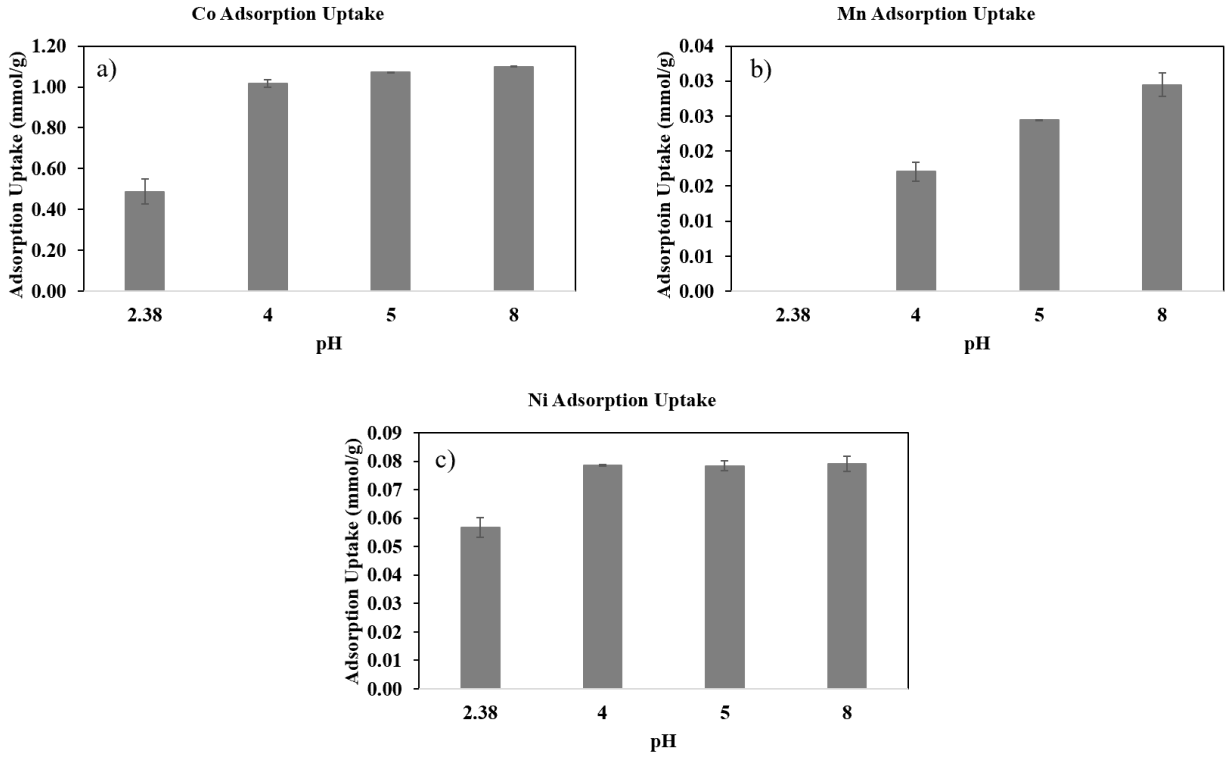

Figure 5.4. Effect of pH on the adsorption capacity (mmol/g ±SD) of a) Co (II), b) Mn (II), and c) Ni (II) under room temperature in 24 h, an adsorbent dosage of 0.5 g per 50 mL, and a dilution factor of 40.

Table 5.4. Effect of pH on adsorption efficiencies (%±SD) of metal ions

Initial pH	Final pH	Recovery efficiency (%)		
		Co (II)	Mn (II)	Ni (II)
2.38	6.38	39.79±4.99	-	59.79±3.75
4	7.16	81.29±1.48	27.02±2.14	83.86±0.32
5	7.40	85.76±0.04	38.69±0.10	83.64±1.93
8	8.03	88.04±0.16	46.69±2.65	84.41±2.76

5.4.2.3. Effect of adsorbent dosage

The amount of adsorbent present in the solution can influence the degree of metal ion uptake. The impact of different chitosan dosages (ranging from 0.1 to 5 g in 50 mL or from 2 to 100 g/L) on adsorption uptake was examined. Figure 5.5 (a-c) displays the equilibrium adsorption uptake and adsorption efficiency of Co(II), Mn(II), and Ni(II). It is evident that increasing the adsorbent dosage enhances the adsorption efficiencies of the metal ions. This phenomenon occurs because a greater amount of adsorbent provides the medium with more available sites for metal ion adsorption. Conversely, the adsorption uptake decreases with increasing adsorbent dose. This reduction in adsorption capacity can be attributed to some adsorption sites remaining unsaturated due to the increased mass of the adsorbent (Babakhani and Sartaj, 2022a; Bakshi et al., 2020; Tofan et al., 2013; Yazidi et al., 2020). Increasing the adsorbent dosage generally reduces the equilibrium concentration of metal ions in solution because more adsorbent provides additional adsorption sites. However, while higher adsorbent dosage can lead to a lower equilibrium concentration, it does not necessarily increase adsorption uptake if adsorption sites become saturated or adsorption efficiency is not sufficiently high. Thus, although higher adsorbent dosage can reduce equilibrium concentration, the adsorption uptake might not increase proportionally beyond a certain dosage. Hence, the dosage of 0.5 g per 50 mL, equivalent to 10 g/L, where both the metal ions' efficiency and adsorption capacity peaked simultaneously, was chosen as the optimal dosage. It is important to note that the mass of the chitosan powder after adsorption was monitored to determine whether

there was any mass loss; although no reduction was observed, a slight increase was observed in all experiments. For instance, under optimal conditions of pH 4, a dilution factor of 40, and a dosage of 10 g/L (0.5 g in 50 mL), the final weight increased slightly to 0.60±0.03 g.

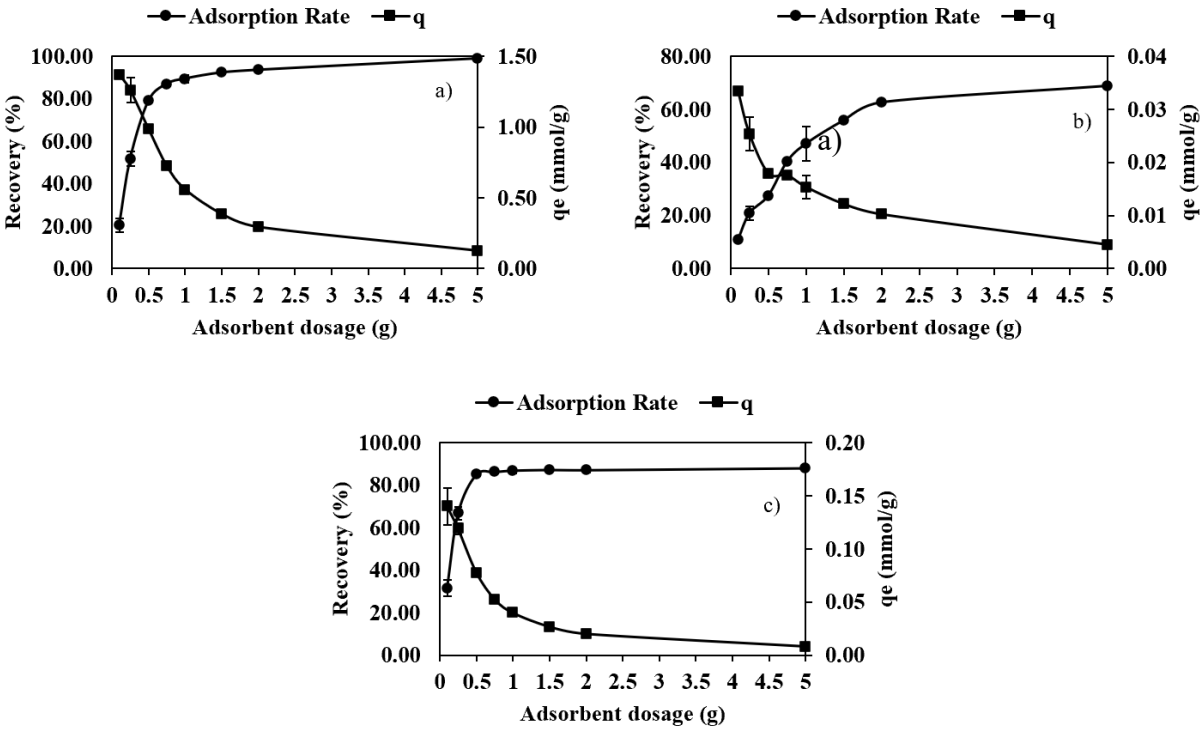

Figure 5.5. Equilibrium adsorption capacity and adsorption efficiency (recovery %) of a) Co (II), b) Mn (II), and c) Ni (II) at different adsorbent dosages, a pH of 4, room temperature, in 24h, and a dilution factor of 40.

5.4.3. Adsorption isotherm modeling

As the effectiveness of adsorption depends on the characteristics of the adsorbent, such as its capacity and kinetics, it is crucial to analyze the adsorption mechanism using isotherm models. This approach enables an understanding of how each metal ion interacts with chitosan, providing insights into their behavior during adsorption. Langmuir, Freundlich, Temkin, and Toth were selected to be investigated in this study (Al-Ghouti and Da'ana, 2020; Babakhani and Sartaj, 2023, 2022a; Piccin et al., 2017).

The Langmuir isotherm assumes molecules are adsorbed onto discrete, uniform active sites, with no interaction between adsorbed molecules. It models monolayer adsorption, where q_m represents the maximum adsorption capacity. Freundlich model describes reversible, non-ideal adsorption. Unlike Langmuir, Freundlich allows for multilayer adsorption and uneven distribution of adsorption heat and affinities on the surface. Stronger binding sites are occupied first, with adsorption energy declining exponentially. The parameter $\frac{1}{n}$ indicates surface heterogeneity and energy distribution; favorable adsorption is $0 < \frac{1}{n} < 1$ and unfavorable is $\frac{1}{n} > 1$. Temkin model considers adsorbent-adsorbate interaction, linearly declining adsorption heat with increasing surface coverage. The Toth model describes heterogeneous adsorption systems, with parameter (t) indicating heterogeneity. Increasing temperature increases (t), showing the independent relation between temperature and (t) (Al-Ghouti and Da'ana, 2020; Piccin et al., 2017).

Figure 5.6 displays the adsorption isotherm models alongside the experimental data for Co(II), Mn(II), and Ni(II) adsorption onto chitosan. Table 5.5 shows the calculated model parameters, R-squared, and MSE values. The calculated coefficient of determination, represented by R-squared values, indicates the degree of fit between the isotherm models and the experimental data. Higher R-squared values approaching 1 indicate that the predictive models closely match the experimental data (Anderson, 2017; Roshanfar et al., 2019). According to Figure 5.6 and Table 5.5, in terms of Co(II) adsorption onto chitosan, Langmuir and Toth models showed the best fits with the experimental data, exhibiting a higher R^2 value of 0.99 and lower values for MSE (0.004 and 0.003, respectively) as well as SSR (0.039 and 0.024, respectively). This suggests that Co (II) adsorption follows a linear pattern and is heterogeneous. Based on the Langmuir model, the calculated maximum adsorption capacity for Co(II) is determined to be 1.86 mmol/g (or 110 mg/g), which is significantly higher than values reported in the literature, such as 22.8 mg/g for Co(II) adsorption using activated mesoporous carbon (Conte and Gómez, 2024), 29.7 mg/g for Co(II) adsorption with diazotization of p-phenylenediamine modified graphene oxide (GO-PPDA) (Iqbal et al., 2022), and 18 mg/g for Co(II) using a lignin-silica composite (Budnyak et al., 2020). Meanwhile, as shown in Figure 5.6 and Table 5.5, all models exhibited a strong R^2 value (above 0.92) for the adsorption of Mn on chitosan, with the Freundlich model being closest to one (0.95). In terms of MSE and SSR, the models are quite low in number (the lowest MSE and SSR values are for the Freundlich model). Thus, for Mn(II), the Freundlich model, which shows a better fit,

suggests the possibility of multilayer adsorption. However, the $\frac{1}{n}$ value exceeding 1 indicates that the adsorption is unfavorable. In the case of Mn (II), the Langmuir isotherm shows an unfavorable adsorption pattern due to competitive adsorption with Ni(II) and Co(II). Mn(II) is outcompeted, as reflected by its much lower affinity constant KL (0.004 L/mmol) compared to Co(II) (0.32 L/mmol) and Ni(II) (1.12 L/mmol). Although the model predicts a high q max for Mn(II), its surface coverage remains low, indicating weak binding. Regarding Ni(II) adsorption, according to Figure 5.6 and Table 5.5, all models have good fits (R^2 more than 0.89), while the Temkin model fits better (0.92), suggesting a linear decline in adsorption heat with increasing surface coverage (Al-Ghouti and Da'ana, 2020). Regarding MSE, all models are quite similar, and for SSR, Temkin's (0.002) and Langmuir's (0.003) values are very close. Therefore, it can be concluded that Ni(II) may also follow the Langmuir isotherm. According to the Langmuir model, the calculated maximum adsorption capacity for Ni(II) is 0.37 mmol/g (or 20 mg/g). This capacity is superior compared to that of other materials, for example, activated carbon produced from the almond husk, which has a capacity of 4.9 mg/g, and is comparable to activated mesoporous carbon, which has a capacity of 24.2 mg/g (Conte and Gómez, 2024).

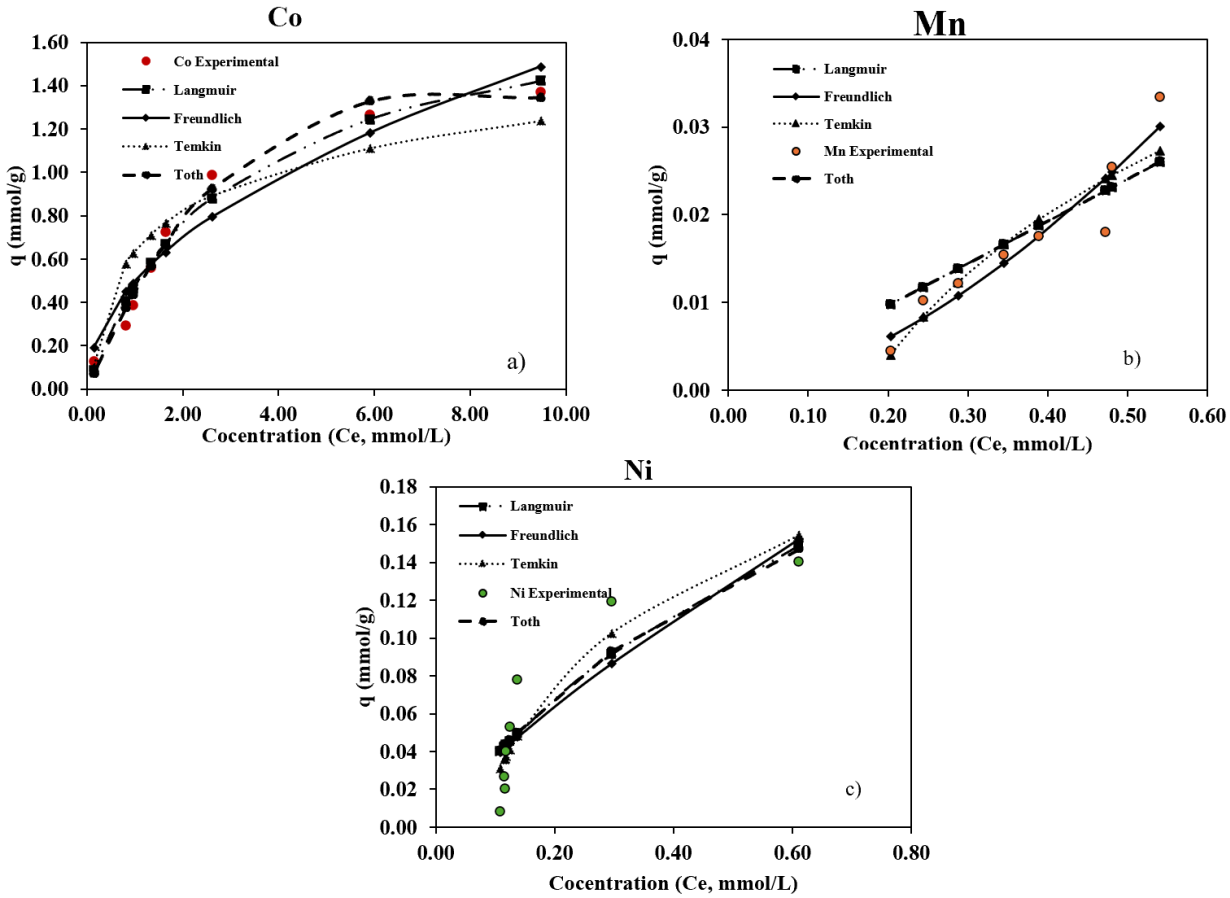

Figure 5.6. Adsorption isotherms and experimental data for a) Co(II), b) Mn(II), and c) Ni(II).

Table 5.5. Calculated adsorption isotherm parameters

Two-Parameters				
Isotherm model	Parameter	Co (II)	Mn (II)	Ni (II)
Langmuir	K_L (L/mmol)	0.32	0.004	1.12
	q_m (mmol/g)	1.86	11.90	0.37
	R-squared	0.99	0.94	0.89
	SSR	3.87E-02	1.19E-04	3.49E-03
	MSE	4.30E-03	1.33E-05	3.88E-04
Freundlich	k_F	0.50	0.08	0.22

	n_F	2.05	0.61	1.28
	R-squared	0.96	0.95	0.87
	SSR	1.06E-01	5.92E-05	3.89E-03
	MSE	1.32E-02	7.41E-06	4.87E-04
Temkin	K_T (L/ mmol)	10.67	5.81	14.13
	ΔQ	170.34	381.62	48.16
	b_T	0.02	0.004	0.001
	R-squared	0.95	0.92	0.92
	SSR	2.14E-01	8.51E-05	2.36E-03
	MSE	2.68E-02	1.06E-05	2.95E-04
	Three-Parameters			
Toth	K_T	5.50E+10	0.05	24613.87
	α	44.31	332064.5	6.50
	t	0.15	92989.85	0.17
	R-squared	0.99	0.94	0.90
	SSR	2.42E-02	1.19E-04	3.40E-03
	MSE	3.02E-03	1.49E-05	4.25E-04

5.4.4. Thermodynamics study results

The adsorption of Co(II), Mn(II), and Ni(II) on chitosan was examined at two different temperatures, 4°C and 22°C. As temperature increased, there was a slight rise in the adsorption uptake of chitosan for all metal ions, indicating a minor influence of temperature on the adsorption process (from 73%±0.07 to 81%±1.55 for Co(II), from 23%±1.83 to 27%±1.63 for Mn(II), and from 75%±0.75 to 84%±0.09 for Ni(II)). Higher temperature boosts the diffusion rate of metal ions from the solution into the adsorbent pores, and it leads to increased active adsorption sites (functional groups), thereby enhancing their adsorption activity towards ions. Also, elevated temperatures facilitate the formation of complexes between metal ions and the chitosan (Liu et al.,

2022). To further understand the characteristics of the adsorption reactions, such as spontaneity, randomness, and whether they are endothermic or exothermic, thermodynamic parameters (ΔG◦, ΔH◦, and ΔS◦) were calculated. These parameters were determined using the Van't Hoof equation:

$$k_C = \frac{C_{ad}}{C_e} \tag{5-1}$$

$$\Delta G^0 = -RTLnk_C \tag{5-2}$$

$$\Delta G^0 = \Delta H^0 - T\Delta S^0 \tag{5-3}$$

$$Lnk_C = \frac{\Delta S^0}{R} - \frac{\Delta H^0}{RT} \tag{5-4}$$

where R represents the universal gas constant (8.314 J/mol/K), and T stands for the absolute temperature (K). k_C denotes the sorption equilibrium constant, while C_{ad} and C_e refer to the equilibrium concentrations of metal ions on the adsorbent (mmol/g) and in the solution (mmol/L), respectively. Plotting Ln(k_C) against $\frac{1}{T}$ allows for the determination of the change in entropy (ΔS°) from the intercept, while the slope enables the calculation of the change in enthalpy (ΔH°) (Babakhani and Sartaj, 2023a, 2022a; Lima et al., 2019).

The calculated thermodynamic parameters for the adsorption of Co(II), Mn(II), and Ni(II) onto chitosan are outlined in Table 5.6. As indicated by the table, there is a rise in randomness observed for all metal ions, and the reactions for each metal ion are found to be endothermic, reflected by the positive ΔH° values. The absolute value of ΔS° reflects the degree of change in disorder or randomness within the system. It is evident that the increase in randomness is greater for Co(II) and Ni(II) compared to Mn(II). A large ΔS° indicates a significant increase or decrease in disorder. Compared to the ΔH° for Mn(II), the ΔH° values for Co(II) and Ni(II) are higher. A high ΔH° in an endothermic reaction signifies significant energy absorption, and such reactions may need a continuous supply of heat. Notably, the adsorption reactions of Co(II) and Ni(II) are spontaneous, with negative ΔG° values observed at both temperatures, whereas Mn(II) adsorption is not spontaneous, as evidenced by the positive ΔG° values. This outcome, combined with the findings of the isotherm investigation, provides additional validation for the moderate adsorption behavior

of Mn(II) onto chitosan. The differences in adsorption behavior, with higher and comparable adsorption of Co and Ni attributed to their similar atomic radii and strong affinity for amine functional groups, and the distinct lower adsorption of Mn due to its interaction with hydroxyl groups, further demonstrate the efficiency and selectivity of this low-energy process (Yang et al., 2023, 2018). The thermodynamic findings also suggest that the adsorption process can occur at room temperature, indicating that it is a low-energy-consumption process (Liu et al., 2022).

Table 5.6. Calculated thermodynamic parameters for Co(II), Mn (II), and Ni (II) adsorption onto chitosan

Temperature (K)	ΔG° (kJ/mol)		ΔH° (kJ/mol)	ΔS° (J/mol K)
	293	277		
Co(II)	-3.23	-2.24	14.60	60.78
Mn(II)	2.70	2.77	4.37	5.79
Ni(II)	-4.21	-2.48	26.74	105.50

5.4.5. Kinetics study results

Adsorption kinetics refers to the rate at which metal ions move from the liquid phase to the chitosan, encompassing the time required for mass transfer of components from the liquid to the adsorbent. Assessing kinetic facets during adsorption studies is crucial for gaining deeper insights into the mechanisms, attributes, and potential applications of the process. In other words, the kinetic profile provides data concerning the rate of adsorption, the time required to reach equilibrium, and the efficacy of the adsorbent (Mohammed et al., 2020; Piccin et al., 2017).

In this study, two kinetic models have been used to replicate the experimental data and examine the step that limits the rate of adsorption. The pseudo-first-order and pseudo-second-order equations are commonly applied in metal ion adsorption, involving the sharing or exchange of electrons between metal ions and functional groups (Metwally et al., 2024). The equations are outlined as follows (Mohammed et al., 2020):

Pseudo-first-order equation:

$$q_t = q_e(1 - \exp(-kt)) \quad (5\text{-}5)$$

Pseudo-second-order equation:

$$q_t = \frac{k_2 q_e^2 t}{1 + k_2 q_e t} \quad (5\text{-}6)$$

where qt and qe (mmol/g) represent the amounts of adsorbate on the adsorbents at time t and at equilibrium, respectively. k_1 (1/min) and k_2 (g/mmol/min) denote the rate constants of the pseudo-first-order and pseudo-second-order kinetic models. Figure 5.7 illustrates the experimental data collected at various time intervals (ranging from 5 min to 48 h), at a dilution factor of 40, an initial pH of 4, room temperature, and the adsorbent dosage of 10 g/L, alongside the pseudo-first-order and pseudo-second-order models. Initially, the adsorption of metal ions onto chitosan occurred rapidly, gradually slowing until equilibrium was reached. This initial rapid adsorption rate can be attributed to the abundant availability of adsorption sites, which gradually decreased as they became occupied during the adsorption process (Liu et al., 2022). The adsorption reactions reached equilibrium after 8 h for Co(II), 24 h for Mn(II), and 3 h for Ni(II), indicating that Mn(II) required a longer time to achieve equilibrium. It should be noted that the kinetics of Co(II) and Ni(II) were notably rapid, with approximately 46% and 66% of Co(II) and Ni(II) being adsorbed within the first 5 min of the process.

Table 5.7 presents the kinetic parameters for the adsorption of Co(II), Mn(II), and Ni(II) onto chitosan. As per the calculated R-squared values in the table, for all metal ions, the theoretical qe values calculated using the pseudo-second-order model closely match the experimental data. Specifically, the calculated qe values for Co(II), Mn(II), and Ni(II) are 0.75 mmol/g, 0.01 mmol/g, and 0.07 mmol/g, respectively. These findings indicate that the pseudo-second-order model is more appropriate than the pseudo-first-order kinetic model for explaining the experimental data of Co(II) and Ni(II), suggesting that the surface reaction may be the rate-limiting step (Babakhani and Sartaj, 2023, 2022a; Piccin et al., 2017). Also, it can be concluded that the adsorption of Co(II) and Ni(II) onto chitosan is achieved through a covalent bond formation, representing chemical adsorption (Liu et al., 2022). Mn adsorption follows the pseudo-first-order model, implying physisorption as the rate-limiting step (B. Liu et al., 2019).

Table 5.7. Kinetics parameters of adsorption of Co(II), Mn(II), and Ni(II) onto chitosan

	Co	Mn	Ni
Pseudo-First-Order Model			
qe (mmol/g)	0.92	0.012	0.08
k_1 (1/min)	0.10	0.02	0.24
R-squared	0.82	0.82	0.76
Pseudo-Second-Order Model			
k_2 (g/mmol/min)	0.44	77.33	8.85
qe (mmol/g)	0.75	0.01	0.07
R-squared	0.91	0.64	0.95

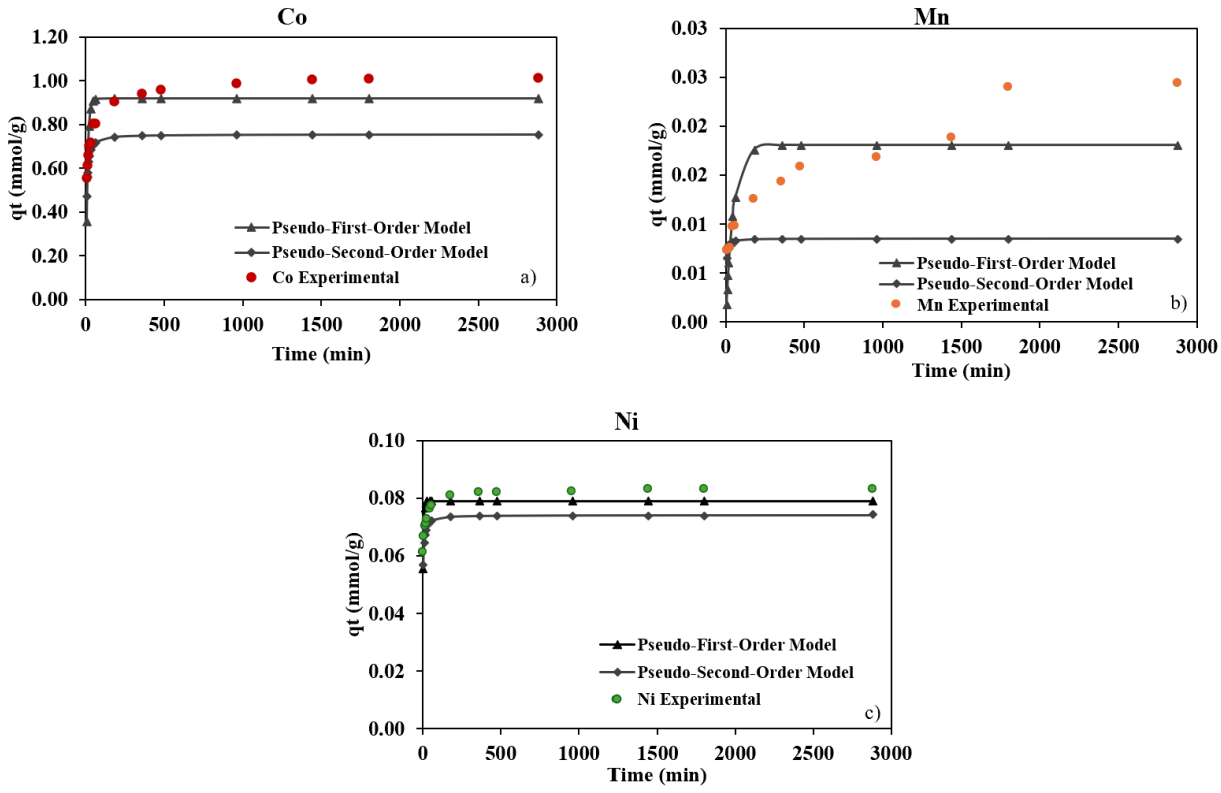

Figure 5.7. The experimental data at different time intervals (5 min to 48 h) as well as the pseudo-first-order and pseudo-second-order models for a) Co(II), b) Mn(II), and c) Ni(II).

5.4.6. Desorption study

The desorption results using DI water could indicate the potential for leaching of metal ions if the adsorbent were disposed of. Desorption also serves the purpose of regenerating the adsorbents for reuse. Given the considerable expenses associated with production, stabilization, and disposal, researchers increasingly prioritize the regeneration and reuse of adsorbents. However, desorption presents challenges due to the strong affinity of adsorbates for the adsorbent surface. From environmental, economic, and practical perspectives, desorption studies are indispensable for retrieving metal ions adsorbed on the adsorbent surface and revitalizing the adsorbent for subsequent use.

Consequently, various desorption agents have been explored in the literature for chitosan-based adsorbents saturated with metal ions, including acidic media, chelators, salt, and alkali reagents. The selection of a suitable desorption agent is crucial for chitosan-based adsorbents. It should be cost-effective, environmentally benign, non-destructive to chitosan, and capable of restoring its physical and adsorption properties to near-original levels (Babakhani and Sartaj, 2023, 2022a; Vakili et al., 2019). Table 5.8 presents the various media investigated in this study—water, HCl (0.1M), NaCl (1M), and H_2SO_4 (0.01-0.1M)—to determine the optimal medium for desorbing Co(II), Mn(II), and Ni(II) from the surface of chitosan. Among these options, only H_2SO_4 exhibited a favorable desorption efficiency, with all Co(II) and Ni(II) being effectively separated even in the presence of 0.01 M H_2SO_4. In addition, more than 82% of Mn(II) was desorbed by H_2SO_4. Considering both the acid usage and environmental concerns, 0.01 M H_2SO_4 was the most suitable desorption medium.

Given the value of the desorbed metal ions, Co(II) and Ni(II) can be recovered after desorption, either by separation or by precipitating them as a mixed hydroxide precipitate (MHP), which requires further investigation.

Table 5.8. The studied desorption media

Desorption percentage (%)	Co (II)	Mn(II)	Ni(II)
DI Water	18.09	36.59	30.43
HCl (0.1 M)	57.42	50.81	53.80
NaCl (1 M)	19.86	68.70	24.01
H_2SO_4 (0.1M)	100.00	86.59	100.00
H_2SO_4 (0.05M)	100.00	83.74	100.00
H_2SO_4 (0.01M)	100.00	82.52	100.00

5.4.7. Mn Removal (precipitation) and Li carbonate production

As mentioned, the selective extraction of Li holds significant importance in battery recycling due to the anticipated scarcity of lithium in the near future. In this study, utilizing 10 g/L of chitosan, over 80% of Co(II) and Ni(II) were separated at an initial pH of 4, room temperature, with a dilution factor of 40, and within 24 h. Conversely, under the same conditions, only 27% of Mn(II) was separated, necessitating a method to remove the remaining Mn(II) while retaining only Li in the solution.

According to previous studies (Rajak et al., 2023; Tobiason et al., 2016), Mn(II) can be separated using potassium permanganate ($KMnO_4$) through oxidation of Mn(II) and subsequent precipitation. However, careful consideration should be given to the amount of $KMnO_4$ added to prevent its dissolution. Therefore, two methods of $KMnO_4$ addition were investigated. Initially, 1.92 times $KMnO_4$ relative to the remaining Mn(II) in the solution was added at room temperature. The results are summarized in Table 5.9, wherein approximately 72% of the remaining Mn precipitated, accounting for approximately 82% of total Mn removal. Mn removal was also achievable at a higher temperature of 80°C, with $KMnO_4$ added dropwise. According to Rajak (Rajak et al., 2023), the optimal concentration of $KMnO_4$ is 0.35M, resulting in 86% removal of the remaining Mn, corresponding to approximately 91% of total Mn removal. Notably, in both cases, the concentration of Li remained unchanged, with all lithium remaining in the solution.

Interestingly, Mn(II) (along with the remaining Co(II) and Ni(II)) could also be removed by increasing the pH to around 12 (Cai et al., 2014), resulting in a removal rate of 95% (totaling 97%). Under this condition, the concentration of Li remained unaffected, with all Li remaining in the solution. Therefore, all of these approaches are feasible, and the choice of method can be determined based on the specific conditions.

Previous studies have shown that ozone can efficiently precipitate manganese as MnO_2 due to its strong oxidative properties (Brennan, 2017). However, ozone is highly reactive and toxic, necessitating specialized equipment for safe generation and handling. These challenges contribute to higher operational costs and safety risks. In comparison, using $KMnO_4$ and pH control provides a more straightforward, safer, and cost-effective solution, removing the need for ozone and allowing for better control over the manganese removal process (Brennan, 2017).

To convert Li to lithium carbonate (Li_2CO_3), a saturated solution of sodium carbonate (Na_2CO_3) should be added to the solution, then heated to around 90 °C to evaporate it. Subsequently, Li_2CO_3 powder will accumulate at the bottom of the reactor (Cai et al., 2014). However, additional purification steps and impurity removal should be further investigated to produce battery-grade lithium carbonate.

Table 5.9. Different methods to remove Mn(II) from the media

Temperature (°C)	pH	Time (h)	Additive	Remaining Mn Removal (%)	Total Mn Removal (%)
Room	-	24	Mn: $KMnO_4$ = 1:1.92	72.15	81.97
80	-	-	Dropwise- $KMnO_4$ (0.35M)	86.35	91.02
Room	12	24	NaOH (10 wt.%)	94.63	96.47

5.5. Conclusions

In conclusion, this study demonstrates the effectiveness of chitosan in the selective recovery of Co(II), Mn(II), and Ni(II) from spent lithium-ion batteries in a sulfate-citrate medium while keeping Li in solution. The high adsorption efficiencies of Co(II) and Ni(II), exceeding 80%,

highlight the potential of chitosan for efficient metal ions recovery. It is important to highlight that chitosan's adsorption capacity for Li is remarkably low, with less than 1% adsorption efficiency, effectively keeping Li in the solution. Moreover, the optimized parameters, including initial metal ions concentration, pH, and adsorbent dosage, were determined to be a dilution factor of 40, a pH of 4, and an adsorbent dosage of 10 g/L. It was observed that increasing pH had a negligible effect on Co(II) and Ni(II) recovery, whereas Mn(II) removal increased with pH. Isotherm models revealed that Co(II), Mn(II), and Ni(II) adsorption followed Langmuir, Freundlich, and Temkin models, respectively, with predicted adsorption capacities calculated for Co(II) and Ni (II) as 1.86 mmol/g (or 110 mg/g), and 0.37 mmol/g (or 20 mg/g), respectively. At optimum conditions, Mn adsorption uptake was 0.02 mmol/g (1.10 mg/g) with an equilibrium concentration of 0.47 mmol/L. FT-IR findings indicated that amine and hydroxyl groups are the primary functional groups involved in metal ions adsorption. Kinetic and thermodynamic studies indicated that Mn(II) removal kinetics were slower compared to Co(II) and Ni(II), with Co(II) and Ni(II) showing rapid adsorption even within 5 minutes (46% and 66% of Co(II) and Ni(II)). The pseudo-second-order kinetics modeling (chemisorption) confirmed that the surface reaction was the rate-limiting step for Co(II) and Ni(II), while Mn(II) adsorption was limited by physisorption. Thermodynamic analysis revealed unfavorable Mn(II) adsorption, while Co(II) and Ni(II) adsorptions were found to be spontaneous and endothermic. Different desorption media (Water, HCl, NaCl, and H_2SO_4) were examined, with 0.01M sulfuric acid identified as the optimal choice, achieving 100% desorption for Co(II) and Ni(II) and over 82% for Mn(II). These findings underscore the promising potential of unmodified chitosan as a sustainable and efficient adsorbent for the recovery of metal ions in battery recycling processes.

5.6. Acknowledgments

The authors express their gratitude to the Ontario Center of Innovation and ERS-International Company for financial support for this project (Application number: OCI 34919).

5.7. References

The references are merged with those of the other chapters and listed at the end of the thesis.

Chapter 6 SYNTHESIS, PROCESS OPTIMIZATION, AND STATISTICAL ANALYSIS OF CHITOSAN-BASED BIOSORBENT BEADS FOR SELECTIVE LITHIUM RECOVERY IN LITHIUM-ION BATTERY RECYCLING

Published as a research article in Mineral Processing and Extractive Metallurgy Reviews, January 2026. DOI: 10.1080/08827508.2026.2616815.

6.1. Abstract

This study explores the application of green crosslinkers for the synthesis of chitosan biosorbent beads as a novel, sustainable method for the selective recovery of metals from spent LIB cathode materials, while offering a pathway to marine waste reuse. The proposed synthesis method alleviates the limitations of powder chitosan as an adsorbent in industrial continuous systems. Two amine-based crosslinkers, L-cystine and L-arginine, were evaluated to identify an optimal crosslinking strategy. Among them, L-cystine-crosslinked chitosan beads proved to be an efficient, stable biosorbent. Crosslinking via the thiol functional group preserved active sites, improved bead integrity without mass loss, and enabled high selectivity for the separation of Co(II) and Ni(II) in a sulfate-citrate medium while retaining Li in solution. Optimal performance was achieved with 1% L-cystine at a dilution factor of 30, pH 4, and an adsorbent dosage of 10 g/L. Response surface modeling indicated adsorption efficiencies of 69.55% for Co(II), 31.18% for Mn(II), and 91.62% for Ni(II), with corresponding uptake capacities of 65.56 mg/g (1.11 mmol/g), 1.47 mg/g (0.03 mmol/g), and 5.92 mg/g (0.10 mmol/g), respectively, while no lithium uptake was observed. Kinetic analysis showed rapid initial adsorption, with 46% of Co(II), 32% of Mn(II), and 88% of Ni(II) adsorbed within the first 3 h. Thermodynamic evaluation revealed endothermic adsorption, with Ni(II) exhibiting the strongest driving force. Regeneration using 0.1 M EDTA over three adsorption-desorption cycles resulted in minimal capacity loss, confirming bead reusability. This work showcases a green, selective, and practically viable biosorbent system that promotes sustainable, circular-economy-based LIB recycling.

Keywords: Lithium-ion battery recycling; Chitosan-based biosorbent beads; Green crosslinkers; Selective metal recovery.

6.2. Introduction

The increasing and excessive use of fossil fuels has exacerbated global environmental problems, particularly those related to greenhouse gas emissions and climate change. As fossil fuel reserves are being depleted, these impacts have created an urgent need to develop sustainable and environmentally friendly energy alternatives (Han et al., 2024; He et al., 2024). Among recent green technologies, lithium-ion batteries (LIBs) have emerged as a leading choice because of their high energy density, efficiency, and long lifespan, allowing widespread use in portable electronics, electric vehicles (EVs), and grid-scale energy storage systems (Han et al., 2024; He et al., 2024). As demand for renewable energy technologies rises, so does demand for LIBs, with projections indicating that by 2030 the global market will require more than 2500 GWh (12.7 million tons) of LIB energy storage capacity (Li et al., 2024). To address the growing demand for LIBs, a continually increasing supply of critical metals is required. However, the sources of these metals are limited. In addition, the widespread adoption of LIBs has led to a growing volume of spent batteries, raising concerns about environmental impacts and resource recovery. By 2030, more than 1 million electric vehicle batteries are expected to reach the end of their useful life (Verma et al., 2017). And by another estimate, the annual generation of waste LIBs could exceed 14 million units by 2040 (Zanoletti et al., 2024). This would, in turn, result in exponential growth in the LIB recycling market, which is projected to reach $15.5 billion by 2030 (Verma et al., 2017). The presence of critical metals such as lithium (Li), cobalt (Co), nickel (Ni), and manganese (Mn) in waste LIBs highlights the need for effective recovery methods that can promote circular economy principles, alleviate environmental and health impacts, and reduce dependency on primary mining resources (Ding et al., 2024b; Meng et al., 2021; Roshanfar et al., 2025, 2024). Pyrometallurgy and hydrometallurgy are the conventional methods for recycling LIBs. Pyrometallurgy, although effective for large-scale applications, requires high energy input and emits toxic gases, leading to the loss of Li and other valuable components (Han et al., 2024; He et al., 2024). In contrast, hydrometallurgy offers higher metal recovery rates, selectivity, lower energy consumption, and reduced environmental impact. However, it is hindered by long pretreatment times, the use of chemical reagents, and challenges in effectively separating metals (Ding et al., 2024; He et al., 2024). Hydrometallurgical techniques employ solvent extraction, chemical precipitation, and ion-exchange processes to separate critical metals (Jing et al., 2024; Tran et al., 2025). However, they have limitations. Solvent extraction is costly due to the use of expensive extractants (Ding et al.,

2024b; Salem et al., 2024). Chemical precipitation, although cost-effective and scalable, faces challenges in resynthesizing LIB cathode materials (Ding et al., 2024b). Ion-exchange offers high removal and recovery rates with simple operation. However, it requires significant pretreatment, generates excessive regeneration waste, consumes substantial amounts of salt, and has limited general applicability (B. Wang et al., 2023). Despite existing limitations, hydrometallurgy remains a promising approach for recycling LIBs, although further improvements are needed to enhance efficiency and simplify the process.

Adsorption has gained recognition as a separation method due to its low cost, ease of operation, high effectiveness, and ease of recovery and regeneration (Syeda et al., 2024; Yücel and Yörükoğlu, 2024). Adsorbents could offer good selectivity, high stability, and high adsorption efficiency. The process can be carried out effectively at ambient temperature and pressure. Additionally, the process is reusable and easier to manage than other techniques (Mahran et al., 2023; Reich et al., 2023; B. Wang et al., 2023). However, adsorbents should be affordable, easy to produce, and possess a high density of oxygen sites, thereby offering high efficacy in metal complexation. The adsorbent materials must have a chemical structure containing either an ion-exchange group or a chelation site (Salem et al., 2024). In recent years, the application of biopolymers as adsorbents has attracted significant attention for the remediation and resource recovery of heavy metals. Chitosan, a biodegradable and non-toxic polysaccharide derived from chitin, has shown exceptional metal-binding capabilities owing to its amino, hydroxyl, and carboxyl functional groups (Manzoor et al., 2019; Roshanfar et al., 2025). Chitosan, as an adsorbent, is environmentally friendly, biocompatible, and biodegradable, making it a promising, sustainable option for LIB recycling and contributing to waste reduction and environmental sustainability (Roshanfar et al., 2025).

Previous research by the authors demonstrated that chitosan powder had great potential as an adsorbent for the recovery of critical metals of LIBs, which highlighted its high efficiency in the selective recovery of Co(II), Ni(II), and Mn(II), and leaving Li in the solution (Roshanfar et al., 2025). Its low toxicity, high adsorption capability, biocompatibility, and biodegradability make it particularly ideal for environmental applications (Syeda et al., 2024). Chitosan's high surface area and porous structure provide numerous active sites for metal binding, and the presence of amino and hydroxyl functional groups allows it to interact with a wide range of metals. Furthermore,

chitosan can be readily modified because it is inexpensive and derived from renewable sources, such as crustacean shells, a waste byproduct of the fisheries industry (Saheed et al., 2021). However, the recovery and separation of chitosan powders from liquid media pose significant challenges for large-scale industrial applications, thereby limiting their practical use. This is because adsorption processes are typically carried out in columns, which are impractical due to clogging and high pressure drops (Al-Ghamdi et al., 2022). To address these issues, chitosan powder can be formed into beads, sheets, thin films, or membranes, improving its flexibility and facilitating adsorption-desorption processes (Balakrishnan et al., 2023). Moreover, chitosan powder has poor mechanical strength; however, its modification and integration into composite materials could enhance its stability and reusability in various aqueous systems. One alternative is crosslinking, which forms a three-dimensional network, thereby improving performance (Vakili et al., 2019). However, modifications of chitosan and the production of biosorbent beads may reduce its adsorption capacity due to the wrapping of the binding group. Thus, introducing many coordinating atoms is necessary to enhance metal-ion binding performance (Verma et al., 2017). Among commonly used crosslinking agents for chitosan, glutaraldehyde and epichlorohydrin are the most widely employed. Glutaraldehyde crosslinks with the free amino groups (NH_2) of chitosan, while epichlorohydrin crosslinks with its hydroxyl groups (OH) (Balakrishnan et al., 2023). Sodium tripolyphosphate has also been reported as a crosslinker for chitosan beads (Babakhani and Sartaj, 2023, 2020; Balakrishnan et al., 2023). However, glutaraldehyde and sodium tripolyphosphate, by interacting with free NH_2 groups, can reduce adsorption efficiency (Babakhani and Sartaj, 2023, 2020). The authors' previous work has shown that amine groups play a crucial role in adsorbing critical metal ions, particularly Co and Ni, making it essential to preserve their availability by avoiding their involvement in crosslinking (Roshanfar et al., 2025).

Additionally, epichlorohydrin is toxic and potentially carcinogenic; therefore, careful selection of crosslinkers is vital to enhance mechanical properties and minimize mass loss. L-Arginine (Arg), found in protein-rich foods (e.g., nuts, seeds, fish, dairy), with its guanidine group, has a strong affinity for metal ions due to its abundant amine groups. When incorporated into chitosan, arginine can improve the adsorption capacity. Manzoor et al. (2019) demonstrated that adding arginine to chitosan/carboxymethyl cellulose greatly enhances the adsorption efficiency. The synthesized beads, with large surface areas and reduced swelling, exhibited high metal-ion removal efficiency and excellent reusability. These beads also showed good degradability, decomposing within five

weeks when buried in soil (Manzoor et al., 2019). L-cystine (Cys), a naturally occurring amino acid present in keratin-rich waste, such as poultry feathers, hog bristles, and human hair, contains thiol (SH), amine, and carboxyl (COOH) groups, making it another promising candidate for metal-ion adsorption. L-cystine, found in high-protein foods (Abou El-Reash, 2016), interacts with chitosan through its SH group. It was reported that combining L-cystine with iron oxide (Fe_3O_4) as an adsorbent exposes COOH and NH_2 groups, enhancing metal uptake (Bashir et al., 2021). When bound to carbon carriers, it also stabilizes iron-based nanoparticles (Zhang et al., 2020). Hence, L-cystine's biocompatibility and metal-binding properties make it valuable for the development of adsorbents (Kotte and Yun, 2014; Taha et al., 2025; Yang et al., 2020). Furthermore, blending chitosan with L-cystine could improve adsorption capacity and mechanical properties by increasing the number of active sites, such as carboxyl, amine, and thiol groups (Bashir et al., 2021; Yang et al., 2020; Zhang et al., 2020).

The present study investigates the feasibility of using L-arginine and L-cystine as crosslinkers for chitosan bead production, aiming to synthesize green bio-sorbent beads with structural integrity and ensuring high adsorption efficiency and selectivity for divalent metal ions (Co(II), Mn(II), and Ni(II)) from high metal ion concentrations sulfate-citrate leachate solutions derived from various cathode types of spent lithium-ion batteries (LIBs). The study evaluates the selection and optimization of the best-performing crosslinker and its dosage, along with key parameters such as initial metal-ion concentrations and pH, to achieve optimal adsorption performance of crosslinked chitosan beads. Despite existing research, optimizing adsorption behavior and kinetic parameters for the application of synthesized crosslinked biosorbent beads under realistic leaching conditions remains a critical area for advancement. Additionally, comprehensive isotherm studies, alongside detailed kinetic and thermodynamic analyses of the adsorption process, were conducted. Understanding the thermodynamic and kinetic aspects of metal adsorption clarifies the mechanisms governing biosorption efficiency and provides insights for process scaling. The synthesized bio-adsorbent beads were characterized using Fourier Transform Infrared Spectroscopy (FT-IR) and Brunauer-Emmett-Teller (BET) methods. These findings provide valuable insights into the practical application of chitosan beads in battery recycling. To the authors' knowledge, no prior research has explored the use of L-arginine- or L-cystine-crosslinked chitosan beads for the selective recovery of critical metal ions from different types of spent LIBs

in a citrate-sulfate medium. In a previous study, the authors demonstrated that commercial chitosan powder was an effective adsorbent for the selective recovery of critical metals and that the sulfate-citrate leaching process was a viable and eco-friendly method for extracting these metals from mixed spent LIBs (Roshanfar et al., 2025, 2024). This study extends these findings, laying the groundwork for future research aimed at further enhancing chitosan's properties by converting it into biosorbent beads to enable its practical application in larger-scale processes, such as adsorption column studies, ultimately contributing to the development of sustainable, environmentally friendly LIB recycling technologies.

6.3. Materials and methods

6.3.1. Materials and Sample Preparation

Spent LIBs were obtained from a recycling facility located in Toronto, Canada. The samples represented a mixture of end-of-life electronic products (laptop batteries, mobile phone batteries, and Li-polymer cells). Sulfuric acid (H_2SO_4, with the purity of 98%), citric acid monohydrate ($C_6H_8O_7 \cdot H_2O$, with the purity of 99%), and acetic acid (CH_3COOH, with the purity of 99.7%) were procured from Fisher Chemical, USA. Chitosan with a deacetylation degree of 85% and sodium hydroxide (NaOH, purity >97%) were supplied by Fisher Scientific (Canada). L-arginine (with the purity of 98%), L-cystine (with the purity of 99%), and ethylenediaminetetraacetic acid (EDTA, disodium salt dihydrate, purity>99%) were obtained from Thermo Scientific, Canada. All chemicals and reagents used were of analytical grade. The solution preparation process followed the methodology outlined by the author's previous study (Roshanfar et al., 2024). In brief, the batteries were discharged and manually dismantled to remove cathode materials. During manual dismantling, aluminum and copper current collectors and steel casings were removed. A black mass (BM) mixture was made from lithium cobalt oxide (LCO), lithium nickel, manganese oxide (NMC), and lithium manganese oxide (LMO) cathodes, using cathodes from used laptops, cellphones, and Li-polymer battery cathodes, with a ratio of 1:1:1. Binder materials were removed by thermal treatment at 570 °C for 2 h in air. The treated material was subsequently leached in a synergistic solution of H_2SO_4 (1.25 M) and citric acid (0.55 M) at 90 °C for 2 h.

6.3.2. Preparation of crosslinked chitosan beads (CBs)

Chitosan beads (CBs) were synthesized following a modified procedure adopted from Babakhani and Sartaj (2023, 2020). A 3.2 g chitosan powder sample was dissolved in 80 mL of a 5% acetic acid solution at 30 °C under continuous stirring for 24 hours. Then, varying amounts of each crosslinker (L-arginine and L-cystine) were introduced at different proportions: 1, 5, 10, 12.5, 25, and 100 wt.% relative to the weight of the chitosan powder. After 3 hours of mixing, the solution was slowly introduced dropwise into 0.6 M NaOH to form spherical, crosslinked chitosan beads. The beads were hardened overnight and then repeatedly rinsed with DI water and air-dried at ambient temperature.

6.3.3. Analytical Methods and Characterization

Metal ion (Li, Co, Ni, Mn) concentrations were determined using Inductively Coupled Plasma-Optical Emission Spectroscopy (ICP-OES; Agilent 5110) spectrometry following complete digestion of the samples in aqua regia (HNO_3: HCl = 1:3) at 120 °C overnight. For adsorption experiments, metal concentrations were measured using Atomic Absorption Spectroscopy (AAS; PinAAcle 500, PerkinElmer). Calibration was performed using a nonlinear curve passing through the origin. All measurements were conducted in triplicate, and mean values were used in data evaluation. Functional groups of raw and crosslinked chitosan beads, before and after adsorption, were characterized by Fourier Transform Infrared Spectroscopy (FT-IR; Thermo IS50, 500-4000 cm^{-1}). Brunauer-Emmett-Teller (BET) surface area measurements were performed at 77 K, with samples pre-activated on either a Quantachrome system (McGill University) or a Micromeritics 3Flex analyzer (University of Ottawa). The pH of the solutions was monitored using a HACH HQ40D meter. (Sing, 1985).

6.3.4. Batch adsorption study

Batch adsorption experiments were conducted by placing 0.5 g of crosslinked CBs and 50 mL of the leached solution in 125 mL Erlenmeyer flasks and agitating at 150 rpm for 24 h at room

temperature (Roshanfar et al., 2025). After equilibrium, the suspensions were filtered through 0.45 μm EZFlow membranes. The effects of initial metal concentration on the uptake of critical metals were assessed by diluting the stock solution with dilution factors of 10 to 50. Once the optimum concentration range was established, additional tests were conducted to assess the influence of pH. The experiments were performed both at the natural leachate pH (~2) and at adjusted pH values of 4 and 5. The desired pH levels were obtained with 10 wt.% NaOH or 1% (v/v) H_2SO_4 solutions. Higher pH values (>8) were excluded to avoid metal hydroxide precipitation (Conte and Gómez, 2024). Initial and equilibrium metal concentrations were quantified using AAS, and adsorption capacity (q_e, mg/g) and adsorption rates (removal efficiency) (%) were calculated as follows:

$$qe = \frac{(C_0 - C_e) \times V}{W} \tag{6-1}$$

$$Adsorption\ rate(\%) = 100 - (\frac{C_e}{C_0}) \times 100 \tag{6-2}$$

where C_0 (mg/L), Ce (mg/L), V (L), and W (g) indicate the initial metal ions concentration, the equilibrium concentration of the adsorbate in the solution, the solution volume, and the dry weight of the adsorbent, respectively. Each experiment was performed in triplicate, and the mean (±standard deviation (SD)) was calculated. Blanks (CBs + DI water) and controls (diluted leaching solution without adsorbent) confirmed no metal uptake or release.

6.3.5. Statistical analysis

To strengthen process reliability, statistical analysis and response surface methodology (RSM) was employed to evaluate the experimental results and determine the optimum conditions using Design Expert 12 (State-Ease Inc., Minneapolis, MN, USA).

6.3.6. Adsorption isotherm Study

Adsorption isotherm data were fitted to three common isotherm models: Langmuir, Freundlich, and Toth models. The adequacy of each model in describing the data was assessed using the coefficient of determination (R^2), the Sum of squared residuals (SSR), and the Mean Squared Error (MSE). Lower SSR and MSE values indicate a better fit. The equations for Langmuir (Eq. 6-3), Freundlich (Eq. 6-4), and Toth (Eq. 6-5) are presented below:

$$q_e = \frac{q_m k_L C_e}{1+k_L C_e} \tag{6-3}$$

$$q_e = k_F C_e^{\frac{1}{n_F}} \tag{6-4}$$

$$q_e = \frac{K_T C_e}{(\alpha_T + C_e)^{\frac{1}{t}}} \tag{6-5}$$

where q_m represents the maximum adsorption capacity (mg/g), k_L is the Langmuir constant (L/mg), k_F and n_F are the Freundlich constants corresponding to adsorption capacity and intensity, respectively, and C_e refers to the equilibrium concentration (mg/L) of the metals in the solution. For the Toth equation, Kt and t are the Toth constant (L/mg) and System heterogeneity (≠ 1 denotes heterogeneity), respectively.

6.3.7. Kinetics study and the effect of contact time

The effect of contact time on adsorption and kinetic behavior was assessed using the optimal conditions identified from the previous phase. The experiments were performed at room temperature for different time intervals (5–1800 min). Kinetic analysis was performed using pseudo-first-order (Eqs. 6-6) and pseudo-second-order (Eq. 6-7) models, which describe electron transfer between metal ions and the adsorbent's functional groups.

Pseudo-first-order equation:

$$q_t = q_e(1 - \exp(-kt)) \quad (6\text{-}6)$$

Pseudo-second-order equation:

$$q_t = \frac{k_2 q_e^2 t}{1 + k_2 q_e t} \quad (6\text{-}7)$$

where qt and qe (mg/g) denote the amounts of adsorbate present on the adsorbents at time t and at equilibrium, respectively. k_1 (1/min) and k_2 (g/mg) are the constants of the first- and second-order equations, respectively.

6.3.8. Thermodynamics study

Adsorption tests under the optimized conditions determined in the previous phase were conducted at 4 °C and 22 °C to investigate the effects of temperature and to determine thermodynamic parameters. Thermodynamic parameters (ΔG°, ΔH°, and ΔS°) were derived from the following equations (Eq. 6-8 and Eq.6-9) to evaluate spontaneity, disorder, and the endothermic or exothermic nature of adsorption.

$$\Delta G^0 = -RTLn\frac{C_{ad}}{C_e} = \Delta H^0 - T\Delta S^0 \quad (6\text{-}8)$$

$$Lnk_C = \frac{\Delta S^0}{R} - \frac{\Delta H^0}{RT} \quad (6\text{-}9)$$

where R represents the universal gas constant (8.314 J/mol/K), and T denotes the absolute temperature (K). The symbol k_C refers to the sorption equilibrium constant, while C_{ad} and C_e indicate the equilibrium concentrations of metal ions on the adsorbent (mg/L) and in the solution, respectively.

6.3.9. Desorption study and reusability

Upon completion of the adsorption tests, the beads were separated by vacuum filtration, rinsed with DI water, and dried at room temperature. Desorption tests were then carried out in 50 mL of DI water, 0.01 M H_2SO_4, and EDTA solutions (0.1 and 0.5 M). Final metal concentrations were

measured using AAS. The reusability (adsorption-desorption) cycles were repeated three times. Desorption efficiency (%) was calculated as:

$$Desorption(\%) = \frac{Amount\ of\ metal\ ions\ desorbed\ (mg)}{Amount\ of\ metal\ ions\ adsorbed\ (mg)} \times 100 \quad (6\text{-}10)$$

6.4. Results and Discussion

6.4.1. Characterization

To characterize the crosslinked CBs, the BET surface area and FT-IR spectra were studied.

6.4.1.1. BET Surface Area Analysis

The measured BET surface area and total pore volume for chitosan powder, CBs without a crosslinker, and chitosan beads with Arg (CS: Arg 1:1) and 1% Cys (CB1%CYS), which were selected as they represent the optimized crosslinker ratios, are 7.45 m^2/g with a total pore volume of 7.18×10^{-3} cm^3/g, 5.47 m^2/g with a total pore volume of 4.48×10^{-3} cm^3/g, 6.46 m^2/g with a total pore volume of 4.75×10^{-3} cm^3/g, and 9.26 m^2/g with a total pore volume of 24.40×10^{-3} cm^3/g, respectively. Generally, bead formation reduces surface area and total pore volume due to crosslinking or physical shaping of functional groups, thereby decreasing the surface area available for adsorption or reactions. Excessive crosslinking can also result in dense beads with reduced surface area. However, as demonstrated, controlled amounts of Arg and Cys, used as crosslinkers, slightly improved the BET surface area by increasing the total pore volume. In the case of Cys, the pronounced increase in total pore volume relative to surface area indicates the formation of larger pore/void domains, which mainly improve accessibility and diffusion within the bead matrix rather than proportionally increasing the number of adsorption sites.

6.4.1.2. FT-IR analysis

Figure 6.1(a-e) shows the characteristic peaks identified in CB, CB1%CYS, the spectra for the CB1%CYS after adsorption, and after desorption (one cycle) with 0.1 M of EDTA. The difference between CB and CB1%CYS (Figure 6.1b and c) is attributed to introducing the thiol functional group, which serves as evidence of crosslinking. A slight shift in the wavenumber is observed, indicating the treatment's effect (Hamza et al., 2022). Figure 1d depicts the CB1%CYS after the adsorption process, where a reduction in the intensity of the amine and hydroxide groups (3273 and 2921 cm^{-1}) is observed. As previous studies have shown (Roshanfar et al., 2025; Yang et al., 2023, 2018), amine groups dominate Ni(II) and Co(II) adsorption via chelation, while hydroxyl groups support Mn(II) uptake through hydrogen bonding and electrostatic interactions. Also, in Figure 6.1e, the recovery of the -NH and -OH bands after desorption indicates regeneration of the active functional groups. The slight shift in the -SH band is attributable to the treatment. These observations confirm that the adsorption-desorption process restores the surface functional groups without causing permanent structural changes to the beads. It should be noted that FT-IR spectra after the adsorption-desorption cycle retain sulfur-related bands, confirming stable -SH crosslinking rather than physical entrapment.

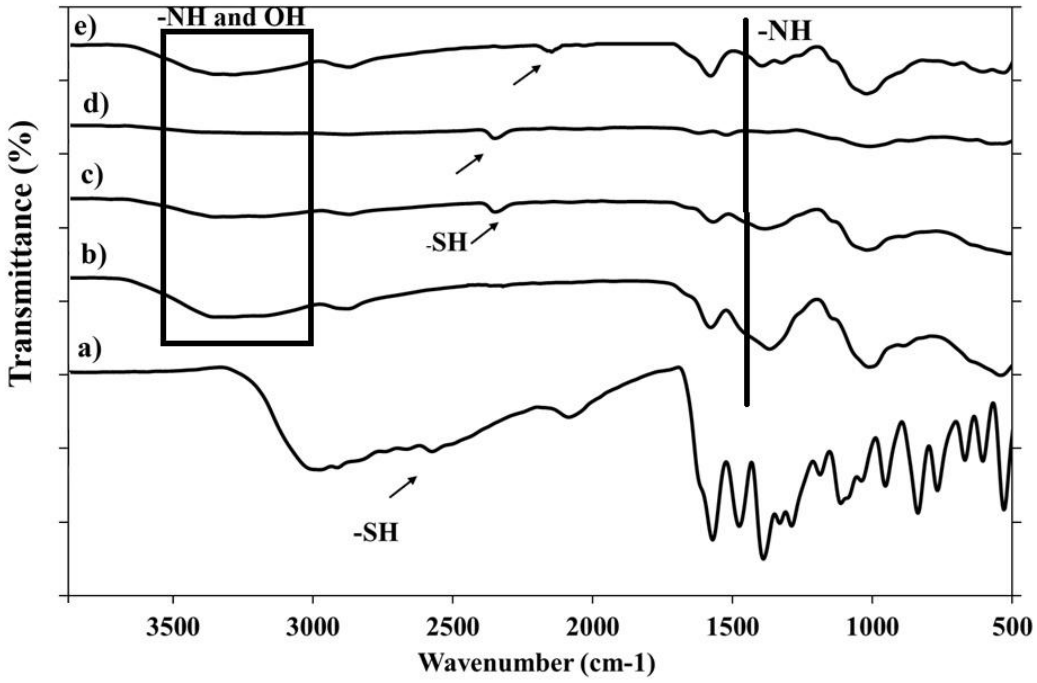

Figure 6.1. FT-IR spectra for a) L-CYS, b) CBs, c) CB1%CYS, d) CB1%CYS after adsorption, and e) after desorption with EDTA.

6.4.2. Crosslinked chitosan beads' optimization

The composition of the black mass and the leachate generated by the acidic leaching of black mass are reported in Table 6.1. These leaching results correspond to average (±SD) leaching recoveries of 98 ± 0.1% for Co(II), 98 ± 0.7% for Li, 91 ± 0.4% for Mn(II), and 89 ± 6.6% for Ni(II). This leachate solution was used for subsequent experiments (Roshanfar et al., 2025, 2024). The high cobalt content in the black mass is attributed to the dominance of LCO in the feedstock, as LCO is the primary cathode material across all battery types, with contributions from LMO in Li-polymer batteries and NMC in cellphone and laptop batteries.

Table 6.1.Chemical composition of black mass and leaching solution

Concentration	Li	Co	Mn	Ni
Black mass (wt.%)	6.28	50.06	2.36	3.37
Acidic leaching of black mass (mg/L ± SD)	4000 ± 123	30,000 ± 500	1336 ± 22	2156 ± 388

6.4.2.1. Effect of crosslinkers and optimization

To evaluate the effect of crosslinking and identify the more effective crosslinker, different amounts of Arg (12.5 wt.%, 25 wt.%, and 100 wt.%) and Cys (1 wt.%, 5 wt.%, 10 wt.%, 12.5 wt.%, 25 wt.%, and 100 wt.%) were added to a chitosan solution. CBs without crosslinkers also served as controls. Experiments were conducted under the optimized conditions reported by Roshanfar et al. (2025), using an adsorbent dose of 10 g/L (0.5 g in 50 mL), pH 4, a dilution factor of 40, and a contact time of 24 h. Adsorption efficiency (%), uptake (mg/g), weight loss (%), and final pH were measured (Table 6.2). Notably, Li-ion uptake remained below 1%, with no significant adsorption detected in most experiments, indicating effective selective separation of Li from Co(II), Mn(II), and Ni(II), similar to that observed for chitosan powder (Roshanfar et al., 2025). Control CBs exhibited weight loss exceeding 12% and final pH values exceeding 8, which could lead to metal-ion precipitation, rendering them impractical for large-scale applications. These results highlight the critical role of crosslinking in preserving the beads' structural integrity and ensuring consistent measurement of adsorption capacity and removal efficiency.

According to Table 6.2, beads crosslinked with Arg showed 81.29%, 27.02%, and 83.86% adsorption efficiencies and uptakes of 56.07, 1.29, and 3.71 mg/g for Co(II), Mn(II), and Ni(II), respectively, which were the results obtained for chitosan powder by Roshanfar et al. (2025). However, Arg-crosslinked beads had final pH values above 8.5 and an 8% weight loss, indicating partial dissolution and potential interference from metal precipitation. In contrast, Cys-crosslinked beads maintained their structural integrity, with no mass loss, and final pH values below 8, confirming the full incorporation of the crosslinker. The higher mass loss observed for the Arg-crosslinked beads is attributed to Arg's high inherent water solubility and positive charge, which

limit the extent of covalent bonding with chitosan and allow unreacted Arg to leach out during adsorption and rinsing. This is why the measured final pH levels were higher (more than 8.5). Previous studies have also demonstrated that the addition of Arg markedly enhances the hydrophilicity and dispersibility of chitosan, favoring leaching (Garcia et al., 2024; Luo et al., 2023). Conversely, Cys introduces disulfide bonds that form a covalently crosslinked, water-insoluble network, thereby preventing leaching (Uddin et al., 2024). Thus, Cys-crosslinked beads were selected. The results showed that increasing the Cys content from 1 wt.% to 100 wt.% did not significantly improve the adsorption performance. For example, the Co(II) adsorption efficiency for 1 wt.% of Cys to 10 wt.% of Cys increased from 77.17% ±0.78 to 80.79% ±0.19, and uptake from 55.10 ±0.56 to 59.86 ±0.14 mg/g, with no mass loss observed. Considering both cost-effectiveness and adsorption performance, 1 wt.% Cys (CS1%CYS) was selected as the optimal crosslinker dosage. This concentration was sufficient to enhance bead stability and maintain efficient metal uptake without the unnecessary material costs associated with higher crosslinker loadings. In addition, compared with the control (CB without crosslinker) and powder, the crosslinked beads showed no loss in performance. This indicates that the functional groups responsible for adsorption were not involved in the crosslinking process. Additionally, the swelling of the selected beads (CS1%CYS) was measured, as it is a crucial property of polymeric beads, reflecting their ability to absorb water, expand, and provide greater accessibility of active sites for metal binding (Babakhani and Sartaj, 2022). The degree of swelling of the beads in DI water was 98%, with a similar swelling observed in the sulfate-citrate medium. The particle size of the optimized beads was also evaluated using sieve analysis. The CS1% CYS beads exhibited a narrow particle-size distribution of 1.18–1.70 mm, corresponding to particles that passed through mesh #12 and were retained on mesh #16.

Table 6.2. The effect of different dosages of ARG and CYS on the adsorption efficiency (%), adsorption uptake (mg/g) of the beads at pH of 4 and dilution factor of 40

$\frac{\textbf{Adsorption rate (\%)}}{\textbf{Adsorption Uptake } (\frac{mg}{g})}$	Co	Mn	Ni	Final pH	Weight Lost (%)
Chitosan Powder (Roshanfar et al., 2025)	81.29± 1.48 56.07± 0.12	27.02 ± 2.14 1.29± 0.01	83.86 ± 0.32 3.71± 0.00	7.16	-
Control (CB without crosslinkers)	69.31±1.05 50.94±0.77	37.74±0.85 1.39±0.03	100.00±0.00 4.42±0.00	8.29	12
CS: Arg	78.27±2.65 65.20±2.21	41.28±3.31 1.63±0.13	87.56±0.19 4.77±0.01	8.68	8
CS: 25%Arg	73.93±2.19 61.58±1.91	32.81±2.59 1.30±0.10	84.34±0.06 4.59±0.00	8.53	8
CS: 12.5%Arg	76.16±0.96 63.44±0.08	37.17±1.25 1.47±0.14	83.98±0.45 4.57±0.02	8.51	8
CS: Cys	79.15±1.35 60.52±1.03	40.76±0.90 1.44±0.03	91.91±2.65 4.57±0.14	7.98	-
CS: 25%Cys	77.96±0.28 59.60±0.22	39.28±0.90 1.39±0.03	91.41±1.40 4.63±0.07	7.86	-
CS: 12.5 %Cys	76.04±0.75 58.13±0.57	33.92±3.09 1.20±0.03	87.61±1.19 4.44±0.06	7.87	-
CS:10%Cys	80.79±0.19 59.86±0.14	28.41±0.61 0.99±0.2	97.43±3.63 5.02±0.19	7.66	-
CS: 5%Cys	77.13±0.08 55.07±0.06	39.00±0.40 1.37±0.14	90.54±00.06 5.29±0.00	7.65	-
CS: 1%Cys	77.17±0.78 55.10±0.56	35.29±0.20 1.23±0.07	90.28±3.21 5.27±0.19	7.58	-

6.4.2.2. The effect of initial concentration and pH

In this study, as the real pregnant solution contained excessively high metal concentrations, the solution was diluted to adjust the initial concentrations for the adsorption experiments (×50, ×40, ×30, ×20, and ×10, corresponding to total metal concentrations of 750, 937, 1250, 1875, and 3749 mg/L, respectively). After dilution, the Co(II) concentrations were 600, 750, 1000, 1500, and 3000 mg/L, respectively. The adsorption behavior of Li, Co(II), Mn(II), and Ni(II) onto CS1%CYS beads was evaluated at room temperature for 24 hours, with a fixed adsorbent dosage of 10 g/L and an initial pH of 4, across a range of initial concentrations. Each experiment was performed in triplicate, and the results are presented as mean values (±SD). Figure 6.2 illustrates the removal efficiency and adsorption uptake of the critical metals onto CS1%CYS beads at different dilution conditions. Lithium exhibited negligible interaction with the adsorbent, remaining largely in solution across all experiments (removal <1%). As the dilution increased, corresponding to lower initial metal concentrations, the percentage removal improved, whereas the adsorption uptake decreased. Conversely, at higher concentrations, adsorption uptake increased until it reached a steady state, suggesting saturation of surface sites and attainment of equilibrium on the CS1%CYS adsorbent. This behavior highlights the influence of initial concentration on mass transfer dynamics and overall adsorption performance (Balakrishnan et al., 2023; Liu et al., 2022; Syeda et al., 2024; Vakili et al., 2019).

As the dilution factor increased from 10 to 40, the removal efficiency rose from approximately 45% to 77% for Co(II), from 25% to 36% for Mn(II), and from 71% to 94% for Ni(II). Beyond a dilution factor of 40, only marginal improvements were observed in all cases. Conversely, adsorption uptake decreased as the dilution factor increased from 10 to 50, with Co(II) uptake dropping from 127.86 mg/g to 43.63 mg/g, Mn(II) uptake from 3.58 mg/g to 1.05 mg/g, and Ni(II) uptake from 13.83 mg/g to 3.66 mg/g. To balance strong adsorption performance with efficient water use (an important aspect of sustainable recycling given potential future water scarcity), a dilution factor of 30 was selected. At this dilution factor, the adsorption efficiencies and uptakes for Co(II), Mn(II), and Ni(II) are 69.55% ± 0.77, 31.18% ± 0.63, and 91.62% ± 0.88 for Co(II), Mn(II), and Ni(II), as well as 65.56 ± 0.71 mg/g (1.11 mmol/g), 1.47 ± .0.03 mg/g (0.03 mmol/g), and 5.92 ± 0.11 mg/g (0.10 mmol/g), respectively. At this dilution factor, Co(II) and Ni(II)

exhibited notably high adsorption efficiencies of approximately 70% and 92%, respectively, whereas Mn(II) showed a moderate efficiency of approximately 31%. This disparity results from the stronger affinity of the amine and hydroxyl functional groups on CS1%CYS for Co(II) and Ni(II) than for Mn(II) (Roshanfar et al., 2025). Under the same conditions, the CBs without any crosslinkers exhibited adsorption uptakes of 63.87 ± 2.45 mg/g (1.08 mmol/g), 1.59 ± 0.29 mg/g (0.03 mmol/g), and 5.27 ± 0.29 mg/g (0.09 mmol/g). Compared to CBs without crosslinkers, CS1%CYS showed a 2.65% increase in Co(II) adsorption uptake, a 7.55% decrease in Mn(II) adsorption uptake, and a 12.34% increase in Ni(II) adsorption uptake. These results indicate that the use of L-cystine effectively maintained adsorption performance while improving the beads' structural stability and integrity. The reported data for CBs without crosslinkers were adjusted to account for the amounts of metals that precipitated. The dilution factor of 30 corresponds to metal ion concentrations of approximately 1000 mg/L for Co, 133.33 mg/L for Li, 44.53 mg/L for Mn, and 71.87 mg/L for Ni, providing a practical compromise between adsorption efficiency and resource conservation.

Solution pH also strongly influences metal adsorption by altering both the adsorbent's surface charge and the chemical forms of metal ions in solution. Experiments were conducted under room temperature for 24 hours, with an adsorbent dosage of 0.5 g per 50 mL, and a dilution factor of 30 using CS1%CYS. According to Conte and Gómez (2024), Co(II), Mn(II), and Ni(II) tend to precipitate as hydroxides at pH levels above 8. To avoid this, adsorption tests were performed at initial pH values of 2 (unadjusted), 4, and 5, yielding final pH values of 5.4, 7.6, and 8.0, respectively (Figure S1). Increasing the initial pH from 2 to 4 significantly enhanced both adsorption efficiency and uptake, whereas further increasing the pH to 5 showed no significant improvement. Therefore, balancing performance with minimal chemical input for pH adjustment indicates that pH 4 would be a better condition. Within the first five minutes of contact, the solution pH increased quickly toward neutrality. This shift suggests that reduced proton availability at moderate pH lowers competition at active sites, enhancing metal binding. At low pH, however, excess H^+ ions strongly compete with metal ions, limiting adsorption, whereas greater ionic competition under acidic conditions further suppresses selectivity (Babakhani and Sartaj, 2022b). After adsorption of Co(II) and Ni(II) and partial removal of Mn(II), the remaining Mn can be removed as described in our previous study: either by raising the pH to around 12 or by dropwise

addition of $KMnO_4$. In contrast, Li remains in solution and can subsequently be converted to Li carbonate (Li_2CO_3) by reacting with a saturated sodium carbonate (Na_2CO_3) solution and heating the mixture to 90 °C to evaporate excess water (Roshanfar et al., 2025).

Several previous studies have also reported the critical metal recovery using various adsorbent systems, though typically under less challenging or less selective conditions. Promkatkaew et al. (2023) investigated chitosan/TPP nanoparticles at alkaline pH (7-9) and low metal concentrations (approximately 100 ppm), achieving high removal efficiencies, but did not address selectivity in multi-metal battery systems. Sharifi et al. (2023) studied a Fe_3O_4-chitosan nanocomposite at pH 6 using synthetic solutions, reporting high adsorption capacities for Co(II) and Ni(II), but did not evaluate lithium behavior or competitive adsorption. In another study, selective adsorption of Co(II) and Ni(II) from a synthetic battery solution at near-neutral pH, with minimal lithium loss, was demonstrated; however, Mn was not considered, and the system relied on inorganic materials (T. Wang et al., 2023). EDTA-functionalized magnetic biochar was employed across a wide pH range and demonstrated good reusability, although experiments were conducted at relatively low initial concentrations (Park and Choi, 2023). Sun et al. (2024) evaluated grafted polyimide fibers using an actual battery solution, achieving stable performance over multiple cycles but requiring elevated temperatures and without explicit lithium selectivity. Complete Co(II) removal using zeolites at low concentrations was reported by Díez et al. (Díez et al., 2023), though significant co-removal of Li limited separation efficiency. In comparison, the present study demonstrates selective recovery of Co(II), Ni(II), and Mn(II) from a real LIB-derived multi-metal solution under acidic conditions (pH 4) and at high metal concentrations, while fully retaining lithium in solution. The use of green L-cystine-crosslinked chitosan beads enables simultaneous selectivity and stability without relying on inorganic supports, elevated temperatures, or idealized synthetic systems, underscoring the approach's greater relevance for sustainable and practical lithium-ion battery recycling.

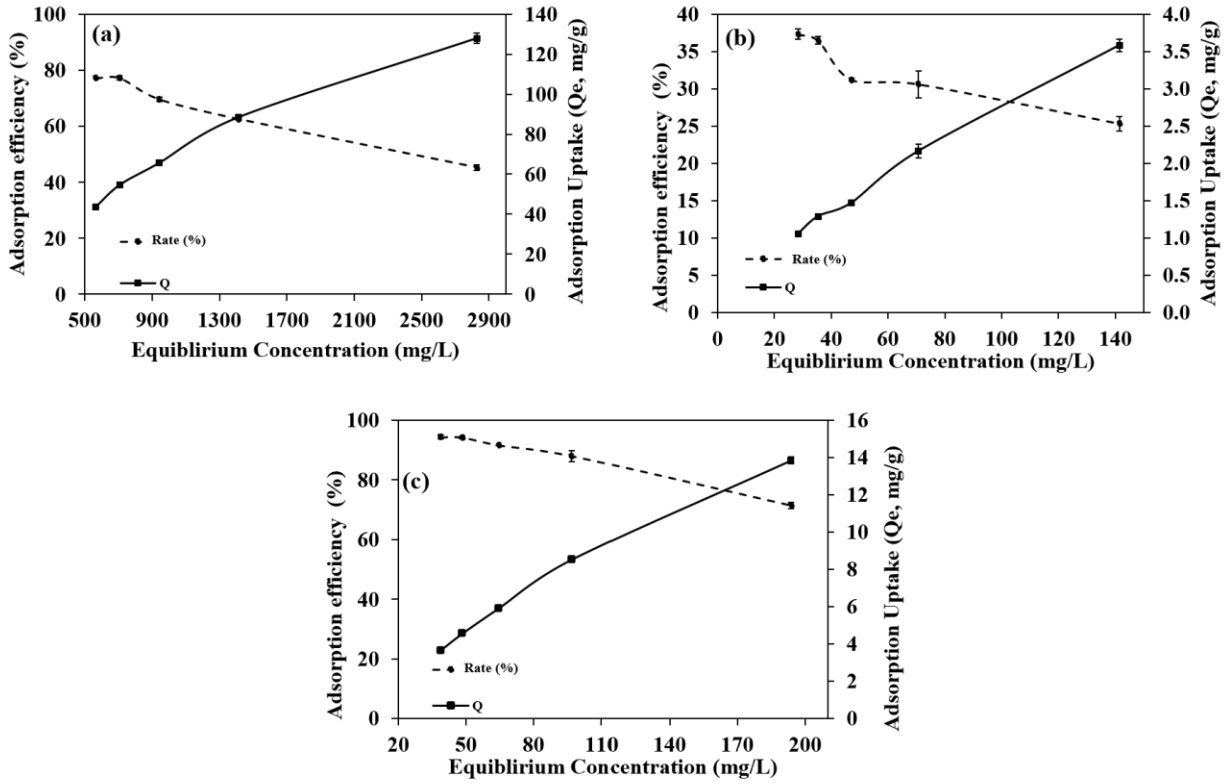

Figure 6.2. Metal ion adsorption efficiency (% ±SD) and adsorption uptake (mg/g ±SD) at various dilution factors (different initial concentrations) were measured at room temperature for 24 hours, using an adsorbent dosage of 10 g/L of CS1%CYS and an initial pH of 4 for a) Co(II), b) Mn(II), and c) Ni(II).

Solution pH also strongly influences metal adsorption by altering both the adsorbent's surface charge and the chemical forms of metal ions in solution. In this section, experiments were conducted under room temperature for 24 hours, with an adsorbent dosage of 0.5 g per 50 mL, and a dilution factor of 30 using CS1%CYS (Figure 6.3). According to Conte and Gómez (2024), Co(II), Mn(II), and Ni(II) tend to precipitate as hydroxides at pH levels above 8. To avoid this, adsorption tests were performed at initial pH values of 2 (unadjusted), 4, and 5, yielding final pH values of 5.4, 7.61, and 7.98, respectively. Increasing the initial pH from 2 to 4 significantly enhanced both the adsorption efficiency and uptake, whereas a further increase to pH 5 showed no significant improvement. Therefore, pH 4 was selected as the optimal condition, balancing performance with minimal chemical input for pH adjustment. Within the first five minutes of

contact, the solution pH increased quickly toward neutrality. This shift suggests that reduced proton availability at moderate pH lowers competition at active sites, enhancing metal binding. At low pH, however, excess H^+ ions compete strongly with metal ions, limiting adsorption, while higher ionic competition under acidic conditions further suppresses selectivity (Babakhani and Sartaj, 2022a). After adsorption of Co(II) and Ni(II) and partial removal of Mn(II), the remaining Mn can be removed, as reported in our previous study, either by raising the pH to around 12 or by dropwise addition of $KMnO_4$. In contrast, Li remains in solution and can subsequently be converted to Li carbonate (Li_2CO_3) by reacting with saturated sodium carbonate (Na_2CO_3) and heating the solution to 90 °C to evaporate the excess water (Roshanfar et al., 2025).

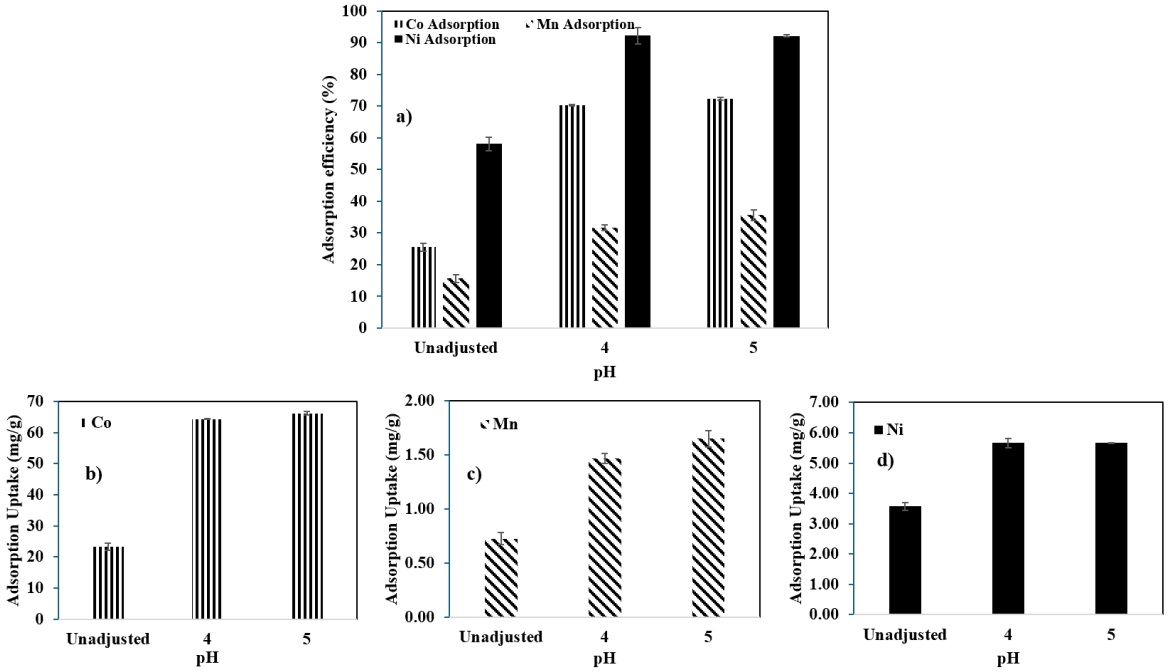

Figure 6.3. Effect of pH on a) the adsorption efficiency (% ±SD) and the adsorption uptake (mg/g ±SD) of CS1%CYS of b) Co (II), c) Mn (II), and d) Ni (II) under room temperature in 24 h, an adsorbent dosage of 0.5 g per 50 mL, and a dilution factor of 30.

6.4.3. Statistical Analysis and Modeling

In the statistical analysis and modeling stage, Mn(II) was excluded because its adsorption was consistently low. In contrast to Co(II) and Ni(II), most removal in the proposed process occurred via precipitation rather than adsorption. From a process design perspective, Mn(II) is also less economically valuable and less strategically important. Therefore, the analysis was focused on optimizing Co(II) and Ni(II) removal. The statistical analysis (Table 6.3) confirms that the constructed models are robust. All four models display high F-values and statistically significant p-values ($p < 0.05$), demonstrating that dilution factor (DF) and pH significantly influence the measured responses. The lack-of-fit terms are not significant for any of the models, indicating that the models fit the experimental data well. Additionally, the R^2 values (0.89–0.99) indicate strong correlation between predicted and observed values, ensuring reliable predictive power (Anderson and Whitcomb, 2017).

Based on the fitted response surfaces, the coded model equations for the four responses are:

$$Q\ (Co) = 52.5 - 40.47A + 24.01B + 26.34A^2 \quad (6\text{-}11)$$

$$Recovery\ (Co) = 56.02 + 15.69A + 25.79B \quad (6\text{-}12)$$

$$\frac{1}{Q}\ (Ni) = 0.2008 + 0.1008A - 0.0610B \quad (6\text{-}13)$$

$$Recovery\ (Ni) = 88.38 + 10.42A + 17.03B - 9.47A^2 - 13.24B^2 \quad (6\text{-}14)$$

where A and B are the coded values of the dilution factor and pH.

The 3D response-surface plots (Figure 6.4(a–d)) show how DF and pH affect adsorption uptake and recovery efficiencies. For Co(II) adsorption uptake (Figure 6.4a), the response surface indicates that higher pH significantly increases Q (Co(II)), with the maximum at a DF of 10 and pH of 5. Co(II) recovery, however, behaves differently (Figure 6.4b), and the optimal point shifts to a DF of 50 and pH of 5. For Ni(II), the model predicts that the highest adsorption uptake (Figure 6.4c) occurs at a DF of 10 and a pH of 5, while the maximum Ni(II) recovery (Figure 6.4d) occurs at a DF of approximately 40 and a pH of 5. These results collectively show that both DF and pH have strong, distinct effects on the behavior of Co(II) and Ni(II), and that their individual optima do not match. Although each individual response has a distinct optimum point, process design

requires a condition that maximizes them simultaneously. Thus, multi-response desirability analysis (Figure 6.4e) was employed to integrate all responses into a single index ranging from 0 (undesirable) to 1 (fully optimal). The desirability map indicates that a DF of 30 and a pH of 4 provide the optimal balance for Co(II) and Ni(II) adsorption uptake and recovery. Under these conditions, the desirability plot (Figure 6.4) shows that the selected point falls within the high-desirability area, confirming that these operational conditions deliver an effective balance of adsorption uptake, recovery rate, and chemical use. As was stated before, a lower pH requires less chemical adjustment, with no significant improvement in adsorption uptake and recovery.

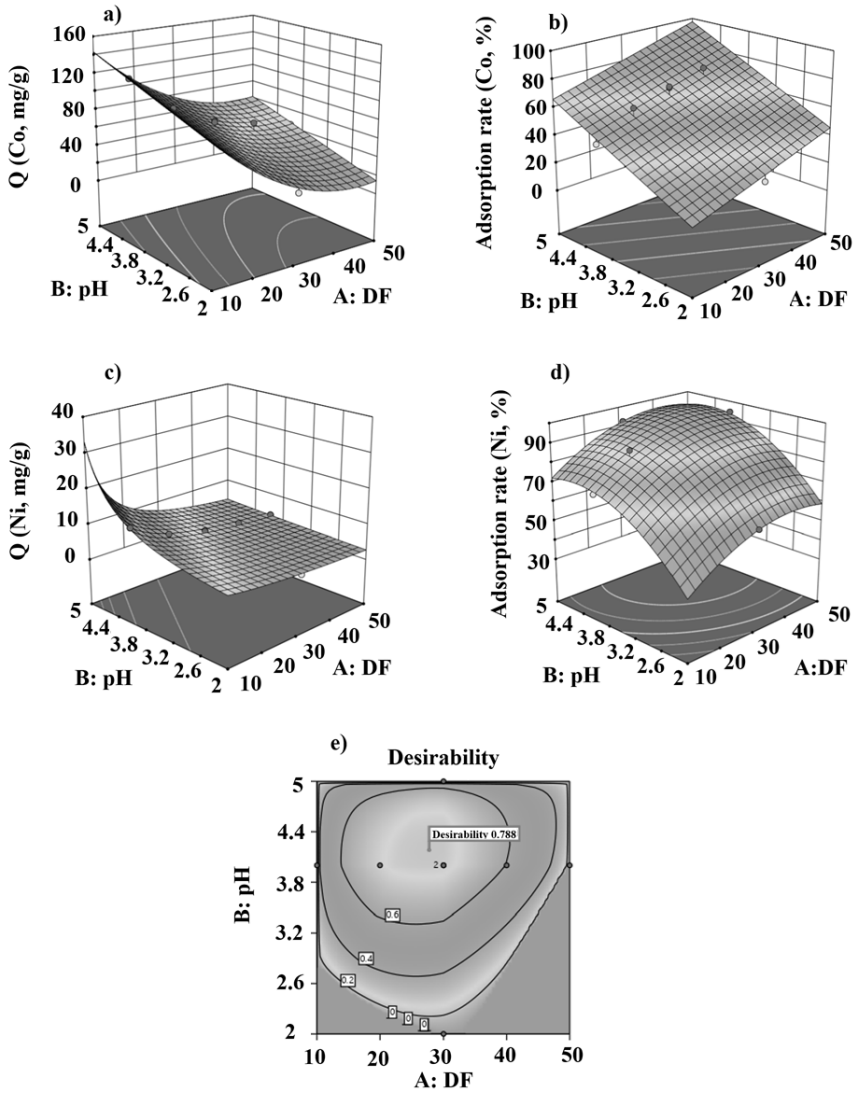

Figure 6.4. 3D diagrams and the effect of pH and dilution factor (DF) on a) adsorption uptake of Co(II), b) recovery efficiency of Co(II), c) adsorption uptake of Ni(II), d) recovery efficiency of Ni(II), and e) the desirability of the optimum condition.

Table 6.3. ANOVA table of the models

Q (Co) (mg/g)				Co Recovery (%)			
	F-value	**p-value**			**F-value**	**p-value**	
Model	36.04	0.0024	significant	**Model**	20.73	0.0038	significant
Lack of Fit	111.89	0.0694	not significant	**Lack of Fit**	184.94	0.0051	not significant
R^2	0.96			**R^2**	0.89		
Q (Ni) (mg/g)				**Ni Recovery (%)**			
Model	36.89	0.0010	significant	**Model**	66.09	0.0030	significant
Lack of Fit	19.35	0.1687	not significant	**Lack of Fit**	35.38	0.1180	not significant
R^2	0.94			**R^2**	0.99		

6.4.4. Adsorption isotherm results

To evaluate the adsorption behavior of metal ions on CS1%CYS beads, the equilibrium data were analyzed using Langmuir, Freundlich, and Toth isotherm models (Figure 6.5). These models provide complementary insights into adsorption capacity, surface heterogeneity, and binding affinity. The corresponding model constants and statistical indicators, including the coefficient of determination (R^2), sum of squared residuals (SSR), and mean squared error (MSE), are presented in Table 4. The R^2 value indicates the proportion of variance in the experimental data accounted for by each model; higher values indicate stronger correlations and greater model reliability (Anderson & Whitcomb, 2017; Roshanfar et al., 2019). The Langmuir model assumes monolayer adsorption on a homogeneous surface and provides an estimate of the maximum adsorption capacity (q_m). In contrast, the Freundlich model describes multilayer adsorption on non-uniform surfaces, where 1/n values between 0 and 1 signify favorable sorption conditions. The Toth model extends these concepts by accounting for pronounced surface heterogeneity and incorporates an adjustable exponent (t) that characterizes deviations from ideal adsorption behavior across concentration ranges (Eissa et al., 2026).

As shown in Figure 6.5 and Table 6.4, all three isotherm models provide an adequate description of the experimental data. Among them, the Toth model demonstrated the highest agreement with observed results, owing to its additional parameter that accounts for variations in surface heterogeneity. Among the two-parameter models, the Freundlich model provided a slightly better fit for all three metal ions, indicating that adsorption occurs primarily via multilayer interactions on non-uniform surfaces. The 1/n values below unity further confirm that the sorption of Co(II), Mn(II), and Ni(II) proceeds favorably (Al-Ghouti and Da'ana, 2020).

The Langmuir model, which also showed satisfactory correlation with the experimental data, was employed to estimate the theoretical maximum adsorption capacities. The calculated q_m values were 153.38 mg/g (2.6 mmol/g) for Co(II), 7.73 mg/g (0.14 mmol/g) for Mn(II), and 15.57 mg/g (0.27 mmol/g) for Ni(II). Compared with unmodified chitosan powder, which exhibits Langmuir capacities of 110 mg/g (1.86 mmol/g) for Co(II) and 20 mg/g (0.37 mmol/g) for Ni(II), the CS1%CYS beads achieved approximately a 39% increase in Co(II) adsorption capacity. In contrast, the Ni(II) capacity decreased by about 22%. Compared to the powder form, CS1%CYS's Mn(II) adsorption is favorable, resulting in a higher maximum adsorption capacity (Roshanfar et al., 2025). This phenomenon can be attributed to the incorporation of Cys, which introduces thiol and carboxylate groups that interact with the native amines and hydroxyl groups of chitosan. Consequently, increasing the number of active sites enhances adsorption capacity (Al-Ghamdi et al., 2022; Grigoraș et al., 2024; Taha et al., 2025). In this context, the increase in active sites reflects a synergistic improvement in functional diversity and accessibility rather than a quantified rise in site density. This obtained adsorption capacity outperformed several previously reported adsorbents, including Cyanex 272-blended PVDF beads (14.1 mg/g) (Xiao et al., 2025), magnetic graphene oxide (29.7 mg/g) (Iqbal et al., 2022), and physicochemically activated mesoporous carbon (22.8 mg/g) (Conte and Gómez, 2024) for Co(II) recovery from spent LIBs.

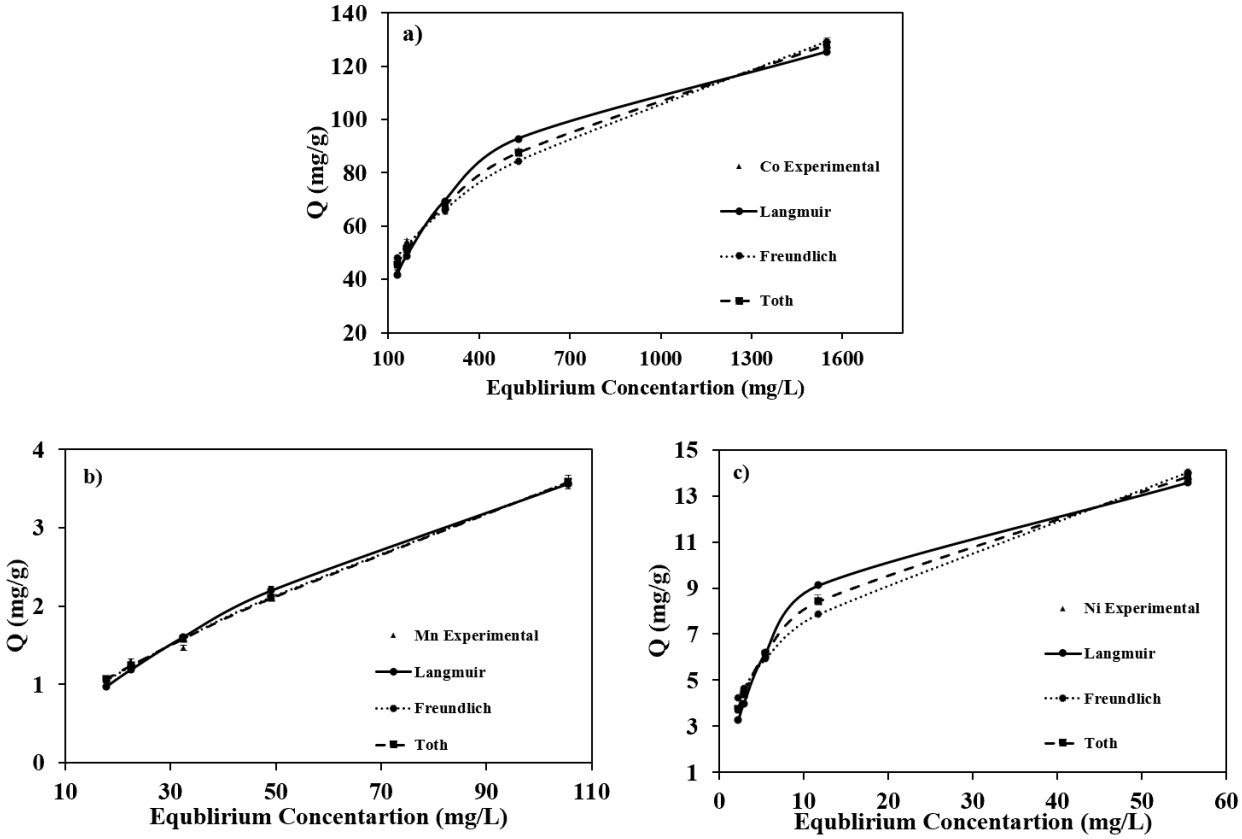

Figure 6.5. Adsorption isotherms and experimental data for a) Co(II), b) Mn(II), and c) Ni(II).

Table 6.4. Calculated adsorption isotherm parameters

Two-Parameters				
Isotherm model	**Parameter**	**Co (II)**	**Mn (II)**	**Ni (II)**
Langmuir	K_L (L/mg)	2.9E-3	8.1E-3	1.2E-1
	q_m (mg/g)	153.38	7.73	15.57
	R-squared	0.991	0.993	0.990
	SSR	262.78	0.17	4.50
	MSE	17.51	0.01	0.30
Freundlich	k_F	6.95	0.14	3.16
	n_F	2.51	1.45	2.70
	R-squared	0.994	0.995	0.990

	SSR	161.17	0.12	3.60
	MSE	10.75	0.00	0.24
Three-Parameters				
Toth	K_T	15.05	0.12	5.03
	α	78.58	-4.35	2.05
	t	1.42	3.57	1.35
	R-squared	0.997	0.995	0.996
	SSR	91.44	0.12	1.64
	MSE	6.10	0.00	0.11

6.4.5. Adsorption kinetics results

Kinetic evaluation is crucial for elucidating adsorption mechanisms, identifying rate-controlling steps, determining equilibrium time, and assessing overall process efficiency, as well as evaluating the stability and practical applicability of the adsorbent (Mohanta and Ahmaruzzaman, 2018; Rahaman et al., 2024). The experimental data were collected at various contact times (5 min to 24 h) under optimized conditions (dilution factor of 30, initial pH 4, room temperature (293 K), and an adsorbent dosage of 10 g/L) (Figure 6.6). The data were modeled using pseudo-first-order and pseudo-second-order kinetic equations. Compared to chitosan powder (Roshanfar et al., 2025), where adsorption occurred relatively quickly (within 8 h for Co(II), 24 h for Mn(II), and 3 h for Ni(II)), the adsorption onto CS1%CYS beads proceeded more gradually, reaching equilibrium at approximately 16 hours for Co(II), 3 hours for Mn(II), and 6 hours for Ni(II). Notably, within the first 3 hours, 46% of Co(II), 32% of Mn(II), and 88% of Ni(II) were adsorbed, indicating a high initial availability of active sites that declined as adsorption approached saturation (Babakhani and Sartaj, 2022). For chitosan powder, the adsorption equilibrium was reached after 8 h for Co(II), 24 h for Mn(II), and 3 h for Ni(II). Co(II) and Ni(II) exhibited rapid initial kinetics (approximately 46% and 66% uptake within the first 5 minutes) (Roshanfar et al., 2025). This slower adsorption on CS1%CYS beads compared with powder can be attributed to their longer diffusion paths, lower surface-area-to-volume ratio, and reduced porosity due to crosslinking, all of which impose additional mass-transfer resistance (Elzahar and Bassyouni, 2023; Watwe and Kulkarni, 2021). Table 6.5 summarizes the kinetic parameters for the adsorption of Co(II), Mn(II), and Ni(II) onto

CS1%CYS. The high R^2 values confirm that the pseudo-second-order model best describes the data, with calculated q_e values of 69.58 mg/g (Co) (1.18 mmol/g), 1.75 mg/g (Mn) (0.03 mmol/g), and 5.51 mg/g (Ni) (0.09 mmol/g) closely matching experimental results. This indicates that the adsorption efficiency is governed by site availability and overall uptake kinetics, rather than by simple first-order mass transfer (Ding et al., 2025; Mohammed et al., 2020).

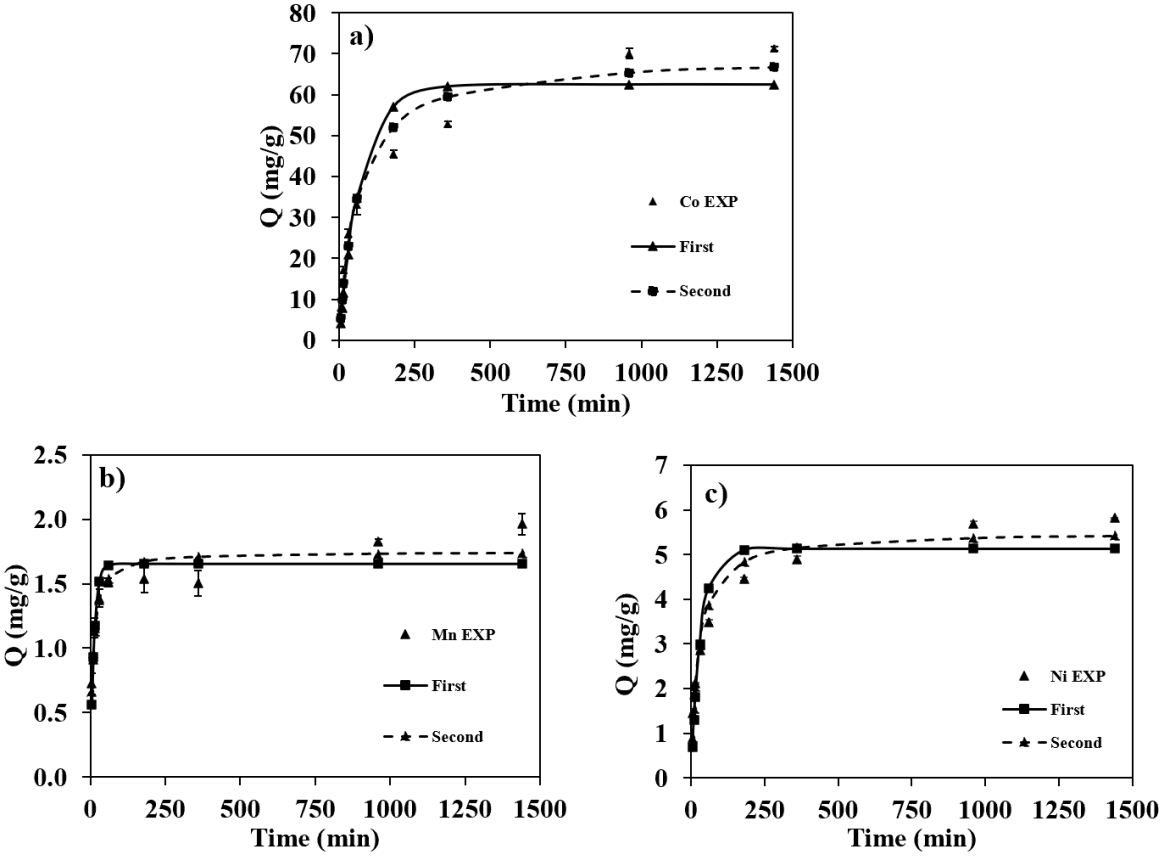

Figure 6.6. The experimental data at different time intervals (5 min–24h) as well as the pseudo-first-order and pseudo-second-order models for a) Co(II), b) Mn(II), and c) Ni(II).

Table 6.5. Kinetic parameters of adsorption of Co(II), Mn(II), and Ni(II) onto CS1%CYS

	Co	Mn	Ni
Pseudo-First-Order Model			
qe (mg/g)	62.40	1.65	5.13
k_1 (1/min)	1.35E-02	8.23E-02	2.92E-02
R-squared	0.96	0.91	0.95
Pseudo-Second-Order Model			
k_2 (g/mg/min)	2.36E-04	6.98E-02	7.11E-03
qe (mg/g)	69.58	1.75	5.51
R-squared	0.98	0.95	0.98

6.4.6. Thermodynamics Study Results

Temperature is a key parameter affecting both adsorption kinetics and equilibrium capacity; therefore, its influence on the adsorption process was examined. Table 6.6 presents the experimental uptake data at 273 K and 293 K under optimized conditions (dilution factor 30, initial pH 4, 24 h contact time, 10 g/L adsorbent). Adsorption of Co(II), Mn(II), and Ni(II) showed only a slight increase with increasing temperature (Co(II) from 65 % ± 1.19 to 70.36 % ± 0.20 and Ni(II) from 83.89 % ± 3.13 to 92.24 % ± 2.51), demonstrating a minor thermal effect. This modest enhancement results from faster ion diffusion into pores, greater availability of binding sites, and improved metal-CS1%CYS complexation at higher temperatures (Liu et al., 2022). At 293 K, Co(II) and Ni(II) adsorption onto CS1%CYS is thermodynamically spontaneous, with $\Delta G°$ values of –22.67 and –54.03 kJ/mol, respectively, whereas Mn(II) adsorption ($\Delta G° = +5.86$ kJ/mol) is non-spontaneous. All three adsorption processes are endothermic, as shown by the positive $\Delta H°$ values of +11.37, +11.94, and +18.88 kJ/mol for Co(II), Mn(II), and Ni(II), respectively, and are accompanied by increased randomness at the adsorbent-solution interface, as indicated by the positive $\Delta S°$ values (+46.89, +38.07, and +82.87 J/mol·K). Since these $\Delta H°$ values fall within the typical range for physisorption (2–40 kJ/mol) rather than chemisorption (>40 kJ/mol) (Egbosiuba et al., 2020), the adsorption is mainly driven by weak electrostatic interactions, suggesting that the process is reversible and favored at higher temperatures.

Although the pseudo-second-order model provided the best fit to the kinetic data, the relatively low enthalpy changes indicate that adsorption is primarily governed by physical interactions. This apparent discrepancy can be explained by a multistep adsorption mechanism, in which rapid electrostatic attraction to surface sites is followed by slower intraparticle diffusion and site reorganization within the crosslinked bead matrix, processes that ultimately control the overall adsorption efficiency.

Among the metals, Ni(II) exhibits the strongest thermodynamic driving force for adsorption uptake, followed by Co(II), while Mn(II) uptake is thermodynamically unfavorable under these conditions. As can be seen, Co(II) and Ni(II) display similarly high adsorption (attributable to their comparable ionic radii and strong binding to amine groups), whereas Mn(II) shows lower uptake due to its preferential interaction with the hydroxyl functional group, highlighting the selectivity and efficacy of this low-energy method (Yang et al., 2023, 2018). Thermodynamic data further confirm that adsorption proceeds readily at ambient temperature, underscoring its minimal energy requirement (Liu et al., 2022).

Table 6.6. Calculated thermodynamic parameters for Co(II), Mn (II), and Ni (II) adsorption onto CS1%CYS

Temperature (K)	**ΔG° (kJ/mol)**		**ΔH° (kJ/mol)**	**ΔS° (J/mol K)**
	293	277		
Co(II)	-2.37	-1.62	11.37	46.89
Mn(II)	0.79	1.40	11.94	38.07
Ni(II)	-5.40	-4.010	18.88	82.87

6.4.7. Desorption Study

Desorption studies are crucial for regenerating adsorbents, given the high costs associated with production and disposal. Despite the challenges posed by strong adsorbate binding, it enables metal recovery and adsorbent reuse, making it vital from both environmental and economic perspectives.

In this study, DI water and 0.01 M H_2SO_4 were initially used for desorption. No noticeable metal desorption was observed with DI water, even after a week. For 0.01 M H_2SO_4, although complete metal removal was achieved, the acidic medium damaged the beads, preventing their reuse. To preserve bead integrity, EDTA (effective at approximately pH 9) was tested instead (Vakili et al., 2019). Each adsorption was carried out for 24 hours, followed by a 24-hour desorption period. As shown in Figure 6.7(a–d), both 0.1 M and 0.5 M EDTA effectively desorbed metals over three cycles with efficiencies exceeding 92%. To minimize chemical use, 0.1 M EDTA was selected for continued testing. The drop in adsorption capacity was minimal (5% from the first to the second cycle and 1% from the second to the third), indicating good bead stability and reusability. As noted in Section 3.1.2, FT-IR analysis after desorption (Figure 6.1e) confirmed that EDTA effectively restored the active functional groups, thereby supporting the observed high desorption efficiencies and consistent performance across successive cycles. In another experiment, for the third cycle, the same EDTA solution from the second cycle (which already contained desorbed metals) was reused. The reused EDTA solution remained effective but slowed desorption, requiring 48 hours rather than 24.

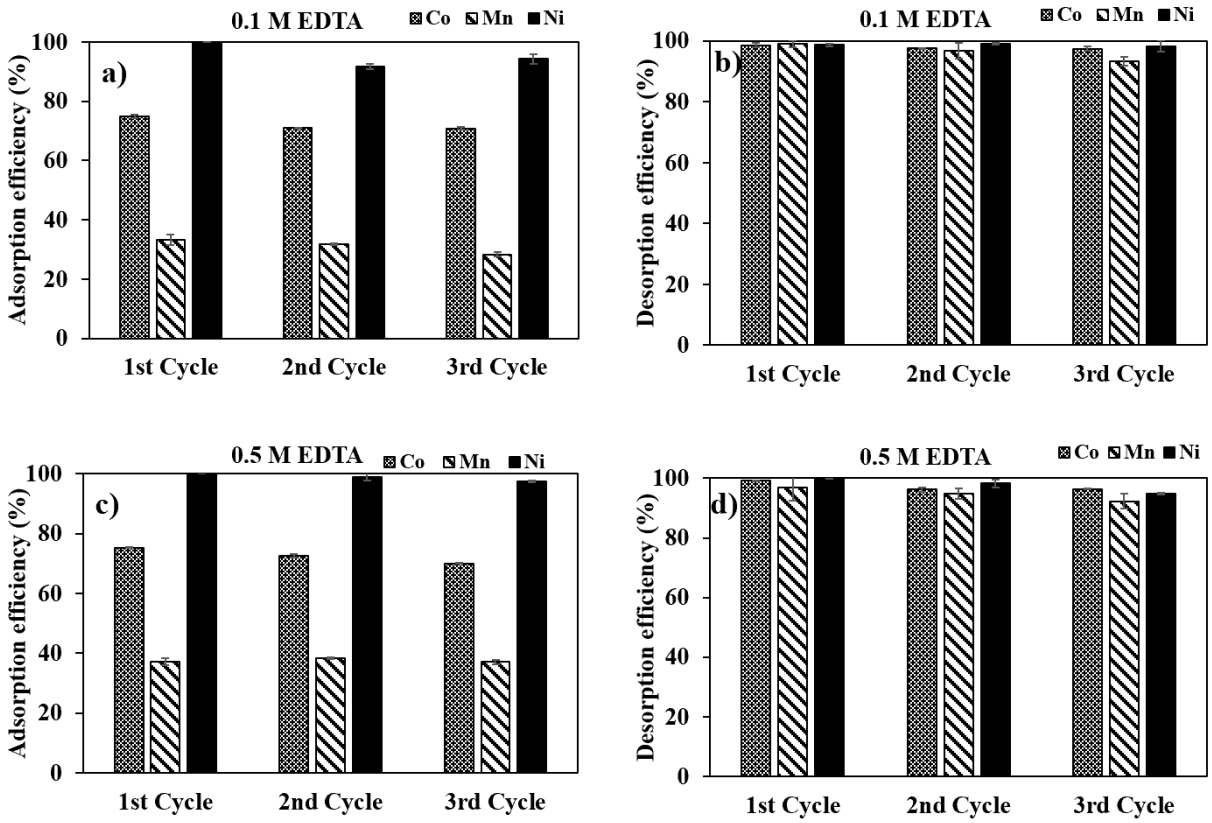

Figure 6.7. a) and b) adsorption and desorption cycles using 0.1 M EDTA, as well as c) and d) adsorption and desorption cycles using 0.5 M EDTA.

6.4.8. Proposed Process Flowsheet

Figure 6.8 illustrates the integrated flowsheet developed in this study for selective metal recovery from spent LIB black mass. The process combines sulfate-citrate leaching with our optimized CS1%CYS beads to achieve highly selective adsorption of Co, Ni, and Mn while keeping Li in solution. Transition metals (Co, Ni, and Mn) are then recovered through EDTA desorption, and the purified Li stream is converted to Li_2CO_3 via standard carbonate precipitation. This combined approach provides a simple, solvent-free, and environmentally friendly route for multi-metal separation and lithium recovery, demonstrating the practical potential of biosorbent bead technology in LIB recycling.

It should be noted that the proposed bead-based system involves deliberate trade-offs between adsorption kinetics, binding mechanism, and process applicability. Compared with chitosan

powder, bead formation leads to slower adsorption kinetics due to internal diffusion limitations within the crosslinked structure; however, high adsorption performance is preserved. Mechanistically, crosslinking through -SH groups rather than amine functionalities maintain the availability of -NH and -OH functional groups for metal binding, resulting in adsorption performance comparable to that of powder chitosan despite bead formation. This trade-off favors selectivity, mechanical stability, and reusability over rapid kinetics, thereby enhancing the system's suitability for practical, scalable lithium-ion battery recycling applications.

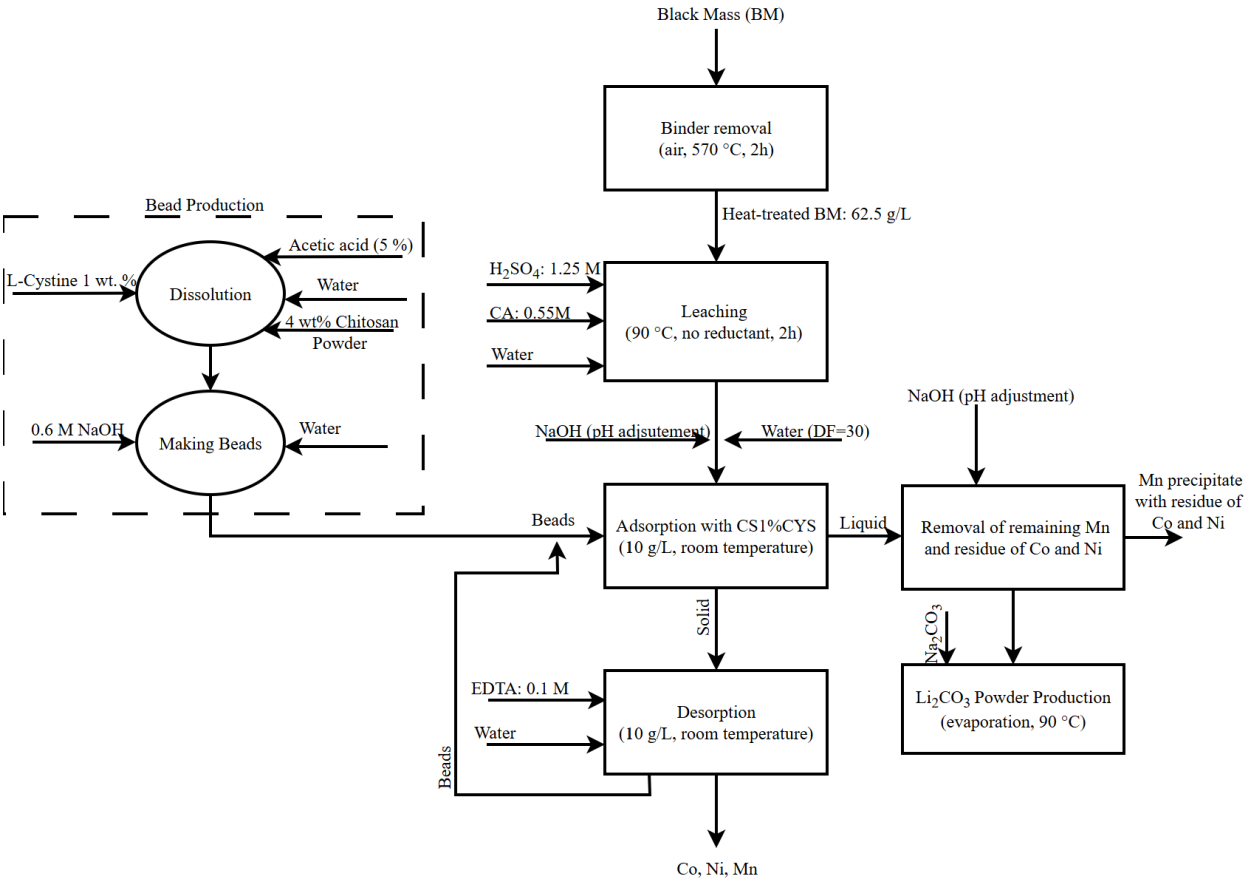

Figure 6.8. Schematic diagram of the proposed flowsheet for Li recovery from waste LIBs using CS1%CYS.

6.5. Conclusions

This study presents a sustainable and selective strategy for recovering critical metals from spent lithium-ion battery cathode materials using chitosan beads crosslinked with green, bio-based amino-acid crosslinkers. The bead form was selected to overcome the limitations of chitosan powder, including clogging, high pressure drop, and poor hydrodynamic behavior, which restrict its use in continuous and scalable separation systems. Two eco-friendly crosslinkers, L-cystine and L-arginine, were thoroughly examined to determine the most effective chemistry for selective metal separation and maintaining bead stability. The results confirm that L-cystine-crosslinked chitosan beads are viable biosorbents that selectively remove Co(II), Ni(II), and Mn(II), while leaving Li in solution, thereby enabling downstream lithium recovery without additional separation steps. Importantly, bead integrity was preserved with no observable mass loss, highlighting their potential for repeated use.

Crosslinking via its thiol group enabled high selectivity in separating Co(II), Mn(II), and Ni(II) in a sulfate-citrate medium. The optimal crosslinked beads (CS1%CYS), which contained 1% L-cystine, exhibited the best performance at a dilution of 30, pH 4, and an adsorbent dosage of 10 g/L. Adsorption efficiencies under optimal conditions were 69.55% ± 0.77 for Co(II), 31.18% ± 0.63 for Mn(II), and 91.62% ± 0.88 for Ni(II), with corresponding adsorption uptakes of 65.56 ± 0.71 mg/g (Co: 1.11 mmol/g), 1.47 ± 0.03 mg/g (0.03 mmol/g), and 5.92 ± 0.11 mg/g (0.1 mmol/g), respectively. These values are comparable to those obtained with chitosan powder, even in the presence of bead formation, whereas Li remained unadsorbed, confirming the process's high selectivity.

Kinetic analysis showed that, compared with chitosan powder, the bead form resulted in slower adsorption efficiencies, with equilibrium reached at 16 h for Co(II), 3 h for Mn(II), and 6 h for Ni(II); however, substantial uptake occurred within the first 3 h, particularly for Ni(II). Thermodynamic evaluation indicated that adsorption was endothermic for all metals, with Ni(II) exhibiting the strongest driving force, followed by Co(II), whereas Mn(II) adsorption was less favorable. Effective regeneration using 0.1 M EDTA over three adsorption-desorption cycles, with minimal capacity loss (5% from the first to second cycle and 1% from the second to third), further confirmed the stability and reusability of the beads. In addition, FT-IR analysis confirmed that -

NH and -OH functional groups were primarily responsible for metal adsorption, and their restoration after EDTA desorption demonstrated effective regeneration of active sites, supporting the observed multicycle reusability. Therefore, these findings highlight the potential of L-cystine-crosslinked chitosan beads as a robust, selective, and reusable biosorbent for sustainable battery recycling. The proposed approach offers a practical pathway toward waste-derived, low-impact separation technologies that align with circular economy principles and support the efficient recovery of critical metals from end-of-life lithium-ion batteries.

6.6. Acknowledgments

The authors gratefully acknowledge and sincerely appreciate the financial support from the Ontario Center of Innovation and ERS-International Company for this project (OCI application number: 36895).

6.7. References

The references are merged with those of the other chapters and listed at the end of the thesis.

Chapter 7 OPTIMIZATION OF PROTIC IONIC LIQUID-ASSISTED CHITOSAN PRODUCTION FROM SHRIMP SHELL WASTE VIA RESPONSE SURFACE METHODOLOGY FOR THE SUSTAINABLE RECOVERY OF CRITICAL METALS FROM SPENT LITHIUM-ION BATTERIES

Published as a research article in Journal of Environmental Chemical Engineering, Volume 14, Issue 3, June 2026. DOI: 10.1016/j.jece.2026.122497

7.1. Abstract

The application of protic ionic liquids (PILs) proved to be a viable and sustainable method for extracting chitin from shrimp shell waste. Among the three amin-based PILs investigated for extracting chitin from shrimp shells (Triethylammonium acetate [Tea][Ac], Triethylenetetrammonium acetate [Teta][Ac], and Ethanolammonium acetate [Eth][Ac]), [Eth][Ac] was selected as the optimum option due to its greener characteristics, lower toxicity, biodegradability, and property enhancement. The PIL-extracted chitosan was then used as a biosorbent for the selective adsorption of Co(II), Mn(II), and Ni(II) from the leachate of spent lithium-ion battery (LIB) cathodes, leached with a synergistic mixture of 1.25 M sulfuric acid and 0.55 M citric acid. Chitin extraction parameters (temperature, time, and liquid-to-solid ratio) were optimized using response surface methodology. The optimal conditions (92 °C, 27.8 h, L/S = 16 g/g) resulted in a chitin yield of 56.67 wt.%, with adsorption efficiencies of 82.42 ± 1.65% for Co(II), 35.09 ± 2.63% for Mn(II), and 98.30 ± 0.63% for Ni(II). Adsorption isotherm analysis of the optimal [Eth]-extracted chitosan revealed adsorption performance that exceeded that of commercial chitosan. FT-IR spectra matched those of commercial chitosan, confirming the preservation of key functional groups, whereas BET analysis indicated a higher specific surface area. Collectively, these results validate a green, waste-biomass-derived adsorbent for the efficient recovery of critical metals from spent lithium-ion batteries while simultaneously valorizing biomass waste.

Keywords: Protic-ionic liquid; chitosan; lithium-ion battery recycling; critical metals; circular economy.

7.2. Introduction

One of the recent urgent global challenges is the safe and effective recycling of used lithium-ion batteries (LIBs), which contain high-value yet potentially hazardous metals such as cobalt (Co), nickel (Ni), manganese (Mn), and lithium (Li). More than 1 million electric vehicle batteries are expected to reach the end of their life by 2030, leading to an estimated 14 million waste LIBs generated each year by 2040 (Ding et al., 2024). In parallel, global demand for these critical materials is projected to increase dramatically by 2050, placing unprecedented strain on primary resources and supply chains (Amer et al., 2025). Market forecasts indicate that the global LIB recycling market could reach USD 15.5 billion by 2030, growing at an annual rate of 8.2%. However, the rapid increase in waste LIBs poses significant environmental risks, particularly due to improper disposal and the loss of recyclable materials (Ding et al., 2024). While various hydrometallurgical techniques have been developed, many rely on corrosive reagents or generate secondary waste, underscoring the urgent need for cleaner, more environmentally friendly alternatives (P. Li et al., 2024). Adsorption has gained increasing attention as an effective method for the recovery of critical materials (e.g., Co, Ni, Li) from spent LIBs due to its cost-effectiveness, operational simplicity, tunability through surface modification (i.e., functionalization), high removal efficiency, reusability, and minimal generation of secondary waste (Balakrishnan et al., 2023; Syeda et al., 2024). As the transition to a circular economy accelerates worldwide, the transformation and repurposing of waste streams into value-added materials represents a viable and sustainable pathway forward. This waste-to-treat-waste approach encourages resource recovery while addressing two environmental challenges: managing organic waste and mitigating the escalating problem of electronic waste. In this context, bio-derived sorbent materials from waste biomass have emerged as promising candidates for sustainable metal recovery. Among these materials, chitosan, a polysaccharide derived from deacetylating chitin, has attracted substantial interest due to its widespread availability, non-toxicity, and the presence of amine and hydroxyl groups that facilitate metal binding (Al-Ghamdi et al., 2022; Manzoor et al., 2019; Verma et al., 2017). A previous study by the authors showed that commercial chitosan selectively adsorbs Co(II), Ni(II), and Mn(II) from spent LIB leachates in a mild citrate-sulfate medium, while leaving Li in solution (Roshanfar et al., 2025).

Chitin is typically derived from crustacean shells, such as shrimp and crab, and converted into chitosan via conventional chemical extraction. These processes involve acid demineralization (e.g., 1-2% HCl), alkaline deproteinization (e.g., 1-5% NaOH), and high-temperature deacetylation using concentrated NaOH (>100 °C). While effective, such methods raise sustainability concerns due to their intensive use of concentrated acids and bases, high energy and water consumption, the generation of hazardous wastewater, and the potential degradation of chitin's molecular structure (Alhamad et al., 2025; Rahman, 2024; Rahman et al., 2023). These harsh, non-selective conditions render the process less environmentally sustainable and reduce its suitability for high-value applications, underscoring the need for cleaner, more selective production technologies (C. Wang et al., 2025b; Y. Wang et al., 2025). To address these challenges, greener processing alternatives have been explored, particularly those using ionic liquids (ILs) and deep eutectic solvents (DES). Recent studies highlight their effectiveness in biomass treatment, polymer dissolution, and metal extraction, highlighting their potential as greener alternatives to conventional chitin and chitosan production methods (Campalani et al., 2024; Durante-Salmerón et al., 2024; Z. Li et al., 2022; Ozel and Elibol, 2024; Tolesa et al., 2019; Y. Wang et al., 2025).

Ionic liquids (ILs) are considered environmentally friendly solvents due to their tunable physicochemical properties, low volatility and vapor pressure, thermal stability, and non-flammability. However, relatively high production costs and limited biodegradability restrict their application in large-scale applications (Y. Wang et al., 2025). Among the broader IL family, protic ILs (PILs) offer a more affordable and potentially greener alternative and are synthesized through a simple acid-base neutralization process in which a Brønsted acid donates a proton to a base, usually an organic amine, generating a protonated cation and the corresponding anion. The choice of acid is crucial for optimizing properties such as viscosity (Ghareh Bagh et al., 2021a, 2021b; Salas et al., 2025; Chi Wang et al., 2024). PILs exhibit higher polarity due to their extensive intra- and intermolecular hydrogen bonding networks, making PILs increasingly attractive for biomass dissolution and fractionation. For example, Tolesa et al. (2019) used ammonium-based PILs (diisopropylethylammonium acetate ([Dipea][Ac]), diisopropylethylammonium propanoate ([Dipea][P]), and dimethylbutylammonium acetate ([Dmba][Ac])) have been successfully applied to extract chitin from shrimp shells, achieving a chitin yield of 13.4% at 110 °C after 24 hours.

To the best of the authors' knowledge, only a limited number of investigations have studied the use of PILs for chitin extraction and chitosan production. The present study aims to develop a sustainable approach to LIB recycling by integrating green chitosan production as a biosorbent to avoid the need for concentrated alkalis and reduce chemical waste, while enabling selective metal recovery. Chitosan was produced using three PIL systems, including Triethylammonium acetate [Tea][Ac], Triethylenetetrammonium acetate [Teta][Ac], and Ethanolammonium acetate [Eth][Ac], and its potential as a bio-adsorbent was subsequently evaluated. The synthesized biopolymer was then examined for its ability to selectively separate Co(II), Ni(II), and Mn(II) from Li in a real sulfate-citrate leaching solution of spent LIBs. The adsorption performance was compared with that of the commercial chitosan in our previous study (Roshanfar et al., 2025), demonstrating the potential of the PIL-derived chitosan as an effective, eco-friendly biosorbent alternative. Overall, this study proposes a closed-loop approach in which organic-waste-derived materials are converted into biosorbents to recycle electronic waste, thereby contributing to the broader goals of a circular economy and sustainable resource management.

7.3. Materials and Methods

7.3.1. Materials and Preparation

Spent LIBs originating from a range of consumer electronics, including laptops, smartphones, and Li-polymer batteries manufactured by brands such as LG, Samsung, and Motorola, were obtained from a recycling facility in Toronto, Canada. Shrimp shell (SS) waste was collected from a local market. Sulfuric acid (H_2SO_4), citric monohydrate ($C_6H_8O_7 \cdot H_2O$), and acetic acid (Ac, CH_3COOH) with purities of 98%, 99%, and 99.7%, respectively, were purchased from Fisher Chemical, USA. Commercial chitosan (deacetylation degree [DD] 85%) and sodium hydroxide (NaOH) were sourced from Fisher Scientific Co., Canada. Deionized water (DI) was used to prepare all solutions. Unless otherwise specified, all materials used were of analytical grade. Triethylamine, triethylenetetramine, and ethanolamine, with purities greater than 98%, 60%, and 99.5%, respectively, were purchased from Sigma-Aldrich, USA. The PILs synthesized for this study were selected based on solvent cost and ease of synthesis and purification processes.

The solution used for the adsorption experiments was obtained from a synergistic leaching process applied to spent LIBs from laptops, cell phones, and Li-polymer devices, representing common

cathode chemistries including lithium cobalt oxide (LCO), lithium nickel manganese cobalt oxide (NMC), and lithium manganese oxide (LMO). These cathode materials were combined at a 1:1:1 mass ratio to produce a representative black mass (BM). Briefly, the spent LIBs were first fully discharged by immersion in a 10 wt% NaCl solution for 24 h. The batteries were then manually dismantled, and the cathode materials were separated, homogenized, and thermally treated at 570 °C in air to remove organic binders. The resulting BM, primarily composed of Li, Co, Mn, and Ni, was leached in a mixed-acid solution of 1.25 M H_2SO_4 and 0.55 M citric acid at 90 °C for 2 h, using a solid-to-liquid ratio (S/L) of 62.5 g/L and without any added reducing agent (Roshanfar et al., 2024). The pregnant leach solution generated by this process was used as the feed solution for the adsorption tests.

7.3.2. Protic Ionic Liquid Synthesis

Three selected PILs ([Eth][Ac], [Tea][Ac], and [Teta][Ac]) were synthesized via an acid-base neutralization method, as reported in the literature (Ghareh Bagh et al., 2021b, 2021a; Tolesa et al., 2019). Ethanolamine ($pK_a \approx 9.50$), triethylenetetramine ($pK_a \approx 9.92$), and triethylamine ($pK_a \approx 10.78$) were chosen for PIL synthesis because of their varying basicity, functional groups, and hydrogen-bonding abilities, which enable adjustment of physicochemical properties such as viscosity, acidity, and stability for various applications. They also represent both simple and branched molecular structures for examining structure-property relationships and are relatively low-cost and commercially available. In the synthesis process, equimolar amounts of [Eth], [Tea], or [Teta] were reacted with acetic acid (Ac). Previous studies have confirmed that reactions between amines and acetic acid yield PILs in excess of 95% (Ghareh Bagh et al., 2021b; MacFarlane et al., 2006). The selected amine was initially transferred to a 250 mL flask, and the acid was then added dropwise under continuous stirring. To control reaction temperature (around 0-5 °C), the flask was maintained in a shallow ice-water bath throughout the mixing process. Once the addition was complete, stirring continued at room temperature for 24 hours to ensure complete reaction. Any unreacted compounds were removed by heating the mixture at 80 °C, yielding the desired PILs as clear to pale-yellow liquids.

7.3.3. Chitin Extraction from Shrimp Shells and Deacetylation

Chitin was extracted from SS waste through several pre-treatment and processing steps. Figure 7.1 illustrates the schematic steps for producing chitosan via conventional and PIL extraction procedures. Initially, shrimp shells were rinsed with water to remove residual tissue, blood, and other surface impurities, then air-dried. The clean, dry shells were milled into a fine powder using a laboratory grinder. For extraction, the powdered SS were mixed with a synthesized PIL at a mass ratio of 1:15 (g/g) and heated under continuous stirring at a predetermined temperature and for a specified duration. Following extraction, the mixture was centrifuged, and the supernatant was demineralized by the addition of 250 mL of a 2.4% (w/v) citric acid solution, with stirring continued for an additional 5 hours (Tolesa et al., 2019). The solution was then allowed to settle overnight. Subsequently, the separated solid was dried in an oven at 60 °C, and the chitin yield was calculated from the initial mass of SS powder. To convert the extracted chitin to chitosan, the dried material was treated with 50 wt.% NaOH at a S/L ratio of 1:15 (w/v), stirred for 6 hours, and subsequently heated at 100 °C as a deacetylation stage (Rahman, 2024; Rahman et al., 2023; Tolesa et al., 2019). The resulting mixture was then filtered, and the solid product was thoroughly rinsed with deionized water. The final chitosan powder was produced by drying the material in an oven at 60 °C for 12 hours.

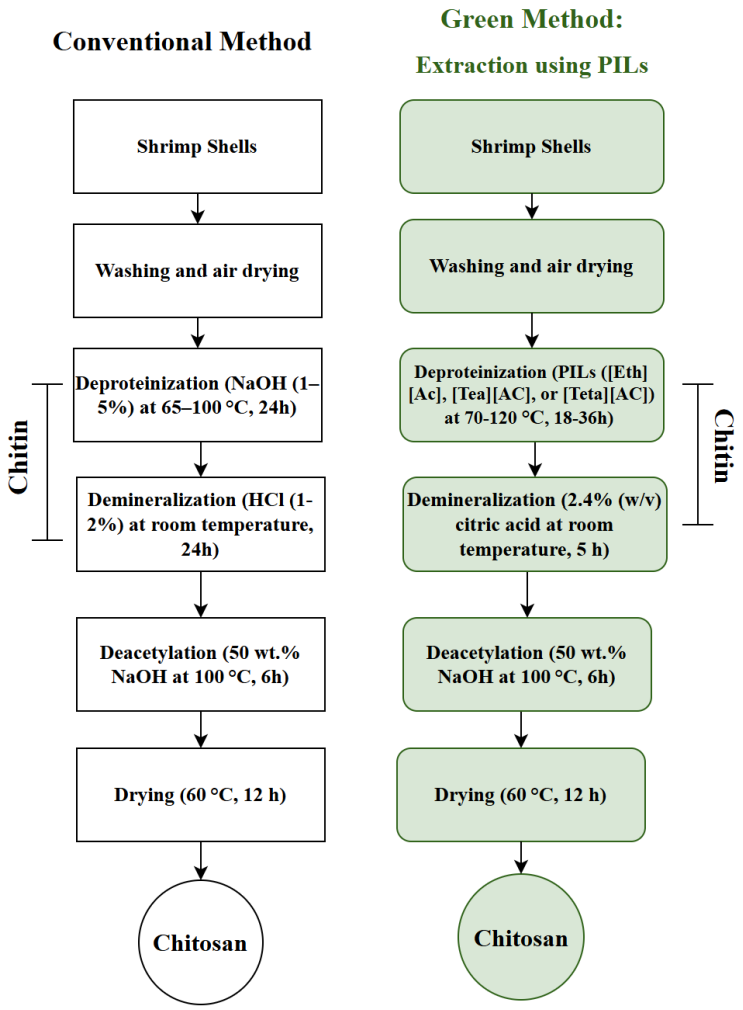

Figure 7.1. The schematic steps of producing chitosan.

7.3.4. Design of Experiment (DOE) and Extraction Optimization Study

Design of experiments for chitin extraction consisted of two stages: screening and optimization. Screening tests were conducted to select the best-performing PIL type among the three systems tested ([Eth][Ac], [Tea][Ac], and [Teta][Ac]). For the screening experiments, the reaction time, temperature, and liquid-to-solid (L/S) ratio were set at 24 hours, 90 °C, and 15 g/g (PIL to SS), respectively. The best PIL was selected based on the adsorption performance of the extracted chitosan, evaluated by the adsorption removal efficiency (%) and uptake (mg/g) for Co and Ni in the leachate solution, while also considering its environmental friendliness.

After selecting the optimal PIL, the experimental design was developed using Design-Expert 12 (State-Ease Inc., Minneapolis, MN, USA) through statistical analysis and optimization of the chitin yield (%) and adsorption performance (metal uptake (mg/g) and removal efficiency (%)) for Co and Ni from leachate solution. The chitin extraction process was optimized using a Box-Behnken design (BBD) based on response surface methodology (RSM). The goal was to optimize the extraction factors by varying the extraction time, temperature, and S/L ratio to maximize adsorption performance and chitin yield. Therefore, time (18, 27, and 36 hours), temperature (70 ± 5 °C, 90 ± 5 °C, and 120 ± 5 °C), and L/S ratio (10, 15, and 20 g/g) were chosen as variables based on previous studies (Setoguchi et al., 2012; Shamshina et al., 2016; Tolesa et al., 2019). At this stage, 3 g of SS was added to a specific amount of each PIL. BBD was chosen for its popularity as a design that requires fewer experimental runs and provides benefits such as orthogonality and rotatability. It also avoids extreme conditions during the design process, ensuring that the adsorbent remains unaffected (Byran Smucker et al., 2018; Ghareh Bagh et al., 2021a, 2021b).

7.3.5. Characterization and Analytical Methods

To characterize the functional groups of the PIL-derived chitosan and compare them to those of commercial chitosan, Fourier Transform Infrared Spectroscopy (FT-IR, IS50, Thermo Scientific) was conducted in the 4000–450 cm^{-1} range. Scanning Electron Microscopy (Field Emission SEM-JEOL JSM-7500F) and Energy-Dispersive X-ray Spectroscopy (EDS-Oxford detector at 30 kV), accompanied by INCA software, were used to investigate the surface morphology and elemental composition of the materials. The specific surface area was measured using Brunauer-Emmett-Teller (BET) N_2 isotherms, conducted on a Quantachrome instrument at McGill University at 77 K. Samples were activated prior to measurement.

To measure the metal concentrations in the BM from the cathode materials, inductively coupled plasma emission spectroscopy (digestion in aqua regia (HNO_3 : HCl = 1:3) at 120 °C, ICP-ES, Agilent 5110) was used. During the adsorption experiments, atomic absorption spectroscopy (AAS; PinAAcle 500, PerkinElmer) was used to quantify the concentration of metals (Co(II), Mn(II), Ni(II), and Li) in solution before and after adsorption. The instrument was calibrated using a zero-intercept nonlinear method (with triplicate measurements).

7.3.6. Batch Adsorption and Isotherm Study

Batch adsorption experiments were conducted to evaluate the efficacy of the extracted chitosan for the adsorption uptake of Li, Co(II), Mn(II), and Ni(II) in the screening and optimization stages, and also to examine the isotherm study by applying various dilution factors (50, 40, 30, and 20). For all adsorption tests, 0.25 g of extracted chitosan powder was added to 25 mL of the leached solution in 125 mL Erlenmeyer flasks, and the mixture was stirred at 180 rpm at room temperature for 24 hours. For screening and optimization experiments, the initial metal concentrations were adjusted by diluting the leaching solution 40 times (with metal concentrations of 765 ± 48.79 mg/L of Co(II), 100 ± 2.61 mg/L of Li(I), 36.81 ± 2.61 mg/L of Mn(II), and 53 ± 1.71 mg/L of Ni(II)). The initial pH of 4 was adjusted using a HACH HQ40D meter with 10 wt.% sodium hydroxide or 1% (v/v) sulfuric acid. After filtration, the equilibrium concentrations of Li, Co(II), Mn(II), and Ni(II) were determined using AAS. All experiments were conducted in duplicate, and the average values were used for analysis. The adsorption removal efficiency and adsorption uptake (qe) were calculated using the following equations:

$$Adsorption\ efficiency\ (\%) = 100 - \left(\frac{Equilibrium\ concentration\ of\ metals}{Initial\ concentration\ of\ metals}\right) \times 100 \quad (7\text{-}1)$$

$$qe = \frac{(C_0 - C_e) \times V}{W} \quad (7\text{-}2)$$

where C_0 (mg/L), C_e (mg/L), V (L), and W (g) represent the initial concentrations of metal ions, the equilibrium concentration of the adsorbate in the solution, the solution volume, and the dry weight of the adsorbent, respectively.

7.3.7. Adsorption Isotherm Modeling for Optimal PLI-extracted Chitosan

The adsorption data were analyzed using the Langmuir and Freundlich isotherm models. To identify the best fit, the coefficient of determination (R^2), Sum of Squares of Residuals (SSR), and Mean Squared Error (MSE) were calculated. Lower SSR and MSE values indicate a more accurate model fit, with MSE providing an easy way to compare models and datasets by normalizing errors. The equations for the Langmuir (7-3) and Freundlich (7-4) models are given as follows:

$$q_e = \frac{q_m k_L C_e}{1+k_L C_e} \quad (7\text{-}3)$$

$$q_e = k_F C_e^{\frac{1}{n_F}} \quad (7\text{-}4)$$

where q_m represents the maximum adsorption capacity (mg/g), k_L is the Langmuir constant (L/mg), k_F is the Freundlich constant $(mg/mg)^{1/n}$, the Freundlich constant associated with adsorption intensity, and C_e is the equilibrium concentration of the adsorbate (mg/L).

7.4. Results and Discussion

The results of the PIL screening and the RSM-based optimization of the chitin extraction process are presented and discussed below.

7.4.1. Screening Results: PIL Type Selection

In this study, for chitin extraction from SS, ammonium-based PILs were selected because they have been reported to be particularly effective solvents (Tolesa et al., 2019). First, a screening stage was performed to select the most suitable PIL for chitin extraction among three candidates: [Eth][Ac], [Tea][Ac], and [Teta][Ac]. Batch adsorption experiments were conducted to assess the performance of PIL-extracted chitosan under the same optimized conditions, as those reported by (Roshanfar et al., 2025), for commercial chitosan, and the results were compared. These included a dilution factor of 40 for the leaching solution, an initial pH of 4, an adsorbent dosage of 10 g/L, and a contact time of 24 hours. The initial metal concentrations in the leachate solution were 765 ± 48.79 mg/L of Co(II), 100 ± 2.61 mg/L of Li(I), 36.81 ± 2.61 mg/L of Mn(II), and 53 ± 1.71 mg/L of Ni(II).

Table 7.1 shows the metal removal efficiency (%) ± standard deviation (SD) and adsorption uptake (mg/g) ± SD. It is worth noting that all three PIL-extracted chitosan powders selectively separated Co(II), Mn(II), and Ni(II) from a synergistic leaching medium of sulfuric acid and citric acid, leaving Li in solution. As shown in Table 7.1, [Tea][Ac] demonstrated lower removal efficiencies and uptake capacities for Co(II) and Ni(II) compared to [Eth][Ac] and [Teta][Ac]. Compared to commercial chitosan (Roshanfar et al., 2025), which achieved adsorption removal efficiencies of

81.29%, 27.02%, and 83.86%, with uptake capacities of 60.11 mg/g for Co(II), 1.10 mg/g for Mn(II), and 4.70 mg/g for Ni(II), both [Eth][Ac]- and [Teta][Ac]-treated chitosan powders demonstrated competitive performance. Among them, [Eth][Ac]-treated chitosan exhibited the best overall performance and was also closest to commercial chitosan.

Adsorption using [Tea][Ac]-treated chitosan resulted in a final pH of 11, compared to approximately 7 for [Eth][Ac]- and [Teta][Ac]-treated chitosan powders. It is well known that metal precipitation in this system typically begins at pH values above 8, which makes the results less reliable due to the combined effects of adsorption and precipitation (Conte and Gómez, 2024). This also explains the unusually high adsorption efficiency and Mn(II) uptake observed, as Mn(II) is highly pH-sensitive and tends to precipitate at higher pH values. The observed differences in final pH among the PILs are attributed to their inherent basicity, with [Tea][Ac] being the most basic due to its tertiary amine structure, [Teta][Ac] exhibiting moderate basicity from its multiple amine groups, and [Eth][Ac] showing the lowest basicity as a result of intramolecular hydrogen bonding between its amine and hydroxyl groups. Inherent basicity can be shown by the pK_a of their conjugate acids: triethylamine ($pK_a \approx 10.78$) is highly basic, triethylenetetramine ($pK_a \approx 9.92$) is moderately basic, and ethanolamine ($pK_a \approx 9.50$) is the least basic of the three. Therefore, the IL-extracted chitosan powders differed in adsorption experiments and exhibited distinct final pH values, particularly for [TEA][Ac]. This disparity can be attributed to differences in residual PIL content, inherent basicity, and surface morphology (Ghareh Bagh et al., 2021b, 2021a). Between [Eth][Ac] and [Teta][Ac], [Eth][Ac] is the more environmentally friendly and cost-effective option. It is readily biodegradable, less toxic, and widely used across industries, posing minimal environmental risk. In contracts, the larger, more complex molecular chain with multiple amine groups makes [Teta][Ac] less biodegradable and more toxic, particularly to aquatic life (Libralato et al., 2010). Therefore, [Eth][Ac] is a more sustainable and practical choice for chitosan production and metal adsorption applications and was selected for subsequent stages and further investigation.

Table 7.1. Adsorption (%) ±SD and uptake (mg/g) ± SD of metal ions in the screening stage at a dilution factor of 40, initial pH of 4, adsorbent dosage of 10 g/L, and a contact time of 24 hours

$\frac{\textbf{Metal adsorption efficiency (\%)}}{\textbf{Adsorption uptake (mg/g)}}$				
Co		**Mn**	**Ni**	**Final pH**
[Eth][Ac]	$\frac{77.92 \pm 2.46}{52.76 \pm 0.70}$	$\frac{29.82 \pm 2.28}{1.06 \pm 0.11}$	$\frac{84.35 \pm 3.51}{3.77 \pm 0.01}$	7.08
[Tea][Ac]	$\frac{55.83 \pm 2.64}{37.32 \pm 0.80}$	$\frac{86.93 \pm 2.42}{3.13 \pm 0.13}$	$\frac{65.82 \pm 3.03}{2.85 \pm 0.01}$	11
[Teta][Ac]	$\frac{67.73 \pm 12.54}{47.95 \pm 8.78}$	$\frac{26.54 \pm 6.67}{0.93 \pm 0.25}$	$\frac{90.42 \pm 7.42}{4.43 \pm 0.29}$	7.04

Chitin and chitosan extracted with the three PILs ([Eth][Ac], [Tea][Ac], and [Teta][Ac]) were analyzed by FT-IR spectroscopy. The resulting spectra, shown in Figure 7.2A and B, were compared with those of untreated SS, conventionally produced chitin, and commercial chitosan. The close similarity of the FT-IR profiles confirms that all three PILs effectively extracted chitin while preserving its characteristic chemical structure. Broad bands near ~3400 cm^{-1}, attributed to O-H and N-H stretching vibrations, are clearly observed in all PIL-treated samples and appear more defined than in untreated SS, particularly for [Tea][Ac] and [Teta][Ac], indicating enhanced exposure of surface functional groups. Bands at 2910-2850 cm^{-1} (C-H stretching) are well preserved in the extracted samples, consistent with a purified polysaccharide backbone.

A reduction in the intensity of the amide I (~1627 cm^{-1}) and amide II (~1500 cm^{-1}) bands, particularly in the chitosan spectra, indicates effective protein removal and deacetylation. This is further supported by the close spectral agreement between PIL-extracted chitosan (Figure 7.2(c–e)) and commercial chitosan (Figure 2b, section B). In addition, diminished peaks near ~1400 cm^{-1} and ~860 cm^{-1} suggest efficient demineralization after PIL treatment, with the effect most pronounced for [Teta][Ac]. The C-O stretching region around ~1020 cm^{-1} remains clearly defined in all treated samples, indicating preservation of the polysaccharide structure. Although [Eth][Ac] showed slightly lower efficiency compared to [Teta][Ac], it effectively preserved the

polysaccharide backbone, demonstrated moderate deproteinization and demineralization, and offered a greener, less toxic, and more cost-effective alternative, making it suitable for sustainable extraction. It should be noted that the chitosan yields obtained with different PILs were relatively similar, further supporting the consistent effectiveness of all three treatments.

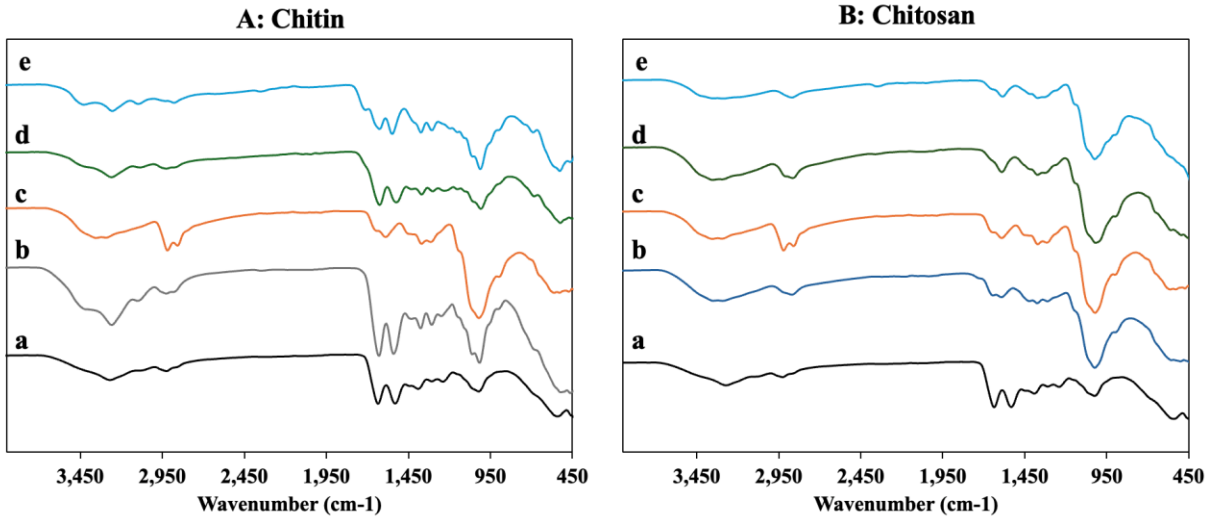

Figure 7.2. FT-IR spectra for A: Chitin a) Shrimp shells b) chitin produced in conventional method, c) [Eth][Ac], d) [Tea][Ac], and e) [Teta][Ac], and B: Chitosan a) SS, b) commercial chitosan, c) [Eth][Ac], d) [Tea][Ac], and e) [Teta][Ac].

7.4.2. Optimization Results

7.4.2.1. Modeling and Statistical Analysis

Following the screening stage, a BBD under RSM was employed to design the optimization experiments and statistically analyze the responses (chitin production yield (%) and adsorption performance (uptake (mg/g) and removal efficiency (%)). The responses considered were chitin yield (after deproteination and demineralization, since the deacetylation step was consistent across all experiments and only the initial extraction stage varied) and the Co(II) adsorption performance. Among the metals, Co(II) was selected as the primary response variable because of its higher concentration in solution, whereas Mn(II) consistently showed the lowest adsorption and Ni(II) the highest across all samples. The average of the three metals did not exhibit a clear adsorption

trend because, when individual data points differ significantly, the average can smooth out any underlying pattern, making it difficult to detect a trend.

Based on previous studies (Setoguchi et al., 2012; Shamshina et al., 2016; Tolesa et al., 2019), the effects of temperature (70–120 °C), extraction time (18–36 h), and liquid-to-solid (L/S) ratio (10–20 g/g) on chitin yield and adsorption performance were systematically investigated. This experimental design enabled evaluation of individual factors and their interactions while minimizing the number of experimental runs. To ensure the reliability and robustness of the developed models, statistical validation was conducted using analysis of variance (ANOVA), including p-values, F-values, coefficients of determination (R^2), and lack-of-fit tests.

Table 7.2 presents the ANOVA results for the proposed models of yield (%) and Co(II) adsorption performance. These metrics were selected for discussion because the p-value indicates the statistical significance of the factors (less than 0.05 indicates 95% confidence in the model), the F-value (F distribution) reflects the strength of their effect relative to random variation (as F-values increase, the model demonstrates greater reliability, indicating a lower likelihood that the observed results are due to random variation), and R^2 illustrates how well the model explains variability in the response (the values are close to one, suggesting that the predicted models closely align with the experimental data). Overall, the results confirm that the models provide a good fit to the experimental data (Anderson and Whitcomb, 2017; Roshanfar et al., 2024). The chitin yield model is statistically significant ($p = 0.0427$), with an R^2 of 0.83 and an F-value of 3.92, indicating a good fit and moderate predictive power. The adsorption uptake model shows even stronger performance, with a highly significant p-value (0.0013), an R^2 of 0.94, and a higher F-value of 13.12, indicating excellent predictive accuracy. The adsorption efficiency model also performs well, as evidenced by a highly significant p-value (0.0013), an R^2 of 0.94, and an F-value of 13.10, demonstrating strong predictive accuracy. The lack-of-fit tests were not significant for all models, confirming that the models are suitable for representing the experimental data (Anderson and Whitcomb, 2017). The models are as follows:

$$Chitin\ Yield\ (\%) = 56.07 - 3.75A - 3.46B + 2.46C - 3.43AB - 3.25AC + 5.34BC - 7.28A^2 - 3.2B^2 - 6.2C^2 \quad (7\text{-}5)$$

$$Adsorption\ uptake\ (mg/g) = 57.98 - 0.8237A + B - 0.055C - 0.2450AB + 0.4825AC + 0.19255BC - 5.96A^2 - 2.91B^2 - 1.08C^2 \quad (7\text{-}6)$$

$$Adsorption\ efficiency\ (\%) = 80.15 - 1.15A + 1.41B - 0.0762C - 0.3425AB + 0.675AC + 0.2725BC - 8.34A^2 - 4.07B^2 - 1.51C^2 \quad (7\text{-}7)$$

where A, B, and C, which are temperature (°C), time (h), and L/S ratio (g/g), respectively, represent the coded values. The models suggest that temperature has a slightly greater impact than time, while the L/S ratio appears to have little effect.

Table 7.2.ANOVA data

Yield (%)					
Source	**Sum of Squares**	**Mean Square**	**F-value**	**p-value**	
Model	931.74	103.53	3.92	0.0427	**significant**
Residual	184.83	26.4			
Lack of Fit	148.95	49.65	5.53	0.0659	**not significant**
Pure Error	35.88	8.97			
Cor Total	1116.57		**R^2**	0.83	
Adsorption uptake (mg/g)					
Source	**Sum of Squares**	**Mean Square**	**F-value**	**p-value**	
Model	218.58	24.29	13.12	0.0013	**significant**
Residual	12.96	1.85			
Lack of Fit	8.34	2.78			**not significant**
Pure Error	4.62	1.15			
Cor Total	231.54		**R^2**	0.94	
Adsorption efficiency (%)					
Source	**Sum of Squares**	**Mean Square**	**F-value**	**p-value**	
Model	427.86	47.54	13.10	0.0013	**significant**
Residual	25.41	3.63			
Lack of Fit	16.38	5.46	2.42	0.2066	**not significant**
Pure Error	9.03	2.26			
Cor Total	453.28		**R^2**	0.94	

7.4.2.2. Effect of Parameters on Yield (%) and Adsorption Performance

At this stage, the effects of temperature (70-120 °C), time (18-36 hours), and L/S ratio (10-20 g/g) were evaluated for the extraction of chitin using the [Eth][Ac]. Table 7.3 shows the experimental design and responses (chitin yield (%), Co(II) adsorption uptake (mg/g), and removal efficiency (%)), and Figure 7.3 (a-c) shows BBD-RSM results and the effect of temperature, time, and L/S ratio on yield (%), Co(II) adsorption uptake (mg/g), and Co(II) removal efficiency (%). According to Figure 7.3 (a), at a fixed time of 27.8 hours and an L/S ratio of 16 g/g, increasing the temperature from 70°C to 92°C resulted in improvements in chitin yield and Co(II) adsorption performance (uptake and removal efficiency). This is due to enhanced chitin decomposition into lower-molecular-weight fragments at higher temperatures, which improves extraction efficiency and adsorption characteristics (Setoguchi et al., 2012; Shamshina et al., 2016; Tolesa et al., 2019). It is worth noting that at lower temperatures, extraction proceeds more slowly. However, raising the temperature to 120 °C further reduced both yield and adsorption capacity, likely due to the onset of chitin thermal degradation. At this temperature, partial depolymerization and deacetylation of chitin chains can occur, leading to a breakdown of its crystalline structure and a reduction in available functional groups such as -OH and -NH_2, which are critical for adsorption performance (Holme et al., 2001; Jung and Zhao, 2011; Yamada et al., 2025). Consequently, 92 °C was selected as the optimal temperature.

Regarding the effect of time, Figure 7.3(b) shows that at 92 °C and an L/S ratio of 16 g/g, increasing the reaction time gradually increased the yield and significantly improved Co(II) adsorption uptake and removal efficiency up to 27.8 hours. Beyond this point, from 27.8 to 36 hours, the parameters declined slightly, suggesting that prolonged exposure at high temperatures may damage the chitin structure. This pattern aligns with previous studies, which reported that extended thermal treatment induces chain scission, deacetylation, and loss of crystallinity in chitin, ultimately reducing its functional group availability and structural integrity (Ghareh Bagh et al., 2021b; Setoguchi et al., 2012; Shamshina et al., 2016; Tolesa et al., 2019).

As illustrated in Figure 7.3(c), when the time and temperature were set to 27.8 hours and 92 °C, respectively, increasing the L/S ratio from 10 g/g to 16 g/g improved the yield due to the greater availability of the PIL for chitin extraction. This enhancement is attributed to improved mass transfer and more efficient penetration of the PIL into the shrimp shell matrix, which facilitates

the disruption of hydrogen bonding within the chitin structure and promotes the solubilization and release of chitin chains from the biomass (Ghareh Bagh et al., 2021b; Tolesa et al., 2019). However, further increasing the L/S ratio caused a slight reduction in yield. At excessively high L/S ratios, the system may experience a decrease in mass-transfer efficiency due to the increased volume and higher viscosity of the PIL, resulting in a slight decline in extraction performance. However, the L/S ratio had no significant effect on Co(II) uptake or removal efficiencies. The unchanged Co(II) removal efficiency across different L/S ratios during the PIL-extraction of chitosan suggests that protein removal was effective in all cases and that the key adsorption sites (amine groups) and the structural properties of chitosan remained unaffected.

Table 7.3. BBD experimental design and responses

Run	A: Temperature (°C)	B: Time (h)	C: L/S (g/g)	Yield (wt. %)	Co(II) Removal efficiency (%)	Adsorption Uptake (mg/g)
1	95	18	10	57	72.72	55.14
2	95	27	15	59.67	79.66	56.92
3	120	36	15	34.33	68.16	48.74
4	95	27	15	57.33	82.29	49.77
5	95	36	20	47	78.97	49.04
6	120	27	10	41.33	69.66	52.47
7	120	18	15	43	68.22	48.7
8	70	27	20	50.33	71.6	51.96
9	70	18	15	50	68.64	58.99
10	95	27	15	57.33	81.83	58.8
11	95	27	15	52.33	79.4	51.16
12	70	27	10	36	74.51	56.42
13	95	36	10	34.33	77.17	58.47
14	70	36	15	55	69.95	56.73
15	95	27	15	53.67	82.56	49.62
16	120	27	20	42.67	69.45	49.98
17	95	18	20	48.33	73.43	53.24

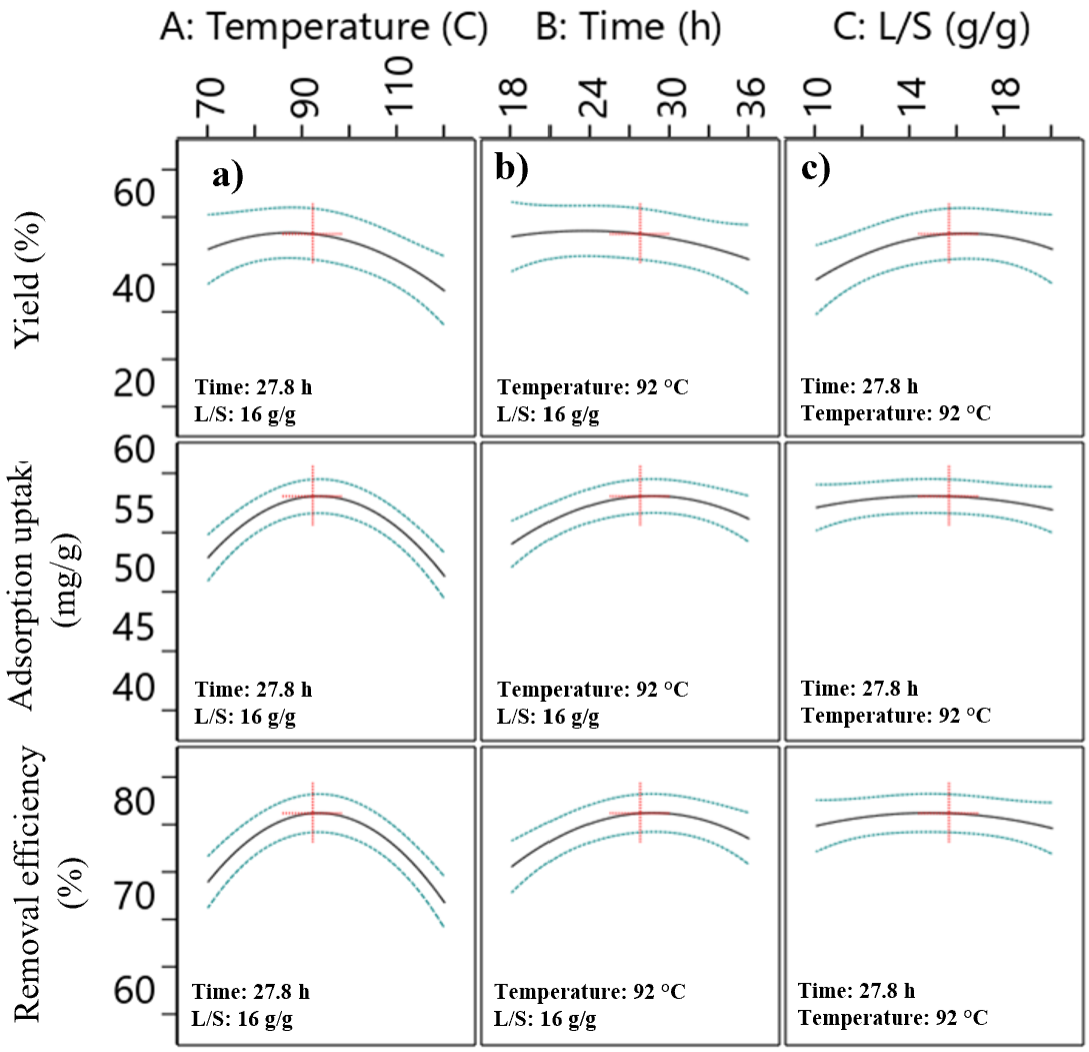

Figure 7.3. Main effect plots based on BBD-RSM design, the effect of temperature (70-120 °C) a) on yield (%), Co(II) adsorption uptake (mg/g), and Co(II) removal efficiency (%), b) the effect of time (18-36 h) on yield (%), Co(II) adsorption uptake (mg/g), and Co(II) removal efficiency (%), as well as c) the effect of L/S (10-20 g/g) on yield (%), Co(II) adsorption uptake (mg/g), and Co(II) removal efficiency (%).

Figure 7.4 illustrates the effect of time and temperature on yield (%), Co(II) adsorption uptake, and removal efficiency (%) through 3D (a, b, and c) and 2D (contour) (d, e, and f) response surface plots based on the BBD-RSM design at a fixed L/S ratio of 16 g/g. As shown in the plots, chitin yield and Co(II) adsorption performance (uptake and efficiency) increased with increasing

temperature and time, reaching optimal predicted values of 56 wt.% yield, 58 mg/g Co(II) adsorption uptake, and 81% Co(II) removal efficiency at approximately 92 °C and 27.8 hours. This trend supports earlier observations, where elevated temperature and prolonged deproteinization enhance chitin solubilization and improve adsorbent quality. For example, in Figure 4(f), the contour lines form a concentric pattern centered on the optimal region, clearly indicating the peak adsorption efficiency at the midpoint of the temperature-time range. The actual experimental results under these optimum conditions yielded 56.67 wt.% chitin, and adsorption efficiencies of $82.42 \pm 1.65\%$ for Co(II), $35.09 \pm 2.63\%$ for Mn(II), and $98.30 \pm 0.63\%$ for Ni(II), all closely matching the predicted values, confirming the model's reliability and the effectiveness of the selected parameters. The observed experimental adsorption uptakes for Co(II), Mn(II), and Ni(II) using [Eth][Ac]-extracted chitosan are 58.11 ± 1.17 mg/g, 1.13 ± 0.08 mg/g, and 4.11 ± 0.03 mg/g, respectively. These values are similar to the commercial chitosan adsorption uptake capacities (Roshanfar et al., 2025), which are 60.11 mg/g for Co(II), 1.10 mg/g for Mn(II), and 4.70 mg/g for Ni(II), along with adsorption efficiencies of 81.29% for Co(II), 27.02% for Mn(II), and 83.86% for Ni(II).

To achieve the simultaneous optimization of chitin yield and adsorption performance, a multi-response desirability function approach was employed within the response surface methodology framework. As shown in Figure 7.5, the resulting desirability contour plots identify a well-defined optimal region where the combined objective function achieves an overall desirability of 0.895. This high desirability value indicates that the selected operating conditions provide an effective balance between maximizing chitin production and achieving high adsorption efficiency, thereby validating the robustness and reliability of the optimized process across the experimental range studied.

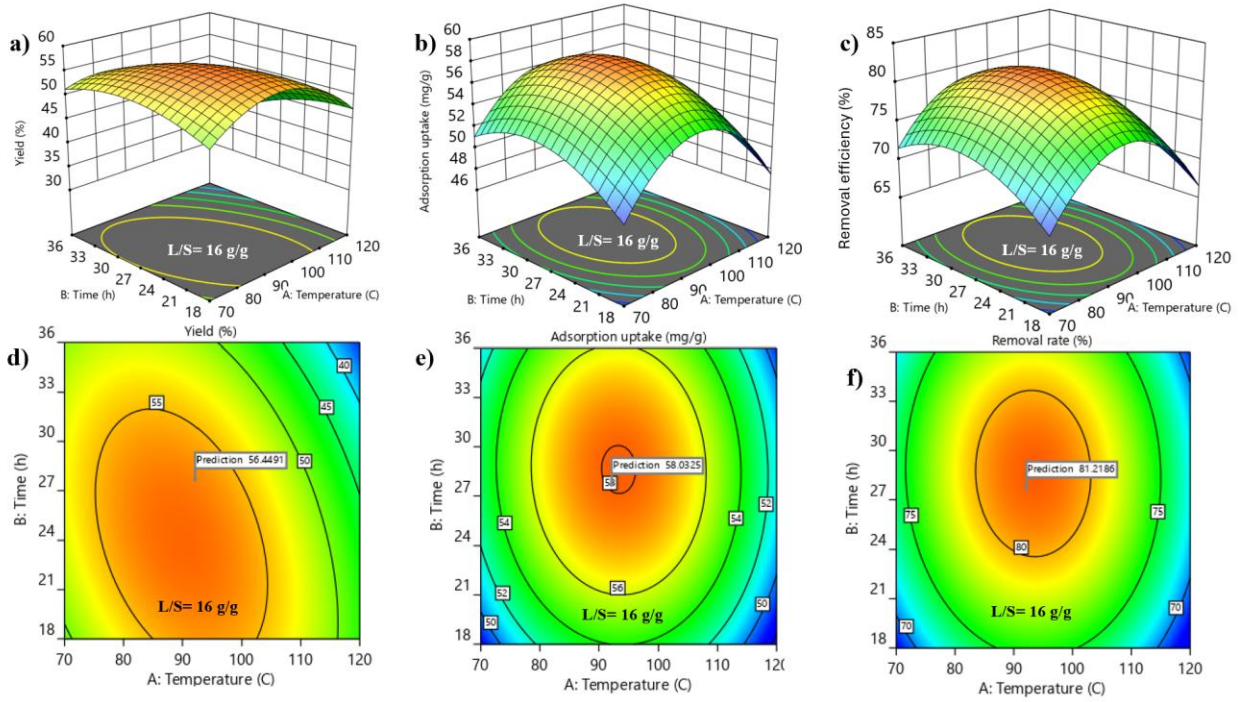

Figure 7.4. 3D plot of the effect of time and temperature on a) yield (%), b) Co(II) adsorption uptake (mg/g), and c) Co(II) removal efficiency (%), as well as 2D plot of the effect of time and temperature on c) yield (%), e) Co(II) adsorption uptake (mg/g), and f) metal removal efficiency (%) based on BBD RSM design at L/S of 16 g/g.

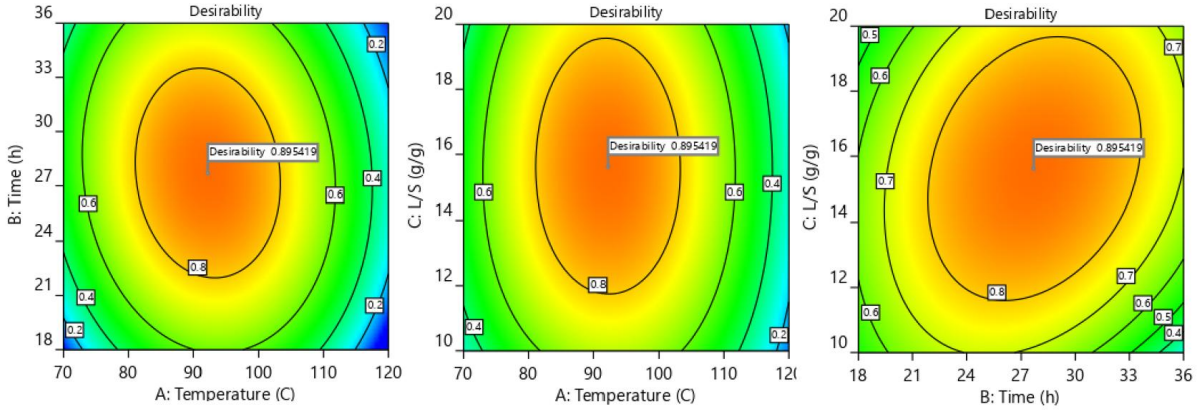

Figure 7.5. Response surface contour plots of the composite desirability function show the combined optimization of yield (%) and adsorption performance as a function of (a) temperature and time, (b) temperature and L/S ratio, and (c) time and L/S ratio. The optimal region, with a maximum desirability of 0.895, corresponds to 92 °C, 27.7 h, and an L/S ratio of 16 g/g.

7.4.2.3. Characterization of Optimized PIL-Extracted Chitosan

In this section, the optimized PIL-extracted chitosan obtained using [Eth][Ac] under the statistically optimized conditions of 92 ± 5 °C for 27.8 hours, with an L/S ratio of 16 g/g, was comprehensively characterized. First, the BET surface area was measured because it reflects both the porosity and the total surface area of an adsorbent, both of which are key determinants of adsorption performance (Metwally et al., 2024, 2017, 2013). FT-IR spectroscopy was then employed to confirm the chemical structure and the availability of key functional groups responsible for metal binding, and to compare it with the commercial chitosan, while SEM-EDS was used to examine surface morphology and elemental composition. The commercial chitosan powder showed a BET surface area of 7.45 m^2/g and a total pore volume of 7.18×10^{-3} cm^3/g. In comparison, the [Eth][Ac]-extracted chitosan, obtained using a greener method to extract chitin, showed a slightly higher surface area of 8.64 m^2/g and a total pore volume of 1.08×10^{-2} cm^3/g, indicating a slight improvement in surface properties.

FT-IR spectra of commercial chitosan and chitosan obtained using [Eth][Ac] under the optimized conditions (92 ± 5 °C, 27.8 hours, and an L/S ratio of 16 g/g) are shown in Figure 7.6. The similarity between the two spectra confirms the effectiveness of the process. The degree of deacetylation (DDA) of the extracted chitin was calculated using the ratio of the amide II absorption at 1560 cm^{-1} to the C=O stretching band at 1070 cm^{-1}. Additionally, the absorption bands at 1320 cm^{-1} and 1420 cm^{-1} were used to determine the degree of acetylation (DA%) of chitosan, as described in Equations (3-4) and (3-5) (Tolesa et al., 2019).

$$DDA\% = 100\text{-}DA\% \quad (7\text{-}8)$$

$$A\_1320/A\_1420 = 0.3822 + 0.03133DA. \quad (7\text{-}9)$$

The measured DDA values for commercial chitosan and the sample produced using [Eth][Ac] were 81% (closely aligning with the manufacturer's reported value of 85%) and 83%, respectively. This indicates that the [Eth][Ac] process yields chitosan with properties comparable to those of commercial chitosan.

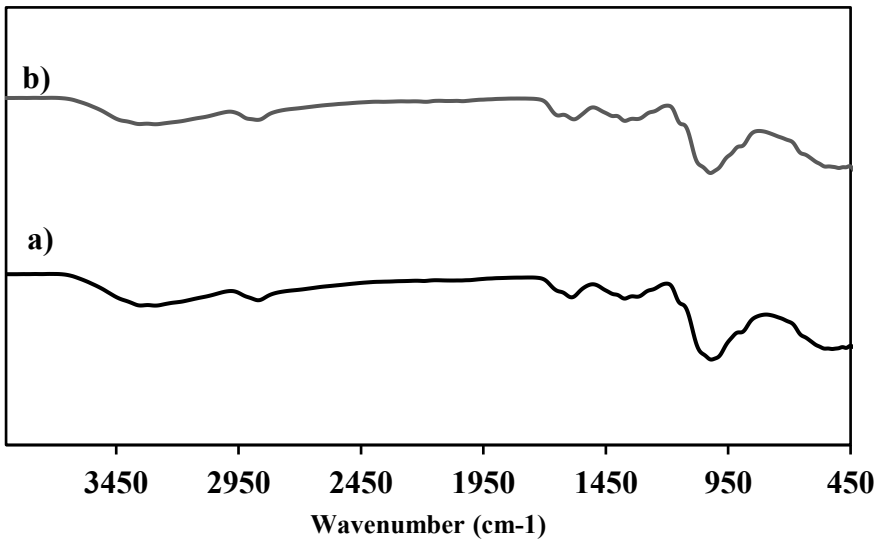

Figure 7.6. FT-IR spectra for a) commercial chitosan and b) [Eth][Ac] produced at the optimum condition (Temperature of 92 ± 5 °C, time of 27.8h, and L/S of 16 g/g).

The SEM images in Figure 7.7 (a-c) reveal that the chitosan produced using [Eth][Ac] exhibits a relatively smooth surface morphology similar to that of commercial chitosan but with noticeably larger particle sizes, due to the absence of a size reduction step. At higher magnification (×10,000), the [Eth][Ac]-derived chitosan shows slightly more surface irregularities, which may enhance its adsorption capacity (Tolesa et al., 2019). Regarding chitosan produced using [Eth][Ac], after adsorption (Figure 7.7(c) at × 10,000), the surface appears more compact and less textured, indicating successful interaction with metal ions. The overall smooth, non-crystalline appearance indicates an amorphous structure, consistent with that observed in commercial chitosan. Figure 8 presents the EDS analysis of [Eth][Ac]-derived chitosan after the adsorption of Co(II), Ni(II), and Mn(II). The presence of the metals is clearly detected, confirming successful adsorption. Among them, Co(II) shows the most prominent peaks, which correspond to its higher concentration in the solution.

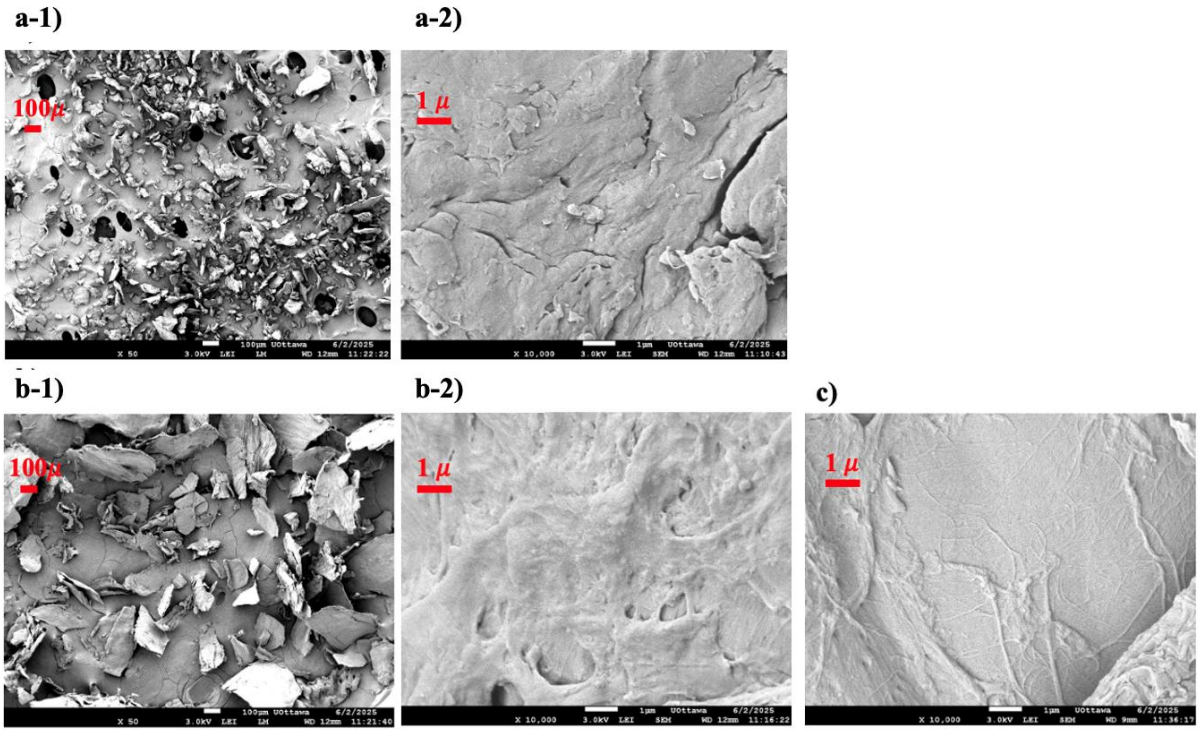

Figure 7.7. SEM analysis of commercial chitosan a-1) × 50 and a-2) × 10,000, the [Eth][Ac]-produced chitosan b-1) × 50 and b-2) × 10,000, and c) the [Eth][Ac]-produced chitosan after adsorption × 10,000.

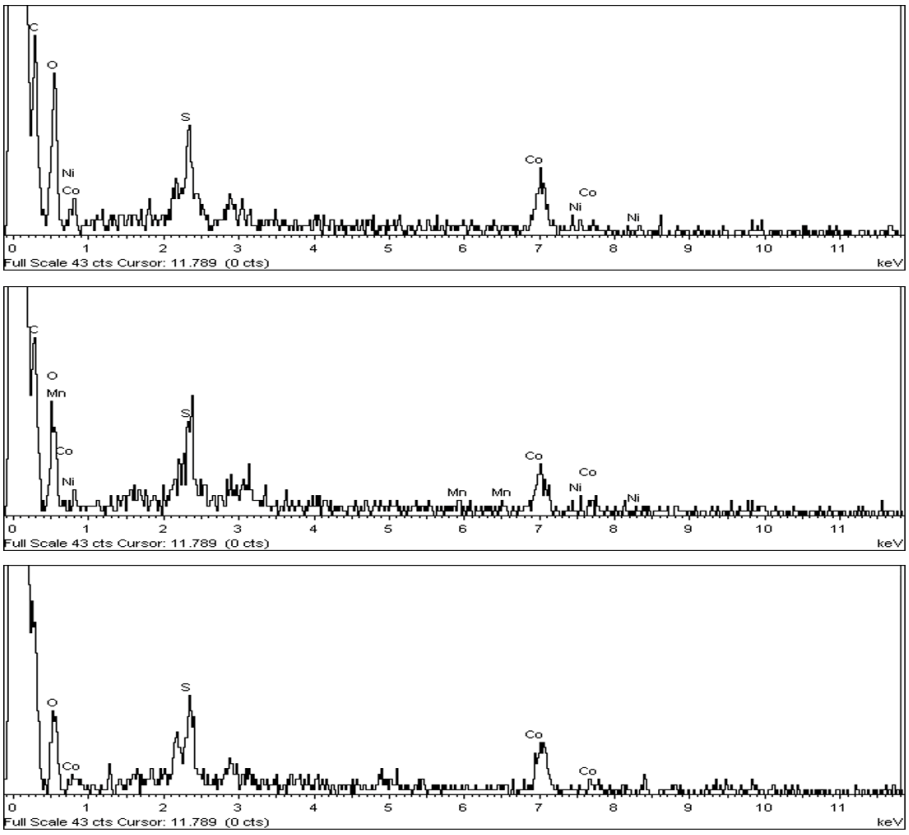

Figure 7.8. SEM-EDS analysis (at 20kV) of different parts of the [Eth][Ac]-produced chitosan after adsorption.

7.4.3. Adsorption Isotherm Study for [Eth]-extracted chitosan

Table 7.4 presents the adsorption uptake and adsorption efficiency of the optimal [Eth]-extracted chitosan powder, examined at four different dilution factors (×50, ×40, ×30, and ×20), to investigate the effect of varying initial concentrations. The results clearly demonstrate the strong affinity of the PLI-extracted chitosan toward Co(II), Ni(II), and Mn(II), leaving Li in the solution with uptake capacities and adsorption efficiencies comparable to those reported for commercial chitosan powders (Roshanfar et al., 2025). This confirms that the green extraction process successfully yielded a high-quality, effective biosorbent capable of competing with commercially available chitosan. Importantly, the observed performance across varying concentrations demonstrates the robustness of the extracted chitosan under different operating conditions, bringing the application closer to a real-world situation. To ensure reliability, each experiment was

triplicated, and the mean values, along with their corresponding standard deviations, were calculated and reported. It should also be noted that the mass of the PLI-extracted chitosan powder, similar to the commercial powder, was carefully monitored after adsorption, and no decrease in weight was observed, confirming the material's structural stability throughout the adsorption process.

Table 7.4. The removal efficiency (%) at different dilution factors using the optimal PLI-extracted chitosan at a pH of 4

Removal efficiency (%)	**Co**	**Mn**	**Ni**	**Final pH**
×50	86.45± 0.24	43.14± 4.70	98.77± 0.21	7.58
×40	82.13± 0.65	41.06± 7.51	97.69± 0.78	7.14
×30	80.54± 0.52	38.53± 1.41	95.42± 1.27	7.07
×20	72.22± 1.67	32.69± 2.78	91.82± 0.53	7.02

For isotherm modeling, the adsorption data for the PIL-extracted chitosan were analyzed using both the Langmuir and Freundlich models to describe the uptake of Co(II), Mn(II), and Ni(II). The results are shown in Figure 7.9 and Table 7.5. The Langmuir model assumes monolayer adsorption onto a homogeneous surface, whereas the Freundlich model accounts for adsorption on heterogeneous sites, allowing for the possible formation of multilayers (Al-Ghouti and Da'ana, 2020; Rahaman et al., 2024).

For the optimal [Eth]-extracted chitosan, the Langmuir maximum adsorption capacities (q_m) were 146.68 mg/g (2.49 mmol/g) for Co(II), 3.77 mg/g (0.07 mmol/g) for Mn(II), and 7.98 mg/g (0.14 mmol/g) for Ni(II). The high values (0.88–0.99, close to 1) confirmed that both the Langmuir and Freundlich models described the data well, with the Freundlich providing a slightly better fit for Co(II) (lower SSR and MSE) and Ni(II) (higher R^2) (Anderson and Whitcomb, 2017). Langmuir

showed a marginally stronger correlation for Mn(II). The Freundlich n_F values ($0 < 1/n < 1$) further indicated favorable adsorption conditions.

Compared with commercially produced chitosan powder (Roshanfar et al., 2025), PIL-extracted chitosan showed significantly enhanced adsorption performance. For Co(II), the commercial chitosan showed a Langmuir maximum capacity of 110 mg/g (1.86 mmol/g), whereas the PIL-extracted chitosan reached 146.68 mg/g (2.49 mmol/g), corresponding to an approximately 33% increase in adsorption capacity. A similar pattern was observed for Ni(II) and Mn(II), with both materials exhibiting lower uptakes than Co(II), but maintaining consistent relative affinities across the metals. These results demonstrate that the PIL extraction strategy not only preserves the inherent adsorption behavior of chitosan but also significantly enhances its adsorption capacity compared with commercial chitosan, underscoring its strong potential as a high-performance, sustainable biosorbent for LIB recycling applications.

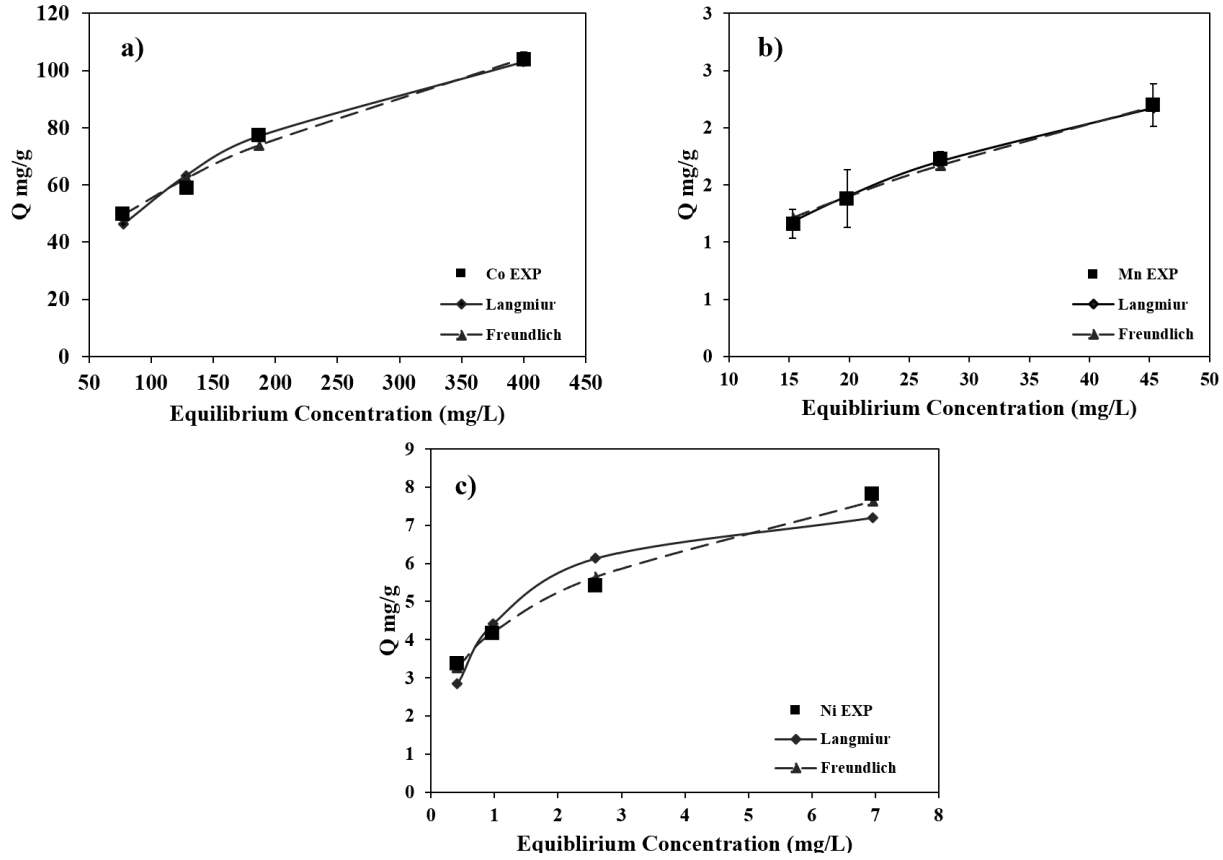

Figure 7.9. Adsorption isotherms and experimental data for: a) Co(II), b) Mn(II), and c) Ni(II).

Table 7.5. Adsorption isotherm parameters

Isotherm model	Parameter	Co (II)	Mn (II)	Ni (II)
Langmuir	K_L (L/mg)	5.92E-03	3.00E-02	1.32E+00
	q_m (mg/g)	146.68	3.77	7.98
	R-squared	0.99	0.88	0.92
	SSR	146.37	0.47	5.61
	MSE	12.20	0.04	0.47
Freundlich	k_F	6.90	0.28	4.26
	n_F	2.21	1.85	3.32
	R-squared	0.99	0.88	0.98
	SSR	131.75	0.46	1.53
	MSE	10.98	0.04	0.13

7.5. Conclusions

This study introduces a sustainable and efficient method for recovering critical metals from shrimp shell waste using green PIL solvents to extract chitosan. A PIL-assisted extraction method was developed as an environmentally friendly alternative to conventional chitosan production processes, avoiding the use of harsh acids and bases. Three PILs, [Tea][Ac], [Teta][Ac], and [Eth][Ac], were evaluated for chitin extraction from shrimp shell waste. Among them, [Eth][Ac] was identified as the optimal medium due to its greener profile, lower toxicity, greater biodegradability, and superior ability to enhance chitosan properties. The resulting chitosan selectively adsorbed Co(II), Mn(II), and Ni(II) from a sulfate-citrate leachate of spent LIBs, leaving Li behind in the solution.

Process optimization (extraction at a temperature of 92 °C, time of 27.8 h, and a liquid-to-solid ratio of 16 g/g) yielded a chitin recovery of 56.67 wt.% and the removal efficiencies of 82.42 ± 1.65% for Co(II), 35.09 ± 2.63 for Mn(II), and 98.30 ± 0.63 for Ni(II), respectively. FT-IR and SEM analyses confirmed a structure comparable to that of commercial chitosan. PIL-extracted chitosan exhibited superior adsorption performance compared with commercial chitosan, owing to its higher specific surface area and improved porosity, as confirmed by BET analysis, and demonstrated a higher Langmuir maximum adsorption capacity.

7.6. References

The references are merged with those of the other chapters and listed at the end of the thesis.

Chapter 8 CROSSLINKED CHITOSAN BIO-ADSORBENT COLUMN FOR CRITICAL METAL RECOVERY FROM SPENT LITHIUM-ION BATTERIES

Submitted as a research article for publication.

8.1. Abstract

Fixed-bed column adsorption offers a practical assessment of adsorbent performance under continuous-flow conditions, where operational parameters are critical. In this study, simultaneous increases in flow rate and bed height revealed that flow rate had a greater influence than bed height and adsorbent mass, with reduced contact time at higher velocities emerging as the dominant factor controlling column performance. Compared with batch equilibrium tests, column adsorption exhibited lower uptake due to mass-transfer limitations and incomplete equilibration, yet maintained clear selectivity for Co(II) and Ni(II) over Li. A two-cycle adsorption-desorption study was conducted to assess reusability, yielding desorption efficiencies of over 80% for Co(II), over 20% for Mn(II), and over 90% for Ni(II). These results confirmed the potential for regeneration. Modeling analysis further showed that the Thomas and Yoon-Nelson equations accurately described the breakthrough curves of Co(II), Mn(II), and Ni(II), with predicted parameters closely matching experimental uptake and breakthrough times. The consistently weaker affinity of Mn(II), compared to Co(II) and Ni(II), was evident across both adsorption and desorption cycles. Importantly, Li concentration remained below 1% in all runs, confirming the system's ability to selectively separate critical metals from Li and underscoring its potential for sustainable recovery of valuable critical metals from spent lithium-ion batteries.

Keywords: Critical metals; Column; Continuous; Adsorption; Chitosan.

8.2. Introduction

As the world moves rapidly towards low-carbon energy systems, lithium-ion batteries (LIBs) have become a fundamental technology supporting this shift. The accelerating electrification across transportation and grid-scale storage is driving unprecedented demand for LIBs. Global battery deployment is projected to exceed 2,000 GWh by 2030, accompanied by a rapid increase in both

manufacturing scrap and end-of-life batteries (Gebeyehu et al., 2025; Kresse et al., 2025). Without effective recovery strategies, this growth trajectory is expected to generate more than 11 million tonnes of spent LIBs by the end of the decade, representing not only a significant environmental liability but also a substantial loss of recoverable critical metals (Chang et al., 2025).

The rapid expansion of lithium-ion battery (LIB) manufacturing has intensified global dependence on a narrow set of critical mineral supply chains. Lithium (Li), cobalt (Co), nickel (Ni), and manganese (Mn) are indispensable to modern battery chemistries, yet their production remains geographically concentrated, exposing energy-transition technologies to significant geopolitical and market vulnerabilities. Current estimates indicate that more than 70% of cobalt is produced in the Democratic Republic of Congo, while 71% of lithium is sourced from Australia and Chile, underscoring the fragility and geopolitical risks of existing supply networks (Gantz et al., 2025). Ensuring long-term energy security and sustainability requires not only efficient recovery of these critical materials but also a more equitable global distribution of their availability.

In response to the above challenges, regulatory and policy frameworks, such as the European Union Battery Regulation, have introduced mandatory recovery targets and recycled-content requirements, including 50% lithium recovery from end-of-life LIBs by 2027 and 80% by 2031 (Gantz et al., 2025). However, current global recycling capacity remains limited at approximately 2 million tons per year, representing only a fraction of projected waste volume, and is heavily concentrated in China, which accounts for 85% of existing capacity. Bridging this gap will require the development of scalable, efficient, and sustainable recycling technologies that reduce reliance on primary extraction and enhance the resilience of critical metal supply chains within the circular battery economy (Gebeyehu et al., 2025).

Although both pyrometallurgical and hydrometallurgical processes are widely used for recycling spent LIBs, the efficient separation of dissolved metals such as Li, Co, Ni, and Mn from cathode active materials after leaching remains a major bottleneck to process scalability (Ma et al., 2025; H. Wang et al., 2025). Hydrometallurgical processes are generally preferred for their lower energy consumption and high metal leaching efficiency. They rely on strong chemical reagents that pose environmental risks, and they involve complex multi-step purification stages that can lead to low recovery rates (Lim et al., 2025; H. Wang et al., 2025). Conventional post-leaching techniques, including chemical precipitation, solvent extraction, ion exchange, and electrochemical

deposition, often suffer from high reagent consumption, limited selectivity in mixed-metal systems, operational complexity, and secondary waste generation, which collectively hinder large-scale implementation (Lim et al., 2025). Adsorption-based separation has emerged as a promising alternative, particularly for treating metal-rich leachate due to its operational simplicity, modularity, scalability, cost-effectiveness, capacity to selectively capture target metal ions under relatively mild conditions, and ability to minimize secondary waste generation (Robeck and Horn, 2024b; H. Wang et al., 2025).

Recently, adsorbent materials derived from sustainable sources and waste streams, such as chitosan, have attracted increasing attention due to their environmental compatibility and functional versatility. Chitosan, a biopolymer obtained from crustacean waste, exhibits strong metal-binding capacity due to its abundant hydroxyl and amine functional groups, making it particularly suitable for selective adsorption in acidic, multi-metal solutions (Manickasundaram et al., 2024; Syeda et al., 2024). Chitosan-based adsorbents are biodegradable, non-toxic, regenerable, and modifiable, making them suitable for environmentally responsible recovery of metals from LIB leachates and other waste streams. Integrating waste-derived biopolymers into fixed-bed adsorption systems thus represents a viable pathway to reduce process complexity, enhance metal selectivity, and align with circular-economy principles in LIB recycling.

Several chitosan-based adsorbents have shown promising performance at batch-mode, including GO/CS/CMC composites with Co(II), chromate, Mn(II), and Cd(II) uptakes of up to approximately 43.55, 77.70, 57.78, and 91.38 mg/g, respectively (Rahaman et al., 2024b), chitosan-grafted polyimide fibres achieving 46 mg/g for Co(II) (Sun et al., 2024), chitosan-magnetic biochar with 122 mg/g for Cr(VI) (Yu et al., 2024), chitosan/TPP nanoparticles with 78% removal efficiency (Promkatkaew et al., 2023), and Fe_3O_4-chitosan nanocomposites with capacities up to 53 mg/g for Co(II) (Sharifi et al., 2023). However, all the above studies were conducted using synthetic solutions in batch systems at relatively low concentrations, limiting their applicability to more practical continuous column operations. To address these limitations, authors have tested the proof-of-concept for chitosan-based bead production tailored for LIB recycling, with potential application for column-based continuous operation. L-cysteine-crosslinked chitosan beads (CB1%CYS) selectively removed metals (Co(II), Ni(II), and Mn(II)) from a realistic, high-

strength LIB leachate, while lithium remained in solution, confirming process-relevant selectivity (Roshanfar et al., 2026, 2025, 2024).

Although batch adsorption experiments have been widely used at the laboratory scale to screen adsorbents, assess process feasibility, elucidate adsorption mechanisms, and estimate equilibrium capacities under well-controlled conditions (Conte and Gómez, 2024; Lin et al., 2025; J. Liu et al., 2024; H. Wang et al., 2025), they do not adequately represent the continuous operation and mass-transfer behavior observed in industrial treatment systems (Malbenia John et al., 2024). As solution volumes increase and adsorption sites approach saturation, batch systems exhibit reduced efficiency and limited throughput, restricting their applicability largely to preliminary feasibility assessment (Patel and In, 2021). To overcome these limitations, adsorption processes are more effectively implemented in fixed-bed (packed-column) configurations, in which metal separation is governed by dynamic breakthrough behavior rather than by equilibrium uptake alone. In such systems, performance is typically evaluated using breakthrough curves and dynamic models, including the Thomas and Yoon-Nelson approaches, which enable quantitative assessment of column capacity, service time, and scale-up potential (Patel, 2022). As a result, fixed-bed column adsorption, often operated at the laboratory-scale or mini-pilot scale, serves as a critical intermediate step between batch adsorption experiments and full-scale industrial deployment. Under continuous-flow operation, metal-bearing solutions pass through a packed adsorbent bed, allowing sustained contact, improved control over hydrodynamic and mass-transfer conditions, and consistent treatment of large solution volumes. (Malbenia John et al., 2024; Robeck and Horn, 2024). The column configuration facilitates realistic assessment of adsorption kinetics and supports systematic optimization of key process parameters, such as bed height, flow rate, pH, and influent concentration, through breakthrough curve analysis (Rahman et al., 2025). Recent studies have demonstrated that low-cost, waste-derived adsorbents can perform effectively in such dynamic systems. For instance, Rahman et al. (2025b) has achieved an adsorption capacity of 179.77 mg/g for lead ion (Pb(II)) using rice husk-derived activated biochar.

Authors' previous results validated the mechanical integrity, selectivity, and operational relevance of chitosan beads under batch conditions, thereby justifying the present study to further evaluate their performance under column and application-oriented conditions for practical LIB recycling. Therefore, this study aims to advance adsorption-based selective recovery of critical metals from

a real multi-metal leachate generated by a synergistic citrate-sulfate leaching process applied to mixed spent LIB cathode materials by investigating the dynamic performance of a mini-pilot fixed-bed column packed with chitosan beads crosslinked with 1 wt. % L-cystine (CS1%CYS) and operated under continuous-flow conditions. The spent LIB cathode mixture contained lithium cobalt oxide (LCO), lithium nickel manganese cobalt oxide (NMC), and lithium manganese oxide (LMO). Unlike most previous adsorption studies that rely on batch experiments and synthetic single-metal solutions, this work focuses on column operation with realistic, multi-metal real-feed chemistry, thereby capturing mass-transfer behavior and competitive adsorption effects. The primary objective of the study is to achieve selective dynamic adsorption of Co(II), Ni(II), and Mn(II) while retaining lithium predominantly in the aqueous phase, thereby enabling targeted metal separation within an integrated LIB recycling framework. Column performance is assessed through breakthrough curve analysis to evaluate adsorption capacity, service time, selectivity, and the effectiveness of regeneration and reuse under continuous operation. By bridging batch adsorption screening and full-scale implementation, this mini-pilot investigation provides critical proof of concept for translating waste-derived adsorbent systems into scalable, sustainable separation technologies for next-generation LIB recycling.

8.3. Materials and Methods

8.3.1. Materials and Sample Preparation

Spent LIBs from various devices (laptops, cellphones, and Li-polymer batteries) and brands (LG, Samsung, TechTrex Inc., and Motorola) were collected from a recycling facility in Toronto, Canada. The cells were discharged in 10% NaCl for 24 h, manually disassembled, and cathode materials combined (black mass (BM)) at a 1:1:1 weight ratio. The BM was calcined at 570 °C to remove binders, then leached in a synergistic solution of 1.25 M H_2SO_4 and 0.55 M citric acid at 90 °C for 2 h (S/L = 62.5 g/L), yielding a pregnant leach solution without the use of reducing agents (Roshanfar et al., 2024). The obtained pregnant solution was diluted 30-fold with deionized water, and its pH was adjusted to 4 (Roshanfar et al., 2026, 2025). Analytical-grade reagents, including sulfuric acid (98%), citric monohydrate (99%), acetic acid (99.7%), chitosan (85% DD), NaOH, L-cystine (99%), and Ethylenediaminetetraacetic acid (EDTA, disodium salt dihydrate),

were obtained from Fisher Chemical and Thermo Scientific. All solutions were prepared using deionized water.

8.3.2. Characterization and Analytical Methods

To compare the surface chemistry before column adsorption, after column adsorption, and following EDTA regeneration of chitosan beads crosslinked with 1 wt. % L-cystine (CS1%CYS), Fourier-transform infrared spectroscopy (FT-IR; IS50, Thermo Scientific) was performed over 4000-450 cm^{-1}. Elemental composition was also analyzed by energy-dispersive X-ray spectroscopy (EDS; Oxford detector, 30 kV) using INCA software. The initial metal concentrations in the mixed cathode BM (1:1:1) were determined by ICP-OES (Agilent 5110) after aqua regia digestion (HNO_3:HCl = 1:3) at 120 °C overnight. During the column study, metal concentrations were measured by atomic absorption spectroscopy (AAS; PinAAcle 500, PerkinElmer), with calibration performed using a nonlinear method with a zero intercept. Each result represents the average of three replicates. The solution pH was monitored using a HACH HQ40D meter.

8.3.3. Preparation of CS1%CYS

CS1%CYS were prepared following a modified procedure based on previous studies (Babakhani and Sartaj, 2022a; Roshanfar et al., 2026). In short, 3.2 g of chitosan was dissolved in 80 mL of 5% acetic acid and stirred at 30 °C for 24 h. Then, 1 wt.% L-cystine was introduced as a crosslinking agent, and the solution was dropped into a 0.6 M NaOH bath to form spherical CS1%CYS beads, which were subsequently washed and air-dried.

8.3.4. Column Study

Column experiments were performed using a 100 cm clear glass column (inner diameter: 2.2 cm; ACE Glass, NJ) packed with crosslinked chitosan beads (CS1%CYS). Two-column runs were conducted at fixed-bed heights of 21.5 cm and 27.5 cm, corresponding to geometric volumes of 82 cm^3 and 105 cm^3, respectively, with two flow rates of 2.33 and 4.33 mL/min. The packed beds in this study exhibited an average inter-particle porosity of approximately 41%, corresponding to effective bed volumes (BVs) of 33.6 mL and 43.1 mL, respectively. A glass perforated disk (2.1

cm diameter) was placed within the bed to promote uniform flow, and a coarse filter at the bottom to support and hold the beads. Figure 8.1 illustrates the experimental setup of this study.

8.3.4.1. Loading Cycle

In stages a to c, the fresh beads begin to adsorb the critical metals (Co(II), Mn(II), and Ni(II)), as indicated by a color change and the development of the mass-transfer zone. The coloration corresponds mainly to Co(II), as it is the dominant metal in the sample. Figure 8.1(c) presents the column at saturation after the adsorption process. It should be noted that the Li concentration was consistently below 1% across all cases, demonstrating the high selectivity achieved in separating critical metals from Li.

A diluted leaching solution of the battery cathode materials (dilution factor 30), containing 964 ± 4.7 mg/L Co, 46.10 ± 1.08 mg/L Mn, 60.10 ± 0.61 mg/L Ni, and 133.33 ± 4.10 mg/L Li, was introduced at a constant flow rate using a peristaltic pump in down-flow mode. It should be noted that, under all conditions, the effluent flow rate was continuously monitored and verified during the column experiments to ensure stable operation. The reported flow rates are the average ± standard deviation (SD) measured during each experimental run. Effluents were collected at set intervals and analyzed for metal concentrations. As the adsorption zone migrated downward, effluent concentrations increased until reaching 95% of the inlet concentration, defined as the bed saturation time (t_s). During the loading experiments, metal uptake by the CS1%CYS beads was determined from the breakthrough curves using a mass-balance approach. The total adsorption (q_{column}) was calculated using Eq. 1 (Kalavathy et al., 2010). To determine $m_{ad,}$ the area under the breakthrough curve, it was integrated using the trapezoidal rule:

$$q_{Column} = \frac{1}{M}\sum_{i=2}^{n}\left(C_{Feed} - \frac{C_{effi}+C_{effi-1}}{2}\right) \times (V_i - V_{i-1}) \quad (8\text{-}1)$$

where q_{column} (mg/g) is the dynamic uptake for a given species, C_{Feed} is the influent concentration (mg/L), C_{Effi} and $C_{Eff(i-1)}$ are effluent concentrations at sampling times i and i-1, and (V_i-V_{i-1}) is the treated volume between two samples (L). The column adsorption capacity (q_{column}) was also

verified by a mass balance calculation using the total volume of the treated solution and the influent and effluent metal concentrations.

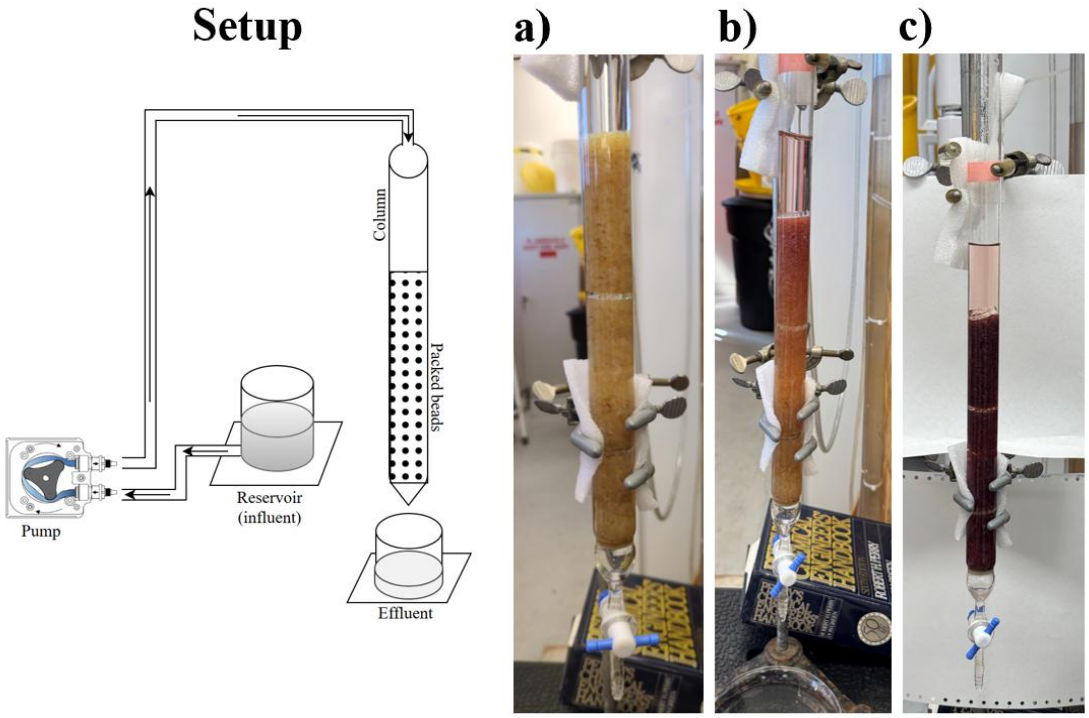

Figure 8.1. Setup of the column study and adsorption stages from a) fresh beads, b) mass transfer zone, and c) saturation.

8.3.4.2. Regeneration Cycle

After the initial loading experiment at a flow rate of 4.33 ± 0.39 mL/min, the column was regenerated by circulating 0.5 M EDTA in downflow mode at 2.36 ± 0.31 mL/min. For the second adsorption-desorption cycle, the column was operated with the same beads as in the first cycle. The EDTA concentration increased to 1.0 M, and the flow rate was maintained at 2.13 ± 0.31 mL/min. Prior to use, the pH of all EDTA solutions was adjusted to 9.5 to enhance metal desorption (Vakili et al., 2019). The loading experiments were continued until the effluent concentration

reached 95% of the influent concentration, and desorption was performed until the residual metal content in the column dropped below 5%.

8.3.5. Mathematical Models for Continuous Column Adsorption

Mathematical modeling of fixed-bed adsorption columns is essential for predicting breakthrough behavior, optimizing operating conditions, and scaling up adsorption processes. Among various models, the Thomas and Yoon-Nelson models are widely applied due to their simplicity, reliability, and ability to describe experimental breakthrough curves (Malbenia John et al., 2024; Patel and In, 2021; Rahman et al., 2025b, 2025a).

8.3.5.1. Thomas Model

The Thomas model is among the most widely used models for describing breakthrough behavior in a fixed-bed column and for analyzing factors affecting the adsorption process. It is based on second-order reversible reaction kinetics, assuming no axial dispersion, even when the bed depth is small, and breakthrough occurs soon after flow begins. This model assumes that adsorption follows the Langmuir isotherm and is widely used to predict experimental data from both batch and continuous systems. It is especially effective when the adsorption process is driven by a combination of chemical reaction kinetics and mass-transfer mechanisms occurring at the adsorbent surface. The model's strength lies in its ability to predict the breakthrough curve and evaluate both the kinetic and equilibrium parameters simultaneously, making it a valuable tool for column design and optimization (Khanam et al., 2025; Rahman et al., 2025b). The Thomas model is formulated as:

$$\frac{C_t}{C_0} = \frac{1}{(1+\exp\left(\left(\frac{k_{Th}}{Q}\right)(q_{Th}m - C_0Qt)\right))} \tag{8-2}$$

where C_0 (mg/L) represents the initial concentration of the feed solution, and C_t (mg/L) is the effluent concentration at a specific time t (min). The parameter k_{Th} (mL/(min.mg)) denotes the

Thomas rate constant, while q_{Th} (mg/g) indicates the maximum solid-phase adsorption capacity of the bio-adsorbent. m (g) refers to the mass bio-adsorbent used in the column, and Q (mL/min) corresponds to the volumetric flow rate of the pregnant solution through the fixed-bed downflow column.

8.3.5.2 Nelson-Yoon Model

The Yoon-Nelson model is another widely used model for describing fixed-bed column adsorption due to its simplicity and minimal parameter requirements. Unlike the Thomas model, it does not require detailed information about the adsorbent's properties, the bed's physical parameters, or the adsorbate's composition, making it broadly applicable. This model assumes that the rate of decrease in the adsorption probability is directly proportional to the adsorbate's breakthrough probability on the adsorbent. Its main utility lies in predicting the time required for a 50% breakthrough of the adsorbate (Khanam et al., 2025; Patel and In, 2021; Rahman et al., 2025b). The Yoon–Nelson model is given by:

$$\frac{C_t}{C_0} = \frac{1}{1+\exp\left(k_{YN}(t-\tau)\right)} \tag{8-3}$$

C_0 and C_t (mg/L) represent the concentrations of critical metals at time (t). k_{YN} indicates the Yoon–Nelson model's rate constant (min^{-1}), and τ represents the half-life of the experimental adsorption column, or the time to reach 50% of the breakthrough curve (BTC).

8.4. Results and Discussion

8.4.1. Characterization

The particle size of the synthesized beads was determined by sieve analysis. The CS1%CYS beads exhibited a narrow particle-size distribution of 1.18-1.70 mm (passing through mesh #12 and retained on mesh #16), ensuring uniform packing in the fixed-bed column. FT-IR spectroscopy was used to compare spectra of the beads before and after the column study and after EDTA

desorption to evaluate functional-group stability during adsorption-desorption cycles. Figure 8.2 shows FT-IR spectra of CS1%CYS in the range of 4000-450 cm^{-1}, with (a) before the column adsorption, (b) after adsorption, and (c) after EDTA desorption. The broad band at approximately 3273 cm^{-1} arises from overlapping O-H/N-H stretching, while the C-H asymmetric and symmetric stretches appear at 2921/2887 cm^{-1}. Additional polysaccharide features include amide I (C=O) near approximately 1650 cm^{-1}, amide II (N-H bending and C-N stretching) at approximately 1560–1590 cm^{-1}, and C-O-C/C-O vibrations at approximately 1155-1020 cm^{-1} (Babakhani and Sartaj, 2022a). A thiol functionality is present, evidenced by a weak S–H stretch at approximately 2550-2600 cm^{-1} and C-S vibrations in the 700-600 cm^{-1} region, consistent with thiol grafting and crosslinking (Hamza et al., 2022). After adsorption (Figure 8.2(b)), the intensities of the bands at 3273 and 2921 cm^{-1} decrease, and small shifts are observed in the amide I/II and C-N regions, indicating the participation of amine and hydroxyl groups in metal binding-amines mainly coordinating Co(II) and Ni(II) through chelation, with hydroxyl groups contributing (for example, to Mn(II) uptake) via hydrogen bonding and electrostatic interactions. Following EDTA treatment (Figure 1(c)), these bands largely return toward their pre-adsorption positions and intensities, demonstrating reversible coordination and the restoration of active functional groups. Figure 8.3 shows the EDS analysis after column adsorption and after EDTA desorption. After adsorption, as shown in Figure 8.3(a), the EDS spectrum displays clear metal signals, with Co(II) being the most prominent, consistent with its higher concentration. Following EDTA desorption, Figure 8.3(b), the peaks for Co(II), Ni(II), and Mn(II) decrease to the spectral baseline (i.e., below the practical EDS detection limit). The Na peak also appears, consistent with residual Na-EDTA. These results demonstrate effective metal removal and adsorbent regeneration.

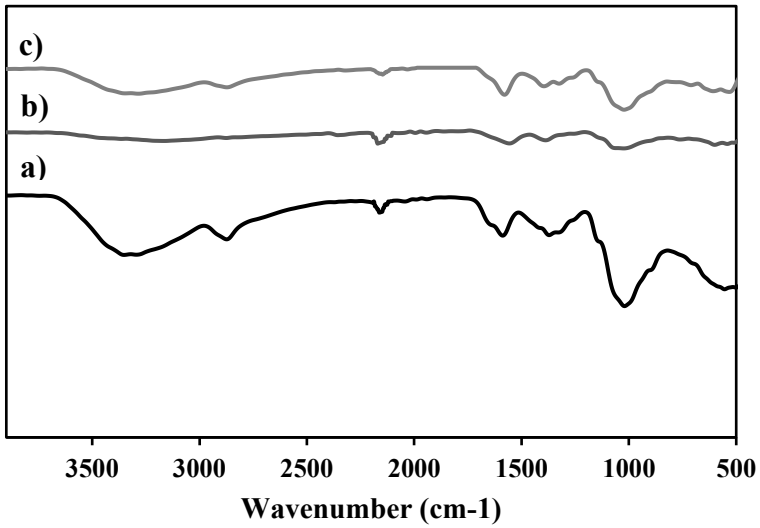

Figure 8.2. FT-IR spectra for the CS1%CYS beads: a) before column study, b) after column study, and c) after desorption using EDTA.

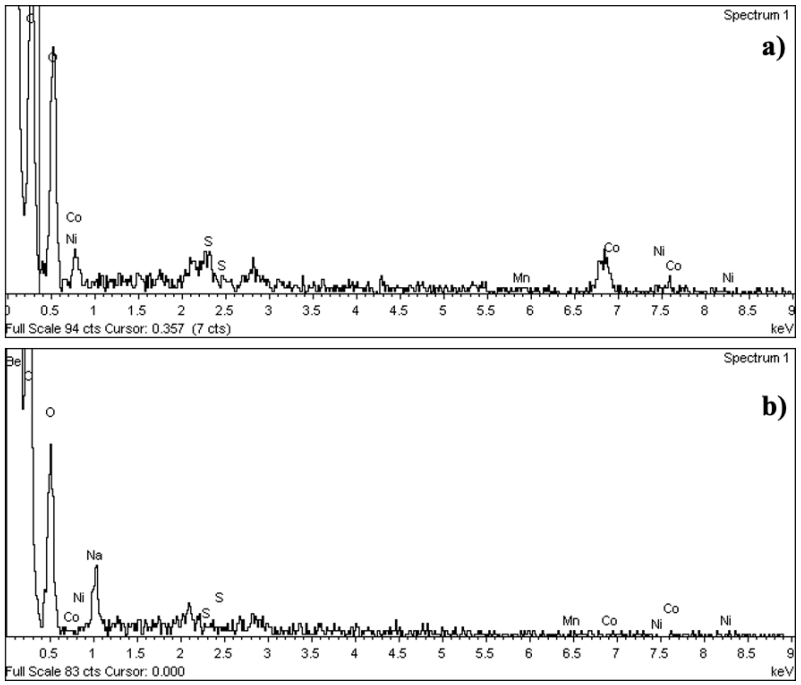

Figure 8.3. EDS analysis (at 20kV) of a) after adsorption of the metals, b) after desorption using EDTA.

8.4.2. Fixed-Bead Column Study

8.4.2.1. Effect of Variables on Breakthrough Curve

Two experimental column configurations were investigated. The first configuration employed a flow rate of 2.33 ± 0.14 mL/min with a bed height of 21.5 cm, corresponding to 25 g of adsorbent. The second configuration was conducted to address limitations associated with such high influent metal concentrations and to better approximate practical operating conditions. At such high influent concentrations, the increased flow velocity (4.34 ± 0.39 mL/min) can increase the risk of channeling and short-circuiting (Malbenia John et al., 2024), thereby reducing the effective contact time between the solution and the adsorbent bed. To counterbalance this effect and ensure more uniform mass transfer, the bed height was increased to 27.5 cm with a corresponding adsorbent mass of 31.5 g. The effects of these configuration changes on the breakthrough behavior of Co(II), Mn(II), and Ni(II) are presented in Figures 8.4 and 8.5. The breakthrough curves are shown as C_t/C_0 versus time and versus the number of processed bed volumes, calculated as the cumulative treated solution volume normalized by the void bed volume. Figure 8.5 presents the breakthrough profiles of all metals together to enable direct comparison of their competitive adsorption behavior, as well as the cumulative adsorption uptake (mg/g) of each metal ion with respect to the number of bead volumes. It is important to note that Li remained fully in solution throughout all column experiments, confirming the selectivity of the separation process.

In the first configuration, a total of 2.81 L of leachate was processed through the column until saturation was achieved, corresponding to saturation percentages of 97% for Co(II), 91% for Mn(II), and 89% for Ni(II). In this study, the saturation point was selected using Co(II), as it was the predominant metal in the leaching solution. When the flow rate was increased to 4.34 ± 0.39 mL/min, the treated volume increased to 3.51 L, consistent with the higher throughput associated with higher flow rates. Since the column cross-sectional area remained constant (3.8 cm^2), the reduced contact time allowed a greater volume of solution to pass before saturation, resulting in saturation percentages of 97% for Co(II), 95% for Mn(II), and 83% for Ni(II). As a result of these operational adjustments, the overall process time decreased from 21.6 h to 14.3 h. Generally, reducing the flow rate and increasing the bed height improve column performance, as longer residence times and greater adsorbent mass enhance mass transfer and delay breakthrough. In

fixed-bed adsorption systems, additional height provides both more bio-adsorbent and an extended diffusion path (Malbenia John et al., 2024; Sazali et al., 2020). In this study, however, where flow rate and bed height were increased simultaneously, the effect of flow rate outweighed that of height and adsorbent mass, indicating that reduced contact time at higher flow velocity was the dominant factor governing column performance.

Considering Co(II), the breakthrough time (t_b, defined at 5% of C_0) was 50 min at a flow rate of 2.33 ± 0.14 mL/min and 20 min at 4.34 ± 0.39 mL/min. In both cases, the breakthrough occurred relatively early, due to the high influent concentration, which rapidly saturated the available adsorption sites. The shorter t_b observed at the higher flow rate is further explained by reduced contact time and an increased likelihood of channeling, both of which limit effective adsorption within the column (Vijayaraghavan et al., 2005). The 50% adsorption also followed the trend of increasing flow rate, decreasing from 6.8 h to 4.3 h.

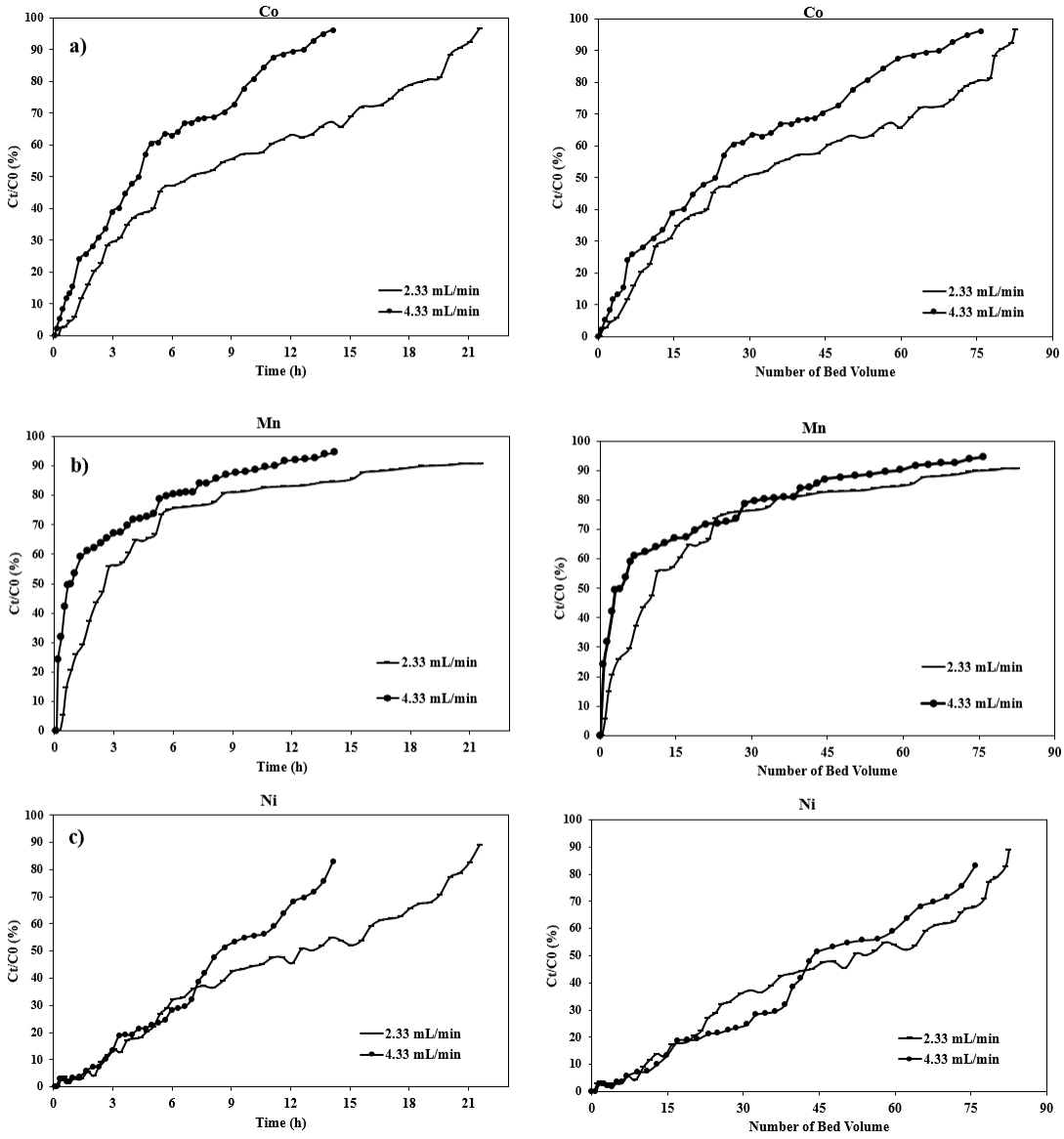

Figure 8.4. Breakthrough curves under various conditions for a) Co, b) Mn, and c) Ni.

According to Figures 8.5(a) and 8.5(c), in this leaching solution, fixed-bed adsorption is competitive among Co(II), Ni(II), and Mn(II). A comparison of breakthrough curves shows that Mn(II) reached 50% of its influent concentration earlier than Co(II) and Ni(II), indicating a faster breakthrough through the bed. This matches the batch results (Roshanfar et al., 2026), in which Mn(II) exhibited the lowest adsorption efficiency (31.18% ± 0.63) and slower kinetics, suggesting

weaker interactions with the adsorbent. Co(II) exhibited intermediate behavior, with a saturation efficiency of approximately 69.55% ± 0.77 in batch experiments and thus reached a breakthrough after Mn(II) but before Ni(II). Despite having a lower influent concentration than Co(II), Ni(II) exhibited the slowest breakthrough in the column, consistent with batch data indicating the highest adsorption efficiency (91.62% ± 0.88) and the fastest kinetics. Batch results showed that the adsorption of Co(II) and Ni(II) is spontaneous, whereas Mn(II) is not. This thermodynamic behavior supports the observed column trends. The system's competitive nature explains why Co(II), despite its higher concentration, does not dominate the bed as strongly as expected, since Ni(II) has a stronger affinity for the adsorbent. Overall, the column results support the batch findings, highlighting that adsorption selectivity is influenced not only by concentration but also by kinetic and thermodynamic factors in multicomponent systems (Jock and Oluwadayo, 2023).

Beyond breakthrough times, the steepness of the curves provides insight into the mass transfer dynamics (Al Mesfer et al., 2020; Rafati et al., 2019). The relatively sharp breakthrough of Mn(II) suggests weak retention and a narrow mass transfer zone (MTZ), whereas Ni(II) exhibited a more gradual breakthrough, consistent with its stronger affinity and broader MTZ. Co(II) demonstrated intermediate behavior, reflecting both its higher influent concentration and moderate affinity. These trends are consistent with the batch data, where Ni(II) showed the highest uptake and spontaneous adsorption, Co(II) displayed moderate performance, and Mn(II) was least favored under competitive conditions.

The competitive behavior among the metals in the multi-component system was also confirmed in Figures 8.5(b) and 8.5(d), which show the corresponding cumulative uptake (q_{Column}) as a function of the number of void-bed volumes processed, indicating progressive capacity development. For both flow rates, Co(II) exhibited the highest uptake, followed by Ni(II) and Mn(II) (also Table 8.1). Increasing the flow rate from 2.33 to 4.34 mL/min reduced the column adsorption capacity for all metals. Co(II) showed the most significant decrease (~15%), followed by Mn(II) (~11%), while Ni(II) exhibited only a minor reduction (~3%). These results indicate that higher flow rates negatively affect metal uptake, particularly for Co(II) and Mn(II), due to reduced contact time and mass-transfer limitations. It should be noted that during the adsorption experiments, the pH was continuously monitored; in all runs, it increased from 4 (initial pH) to approximately 6.5-7 until

the 50% breakthrough point, then gradually decreased, returning to pH 4 at column exhaustion. The observed increase in pH during adsorption is due to proton exchange and deprotonation of chitosan's amine groups upon metal binding. As the adsorption sites become saturated, proton exchange decreases, and the effluent's composition begins to match that of the influent solution, causing the pH to revert to its original level at the column exhaustion. For example, Figure 8.6(e) shows the effluent pH trend at a flow rate of 4.34 ± 0.39 mL/min.

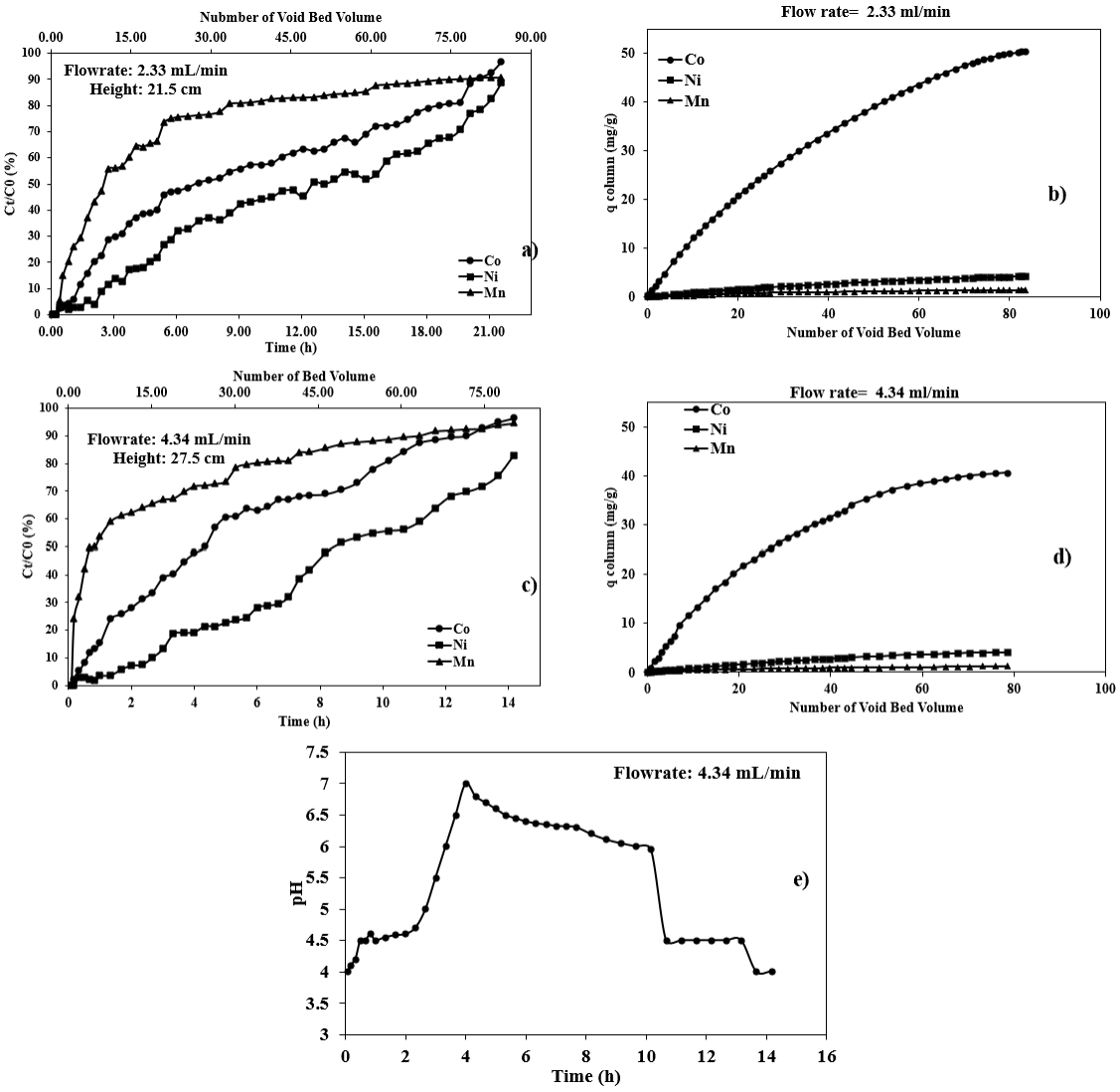

Figure 8.5. Breakthrough curves and adsorption uptakes (mg/g) for all metals: a) and b) flow rate of 2.33 ± 0.14 mL/min and height of 21.5 cm, c) and d) flow rate of 4.34 ± 0.39 mL/min and height of 27.5 cm, as well as e) pH trend of the effluent for the loading column at the flow rate of 4.34 ± 0.39 mL/min.

Table 8.1 shows the batch isotherm adsorption capacity estimated at pH 4 with an initial concentration of 964 ± 4.7 mg/L for Co(II), 46.10 ± 1.08 mg/L for Mn(II), 60.10 ± 0.61 mg/L for Ni(II), and 133.33 ± 4.10 mg/L for Li (Roshanfar et al., 2026) and those obtained from column

runs in this study. The results indicate that the adsorption capacity from batch isotherms is higher than what is achieved in column operation. For example, Co(II) uptake was estimated at 51.34 mg/g and 43.83 mg/g in columns at flow rates of 2.33 ± 0.14 mL/min and 4.34 ± 0.39 mL/min, respectively, compared with 100.97 mg/g estimated for batch adsorption mode. This decrease highlights the effects of flow dynamics, mass-transfer resistance, and incomplete equilibration in column systems, resulting in lower practical uptake than under equilibrium conditions in batch experiments (Patel and In, 2021). Additionally, increasing the flow rate from 2.33 ± 0.14 to 4.34 ± 0.39 mL/min further reduces the adsorption capacities, likely due to a shorter contact time between the adsorbate and the adsorbent, which limits diffusion into active binding sites (Malbenia John et al., 2024).

Table 8.1. Comparison of batch isotherm adsorption capacities and column adsorption uptakes at different variables

Q (mg/g)	Co(II)	Mn(II)	Ni(II)
Batch Langmuir isotherm	100.97	2	10.98
Column- 2.33 mL/min	51.34	1.44	4.3
Column 4.34 mL/min	43.83	1.28	4.17

Table 8.2 compares results from existing studies with those of the current research. Compared to the literature, this study offers several key advantages. While most previous column studies used relatively low influent concentrations (typically 5-50 mg/L), this study employed significantly higher influent concentrations (964 ± 4.7 mg/L Co, 46.10 ± 1.08 mg/L Mn, 60.10 ± 0.61 mg/L Ni, and 133.33 ± 4.10 mg/L Li), thereby more closely replicating real-world effluent conditions. The flow rates used (2.33-4.33 mL/min) fall within the range reported in earlier studies (1-12 mL/min), ensuring comparability and proving the system's operational feasibility. Notably, the CS1%CYS beads exhibited selective separation, with significantly higher uptake of Co(II) and Ni(II) than Mn(II), whereas Li was not adsorbed. Although the adsorption capacities are moderate relative to

some low-concentration systems reported in other studies, the ability to achieve meaningful breakthrough and saturation times under high-strength influent conditions demonstrates the robustness and practical importance of this research.

Table 8.2. Literature comparison with the results of this study

Metals	Adsorbents	Column Conditions	Flowrate (mL/min)	Inflow Metal Concertation	Results	Ref.
Pb(II), Cd(II), As(III), Cr(VI)	Sand enriched with Graphene Oxide	2.5 cm diameter × 16.5 cm height; 140 g sand + 140 mg GO	1	10 mg/L (single and mixed solutions)	q_{column} from Thomas model in mixed media: Pb(II): 283.1 mg/g, Cd(II): 64.6 mg/g; As(III): 15.5 mg/g (decrease from single media 14%, 21%, 39%) Saturation time: Pb(II), Cd(II), and As(III): 10.83 h, 4.23 h, and 2.57 h	(Abbasi et al., 2021)
Dy(III) and Nd(III)	Modified phosphorylated chitosan resin (PCs/MB)	1 mL syringe, 0.5 cm diameter × length 8 cm; 0.6, 1.4, and 1.8 cm (corresponding to 0.045–0.13 g adsorbent).	0.1 -0.43	Dy(III) and Nd(III): 12–15 and 12 mg/L usually at pH 5.2;	In batch: 34 mg/g (maximum equilibrium). In column (1.8 cm bed): 6.35 mg/g Saturation time: 180–260 min, depending on flow cycle	(Romal et al., 2025)

					single-component systems; Thomas: Pb(II): 41.3 mg/g	
Pb(II) and Cd(II)	Rice husk–derived activated biochar (RHB-AC)	2 cm diameter × 20 cm height; 5 g biochar; bed height: 2.5–7.5 cm	2–6	50 mg/L	Cd(II): 38.2 mg/g Saturation time **(**2.5 cm bed height and 2 mL/min)**:** Pb(II) and Cd(II) 420 and 400 min	(Rahman et al., 2025b)
Pb(II)	Two-layer system: Partially hydrolyzed acrylamide-grafted alkali-lignin hydrogel (AM-g-AL)**.** Composite beads of Fuller's Earth + Activated Carbon + Carboxymethylcellulose (FE-CMC-AC)**.**	1 g AM-g-AL hydrogel + 0.5 g FE-CMC-AC beads + 100 g sand	1–10	5-100 mg/L	Individual adsorbents (batch): AM-g-AL hydrogel: 111.2 mg/g FE-CMC-AC beads: 278.45 mg/g Packed column (all layers): 476.75 mg/g (total capacity) Saturation: after 17 L of 100 mg/L Pb	(Khanam et al., 2025)
REE mixtures: Nd, Gd, Ho	Polymeric resin beads (divinylbenzene-crosslinked polystyrene,	0.46 cm diameter × bed depth 4.98 cm	0.1–0.5	0.1–10 mg/L each	Multi-element column test: q= 1.99 mg-REE/g 80% after 600 bed volume	(Callura et al., 2021)

	~0.6 mm) functionalized with N,N-bis(phosphonomethyl)glycine (BPG) ligands.					
Co(II) and Ni(II)	brown seaweed *Sargassum wightii*	2 cm diameter × length 35 cm; 15, 20, 25 cm (7.05–11.73 g biomass); pH: 4.5 for Co(II), 4.0 for Ni(II).	5, 10, 20	100 mg/L	Column uptake capacities at optimal conditions (25 cm bed height, 5 mL/min): Co(II): 50.69 mg/g and Ni(II): 39.74 mg/g Saturation time: Co(II) and Ni(II) 25.2 h and 21.9h	(Vijayaraghavan et al., 2005)
Cu(II), Zn(II), Ni(II), Ag(II),	Polythiosemicarbazide (PTSC) polymer	1.5 cm diameter × length 20 cm; 0.5 g PTSC powder; pH 2–12	2–5	Single-metal and Mixed system tests: 1mg/L	1 L fixed volume; q: 0.11–0.50 mg/g depending on metal/pH/flow Mixture (1 ppm each, pH 2): Only Ag strongly adsorbed, Cu moderately; others negligible. Saturation time (1mg/L, pH 2, 5 mL/min): Cu and Zn ~150 and 250 min; No breakthrough for Ag	(Aburabie et al., 2025)

Pb(II), Zn(II), Cu(II)	Functionalized cellulose nanofiber/sodium alginate/polyglutamic acid aerogel beads (CNF-SP aerogels)	2 cm diameter × 40 cm length; Bed heights: 5, 10, 15 cm	1, 3, 5	5–20 mg/L single metals; 10 mg/L each in multi-metal	Single-metal system (20 mg/L, 10 cm bed, 1 mL/min): Pb: 128–194 mg/g Zn: 39–51 mg/g Cu: 45–54 mg/g Multi-metal system (10 mg/L each): Pb: 110 mg/g; Zn: 30.9 mg/g; Cu: 40.6 mg/g Breakthrough/saturation time: Pb ~5359 min / >10,000 min (1 mL/min, 10 cm bed); Zn and Cu breakthrough earlier	(Syeda et al., 2025)
Ni(II)	Powdered clamshell adsorbent (PCSA)	5 cm diameter × 35 cm length; Bed height: 5–25 cm	8–12	50 mg/L.	q: up to 1.05 mg/g (25 cm, 8 mL/min); Breakthrough/saturation time: 65/150 min at best conditions	(Baskar et al., 2025)
Co(II), Ni(II), Mn(II), Li	CS1%CYS beads	2.2 cm diameter × 100 cm length; Bed height: 21.5 (25 g) and 27.cm (31.5 g)	2.33 and 4.33	Co: 964 mg/L, Li: 133.33 mg/L, Mn: 46.10 mg/L, Ni: 60.10mg/L	No uptake of Li (selective separation); Batch Langmuir q= Co: 100.7 mg/g, Mn; 2 mg/g; and Ni(II); 10.98 mg/g Column: ≈Co(II)=44-51 mg/g; Mn(II)= 1.28-1.44	This study and previous study (Roshanfar et al., 2025b)

	mg/g; Ni(II)= 4.17-4.3 mg/g Saturation time: 14.3 h (4.33 mL/min) and 21.6 h (2.33 mL/min)

8.4.3. Column Regeneration Results

In addition to adsorption capacity, the material's reusability through effective regeneration is a crucial factor for sustainable metal recovery and potential scale-up. Figure 8.6 illustrates the breakthrough curves for the loading-regeneration experiments. Figure 8.6 (a) and (b) show the first cycle of loading and regeneration, while (c) and (d) correspond to the second cycle. Table 8.3 also shows the adsorption uptake (mg/g) and efficiency (%), as well as the regeneration rate (%) for the column regeneration. As shown in Figure 8.6(a), loading (adsorption) at a flow rate of 4.34 ± 0.39 mL/min required 14.17 hours to reach $C_t/C_0 \approx 97\%$. In contrast, the second cycle (Figure 8.6c) achieved a breakthrough in 10.17 h, compared with 14.17 h in the first run. This faster saturation can be attributed not only to incomplete desorption and the partial occupation of active sites, but also to changes in surface chemistry, possible pore blocking, and increased competition from residual metal ions. Furthermore, small changes in column hydrodynamics after regeneration may have further reduced contact efficiency, thereby contributing to the faster breakthrough (X. Liu et al., 2025; Mourak et al., 2025; Upadhyay et al., 2024). The regeneration efficiency was 87.07% for Co(II), 30.95% for Mn(II), and 100% for Ni(II). This incomplete desorption was further evidenced by the reduced adsorption uptake in the second cycle. The capacity decreased from 43.83 to 34.40 mg/g for Co(II), from 4.17 to 3.43 mg/g for Ni(II), while Mn(II) remained unchanged. Similarly, the removal efficiencies in the first cycle were 40.70%, 23.73%, and 62.83% for Co(II), Mn(II), and Ni(II), respectively, which were lower than those achieved in the batch study (69.55% ± 0.77 for Co(II), 31.18% ± 0.63 for Mn(II), and 91.62% ± 0.88 for Ni(II)). These lower removal efficiencies, compared with the batch experiments, are primarily due to the fact that batch systems allow sufficient time for adsorbate-adsorbent interactions to reach equilibrium. In contrast, fixed-bed columns operate under dynamic flow conditions, in which contact time is

limited, leading to incomplete equilibration between the solution and the active sites. Additionally, flow dynamics and mass-transfer resistance within the packed bed further constrain adsorption, resulting in lower overall uptake than that achieved under equilibrium conditions in batch tests (Ayoub et al., 2019; Du et al., 2019).

In the second loading cycle, removal further declined by ~3% for Co(II) and ~7% for Ni(II), consistent with the ~5% drop observed in the batch system, whereas Mn(II) removal remained relatively stable. To explore whether a stronger desorbing agent could improve regeneration, 1 M EDTA was applied in the second regeneration cycle. However, the higher concentration did not significantly accelerate regeneration. Instead, a modest decrease was observed for Co(II) (-6%) and Ni(II) (-9%), whereas Mn(II) desorption improved notably from 30.95% to 50.22%.

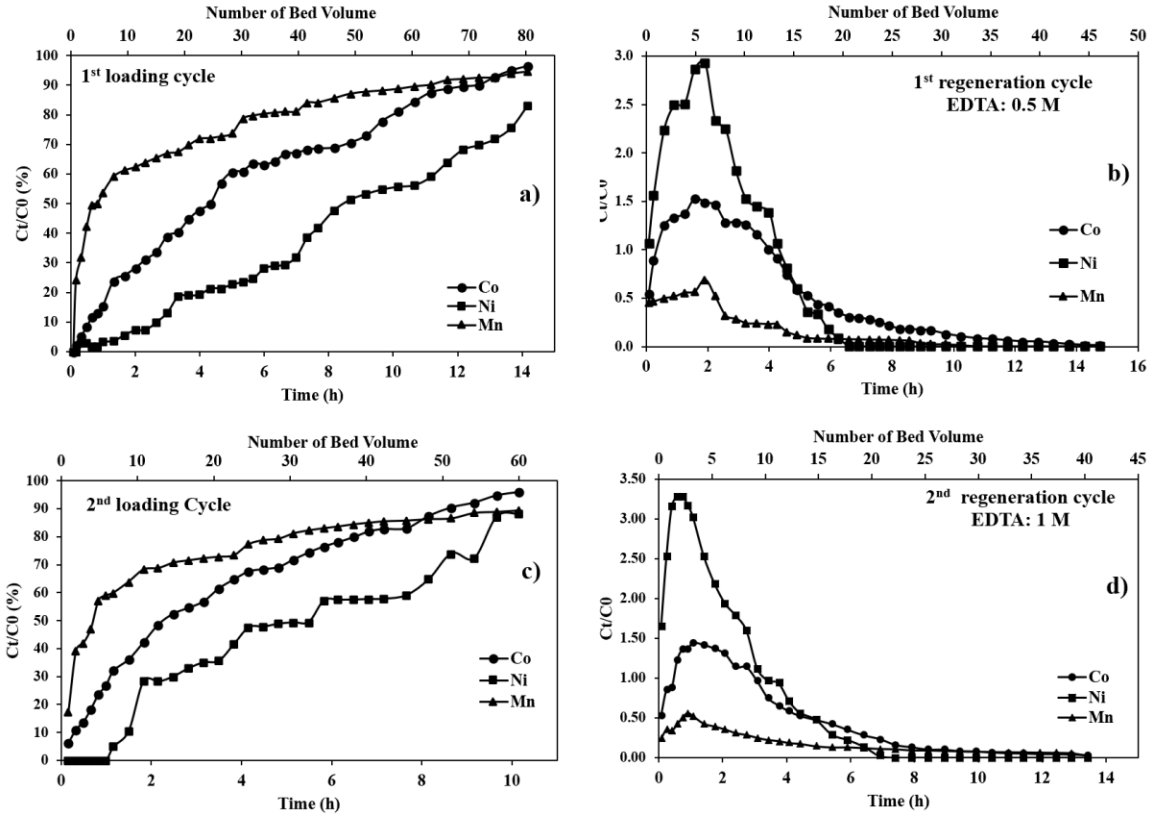

Figure 8.6. Loading-regeneration cycles.

Table 8.3. Adsorption uptake for loading and regeneration of the regeneration columns

1st Cycle	**Co**	**Mn**	**Ni**
Adsorption uptake (mg/g)	43.83	1.28	4.17
Removal (%)	40.70	23.73	62.83
Desorption (%)	87.07	30.95	100.00
2nd Cycle			
Adsorption uptake (mg/g)	34.40	1.32	3.43
Removal (%)	37.78	29.62	55.8
Desorption (%)	81.00	50.22	90.88

8.4.4. Modeling of Fixed-bed Adsorption Column

The applicability of the Thomas and Yoon-Nelson models was examined by fitting breakthrough curves for Co(II), Mn(II), and Ni(II) at different flow rates (Figure 8.7). The corresponding model parameters are summarized in Table 8.4. As shown in Figure 8.7, both models provided a reasonable fit for Co(II) and Ni(II), particularly at higher flow rates, where the adsorption process was more consistent with the models' kinetic assumptions. At 2.33 ± 0.14 mL/min, Co(II) and Ni(II) exhibited gradual breakthrough curves with saturation after 21.6 h, whereas at 4.34 ± 0.39 mL/min, the breakthrough time decreased to 14.2 h due to reduced residence time. In contrast, Mn(II) exhibited a steep, early breakthrough at both flow rates, reflecting its weaker affinity for the adsorbent and confirming the thermodynamic results indicating non-spontaneous uptake in the batch study. The model-fitting results confirm that Co(II) and Ni(II) are more strongly adsorbed by CS1%CYS beads, whereas Mn(II) is poorly adsorbed. Additionally, flow rate significantly affects breakthrough behavior by impacting contact time and mass-transfer limitations.

For Co(II) and Ni(II), both the Thomas and Yoon-Nelson models provided an excellent fit to the experimental breakthrough behavior at both investigated flow rates, as evidenced by high coefficients of determination ($R^2 \approx 0.97$-0.99) (Anderson and Whitcomb, 2017; Roshanfar et al., 2019). Within the Thomas framework, the kinetic constant (k_{TH}) increased from 2.33 to 4.33

mL/min as the flow rate increased, indicating enhanced mass-transfer kinetics under higher hydrodynamic conditions. Conversely, the predicted maximum adsorption capacity (q_{TH}) decreased with increasing flow rate, attributable to shorter residence time and reduced metal-biosorbent contact, thereby limiting the full utilization of available binding sites. Despite this, q_{TH} and the experimentally determined uptake (q_{exp}) are close to one another, particularly for Co(II) and Ni(II), confirming the reliability and predictive strength of the Thomas model for these metals under dynamic column operation.

The Yoon-Nelson model further supported these observations by accurately capturing the progression of breakthroughs. The characteristic time required to reach 50% breakthrough (t_{50}) showed good agreement with the experimental breakthrough midpoints for Co(II), Mn(II), and Ni(II). Lower flow rates resulted in larger t_{50} values, indicating delayed breakthrough due to increased contact time and improved mass transfer, whereas higher flow rates produced significantly shorter t_{50} values and earlier column saturation. This systematic shift in t_{50} with flow rate highlights the dominant role of hydrodynamics in governing column performance. Therefore, the strong correspondence between the experimental data and both the Thomas and Yoon-Nelson models demonstrates that these models effectively describe the fixed-bed adsorption behavior of Co(II) and Ni(II). In contrast, the comparatively lower q_{TH} values and shorter t_{50} observed for Mn(II) indicate weaker interactions with the CS1%CYS beads and a faster breakthrough, consistent with its reduced affinity relative to Co(II) and Ni(II).

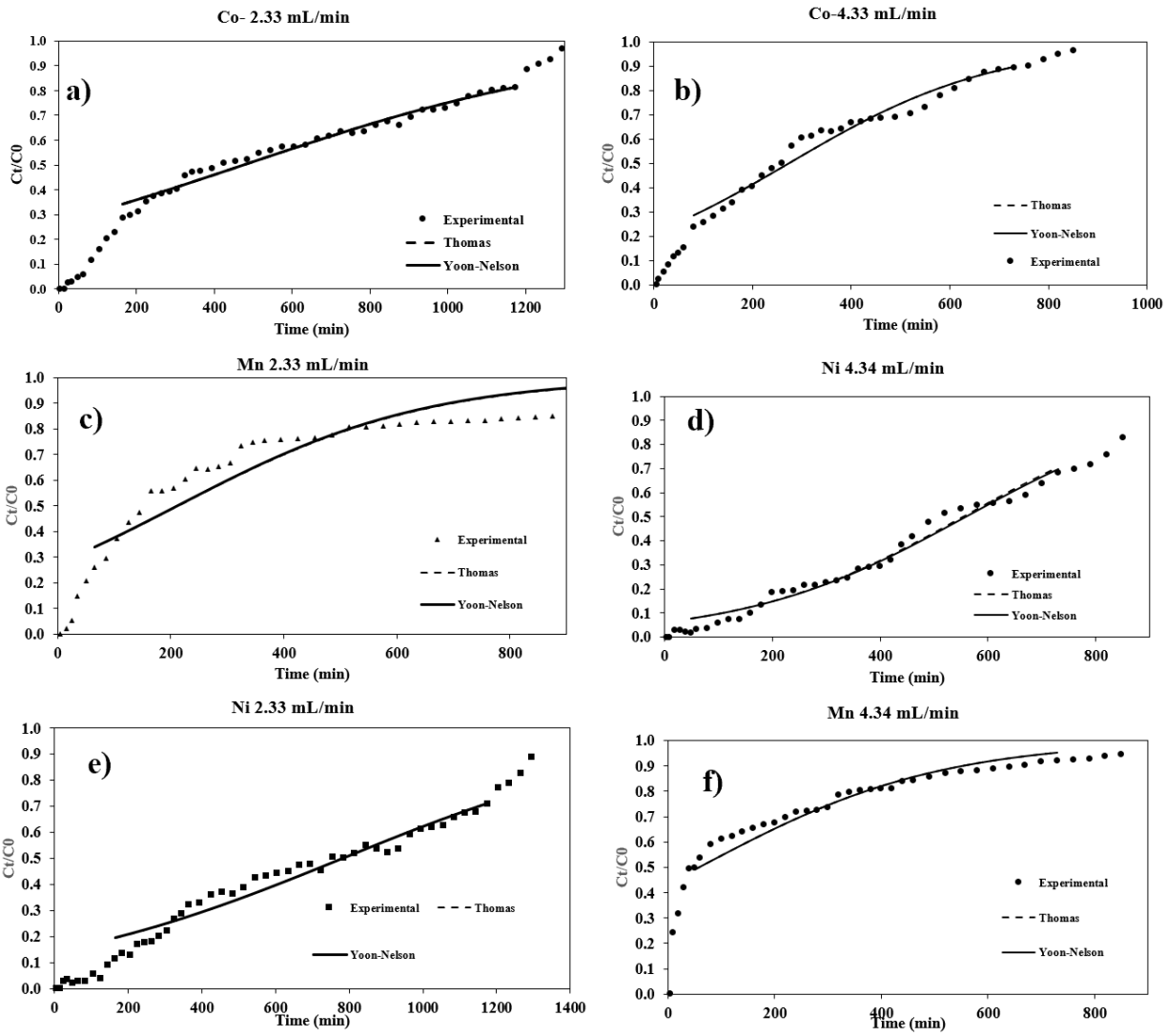

Figure 8.7. Breakthrough curves showing the fit of Thomas and Yoon–Nelson models to experimental data.

Table 8.4. Calculated modeling parameters

	Flow rate (mL/min) =2.33	**Mass (g)= 25**	
	Thomas		
	Co	**Mn**	**Ni**
K_{Th} (mL/min mg)	2.19E-03	1.00E-01	3.80E-02
q_{Th} (mg/g)	42.78	0.90	4.41
q_{exp} (mg/g)	51.34	1.44	4.3
R^2	0.99	0.94	0.97
	Yoon-Nelson		
K_{YN} (1/min)	2.10E-03	3.78E-03	2.30E-03
t_{50} (min)	478	212	782
R^2	0.99	0.94	0.97
	Flow rate (mL/min) =4.32	**Mass (g)= 31.5**	
	Thomas		
K_{Th} (mL/min mg)	4.91E-03	9.47E-02	8.33E-02
q_{Th} (mg/g)	36.33	0.38	4.56
q_{exp} (mg/g)	43.83	1.28	4.17
R^2	0.98	0.97	0.99
	Yoon-Nelson		
K_{YN} (1/min)	4.75E-03	4.37E-03	4.9E-03
t_{50} (min)	273	59	560
R^2	0.98	0.97	0.99

8.5. Conclusions

Overall, this study demonstrated that CS1%CYS performs effectively under continuous column conditions, confirming its scalability beyond batch experiments. However, column performance

was strongly influenced by operational parameters, particularly flow rate and bed height. When both parameters were increased simultaneously, the flow rate had a more pronounced effect than either bed height or adsorbent mass, indicating that reduced contact time at higher velocities was the primary factor governing column behavior. Compared with batch equilibrium tests based on the Langmuir isotherm, the column system exhibited lower adsorption capacities, due to mass-transfer limitations and incomplete equilibration under dynamic conditions. Nevertheless, the column maintained clear selectivity, particularly for Co(II) and Ni(II) over Li, demonstrating its practical potential for selective metal separation. Regeneration tests showed partial recovery of the critical metals, with over 80% for Co(II), over 20% for Mn(II), and over 90% for Ni(II). Although incomplete desorption lowered long-term efficiency, it still indicated potential for future reuse. Modeling results confirmed that the Thomas and Yoon–Nelson models adequately fit the breakthrough curves for Co(II), Mn(II), and Ni(II), with predicted parameters closely matching the experimental uptake and breakthrough times. It was also confirmed that Mn(II) has a lower affinity than Co(II) and Ni(II). Importantly, Li remained below 1% in all runs, confirming the process's selective separation of critical metals from Li and demonstrating its potential for the sustainable recovery of valuable metals from spent LIBs. Additionally, EDS verified metal accumulation on the CS1%CYS surface after adsorption, and FT-IR analysis revealed functional-group interactions and their restoration after regeneration, demonstrating reversible binding and structural stability.

8.6. Acknowledgments

The authors gratefully acknowledge financial support from the Ontario Center of Innovation and ERS-International Company for this project (OCI application number: 36895).

8.7. References

The references are merged with those of the other chapters and listed at the end of the thesis.

Chapter 9 INTEGRATION OF RESULTS

Figure 9.1 outlines the sequence followed for presenting the results in this section.

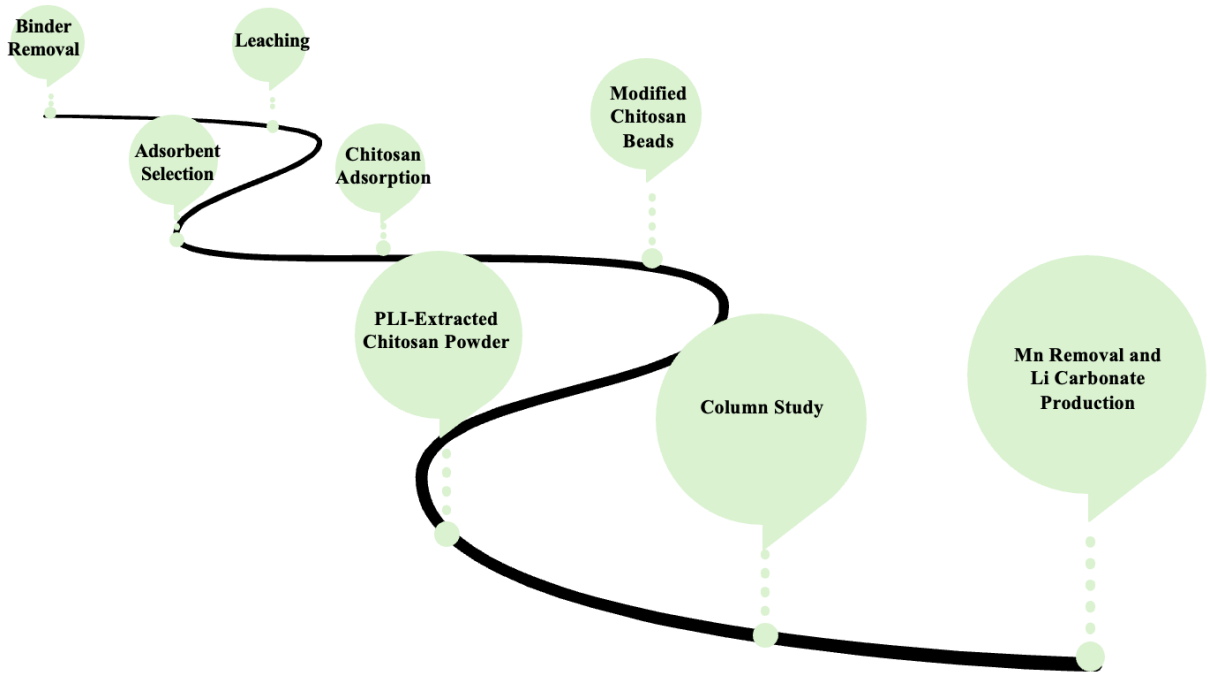

Figure 9.1. The flowchart of the current study's stages.

9.1. Initial Characterization

XRD analysis revealed that all tested batteries contained $LiCoO_2$ (LCO) as the primary cathode material. At the same time, Li-polymer batteries also showed $LiMn_2O_4$ (LMO), a material commonly used in portable electronics. Cellphone and laptop batteries exhibited NMC phases, consistent with their higher energy density. The results were also confirmed by ICP. SEM-EDS analysis of the mixed samples confirmed the presence of Co, Ni, Mn, and Li on the cathode surface, along with carbon originating from the binder materials.

FT-IR analysis was employed to confirm the behavior of functional groups during adsorption using chitosan, after adsorption, and column regeneration. The reduction in O–H/N–H and C–H

stretching band intensities after adsorption indicated that amine and hydroxyl groups participated in metal binding (amines mainly chelating Co(II) and Ni(II), and hydroxyls contributing to Mn(II) uptake through hydrogen bonding and electrostatic interactions). In bead production, the detection of thiol and C–S vibrations confirmed the successful incorporation of cystine, introducing additional active sites and improving structural stability. After EDTA desorption in the column study, these characteristic bands largely returned to their original positions, signifying reversible metal coordination and restoration of active functional groups. Similarly, for the PIL-extracted chitosan, FT-IR spectra showed functional features closely matching those of the commercial chitosan powder, indicating that the green extraction process preserved the polymer's chemical integrity and adsorption-active sites.

The measured BET surface area and total pore volume for chitosan powder, chitosan beads (CB) without a crosslinker, and CS1%CYS beads were 7.45 m^2/g with a total pore volume of 7.18 × 10^{-3} cm^3/g, 5.47 m^2/g with a total pore volume of 4.48 × 10^{-3} cm^3/g, , and 9.26 m^2/g with a total pore volume of 24.40 × 10^{-3} cm^3/g respectively. Bead formation typically reduces surface area and pore volume due to crosslinking and structural densification. However, the controlled incorporation of the crosslinker slightly enhanced the BET surface area by increasing the total pore volume. [Eth][Ac]-extracted chitosan, showed a slightly higher surface area of 8.64 m^2/g and a total pore volume of 10.80 × 10^{-3} cm^3/g compared to commercial powder, indicating a slight improvement in surface properties.

9.2. Binder Removal

Binder materials, primarily PVDF, present on the cathode surface can considerably hinder metal recovery and thus require removal through a suitable pretreatment process. Among the evaluated approaches, thermal treatment was found to be the most environmentally friendly and industrially practical option. TG (%) and DTG (%/min) analyses of mixed battery samples (laptop: cellphone: Li-polymer = 1 1 1) under argon (a) and simulated air (b) atmospheres within the 25–800 °C range revealed similar decomposition behaviors. The process occurs in three distinct stages: volatilization of residual electrolytes and adsorbed moisture (30–400 °C), decomposition of the

PVDF binder (450–600 °C), and subsequent carbothermal reactions or metal alloy formation, which must be avoided to prevent unwanted reduction. Considering both thermal analysis and environmental impact, 570 °C under an air atmosphere was selected as the optimal condition. According to XRD, Co_3O_4 was not observed in either environment. XRD and SEM-EDS results further indicated that a 2-hour treatment was optimal. XRD also confirmed that binder materials were completely removed after 2 and 4 hours. However, this was not the case for the 30-minute period. Therefore, 2 h was selected.

9.3. Leaching

The experimental procedure was conducted in three main phases: (i) screening, (ii) optimization of the solid-to-liquid ratio (S/L, 25–150 g/L), and (iii) optimization of leaching time (30–200 min) and temperature (40–90 °C). Statistical design of experiments (DOE) was used to plan and analyze tests. In the screening phase, the effects of acid concentration (inorganic: 0.5–2 M; organic: 0.1–1 M) and the type of organic acid (citric acid or acetic acid) were systematically evaluated. The results showed that both organic acids, when combined with sulfuric acid, were effective in dissolving metal ions. However, citric acid achieved higher recovery efficiency at lower concentrations due to its superior metal-complexing ability. The interaction between sulfuric and organic acid concentrations was significant, and the optimal combination of 1.25 M H_2SO_4 and 0.55 M citric acid provided the highest recovery rates. Citric acid also demonstrated a dual role as both a lixiviant and a reducing agent, eliminating the need for an external reductant, unlike acetic acid, which lacks this functionality.

Since the S/L ratio strongly influences acid consumption and metal recovery, it was optimized in the second phase, followed by the evaluation of time and temperature in the third phase. A high S/L ratio was found to hinder leaching efficiency because the reduced liquid volume limits acid contact with solid particles. An S/L ratio of 62.5 g/L was determined to be optimal, balancing recovery efficiency with economic and environmental considerations. Increasing leaching time and temperature enhanced metal recovery, with the optimal conditions identified as 189 min and 95 °C. Under these optimized parameters, the recovery efficiencies for Li, Co, Ni, and Mn reached 99 ± 0.7%, 98 ± 0.0%, 90 ± 6.6%, and 92 ± 0.5%, respectively.

9.4. Adsorbent Selection

Adsorption experiments were conducted at room temperature and an initial pH of 7, using a 100-fold dilution factor for 24 hours. Modified flax, chitosan, and activated carbon were tested at 10 g/L, while graphene oxide was tested at 3.6 g/L. The results revealed distinct adsorption behaviors among the adsorbents. Modified flax showed poor selectivity at pH 7, with low recovery of Co(II), Mn(II), and Ni(II) and slight Li adsorption (q_e = 0.11 mg/g), likely due to its –COOH and –CHO functional groups. In contrast, both chitosan and activated carbon effectively adsorbed divalent metals (Co, Ni, Mn) while leaving Li in solution. Chitosan exhibited strong adsorption for Co(II) and Ni(II) and moderate uptake of Mn(II), attributed to its amine and hydroxyl groups. Activated carbon showed higher affinity for Mn(II), consistent with its carboxyl and hydroxyl functionalities. Graphene oxide preferentially adsorbed Mn(II) (over 65%), followed by Co(II) (32%) and Ni(II) (7%), while also adsorbing Li (4%), indicating limited selectivity. Equilibrium data confirmed that chitosan had the highest adsorption capacity for Co(II) (27.23 mg/g) and Ni(II) (1.78 mg/g), while activated carbon had the highest for Mn(II) (1.05 mg/g). Further tests under unadjusted acidic conditions (pH = 2.5) showed that activated carbon became ineffective, whereas chitosan maintained high performance, adsorbing over 80% of Co(II) and Ni(II) and 15% of Mn(II). These findings highlight chitosan's strong adsorption efficiency and stability under acidic conditions, making it the most suitable adsorbent for further studies (the detailed results are provided in the appendix).

9.5. Adsorption Performance of Chitosan Powder

The adsorption performance of chitosan was evaluated under varying initial metal ion concentrations, pH levels, and adsorbent dosages to determine the optimal operating conditions. Results showed that adsorption uptake increased with rising metal ion concentration (dilution factors ×100 to ×20) until equilibrium was reached, reflecting the saturation of available sites on the chitosan surface. This increase at higher concentrations is attributed to a reduction in mass-transfer resistance between the liquid and solid phases. However, to balance efficiency and water

use, a dilution factor of 40 was selected as optimal. Lithium adsorption remained below 1% under all conditions, confirming chitosan's selectivity toward transition metals.

The effect of pH revealed that increasing the initial pH from 2.38 to 4 enhanced the uptake of Co(II), Mn(II), and Ni(II) to 60.01 mg/g, 1.10 mg/g, and 4.70 mg/g (1.02, 0.02, and 0.08 mmol/g), respectively. Beyond pH 4, Co(II) and Ni(II) adsorption plateaued, while Mn(II) uptake slightly improved (up to 1.65 mg/g (0.03 mmol/g), approximately 47%). Therefore, pH 4 was identified as the optimal condition, ensuring efficient adsorption while maintaining the final pH below 7.5 to avoid precipitation. Varying chitosan dosage (2-100 g/L) demonstrated that increasing adsorbent mass initially enhanced metal removal but eventually reduced uptake per unit mass due to site saturation. The best performance was achieved at 10 g/L (0.5 g/50 mL), where both metal recovery and adsorption capacity reached their peak values. Overall, the optimal parameters (dilution factor of 40, initial pH of 4, and adsorbent dosage of 10 g/L) yielded the highest metal recovery rates while maintaining process efficiency and sustainability.

The isotherm and thermodynamic analyses collectively confirm that chitosan shows a strong and selective affinity for Co(II) and Ni(II), whereas Mn(II) adsorption remains limited. The Langmuir and Toth models best described Co(II) adsorption, indicating monolayer adsorption on heterogeneous sites, whereas Ni(II) followed the Langmuir and Temkin models, suggesting uniform surface binding. In contrast, Mn(II) adsorption was best described by the Freundlich model, suggesting weak multilayer adsorption influenced by competition with other metals. Thermodynamic parameters further support these findings (negative $\Delta G°$ values for Co(II) and Ni(II) indicate spontaneous adsorption, while Mn(II)'s positive $\Delta G°$ confirms non-spontaneity). The endothermic nature (positive $\Delta H°$) and positive $\Delta S°$ values for Co(II) and Ni(II) suggest enhanced disorder at the solid–liquid interface and stronger metal–adsorbent interactions, emphasizing chitosan's high selectivity and favorable thermodynamic behavior toward Co(II) and Ni(II). Kinetic analysis showed that the pseudo-second-order model best described the adsorption of Co(II) and Ni(II), indicating surface reactions govern the rate. Equilibrium was achieved after 8 h for Co(II), 3 h for Ni(II), and 24 h for Mn(II), confirming the slower adsorption of Mn(II).

Among the tested desorption agents (water, HCl, NaCl, and H_2SO_4), only H_2SO_4 showed effective metal recovery, achieving complete desorption of Co(II) and Ni(II) and over 82% for Mn(II).

Therefore, 0.01 M H_2SO_4 was identified as the best and most environmentally suitable desorption agent medium.

9.6. Synthesized Chitosan Beads

Chitosan powder, although effective, suffers from poor mechanical strength and clogging issues, which can be reduced through crosslinking or compositing. Various crosslinkers and additives, including L-arginine, L-cystine, Triethylamine, Pyrazine, Tricotylamine, and STPP (a common crosslinker), as well as activated carbon (AC) and Fe_3O_4, were tested. L-cystine (Cys) proved to be the most effective in improving bead stability without compromising adsorption performance. While magnetic and AC composites could preserve the beads' integrity, their extra cost and complexity made them less practical for large-scale use. However, the Cys-crosslinked beads (CS1%CYS) formed a stable, covalently bonded network that prevented leaching and maintained their structure. Increasing Cys content beyond 1 wt.% did not provide significant benefits, making CS1%CYS the best formulation. Under optimized conditions (dilution factor 30, pH 4, dosage 10 g/L), the adsorption efficiencies for Co(II), Mn(II), and Ni(II) were 69.6%, 31.2%, and 91.6%, with corresponding capacities of 65.56, 1.47, and 5.92 mg/g (1.11, 0.03, and 0.10 mmol/g). Compared to chitosan powder, the beads exhibited improved Co(II) and Mn(II) uptake but a slightly reduced Ni(II) capacity, likely due to Cys, which introduces thiol and carboxylate groups that enhance selectivity and binding strength.

Isotherm modeling confirmed that adsorption on CS1%CYS beads followed the Toth and Freundlich models, indicating heterogeneous, multilayer adsorption. The Langmuir capacities were 153.4 mg/g (2.60 mmol/g) for Co(II), 7.7 mg/g (0.14 mmol/g) for Mn(II), and 15.6 mg/g (0.27 mmol/g) for Ni(II). Compared with chitosan powder, the beads exhibited a 39% higher Co(II) capacity and improved Mn(II) uptake, attributed to the thiol and carboxylate groups introduced by cystine, whereas Ni(II) capacity decreased slightly (approximately 22%). Adsorption followed the pseudo-second-order model, reaching equilibrium at 16 hours for Co(II), 3 hours for Mn(II), and 6 hours for Ni(II). Thermodynamic analysis confirmed that Ni(II) adsorption was most favorable, followed by Co(II), while Mn(II) remained less spontaneous. For desorption, DI water, 0.01 M

H_2SO_4, and EDTA were investigated, with 0.1 M EDTA achieving over 92% metal recovery across three cycles, demonstrating minimal capacity loss (<5%) and excellent reusability and chemical stability of the CS1%CYS beads. Regarding H_2SO_4, the acidic medium damaged the beads, rendering them unusable for reuse.

9.7. PLI-Extracted Chitosan Powder

The conventional chitin extraction process, which utilizes strong acids and bases (HCl and NaOH), is environmentally unsustainable due to high energy and water consumption, the generation of hazardous effluents, and the structural degradation of chitin. To develop a greener alternative, protic ionic liquids (PILs) were investigated using a design-of-experiments approach. Two stages were designed: Screening Results (PIL Type Selection) and Optimization Results. In the screening stage, among the PILs tested ([Tea][Ac], [Eth][Ac], and [Teta][Ac]), [Eth][Ac]-extracted chitosan demonstrated adsorption behavior most comparable to commercial chitosan, due to better performance, its biodegradability, low toxicity, and cost-effectiveness. Considering parameter ranges of temperature 70-120 °C, time 18-36 hours, and an L/S ratio of 10-20 g/g, optimal conditions at 91 °C, 27 hours, and an L/S ratio of 16.16 g/g yielded 56.67 wt.% chitin and adsorption efficiencies of 82.42 ± 1.65%, 35.09 ± 2.63%, and 98.30 ± 0.63% for Co(II), Mn(II), and Ni(II) respectively. At optimum conditions of chitin extraction using [Eth][Ac]-extracted chitosan, the adsorption uptakes for Co(II), Mn(II), and Ni(II) were 58.11 mg/g (1.00 mmol/g), 1.13 mg/g (0.02 mmol/g), and 4.11 mg/g (0.07 mmol/g), respectively.

Isotherm study showed that Langmuir modeling yielded maximum adsorption capacities of 146.68 mg/g (2.49 mmol/g, Co(II)), 3.77 mg/g (0.07 mmol/g, Mn(II)), and 7.98 mg/g (0.14 mmol/g, Ni(II)), with strong correlation coefficients, confirming an excellent model fit. Compared to commercial chitosan (110 mg/g (1.87 mmol/g) for Co(II), 1.10 mg/g (0.02 mmol/g) for Mn(II), and 4.70 mg/g (0.08 mmol/g) for Ni(II)), the PIL-extracted chitosan achieved comparable or superior performance while maintaining structural integrity and stability after adsorption, confirming its suitability as a sustainable alternative for high-performance metal recovery.

9.8. Adsorption Column Study

Batch adsorption provided valuable insight into equilibrium behavior and adsorption capacity under controlled conditions. However, it is limited for large-scale applications due to restricted solution volume, long equilibration times, and static operation. In contrast, fixed-bed column adsorption allows continuous flow and steady-state operation, offering better control over mass transfer and more realistic process scalability. In this study, two column configurations were tested, revealing that adsorption performance was strongly influenced by flow rate and contact time. It is worth noting that the concentration studied is significantly higher than those reported in the literature review. Compared with batch experiments, column adsorption capacities were lower; for example, Co(II) decreased from 100.97 mg/g in batch to 51.34 and 43.83 mg/g at flow rates of 2.33 and 4.34 mL/min, respectively, mainly due to mass-transfer resistance and incomplete equilibration under dynamic flow conditions.

The breakthrough curves further clarified these differences: Co(II) and Ni(II) displayed gradual breakthrough profiles, reflecting strong adsorption and effective interactions with the CS1%CYS beads, while Mn(II) showed a sharp, early breakthrough, indicating weaker binding and faster elution. Increasing the flow rate reduced both breakthrough and saturation times, indicating that contact time is a dominant factor in column efficiency. These findings align with batch and thermodynamic results, which showed that Co(II) and Ni(II) adsorption are spontaneous and kinetically favored, whereas Mn(II) adsorption is weaker and non-spontaneous. Regeneration tests demonstrated good bead stability and reusability, with desorption efficiencies of 87.07% for Co(II), 30.95% for Mn(II), and 100% for Ni(II), and minor capacity declines across cycles due to partial pore blockage and incomplete desorption. Finally, the Thomas and Yoon–Nelson models accurately fit the breakthrough data, confirming their reliability for predicting adsorption kinetics and highlighting that flow rate, metal affinity, and mass-transfer effects govern the overall column performance.

9.9. Mn Removal and Li Carbonate Production

The remaining Mn removal was further investigated at an elevated temperature (80 °C) by gradually adding $KMnO_4$ to an optimal concentration of 0.35 M, achieving approximately 86% Mn removal and a total efficiency of around 91%. Alternatively, increasing the pH to about 12 also enabled the removal of Mn(II), along with residual Co(II) and Ni(II), reaching up to 95% efficiency. In both approaches, the lithium concentration remained unaffected, with all Li retained in the solution. The recovered Li can then be converted to Li_2CO_3 by adding a saturated Na_2CO_3 solution and heating to 90 °C, leading to the precipitation of Li_2CO_3 crystals at the reactor's bottom.

Chapter 10 CONCLUSIONS AND RECOMMENDED FUTURE WORK

The proposed process developed in this study offers a novel, unified, and sustainable approach to processing mixed cathode materials from spent LIBs through a series of pretreatment, leaching, adsorption, and product recovery steps, each optimized for environmental and operational efficiency.

The pretreatment stage involved removing the thermal binder, which proved to be the most environmentally friendly and scalable method for industry. Thermal analysis showed that heating PVDF to 570 °C in air for 2 hours completely decomposed PVDF without forming any unwanted alloy or oxide phases. This process yielded clean, reactive powders suitable for downstream metal extraction. Optimization of the leaching process using a mixed citric–sulfuric acid system led to nearly complete metal dissolution, with recovery rates of 99% for Li, 98% for Co, 90% for Ni, and 92% for Mn under conditions of 95 °C, 189 minutes, and an S/L ratio of 62.5 g/L. Using citric acid as both a complexing and reducing agent eliminated the need for external reductants, reducing chemical use and improving process sustainability.

Adsorption was selected over traditional separation methods because it is simple, cost-effective, and environmentally friendly, and it enables selective recovery of target metals without generating secondary waste. Among the tested adsorbents, chitosan demonstrated superior selectivity toward Co(II), Mn(II), and Ni(II), while leaving Li in solution, confirming its potential as a bio-based, cost-effective sorbent. Under optimal conditions (pH 4, dosage 10 g/L, dilution ×40), chitosan achieved high metal uptake and remained stable even under acidic conditions. To address the mechanical limitations of chitosan powder, it was crosslinked with 1 wt.% L-cystine to produce CS1%CYS beads, which demonstrated improved stability, increased surface area, and enhanced metal affinity. These beads achieved predicted maximum adsorption capacities of 153 mg/g (2.6 mmol/g) for Co(II), 15.6 mg/g (0.27 mmol/g) for Ni(II), and 7.7 mg/g (0.14 mmol/g) for Mn(II), while showing excellent reusability and desorption efficiency (>92%) with 0.1 M EDTA. FT-IR confirmed the involvement of amine and hydroxyl groups in reversible metal coordination.

To further enhance sustainability, chitin was extracted using a protic ionic liquid ([Eth][Ac]) as a green alternative to conventional acid–base extraction. The obtained chitosan exhibited

comparable or superior adsorption performance to commercial chitosan, while preserving its structural integrity, confirming its potential for sustainable large-scale applications.

Column studies validated the process's scalability under continuous-flow conditions. Breakthrough data aligned well with the Thomas and Yoon-Nelson models, confirming the predictability of adsorption kinetics. Co(II) and Ni(II) showed strong retention, whereas Mn(II) exhibited earlier breakthrough, consistent with the batch results. The beads maintained high recovery rates (87% for Co, 100% for Ni) and stability over multiple cycles, demonstrating operational feasibility for industrial use.

The remaining Mn(II) was removed through oxidation with 0.35 M $KMnO_4$ or by raising the pH to around 12, achieving over 90% removal without impacting the lithium concentration. The purified lithium solution was then converted to Li_2CO_3 by reacting it with a saturated Na_2CO_3 solution at 90 °C, yielding high-purity lithium carbonate crystals suitable for reuse in battery manufacturing.

Generally, this study introduces a universal, scalable, and sustainable process for recovering critical metals from spent lithium-ion batteries with various cathode chemistries. By combining green chemistry, bio-based materials, and thermally optimized pretreatment, this method not only ensures efficient resource recovery but also reduces environmental impact, advancing a circular and low-carbon battery economy.

10.1. Recommendations for Future Work

Future work may focus on advancing the current adsorption-based battery-recycling framework in the following directions:

- Further optimization of cross-linked chitosan beads, including exploration of functionalization strategies, to enhance selectivity, capacity, and competitive separation of Co(II), Ni(II), and Mn(II) in complex LIB leachates.
- Advanced surface and chemical characterization, such as X-ray photoelectron spectroscopy (XPS), Raman spectroscopy, and solid-state NMR, to elucidate metal-ligand

interactions, binding mechanisms, and the role of functional groups before and after adsorption-desorption cycles.

- Scale-up of continuous fixed-bed column studies under more industrially relevant conditions, including higher metal concentrations and reduced dilution factors, to minimize downstream evaporation requirements for lithium carbonate production and improve overall process efficiency.
- Comprehensive evaluation of bead physical and mechanical properties, including compressive strength, abrasion resistance, swelling under dynamic flow, and long-term stability, to assess suitability for prolonged column operation.
- Application of protic ionic liquid (PIL)-extracted chitosan beads in continuous systems, enabling a direct comparison with commercial chitosan and further validating the waste-to-treat-waste and circular-economy concept.
- Integration of adsorption with downstream recovery steps, such as selective desorption, metal precipitation, or electrochemical recovery, to establish a complete and scalable separation flowsheet for spent lithium-ion batteries to separate Co and Ni.
- Preliminary techno-economic and life-cycle assessments, to quantify cost, energy demand, and environmental benefits relative to conventional solvent extraction and electrochemical separation routes.

Chapter 11 REFERENCES

Aaltonen, M., Peng, C., Wilson, B.P., Lundström, M., 2017. Leaching of metals from spent lithium-ion batteries. Recycling 2, 20.

Abbasi, M., Safari, E., Baghdadi, M., Janmohammadi, M., 2021. Enhanced adsorption of heavy metals in groundwater using sand columns enriched with graphene oxide: Lab-scale experiments and process modeling. Journal of Water Process Engineering 40, 101961. https://doi.org/10.1016/J.JWPE.2021.101961

Abou El-Reash, Y.G., 2016. Magnetic chitosan modified with cysteine-glutaraldehyde as adsorbent for removal of heavy metals from water. J. Environ. Chem. Eng. 4, 3835–3847. https://doi.org/10.1016/j.jece.2016.08.014

Aburabie, J., Mohammed, S., Hashaikeh, R., 2025. Chelating packed bed adsorption column for selective trace metal recovery from seawater and brine. Sep. Purif. Technol. 369, 133112. https://doi.org/10.1016/J.SEPPUR.2025.133112

Al Mesfer, M.K., Danish, M., Khan, M.I., Ali, I.H., Hasan, M., Jery, A. El, 2020. Continuous Fixed Bed CO2 Adsorption: Breakthrough, Column Efficiency, Mass Transfer Zone. Processes 2020, Vol. 8, Page 1233 8, 1233. https://doi.org/10.3390/PR8101233

Al-Ghamdi, A.A., Galhoum, A.A., Alshahrie, A., Al-Turki, Y.A., Al-Amri, A.M., Wageh, S., 2022. Mesoporous Magnetic Cysteine Functionalized Chitosan Nanocomposite for Selective Uranyl Ions Sorption: Experimental, Structural Characterization, and Mechanistic Studies. Polymers (Basel). 14, 2568. https://doi.org/10.3390/POLYM14132568/S1

Al-Ghouti, M.A., Da'ana, D.A., 2020. Guidelines for the use and interpretation of adsorption isotherm models: A review. J. Hazard. Mater. 393. https://doi.org/10.1016/J.JHAZMAT.2020.122383

Alhamad, A.A., Amor, I. Ben, Zeghoud, S., Gheraissa, N., Laouini, S.E., Fouad Ferhat, M., Sadok, N., Ahmed, S., 2025. Preparation of Chitin and Chitosan. Chitin and Chitosan 63–93. https://doi.org/10.1201/9781003589778-3

Aliyev, E., Filiz, V., Khan, M.M., Lee, Y.J., Abetz, C., Abetz, V., 2019. Structural characterization of graphene oxide: Surface functional groups and fractionated oxidative debris. Nanomaterials 9, 1180.

Amer, M., Elmojarrush, A., Nassar, Y.F., Khaleel, M., 2025. Critical Materials for EV Batteries: Challenges, Opportunities, and Policymakers. Int. J. Electr. Eng. and Sustain. 274, 119–133.

Anderson, M.J., Whitcomb, P.J., 2017. DOE simplified: practical tools for effective experimentation. CRC press.

Anh Nguyen, T.H., Oh, S.Y., 2021. Anode carbonaceous material recovered from spent lithium-ion batteries in electric vehicles for environmental application. Waste Management 120, 755–761. https://doi.org/10.1016/J.WASMAN.2020.10.044

Asadi Dalini, E., Karimi, G., Zandevakili, S., 2021. Treatment of valuable metals from leaching solution of spent lithium-ion batteries. Miner. Eng. 173. https://doi.org/10.1016/J.MINENG.2021.107226

Asadi Dalini, E., Karimi, G., Zandevakili, S., Goodarzi, M., 2020. A Review on Environmental, Economic and Hydrometallurgical Processes of Recycling Spent Lithium-ion Batteries. https://doi.org/10.1080/08827508.2020.1781628 1–22. https://doi.org/10.1080/08827508.2020.1781628

Ayoub, G.M., Damaj, A., El-Rassy, H., Al-Hindi, M., Zayyat, R.M., 2019. Equilibrium and kinetic studies on adsorption of chromium(VI) onto pine-needle-generated activated carbon. SN Appl. Sci. 1, 1–13. https://doi.org/10.1007/S42452-019-1617-7/TABLES/7

Babakhani, A., Sartaj, · Majid, 2025. Synthesis, Characterization, and Application of Ion-Imprinted Crosslinked Chitosan for Competitive Adsorption of Cd(II), Ni(II), and Co(II). Mining, Metallurgy & Exploration 2025 1–20. https://doi.org/10.1007/S42461-025-01378-Y

Babakhani, A., Sartaj, M., 2023. Optimization of Nickel(II) adsorption by sodium tripolyphosphate crosslinked chitosan using response surface methodology (RSM). Sustainable Chemistry for the Environment 2, 100019. https://doi.org/10.1016/J.SCENV.2023.100019

Babakhani, A., Sartaj, M., 2022a. Synthesis, characterization, and performance evaluation of ion-imprinted crosslinked chitosan (with sodium tripolyphosphate) for cadmium biosorption. J. Environ. Chem. Eng. 10, 107147.

Babakhani, A., Sartaj, M., 2022b. Competitive adsorption of nickel(II) and cadmium(II) ions by chitosan cross-linked with sodium tripolyphosphate. Chem. Eng. Commun. 209, 1348–1366. https://doi.org/10.1080/00986445.2021.1966424

Babakhani, A., Sartaj, M., 2020. Removal of Cadmium (II) from aqueous solution using tripolyphosphate cross-linked chitosan. J. Environ. Chem. Eng. 8, 103842. https://doi.org/10.1016/J.JECE.2020.103842

Bakshi, P.S., Selvakumar, D., Kadirvelu, K., Kumar, N.S., 2020. Chitosan as an environment friendly biomaterial – a review on recent modifications and applications. Int. J. Biol. Macromol. 150, 1072–1083. https://doi.org/10.1016/J.IJBIOMAC.2019.10.113

Balakrishnan, A., Appunni, S., Chinthala, M., Jacob, M.M., Vo, D.V.N., Reddy, S.S., Kunnel, E.S., 2023. Chitosan-based beads as sustainable adsorbents for wastewater remediation: a review. Environ. Chem. Lett. https://doi.org/10.1007/s10311-023-01563-9

Bashir, A., Pandith, A.H., Malik, L.A., Qureashi, A., Ganaie, F.A., Dar, G.N., 2021. Magnetically recyclable L-cysteine capped Fe3O4 nanoadsorbent: A promising pH guided removal of Pb(II), Zn(II) and HCrO4- contaminants. J. Environ. Chem. Eng. 9. https://doi.org/10.1016/j.jece.2021.105880

Baskar, S., Sidhaarth, K.R.A., Mangaleshwaran, L., Lakkaboyana, S.K., Trilaksana, H., Kalla, R.M.N., Lee, J., Atanase, L.I., Kazi, M., Praveenkumar, S., 2025. Elimination of nickel ions in a packed column using clamshell waste as an adsorbent. Sci. Rep. 15, 1–16. https://doi.org/10.1038/S41598-024-82267-0;SUBJMETA

Baudino, L., Pedico, A., Bianco, S., Periolatto, M., Pirri, C.F., Lamberti, A., 2022. Crown-Ether Functionalized Graphene Oxide Membrane for Lithium Recovery from Water. Membranes (Basel). 12, 233.

Baum, Z.J., Bird, R.E., Yu, X., Ma, J., 2022. Lithium-Ion Battery Recycling─Overview of Techniques and Trends. ACS Energy Lett. 7, 712–719. https://doi.org/10.1021/ACSENERGYLETT.1C02602/ASSET/IMAGES/LARGE/NZ1C02602_0005.JPEG

Bhattacharyya, S., Roy, S., Vajtai, R., 2025. Emerging Processes for Sustainable Li-Ion Battery Cathode Recycling. Small 21. https://doi.org/10.1002/SMLL.202400557

Brennan, J., 2017. Ozone Water Treatment Disadvantages [WWW Document]. https://www.sciencing.com/ozone-water-treatment-disadvantages-22555/.

Budnyak, T.M., Piątek, J., Pylypchuk, I. V., Klimpel, M., Sevastyanova, O., Lindström, M.E., Gun'Ko, V.M., Slabon, A., 2020. Membrane-Filtered Kraft Lignin-Silica Hybrids as Bio-

Based Sorbents for Cobalt(II) Ion Recycling. ACS Omega 5, 10847–10856. https://doi.org/10.1021/ACSOMEGA.0C00492/ASSET/IMAGES/LARGE/AO0C00492_0008.JPEG

Byran Smucker, Martin Krzywinski, Naomi Altman, 2018. Optimal experimental design, Customize the experiment for the setting instead of adjusting the setting to fit a classical design. Nat. Methods 15, 557–560.

Cai, G., Fung, K.Y., Ng, K.M., Wibowo, C., 2014. Process development for the recycle of spent lithium ion batteries by chemical precipitation. Ind. Eng. Chem. Res. 53, 18245–18259. https://doi.org/10.1021/IE5025326/ASSET/IMAGES/LARGE/IE-2014-025326_0017.JPEG

Callura, J.C., Shi, Q., Dzombak, D.A., Karamalidis, A.K., 2021. Selective recovery of rare earth elements with ligand-functionalized polymers in fixed-bed adsorption columns. Sep. Purif. Technol. 265, 118472. https://doi.org/10.1016/J.SEPPUR.2021.118472

Campalani, C., Bertuol, I., Bersani, C., Calmanti, R., Filonenko, S., Rodríguez-Padrón, D., Selva, M., Perosa, A., 2024. Green extraction of chitin from hard spider crab shells. Carbohydr. Polym. 345. https://doi.org/10.1016/j.carbpol.2024.122565

Chang, H.F., Lin, J.Y., Cheng, T.M., Lai, C.H., 2025. Advanced absolute chemical precipitation for high-purity metal recovery in all-types of lithium-ion battery recycling. Sep. Purif. Technol. 361, 131454. https://doi.org/10.1016/J.SEPPUR.2025.131454

Chang, Y. C., & Chen, D. H., 2005. Preparation and adsorption properties of monodisperse chitosan-bound Fe3O4 magnetic nanoparticles for removal of Cu (II) ions. Journal of colloid and interface science, 283(2), 446-451.

Chaudhary, V., Lakhera, P., Kim, K.H., Deep, A., Kumar, P., 2023. Insights into the Eco-Friendly Recovery Process for Valuable Metals from Waste Lithium-ion Batteries by Organic Acids Leaching. https://doi.org/10.1080/15422119.2022.2164650. https://doi.org/10.1080/15422119.2022.2164650

Chen, C., Wang, Y., Zou, Q., Ding, L., Ji, L., Lu, J., Song, Y., Xiong, W., Yuan, G., 2025. Selective separation of Co(II) from leachate of lithium-ion battery cathode material using novel molecular sieve-based MOFs composite NaA-MOFs(Al). Sep. Purif. Technol. 359, 130560. https://doi.org/10.1016/J.SEPPUR.2024.130560

Chen, D., Rao, S., Wang, D., Cao, H., Xie, W., Liu, Z., 2020. Synergistic leaching of valuable metals from spent Li-ion batteries using sulfuric acid-L-ascorbic acid system. Chemical Engineering Journal 388, 124321.

Chen, H., Gu, S., Guo, Y., Dai, X., Zeng, L., Wang, K., He, C., Dodbiba, G., Wei, Y., Fujita, T., 2021. Leaching of cathode materials from spent lithium-ion batteries by using a mixture of ascorbic acid and HNO3. Hydrometallurgy 205, 105746.

Chen, X., Cao, L., Kang, D., Li, J., Zhou, T., Ma, H., 2018a. Recovery of valuable metals from mixed types of spent lithium ion batteries. Part II: Selective extraction of lithium. Waste Management 80, 198–210. https://doi.org/10.1016/J.WASMAN.2018.09.013

Chen, X., Chen, Y., Zhou, T., Liu, D., Hu, H., Fan, S., 2015. Hydrometallurgical recovery of metal values from sulfuric acid leaching liquor of spent lithium-ion batteries. Waste management 38, 349–356.

Chen, X., Guo, C., Ma, H., Li, J., Zhou, T., Cao, L., Kang, D., 2018b. Organic reductants based leaching: A sustainable process for the recovery of valuable metals from spent lithium ion batteries. Waste Management 75, 459–468.

Chen, X., Ma, H., Luo, C., Zhou, T., 2017. Recovery of valuable metals from waste cathode materials of spent lithium-ion batteries using mild phosphoric acid. J. Hazard. Mater. 326, 77–86. https://doi.org/10.1016/J.JHAZMAT.2016.12.021

Cheng, Q., Zhang, Y., Zheng, X., Sun, W., Li, B., Wang, D., Li, Z., 2021. High specific surface crown ether modified chitosan nanofiber membrane by low-temperature phase separation for efficient selective adsorption of lithium. Sep. Purif. Technol. 262, 118312.

Chernyaev, A., Partinen, J., Klemettinen, L., Wilson, B.P., Jokilaakso, A., Lundström, M., 2021. The efficiency of scrap Cu and Al current collector materials as reductants in LIB waste leaching. Hydrometallurgy 203, 105608. https://doi.org/10.1016/J.HYDROMET.2021.105608

Chung, Y.H., Sivasubramanian, P.D., Chen, C.L., 2025. Novel deep eutectic solvent systems for selective transition metal recovery and sustainable battery recycling. Sep. Purif. Technol. 368, 133098. https://doi.org/10.1016/J.SEPPUR.2025.133098

Ciez, R.E., Whitacre, J.F., 2019. Examining different recycling processes for lithium-ion batteries. Nat. Sustain. 2, 148–156. https://doi.org/10.1038/S41893-019-0222-5

Conte, N., Gómez, J.M., 2024. Improving the sorption properties of mesoporous carbons for the removal of cobalt, nickel and manganese from spent lithium-ion batteries effluent. Sep. Purif. Technol. 328, 125095. https://doi.org/10.1016/J.SEPPUR.2023.125095

Dąbrowski, A., 2001. Adsorption—from theory to practice. Adv. Colloid Interface Sci. 93, 135–224.

Dagdeviren, R., Sevinc, R., Unlu, D., 2025. Lithium recovery from lithium/magnesium containing waters with biodegradable chitosan based EDTA doped adsorbent. Sep. Sci. Technol. 60, 1491–1501. https://doi.org/10.1080/01496395.2025.2508234

Das, D., R, A., Kay, P., Ramamurthy, V., Goycoolea, F.M., Das, N., 2022. Selective recovery of lithium from spent coin cell cathode leachates using ion imprinted blended chitosan microfibers: Pilot scale studies provide insights on scalability. J. Hazard. Mater. 431, 128535. https://doi.org/10.1016/J.JHAZMAT.2022.128535

Díez, E., Redondo, C., Gómez, J.M., Miranda, R., Rodríguez, A., 2023. Zeolite Adsorbents for Selective Removal of Co(II) and Li(I) from Aqueous Solutions. Water 2023, Vol. 15, Page 270 15, 270. https://doi.org/10.3390/W15020270

Ding, G., Liu, F., Fan, X., Gao, X., Cao, G., Ban, J., Li, Z., Hu, J., 2024. Research on green recycling of lithium-ion batteries cathode waste powder. Chemical Engineering Journal 493, 152837. https://doi.org/10.1016/J.CEJ.2024.152837

Ding, J., Templeton, M.R., He, Y., Peng, C., Chu, W., 2025. Optimizing multi-cycle atmospheric water harvesting via sorbent utilization efficiency. Energy & Environmental Sustainability 1, 100025. https://doi.org/10.1016/J.EESUS.2025.100025

Dobó, Z., Dinh, T., Kulcsár, T., 2023. A review on recycling of spent lithium-ion batteries. Energy Reports 9, 6362–6395. https://doi.org/10.1016/J.EGYR.2023.05.264

Dorella, G., Mansur, M.B., 2007. A study of the separation of cobalt from spent Li-ion battery residues. J. Power Sources 170, 210–215.

Du, J., Dong, Z., Lin, Z., Yang, X., Zhao, L., 2019. Radiation Synthesis of Pentaethylene Hexamine Functionalized Cotton Linter for Effective Removal of Phosphate: Batch and Dynamic Flow Mode Studies. Materials 12, 3393. https://doi.org/10.3390/MA12203393

Durante-Salmerón, D.A., Fraile-Gutiérrez, I., Gil-Gonzalo, R., Acosta, N., Aranaz, I., Alcántara, A.R., 2024. Strategies to Prepare Chitin and Chitosan-Based Bioactive Structures Aided by

Deep Eutectic Solvents: A Review. Catalysts 2024, Vol. 14, Page 371 14, 371. https://doi.org/10.3390/CATAL14060371

Egbosiuba, T.C., Abdulkareem, A.S., Kovo, A.S., Afolabi, E.A., Tijani, J.O., Auta, M., Roos, W.D., 2020. Ultrasonic enhanced adsorption of methylene blue onto the optimized surface area of activated carbon: Adsorption isotherm, kinetics and thermodynamics. Chemical Engineering Research and Design 153, 315–336. https://doi.org/10.1016/J.CHERD.2019.10.016

Eissa, M.E., Abdel-Megid, M., Atia, B.M., Gado, M.A., Cheira, M.F., Hassanein, T.F., 2026. A sustainable approach to the Ugi-one-pot multi-component system (Ugi-4CRs) for a novel chelating α-acylamido carboxamide: design, synthesis, and sorption aspects for Co(II) ions from discarded lithium-ion batteries. Chem. Eng. Sci. 320, 122642. https://doi.org/10.1016/J.CES.2025.122642

Elnour, A.Y., Alghyamah, A.A., Shaikh, H.M., Poulose, A.M., Al-Zahrani, S.M., Anis, A., Al-Wabel, M.I., 2019. Effect of pyrolysis temperature on biochar microstructural evolution, physicochemical characteristics, and its influence on biochar/polypropylene composites. Applied sciences 9, 1149.

Elzahar, M.M.H., Bassyouni, M., 2023. Removal of direct dyes from wastewater using chitosan and polyacrylamide blends. Scientific Reports 2023 13:1 13, 1–16. https://doi.org/10.1038/s41598-023-42960-y

Fathi, B., Harirforoush, M.J., Foruzanmehr, Mr.R., Elkoun, S., Robert, M., 2017. Effect of TEMPO oxidation of flax fibers on the grafting efficiency of silane coupling agents. J. Mater. Sci. 52, 10624–10636. https://doi.org/10.1007/S10853-017-1224-1

Foxworth, C., Strauss, C., Torres, A., Hydrometallurgical recovery of materials from lithium-ion batteries.

Gaines, L., 2018. Lithium-ion battery recycling processes: Research towards a sustainable course. Sustainable Materials and Technologies 17, e00068. https://doi.org/10.1016/J.SUSMAT.2018.E00068

Gantz, P.C., Panjiyar, L., Neumann, A., Neumann, M., Roggendorf, H., Wehrspohn, R., Stöber, S., Stephan-Scherb, C., 2025. Lithium-Phase Identification in an Industrial Lithium-Ion-Battery Recycling Slag: Implications for the Recovery of Lithium. Advanced Energy and

Sustainability Research 6, 2400338. https://doi.org/10.1002/AESR.202400338;REQUESTEDJOURNAL:JOURNAL:26999412;WGROUP:STRING:PUBLICATION

Gao, S.J., Liu, W.F., Fu, D.J., Liu, X.G., 2022. Research progress on recovering the components of spent Li-ion batteries. New Carbon Materials 37, 435–460. https://doi.org/10.1016/S1872-5805(22)60605-X

Garcia, B.B.M., Mertins, O., da Silva, E.R., Han, S.W., 2024. Influence of the degree of arginine substitution on chitosan-N-arginine-based chitosomes: Insights for improved gene delivery systems. J. Drug Deliv. Sci. Technol. 92, 105368. https://doi.org/10.1016/J.JDDST.2024.105368

Gaye, N., Gueye, R.S., Ledauphin, J., Balde, M., Seck, M., Wele, A., Diaw, M., 2019. Alkaline Leaching of Metals from Cathodic Materials of Spent Lithium-Ion Batteries. Asian Journal of Applied Chemistry Research 1–7. https://doi.org/10.9734/AJACR/2019/V3I230088

Gebeyehu, K.B., Chen, L., Fan, L., Chao, Y., Zhu, W., 2025. Recovery of high-value metals from the cathode of spent lithium-ion batteries via acid leaching: A review. J. Environ. Chem. Eng. 13, 116174. https://doi.org/10.1016/J.JECE.2025.116174

Ghareh Bagh, F.S., Ray, S., Seth, R., 2021a. Characteristics of acetate and lactate protic ionic liquids and their suitability to extract lignin from black liquor. Journal of Ionic Liquids 1, 100005. https://doi.org/10.1016/J.JIL.2021.100005

Ghareh Bagh, F.S., Ray, S., Seth, R., 2021b. Optimizing lignin extraction from Kraft black liquor using protic Ionic liquids. Biomass Bioenergy 154, 106249. https://doi.org/10.1016/J.BIOMBIOE.2021.106249

Ghassa, S., Farzanegan, A., Gharabaghi, M., Abdollahi, H., 2021. Iron scrap, a sustainable reducing agent for waste lithium ions batteries leaching: An environmentally friendly method to treating waste with waste. Resour. Conserv. Recycl. 166, 105348. https://doi.org/10.1016/J.RESCONREC.2020.105348

Golmohammadzadeh, R., Dimachki, Z., Bryant, W., Zhang, J., Biniaz, P., Holl, M.M.B., Pozo-Gonzalo, C., Banerjee, P.C., 2023. Removal of polyvinylidene fluoride binder and other organics for enhancing the leaching efficiency of lithium and cobalt from black mass. J. Environ. Manage. 343, 118205.

Golmohammadzadeh, R., Faraji, F., Jong, B., Pozo-Gonzalo, C., Banerjee, P.C., 2022. Current challenges and future opportunities toward recycling of spent lithium-ion batteries. Renewable and Sustainable Energy Reviews 159, 112202. https://doi.org/10.1016/J.RSER.2022.112202

Golmohammadzadeh, R., Rashchi, F., Vahidi, E., 2017. Recovery of lithium and cobalt from spent lithium-ion batteries using organic acids: Process optimization and kinetic aspects. Waste Management 64, 244–254.

Grigoraș, C.G., Simion, A.I., Drob, C., 2024. Hydrogels Based on Chitosan and Nanoparticles and Their Suitability for Dyes Adsorption from Aqueous Media: Assessment of the Last-Decade Progresses. Gels 10, 211. https://doi.org/10.3390/GELS10030211

Guimarães, L.F., Junior, A.B.B., Espinosa, D.C.R., 2022. Sulfuric acid leaching of metals from waste Li-ion batteries without using reducing agent. Miner. Eng. 183, 107597.

Guo, T.Y., Xia, Y.Q., Hao, G.J., Song, M.D., Zhang, B.H., 2004. Adsorptive separation of hemoglobin by molecularly imprinted chitosan beads. Biomaterials 25, 5905–5912. https://doi.org/10.1016/J.BIOMATERIALS.2004.01.032

Hamza, M.F., Mira, H., Wei, Y., Aboelenin, S.M., Guibal, E., Salem, W.M., 2022. Sulfonation of chitosan for enhanced sorption of Li(I) from acidic solutions – Application to metal recovery from waste Li-ion mobile battery. Chemical Engineering Journal 441, 135941. https://doi.org/10.1016/J.CEJ.2022.135941

Han, J., Gao, X., Gu, K., 2025. Lithium-ion batteries: Future market, challenges, and recycling. Nanostructured Lithium-ion Battery Materials: Synthesis, Characterization, and Applications 587–620. https://doi.org/10.1016/B978-0-443-13338-1.00021-6

Han, S., Zhenghao, M., Meilin, L., Xiaohui, Y., Xiaoxue, W., 2023. Global supply sustainability assessment of critical metals for clean energy technology. Resources Policy 85, 103994. https://doi.org/10.1016/J.RESOURPOL.2023.103994

He, B., Zheng, H., Tang, K., Xi, P., Li, M., Wei, L., Guan, Q., 2024. A Comprehensive Review of Lithium-Ion Battery (LiB) Recycling Technologies and Industrial Market Trend Insights. Recycling. https://doi.org/10.3390/recycling9010009

Holme, H.K., Foros, H., Pettersen, H., Dornish, M., Smidsrød, O., 2001. Thermal depolymerization of chitosan chloride. Carbohydr. Polym. 46, 287–294. https://doi.org/10.1016/S0144-8617(00)00332-5

Hossain, R., Sahajwalla, V., 2022. Microrecycled Co3O4 from waste lithium-ion battery: Synthesis, characterisation and implication in environmental application. J. Environ. Chem. Eng. 10, 107858. https://doi.org/10.1016/J.JECE.2022.107858

Hu, J., Zhang, J., Li, H., Chen, Y., Wang, C., 2017. A promising approach for the recovery of high value-added metals from spent lithium-ion batteries. J. Power Sources 351, 192–199. https://doi.org/10.1016/J.JPOWSOUR.2017.03.093

Huang, H., Liu, C., Sun, Z., 2022. Transformation and migration mechanism of fluorine-containing pollutants in the pyrolysis process of spent lithium-ion battery. J. Hazard. Mater. 435. https://doi.org/10.1016/J.JHAZMAT.2022.128974

Huang, Y., Li, X., Chen, L., Luo, G., Tao, D., Sun, J., Qiu, Z., Chao, Y., Zhu, W., 2022. Synthesis of a magnetic crown ether ion imprinted polymer material for the selective adsorption of lithium. New Journal of Chemistry 47, 3134–3139. https://doi.org/10.1039/D2NJ05377B

Iqbal, A., Jan, M.R., Shah, J., 2022. Recovery of cobalt from spent lithium ion batteries utilizing surface modified graphene oxide. Hydrometallurgy 213, 105911. https://doi.org/10.1016/J.HYDROMET.2022.105911

Jing, C., Tuan Tran, T., Seung Lee, M., 2024. A Review on the Recovery of Lithium and Iron from Spent Lithium Iron Phosphate Batteries. Mineral Processing and Extractive Metallurgy Review 45, 892–903. https://doi.org/10.1080/08827508.2024.2305382

Jock, A., OLUWADAYO, F., 2023. Application of Adsorption Thermodynamics and Column Studies for Pb2+, Cd2+ and Mn2+ Ions Removal in Multicomponents Model Solution Using Low-Cost Bentonite Clay Adsorbent. ABUAD Journal of Engineering Research and Development (AJERD) 6, 44–50. https://doi.org/10.53982/AJERD.2023.0601.06-J

Jonathan Wilkinson, François-Philippe Champagne, 2022. The Canadian Critical Minerals Strategy: From Exploration to Recycling: Powering the Green and Digital Economy for Canada and the World [WWW Document]. Government of Canada.

Joulié, M., Billy, E., Laucournet, R., Meyer, D., 2017. Current collectors as reducing agent to dissolve active materials of positive electrodes from Li-ion battery wastes. Hydrometallurgy 169, 426–432.

Jóźwiak, T., Filipkowska, U., Szymczyk, P., Rodziewicz, J., Mielcarek, A., 2017. Effect of ionic and covalent crosslinking agents on properties of chitosan beads and sorption effectiveness of Reactive Black 5 dye. React. Funct. Polym. 114, 58–74.

Jung, J., Zhao, Y., 2011. Characteristics of deacetylation and depolymerization of β-chitin from jumbo squid (Dosidicus gigas) pens. Carbohydr. Res. 346, 1876–1884. https://doi.org/10.1016/J.CARRES.2011.05.021

Kader, Z.A., Marshall, A., Kennedy, J., 2021. A review on sustainable recycling technologies for lithium-ion batteries. Emergent Mater. 4, 725–735.

Kalavathy, H., Karthik, B., Miranda, L.R., 2010. Removal and recovery of Ni and Zn from aqueous solution using activated carbon from Hevea brasiliensis: Batch and column studies. Colloids Surf. B Biointerfaces 78, 291–302. https://doi.org/10.1016/J.COLSURFB.2010.03.014

Kamran, U., Park, S.-J., 2022. Hybrid biochar supported transition metal doped MnO2 composites: Efficient contenders for lithium adsorption and recovery from aqueous solutions. Desalination 522, 115387.

Karimi, S., Mafton-Azad, L., Behnajady, B., Tüzün, B., 2025. Response Surface Methodology (RSM) Design to Optimize the Cathode of Li-Ions Batteries Recycling in Deep Eutectic Solvent and DFT Simulation. Korean Journal of Chemical Engineering 42, 361–381. https://doi.org/10.1007/S11814-024-00288-X/FIGURES/10

Khajavian, M., Vatanpour, V., Castro-Muñoz, R., Boczkaj, G., 2022. Chitin and derivative chitosan-based structures — Preparation strategies aided by deep eutectic solvents: A review. Carbohydr. Polym. 275, 118702. https://doi.org/10.1016/J.CARBPOL.2021.118702

Khanam, S., Eti, S.A., Bashar, M.S., Sujan, S.M.A., Sharmin, N., Ray, S.K., 2025. Dynamic absorption of heavy metal from aqueous solution using lignin-hydrogel and natural filter materials in a packed column system. Int. J. Biol. Macromol. 302, 140356. https://doi.org/10.1016/J.IJBIOMAC.2025.140356

Kong, L., Wang, Z., Shi, Z., Hu, X., Liu, A., Tao, W., Wang, B., Wang, Q., 2023. Leaching valuable metals from spent lithium-ion batteries using the reducing agent methanol. Environmental Science and Pollution Research 30, 4258–4268.

Kotte, P., Yun, Y.S., 2014. L-cysteine impregnated alginate capsules as a sorbent for gold recovery. Polym. Degrad. Stab. 109, 424–429. https://doi.org/10.1016/j.polymdegradstab.2014.02.014

Kresse, C., Bookhagen, B., Andrade, L.B., Frenzel, M., 2025. Global Supply of Secondary Lithium from Lithium-Ion Battery Recycling. Recycling 2025, Vol. 10, Page 122 10, 122. https://doi.org/10.3390/RECYCLING10040122

Lei, Q., Zhou, K., Zhang, X., Yang, Q., Qiu, Z., Peng, C., He, D., Chen, W., 2025. Selective extraction of valuable metals from the organic leachate of spent LiNixCoyMn1-x-yO2 battery through a sequential co-precipitation-resin adsorption approach. Sep. Purif. Technol. 353, 128501. https://doi.org/10.1016/J.SEPPUR.2024.128501

Li, J., Wang, G., Management, Z.X.-W., 2016, Generation and detection of metal ions and volatile organic compounds (VOCs) emissions from the pretreatment processes for recycling spent lithium-ion. Elsevier.

Li, P., Luo, S., Lin, Y., Xiao, J., Xia, X., Liu, X., Wang, L., He, X., 2024. Fundamentals of the recycling of spent lithium-ion batteries. Chem. Soc. Rev. 53, 11967–12013. https://doi.org/10.1039/D4CS00362D

Li, P., Luo, S.H., Su, F., Zhang, L., Yan, S., Lei, X., Mu, W., Wang, Q., Zhang, Y., Liu, X., Hou, P., 2022b. Optimization of Synergistic Leaching of Valuable Metals from Spent Lithium-Ion Batteries by the Sulfuric Acid-Malonic Acid System Using Response Surface Methodology. ACS Appl. Mater. Interfaces 14, 11359–11374. https://doi.org/10.1021/ACSAMI.1C23258/ASSET/IMAGES/MEDIUM/AM1C23258_M040.GIF

Li, S., Zhang, W., Xia, Y., Li, Q., 2024. Enhanced reducing capacity of citric acid for lithium-ion battery recycling under microwave-assisted leaching. Waste Management 189, 23–33. https://doi.org/10.1016/J.WASMAN.2024.08.004

Li, Xifan, Li, Xin, Chen, G., Li, H., Duan, Y., Sun, Y., Tiraferri, A., Liu, B., 2025. Efficient recovery of lithium from spent lithium-ion battery raffinate by Mn and Al-based adsorbents:

pretreatment, adsorption mechanism, and performance comparison. Sep. Purif. Technol. 354, 128652. https://doi.org/10.1016/J.SEPPUR.2024.128652

Li, Z., Liu, C., Hong, S., Lian, H., Mei, C., Lee, J., Wu, Q., Hubbe, M.A., Li, M.C., 2022. Recent advances in extraction and processing of chitin using deep eutectic solvents. Chemical Engineering Journal 446, 136953. https://doi.org/10.1016/J.CEJ.2022.136953

Liang, Q., Zhang, E., Yan, G., Yang, Y., Liu, W., Materials, X.L.-N.C., 2020, undefined, n.d. A lithium ion-imprinted adsorbent using magnetic carbon nanospheres as a support for the selective recovery of lithium ions. Elsevier.

Libralato, G., Volpi Ghirardini, A., Avezzù, F., 2010. Seawater ecotoxicity of monoethanolamine, diethanolamine and triethanolamine. J. Hazard. Mater. 176, 535–539. https://doi.org/10.1016/J.JHAZMAT.2009.11.062

Lim, J., Jang, Y., Lee, J., Lee, C., Jbari, O., Kwon, K., Chung, E., 2025. Hydrometallurgical process of spent lithium-ion battery recycling Part. 2 Recovery of valuable metals from the cathode active material leachates: Review and cost analysis. Hydrometallurgy 236, 106516. https://doi.org/10.1016/J.HYDROMET.2025.106516

Lima, E.C., Hosseini-Bandegharaei, A., Moreno-Piraján, J.C., Anastopoulos, I., 2019. A critical review of the estimation of the thermodynamic parameters on adsorption equilibria. Wrong use of equilibrium constant in the Van't Hoof equation for calculation of thermodynamic parameters of adsorption. J. Mol. Liq. 273, 425–434. https://doi.org/10.1016/J.MOLLIQ.2018.10.048

Lin, X., Wu, J., Lin, J., Wang, N., Su, M., Tang, J., Shih, K., Xu, J., 2025. Selective recovery of Ni, Co, and Li from spent NCA lithium-ion batteries: 3D macroporous bio-based adsorbent and innovative leaching–adsorption strategy. J. Environ. Chem. Eng. 13, 118063. https://doi.org/10.1016/J.JECE.2025.118063

Liu, B., Luo, H., Rong, H., Zeng, X., Wu, K., Chen, Z., Lu, H., Xu, D., 2019. Temperature-induced adsorption and desorption of phosphate on poly(Acrylic acid-co-N-[3-(dimethylamino)propyl]acrylamide) hydrogels in aqueous solutions. Desalination Water Treat. 160, 260–267. https://doi.org/10.5004/DWT.2019.24351

Liu, C., Lin, J., Cao, H., Zhang, Y., Sun, Z., 2019. Recycling of spent lithium-ion batteries in view of lithium recovery: A critical review. J. Clean. Prod. 228, 801–813. https://doi.org/10.1016/J.JCLEPRO.2019.04.304

Liu, H., Xue, K., Zhu, W., Fan, D., Dong, Z., Wang, Y., Qi, J., Zhu, Z., Cui, P., 2024. Cobalt recovery from lithium battery leachate using hydrophobic deep eutectic solvents: Performance and mechanism. Process Safety and Environmental Protection 190, 1–10. https://doi.org/10.1016/J.PSEP.2024.07.047

Liu, J., An, X., Huang, L., Zhou, H., Liang, D., Xie, Q., Fan, M., 2024. In-situ magnetization of porous carbon beads for lithium-ion adsorption from strongly acidic solution. J. Clean. Prod. 435, 140625. https://doi.org/10.1016/J.JCLEPRO.2024.140625

Liu, J., Wang, H., Hu, T., Bai, X., Wang, S., Xie, W., Hao, J., He, Y., 2020. Recovery of LiCoO2 and graphite from spent lithium-ion batteries by cryogenic grinding and froth flotation. Miner. Eng. 148, 106223. https://doi.org/10.1016/J.MINENG.2020.106223

Liu, P., Mi, X., Zhao, H., Cai, L., Luo, F., Liu, C., Wang, Z., Deng, C., He, J., Zeng, G., 2023. Effects of incineration and pyrolysis on removal of organics and liberation of cathode active materials derived from spent ternary lithium-ion batteries. Waste Management 169, 342–350.

Liu, P., Xiao, L., Chen, Y., Tang, Y., Wu, J., Chen, H., 2019. Recovering valuable metals from LiNixCoyMn1-x-yO2 cathode materials of spent lithium ion batteries via a combination of reduction roasting and stepwise leaching. J. Alloys Compd. 783, 743–752. https://doi.org/10.1016/J.JALLCOM.2018.12.226

Liu, R., Li, J., Liu, X., Yin, X., Yang, Y., 2025. Novel ternary deep eutectic solvents used for recycling lithium and cobalt from waste lithium-ion batteries. Sep. Purif. Technol. 354, 128934. https://doi.org/10.1016/J.SEPPUR.2024.128934

Liu, X. qi, Zhao, X. xin, Liu, Y., Zhang, T. an, 2022. Review on preparation and adsorption properties of chitosan and chitosan composites. Polymer Bulletin 79, 2633–2665. https://doi.org/10.1007/S00289-021-03626-9

Liu, X., Ren, W., Song, W., Zhang, W., Wang, Yuhan, Wang, Yi, Fan, G., Zhang, L., Huang, Y., 2025. Novel EDTA-chitosan/alginate porous composite beads for the removal of Pb(II) and methylene blue from aqueous solutions †. https://doi.org/10.1039/d5ra00940e

Liu, Y., Nam, S.H., Lee, M.S., 2015. A Study on the Separation of Co(II), Ni(II), and Mg(II) by Solvent Extraction with Cationic Extractants. Bull. Korean Chem. Soc. 36, 2646–2650. https://doi.org/10.1002/BKCS.10535

Luo, J., Chen, J., Liu, Y., He, Y., Dong, W., 2023. A Novel Form of Arginine-Chitosan as Nanoparticles Efficient for siRNA Delivery into Mouse Leukemia Cells. International Journal of Molecular Sciences 2023, Vol. 24, Page 1040 24, 1040. https://doi.org/10.3390/IJMS24021040

Ma, Q., Mu, J., Lv, X., Meng, J., Cui, H., Qiu, Y., Ruan, H., Shen, J., 2023. Sustainable Recovery of Ionic Resources from Resin Regeneration Wastewater: Long-Term Evaluation, Membrane Fouling Analysis, and Cleaning. ACS ES and T Water 3, 1855–1864. https://doi.org/10.1021/ACSESTWATER.2C00367/ASSET/IMAGES/LARGE/EW2C00367_0010.JPEG

Ma, X., Meng, Z., Bellonia, M.V., Spangenberger, J., Harper, G., Gratz, E., Olivetti, E., Arsenault, R., Wang, Y., 2025. The evolution of lithium-ion battery recycling. Nature Reviews Clean Technology 2025 1:1 1, 75–94. https://doi.org/10.1038/s44359-024-00010-4

MacFarlane, D.R., Pringle, J.M., Johansson, K.M., Forsyth, S.A., Forsyth, M., 2006. Lewis base ionic liquids. Chemical Communications 1905–1917. https://doi.org/10.1039/B516961P

Mahran, G.M.A., Gado, M.A., Fathy, W.M., ElDeeb, A.B., 2023. Eco-Friendly Recycling of Lithium Batteries for Extraction of High-Purity Metals. Materials 2023, Vol. 16, Page 4662 16, 4662. https://doi.org/10.3390/MA16134662

Malbenia John, M., Benettayeb, A., Belkacem, M., Ruvimbo Mitchel, C., Hadj Brahim, M., Benettayeb, I., Haddou, B., Al-Farraj, S., Alkahtane, A.A., Ghosh, S., Chia, C.H., Sillanpaa, M., Baigenzhenov, O., Hosseini-Bandegharaei, A., 2024. An overview on the key advantages and limitations of batch and dynamic modes of biosorption of metal ions. Chemosphere 357, 142051. https://doi.org/10.1016/J.CHEMOSPHERE.2024.142051

Manickasundaram, M., Lakshmanan, K., Vediappan, K., Kancharla, S., 2024. Chitosan-based copper recovery from e-waste and its application in sustainable energy storage. Chemical Engineering Journal 484, 149605. https://doi.org/10.1016/J.CEJ.2024.149605

Mansur, M.B., Guimarães, A.S., Petraniková, M., 2021. An Overview on the Recovery of Cobalt from End-of-life Lithium Ion Batteries. Mineral Processing and Extractive Metallurgy Review 43, 489–509. https://doi.org/10.1080/08827508.2021.1883014

Manzoor, K., Ahmad, M., Ahmad, S., Ikram, S., 2019. Removal of Pb(II) and Cd(II) from wastewater using arginine cross-linked chitosan–carboxymethyl cellulose beads as green adsorbent. RSC Adv. 9, 7890–7902. https://doi.org/10.1039/C9RA00356H

Mao, C., Imtiaz, S.A., Zhang, Y., 2015. Competitive adsorption of Ag (I) and Cu (II) by tripolyphosphate crosslinked chitosan beads. J. Appl. Polym. Sci. 132.

Mariana, M., Abdul, A.K., Mistar, E.M., Yahya, E.B., Alfatah, T., Danish, M., Amayreh, M., 2021. Recent advances in activated carbon modification techniques for enhanced heavy metal adsorption. Journal of Water Process Engineering 43, 102221. https://doi.org/10.1016/J.JWPE.2021.102221

Meng, F., Liu, Q., Kim, R., Wang, J., Liu, G., Ghahreman, A., 2020. Selective recovery of valuable metals from industrial waste lithium-ion batteries using citric acid under reductive conditions: Leaching optimization and kinetic analysis. Hydrometallurgy 191, 105160.

Meng, F., McNeice, J., Zadeh, S.S., Ghahreman, A., 2021. Review of Lithium Production and Recovery from Minerals, Brines, and Lithium-Ion Batteries. Mineral Processing and Extractive Metallurgy Review 42, 123–141. https://doi.org/10.1080/08827508.2019.1668387;WGROUP:STRING:PUBLICATION

Metwally, S.S., Ayoub, R.R., Aly, H.F., 2013. Amidoximation of cyano group for chelating ion exchange of some heavy metal ions from wastewater. Sep. Sci. Technol. 48, 1830–1840.

Metwally, S.S., Emad, ·, Borai, H., Mostafa, ·, Hamed, M., Reham, ·, Hassan, S., 2024. Sorption behavior of selected fission products on spent alum sludge. J. Radioanal. Nucl. Chem. 333, 4675–4686. https://doi.org/10.1007/s10967-024-09612-5

Metwally, S.S., Hassan, M.A., Aglan, R.F., 2013c. Extraction of copper from ammoniacal solution using impregnated amberlite XAD-7 resin loaded with LIX-54. J. Environ. Chem. Eng. 1, 252–259.

Metwally, S.S., Rizk, H.E., Gasser, M.S., 2017. Biosorption of strontium ions from aqueous solution using modified eggshell materials. Radiochim. Acta 105, 1021–1031. https://doi.org/10.1515/RACT-2016-2729/MACHINEREADABLECITATION/RIS

Mirzaee, E., Sartaj, M., 2022. Activated carbon-based magnetic composite as an adsorbent for removal of polycyclic aromatic hydrocarbons from aqueous phase: Characterization, adsorption kinetics and isotherm studies. Journal of Hazardous Materials Advances 6, 100083.

Mishra, G., Jha, R., Meshram, A., Singh, K.K., 2022. A review on recycling of lithium-ion batteries to recover critical metals. J. Environ. Chem. Eng. 10, 108534. https://doi.org/10.1016/J.JECE.2022.108534

Mohammed, A.A., Abdel Moamen, O.A., Metwally, S.S., El-Kamash, A.M., Ashour, I., Al-Geundi, M.S., 2020. Utilization of Modified Attapulgite for the Removal of Sr(II), Co(II), and Ni(II) Ions from Multicomponent System, Part I: Kinetic Studies. Environmental Science and Pollution Research 27, 6824–6836. https://doi.org/10.1007/S11356-019-07292-3/TABLES/5

Mohan, K., Ganesan, A.R., Ezhilarasi, P.N., Kondamareddy, K.K., Rajan, D.K., Sathishkumar, P., Rajarajeswaran, J., Conterno, L., 2022. Green and eco-friendly approaches for the extraction of chitin and chitosan: A review. Carbohydr. Polym. https://doi.org/10.1016/j.carbpol.2022.119349

Mohanta, D., Ahmaruzzaman, M., 2018. Bio-inspired adsorption of arsenite and fluoride from aqueous solutions using activated carbon@ SnO 2 nanocomposites: Isotherms, kinetics, thermodynamics, cost estimation and regeneration studies. J. Environ. Chem. Eng. 6, 356–366.

Mourak, A., Hajjaji, M., Alagui, A., 2025. Preparation and characterization of chitosan clay beads for water adsorption. Sci. Rep. 15, 1–20. https://doi.org/10.1038/S41598-025-14662-0;SUBJMETA

Muhammad, S., Javed, M.N., Gill, K.A., Ali, F.I., Henderson, W., Bari, A., Musharraf, S.G., Baig, J.A., Hashmi, I.A., 2022. Selective extraction of heavy metals (Fe, Co, Ni) from their aqueous mixtures by Task-Specific salicylate functionalized imidazolium based ionic liquid. J. Clean. Prod. 344, 131119.

Musariri, B., Akdogan, G., Dorfling, C., Bradshaw, S., 2019. Evaluating organic acids as alternative leaching reagents for metal recovery from lithium ion batteries. Miner. Eng. 137, 108–117. https://doi.org/10.1016/J.MINENG.2019.03.027

Mwanat, M.H.M., Kasongo, K.B., Muliangala, F., Mwema, E., Makhatha, M.E., Ngenda, R., 2024. Removal of Fe and Mn from Co leach solutions by adsorption on activated carbon based on post-consumer polyethylene terephthalate (PET) - Mechanism insights through linear and nonlinear isotherm and kinetic models. Sep. Sci. Technol. https://doi.org/10.1080/01496395.2024.2315607

Nancharaiah, Y. V., Mohan, S.V., Lens, P.N.L., 2016. Biological and Bioelectrochemical Recovery of Critical and Scarce Metals. Trends Biotechnol. 34, 137–155. https://doi.org/10.1016/J.TIBTECH.2015.11.003

Natarajan, S., Bajaj, H.C., Aravindan, V., 2019. Template-free synthesis of carbon hollow spheres and reduced graphene oxide from spent lithium-ion batteries towards efficient gas storage. J. Mater. Chem. A Mater. 7, 3244–3252.

Naz, H., Khalid, Z., Arif, S., Sattar, A., Ahmed, M.N., Waseem, M., 2025. High removal efficiency of arsenite from aqueous solution by cobalt ferrite functionalized sawdust driven activated carbon. Inorg. Chem. Commun. 178, 114615. https://doi.org/10.1016/J.INOCHE.2025.114615

Nguyen, T.H., Khanh Son, T., Hue, B.T.B., Van Hieu, M., 2021. Fatty acid methyl esters from catfish oil as a potential diluent for separation of Co(II) and Li(I) from spent lithium-ion batteries by solvent extraction. https://doi.org/10.1080/01496395.2021.1886116 57, 94–102. https://doi.org/10.1080/01496395.2021.1886116

Nguyen, V.N.H., Lee, M.S., 2020. Separation of Co(II), Cu(II), Ni(II) and Mn(II) from synthetic hydrochloric acid leaching solution of spent lithium ion batteries by solvent extraction. Physicochemical Problems of Mineral Processing 56, 599–610. https://doi.org/10.37190/PPMP/122784

Ofudje, E.A., Adedapo, A.E., Oladeji, O.B., Sodiya, E.F., Ibadin, F.H., Zhang, D., 2021. Nano-rod hydroxyapatite for the uptake of nickel ions: Effect of sintering behaviour on adsorption parameters. J. Environ. Chem. Eng. 9. https://doi.org/10.1016/J.JECE.2021.105931

Orooji, Y., Nezafat, Z., Nasrollahzadeh, M., Shafiei, N., Afsari, M., Pakzad, K., Razmjou, A., 2022. Recent advances in nanomaterial development for lithium ion-sieving technologies. Desalination 529, 115624. https://doi.org/10.1016/J.DESAL.2022.115624

Ozel, N., Elibol, M., 2024. Chitin and chitosan from mushroom (Agaricus bisporus) using deep eutectic solvents. Int. J. Biol. Macromol. 262, 130110. https://doi.org/10.1016/J.IJBIOMAC.2024.130110

Park, B., Choi, S.J., 2023. Magnetic biochar modified with crosslinked chitosan and EDTA for removing cobalt from aqueous solutions. Journal of Radioanalytical and Nuclear Chemistry 2023 332:6 332, 2077–2091. https://doi.org/10.1007/S10967-023-08831-6

Park, M., Lee, Y., Kyung, J., Yoon, C.M., Song, S., 2025. Optimized activated carbon pellets for effective cobalt ion adsorption. Macromol. Res. 33, 523–531. https://doi.org/10.1007/S13233-024-00340-Z

Patel, H., 2022. Comparison of batch and fixed bed column adsorption: a critical review. International Journal of Environmental Science and Technology 19, 10409–10426. https://doi.org/10.1007/S13762-021-03492-Y

Patel, H., In, C., 2021. Comparison of batch and fixed bed column adsorption: a critical review. International Journal of Environmental Science and Technology 2021 19:10 19, 10409–10426. https://doi.org/10.1007/S13762-021-03492-Y

Paul, S., Shrotriya, P., 2025. Efficient Recycling Processes for Lithium-Ion Batteries. Materials 18, 613.

Pei, S., Yan, S., Chen, X., Li, J., Xu, J., 2024. Novel electrochemical process for recycling of valuable metals from spent lithium-ion batteries. Waste Management 188, 1–10. https://doi.org/10.1016/J.WASMAN.2024.07.018

Peng, C., Hamuyuni, J., Wilson, B.P., Lundström, M., 2018. Selective reductive leaching of cobalt and lithium from industrially crushed waste Li-ion batteries in sulfuric acid system. Waste Management 76, 582–590.

Peschel, C., van Wickeren, S., Preibisch, Y., Naber, V., Werner, D., Frankenstein, L., Horsthemke, F., Peuker, U., Winter, M., Nowak, S., 2022. Comprehensive Characterization of Shredded Lithium-Ion Battery Recycling Material. Chemistry – A European Journal 28, e202200485. https://doi.org/10.1002/CHEM.202200485

Piątek, J., Budnyak, T.M., Monti, S., Barcaro, G., Gueret, R., Grape, E.S., Jaworski, A., Inge, A.K., Rodrigues, B.V.M., Slabon, A., 2021. Toward Sustainable Li-Ion Battery Recycling: Green Metal-Organic Framework as a Molecular Sieve for the Selective Separation of Cobalt

and Nickel. ACS Sustain. Chem. Eng. 9, 9770–9778. https://doi.org/10.1021/ACSSUSCHEMENG.1C02146

Piccin, J.S., Cadaval, T.R.S.A., De Pinto, L.A.A., Dotto, G.L., 2017. Adsorption isotherms in liquid phase: Experimental, modeling, and interpretations. Adsorption Processes for Water Treatment and Purification 19–51. https://doi.org/10.1007/978-3-319-58136-1_2

Pinna, E.G., Toro, N., Gallegos, S., Rodriguez, M.H., 2021. A Novel Recycling Route for Spent Li-Ion Batteries. Materials 2022, Vol. 15, Page 44 15, 44. https://doi.org/10.3390/MA15010044

Portia Makwarimba, C., Tang, M., Peng, Y., Lu, S., Zheng, L., Zhao, Z., Zhen, A., 2022. Assessment of recycling methods and processes for lithium-ion batteries. cell.com 25, 104321. https://doi.org/10.1016/j.isci

Porvali, A., Shukla, S., Lundström, M., 2020. Low-acid leaching of lithium-ion battery active materials in Fe-catalyzed Cu-H2SO4 system. Hydrometallurgy 195, 105408. https://doi.org/10.1016/J.HYDROMET.2020.105408

Promkatkaew, M., Baiya, S., Tongwanichniyom, S., Kitjaruwankul, S., 2023. Experimental and Molecular Dynamics Simulation Insights into Adsorption of Co(II), Cr(III), and Cu(II) on Chitosan and Chitosan/Tripolyphosphate Nanoparticles. ACS Omega. https://doi.org/10.1021/ACSOMEGA.3C08835/ASSET/IMAGES/LARGE/AO3C08835_0009.JPEG

Promkatkaew, M., Srisuratsiri, P., Sangpanich, U., Somboonviwat, K., Kitjaruwankul, S., 2025. Graphene Oxide–Chitosan Composite for Efficient Adsorptive Removal of Cu(II), Co(II), and Ni(II) from Simulated E-Waste Effluents. ACS Omega 10, 44111–44124. https://doi.org/10.1021/ACSOMEGA.5C05350

Punt, T., Akdogan, G., Bradshaw, S., van Wyk, P., 2021. Development of a novel solvent extraction process using citric acid for lithium-ion battery recycling. Miner. Eng. 173, 107204. https://doi.org/10.1016/J.MINENG.2021.107204

Purnomo, C.W., Kesuma, E.P., Perdana, I., Aziz, M., 2018. Lithium recovery from spent Li-ion batteries using coconut shell activated carbon. Waste Management 79, 454–461.

Qu, X., Zhang, B., Zhao, J., Qiu, B., Chen, X., Zhou, F., Li, X., Gao, S., Wang, D., Yin, H., 2023. Salt-thermal methods for recycling and regenerating spent lithium-ion batteries: a review. Green Chemistry 25, 2992–3015. https://doi.org/10.1039/D2GC04620B

Rafati, L., Ehrampoush, M.H., Rafati, A.A., Mokhtari, M., Mahvi, A.H., 2019. Fixed bed adsorption column studies and models for removal of ibuprofen from aqueous solution by strong adsorbent Nano-clay composite. J. Environ. Health Sci. Eng. 17, 753. https://doi.org/10.1007/S40201-019-00392-9

Rahaman, M.H., Islam, M.R., Islam, R., Alam, S.M.N., Rahman, M.S., Rahman, M.A., Begum, B.A., 2024. Preparation, characterization, and adsorption kinetics of graphene oxide/chitosan/carboxymethyl cellulose composites for the removal of environmentally relevant toxic metals. Int. J. Biol. Macromol. 257, 128357. https://doi.org/10.1016/J.IJBIOMAC.2023.128357

Rahman, A., 2024. Promising and Environmentally Friendly Removal of Copper, Zinc, Cadmium, and Lead from Wastewater Using Modified Shrimp-Based Chitosan. Water 2024, Vol. 16, Page 184 16, 184. https://doi.org/10.3390/W16010184

Rahman, A., Haque, M.A., Ghosh, S., Shinu, P., Attimarad, M., Kobayashi, G., 2023. Modified Shrimp-Based Chitosan as an Emerging Adsorbent Removing Heavy Metals (Chromium, Nickel, Arsenic, and Cobalt) from Polluted Water. Sustainability 2023, Vol. 15, Page 2431 15, 2431. https://doi.org/10.3390/SU15032431

Rahman, M.M., Hossain, M.I., Ghos, B.C., Uddin, M.J., Knani, S., Waliullah, M., 2025a. A state-of-the-art review focusing on the fabrication technique of activated chitosan-bitumin coal based multifunctional bionanocomposites for industrial wastewater treatment: Production, characterization, and fixed bed column adsorption study. J. Environ. Chem. Eng. 13, 115908. https://doi.org/10.1016/J.JECE.2025.115908

Rahman, M.M., Maniruzzaman, M., ealam, N., Mahmud, P., Khatun, S., Hossain, M.K., Hossain, M.I., Hasanuzzaman, M., Alam, M.A., Al-amin, M., Ghos, B.C., 2025b. Adsorptive removal of toxic heavy metal and dyes from wastewater by rice husk (lignocellulosic biomass) derived activated biochar: A fixed-bed column adsorption study. Carbohydrate Polymer Technologies and Applications 9, 100698. https://doi.org/10.1016/J.CARPTA.2025.100698

Rajak, D.K., Guria, C., Gope, L., Jibran, J.A., 2023. Hydrometallurgical recovery of critical metals from spent Li-ion batteries using simple leaching-precipitation techniques. Geosystem Engineering 26, 239–249. https://doi.org/10.1080/12269328.2023.2208124

Reich, R., Slunitschek, K., Danisi, R.M., Eiche, E., Kolb, J., 2023. Lithium Extraction Techniques and the Application Potential of Different Sorbents for Lithium Recovery from Brines Lithium Extraction Techniques and the Application Potential of Different Sorbents for Lithium Recovery from Brines, Mineral Processing and …. Review 44, 261–280. https://doi.org/10.1080/08827508.2022.2047041

Ritcey, G.M., 1986. Silica Fouling in Ion Exchange, Carbon-in-Pulp and Solvent Extraction Circuits. Canadian Metallurgical Quarterly 25, 31–43. https://doi.org/10.1179/CMQ.1986.25.1.31

Robeck, B., Horn, H., 2024. Towards sustainable battery recycling: selective dynamic adsorption of nickel(II) and cobalt(II) in an adsorbent fixed-bed reactor at elevated temperature. Discover Chemical Engineering 4. https://doi.org/10.1007/S43938-023-00037-2

Rodrigues, S., Da Costa, A.M.R., Grenha, A., 2012. Chitosan/carrageenan nanoparticles: Effect of cross-linking with tripolyphosphate and charge ratios. Carbohydr. Polym. 89, 282–289.

Romal, J.R.A., Cheng, M.H., Ong, S.K., 2025. The recovery of dysprosium(III) using a modified phosphorylated chitosan resin by rapid small-scale column testing and its environmental impact assessment. J. Environ. Manage. 380, 125117. https://doi.org/10.1016/J.JENVMAN.2025.125117

Roshanfar, M., Golmohammadzadeh, R., Rashchi, F., 2019. An environmentally friendly method for recovery of lithium and cobalt from spent lithium-ion batteries using gluconic and lactic acids. J. Environ. Chem. Eng. 7. https://doi.org/10.1016/j.jece.2018.11.039

Roshanfar, M., Sartaj, M., Kazemeini, S., 2026. Synthesis, Process Optimization, and Statistical Analysis of Chitosan-Based Biosorbent Beads for Selective Lithium Recovery in Lithium-Ion Battery Recycling. Mineral Processing and Extractive Metallurgy Review 1–16. https://doi.org/10.1080/08827508.2026.2616815

Roshanfar, M., Sartaj, M., Kazemeini, S., 2025. Sustainable recovery of critical metals from spent lithium-ion batteries using chitosan as biosorbent in citrate-sulfate media: A comprehensive

isotherm, kinetic, and thermodynamic analysis. J. Environ. Manage. 375, 124400. https://doi.org/10.1016/J.JENVMAN.2025.124400

Roshanfar, M., Sartaj, M., Kazemeini, S., 2024. A greener method to recover critical metals from spent lithium-ion batteries (LIBs): Synergistic leaching without reducing agents. J. Environ. Manage. 366, 121862. https://doi.org/10.1016/J.JENVMAN.2024.121862

Rostami, M.S., Khodaei, M.M., 2024. Recent advances in chitosan-based nanocomposites for adsorption and removal of heavy metal ions. Int. J. Biol. Macromol. 270, 132386. https://doi.org/10.1016/J.IJBIOMAC.2024.132386

Saheed, I.O., Oh, W. Da, Suah, F.B.M., 2021. Chitosan modifications for adsorption of pollutants – A review. J. Hazard. Mater. 408, 124889. https://doi.org/10.1016/J.JHAZMAT.2020.124889

Salas, R., Villa, R., Velasco, F., Cirujano, F.G., Nieto, S., Martin, N., Garcia-Verdugo, E., Dupont, J., Lozano, P., 2025. Ionic liquids in polymer technology. Green Chemistry 27, 1620–1651. https://doi.org/10.1039/D4GC05445H

Salces, A.M., Bremerstein, I., Rudolph, M., Vanderbruggen, A., 2022. Joint recovery of graphite and lithium metal oxides from spent lithium-ion batteries using froth flotation and investigation on process water re-use. Miner. Eng. 184, 107670. https://doi.org/10.1016/J.MINENG.2022.107670

Salem, O.M., Khalek, A.A., Mohamed, F., 2024. Novel biocomposites based on carbon xerogel derived from tannin for improved cobalt (II) adsorption: practical and theoretical approaches. Diam. Relat. Mater. 147, 111302. https://doi.org/10.1016/J.DIAMOND.2024.111302

Sazali, Norsuhailizah, Harun, Z., Sazali, Norazlianie, 2020. A Review on Batch and Column Adsorption of Various Adsorbent Towards the Removal of Heavy Metal. Journal of Advanced Research in Fluid Mechanics and Thermal Sciences Journal homepage 67, 66–88.

Schaeffer, N., Passos, H., Gras, M., Rodriguez Vargas, S.J., Neves, M.C., Svecova, L., Papaiconomou, N., Coutinho, J.A.P., 2020. Selective separation of manganese, cobalt, and nickel in a fully aqueous system. ACS Sustain. Chem. Eng. 8, 12260–12269. https://doi.org/10.1021/ACSSUSCHEMENG.0C04043

Sethurajan, M., Gaydardzhiev, S., 2021. Bioprocessing of spent lithium ion batteries for critical metals recovery–A review. Resour. Conserv. Recycl. 165, 105225.

Setoguchi, T., Kato, T., Yamamoto, K., Kadokawa, J. ichi, 2012. Facile production of chitin from crab shells using ionic liquid and citric acid. Int. J. Biol. Macromol. 50, 861–864. https://doi.org/10.1016/J.IJBIOMAC.2011.11.007

Shamshina, J.L., Barber, P.S., Gurau, G., Griggs, C.S., Rogers, R.D., 2016. Pulping of crustacean waste using ionic liquids: To extract or not to extract. ACS Sustain. Chem. Eng. 4, 6072–6081. https://doi.org/10.1021/ACSSUSCHEMENG.6B01434/ASSET/IMAGES/SC-2016-01434H_M004.GIF

Sharifi, M.J., Nouralishahi, A., Hallajisani, A., 2023. Fe3O4-chitosan nanocomposite as a magnetic biosorbent for removal of nickel and cobalt heavy metals from polluted water. Int. J. Biol. Macromol. 248, 125984.

Shaw-Stewart, J., Alvarez-Reguera, A., Greszta, A., Marco, J., Masood, M., Sommerville, R., Kendrick, E., 2019. Aqueous solution discharge of cylindrical lithium-ion cells. Sustainable Materials and Technologies 22, e00110.

Shin, S.M., Kim, N.H., Sohn, J.S., Yang, D.H., Kim, Y.H., 2005. Development of a metal recovery process from Li-ion battery wastes. Hydrometallurgy 79, 172–181.

Sing, K.S.W., 1985. Reporting physisorption data for gas/solid systems with special reference to the determination of surface area and porosity (Recommendations 1984). Pure and applied chemistry 57, 603–619.

Siyu, G., Enhua, D., Bingguo, L., Chao, Y., Yifan, N., Guangxiong, J., Wang, C., Keren, H., Shenghui, G., Libo, Z., 2024. Eco-friendly closed-loop recycling of nickel, cobalt, manganese, and lithium from spent ternary lithium-ion battery cathodes. Sep. Purif. Technol. 348, 127771. https://doi.org/10.1016/J.SEPPUR.2024.127771

Sloop, S., Crandon, L., Allen, M., Koetje, K., Reed, L., Gaines, L., Sirisaksoontorn, W., Lerner, M., 2020. A direct recycling case study from a lithium-ion battery recall. Sustainable Materials and Technologies 25, e00152.

Solberg, S.B.B., Gómez-Coma, L., Wilhelmsen, Ø., Forsberg, K., Burheim, O.S., 2024. Electrodialysis for efficient antisolvent recovery in precipitation of critical metals and lithium-ion battery recycling. Chemical Engineering Journal 486, 150281. https://doi.org/10.1016/J.CEJ.2024.150281

Sommerville, R., Shaw-Stewart, J., Goodship, V., Rowson, N., Kendrick, E., 2020. A review of physical processes used in the safe recycling of lithium ion batteries. Sustainable Materials and Technologies 25, e00197. https://doi.org/10.1016/J.SUSMAT.2020.E00197

Song, D., Wang, T., Liu, Z., Zhao, S., Quan, J., Li, G., Zhu, H., Huang, J., He, W., 2022. Characteristic comparison of leaching valuable metals from spent power Li-ion batteries for vehicles using the inorganic and organic acid system. J. Environ. Chem. Eng. 10, 107102. https://doi.org/10.1016/J.JECE.2021.107102

Strauss, M.L., Diaz, L.A., McNally, J., Klaehn, J., Lister, T.E., 2021. Separation of cobalt, nickel, and manganese in leach solutions of waste lithium-ion batteries using Dowex M4195 ion exchange resin. Hydrometallurgy 206, 105757. https://doi.org/10.1016/J.HYDROMET.2021.105757

Su, F., Zhou, X., Liu, X., Yang, J., Tang, J., Yang, W., Li, Z., Wang, H., Ma, Y., 2023. Efficient recovery of valuable metals from spent Lithium-ion batteries by pyrite method with hydrometallurgy process. Chemical Engineering Journal 455, 140914. https://doi.org/10.1016/J.CEJ.2022.140914

Sulthan, R., Reghunadhan, A., Sambhudevan, S., 2023. A new era of chitin synthesis and dissolution using deep eutectic solvents- comparison with ionic liquids. J. Mol. Liq. 380, 121794. https://doi.org/10.1016/J.MOLLIQ.2023.121794

Sun, X., Wang, Q., Chen, J., Deng, Y., Wang, X., Niu, H., Wu, D., 2024. Surface chitosan-grafting modification of polyimide fibers for cobalt ion adsorption. Colloids Surf. A Physicochem. Eng. Asp. 697, 133935. https://doi.org/10.1016/J.COLSURFA.2024.133935

Sushma, Keshav, A., Ramachandran, M., 2025. Biosorptive removal of cobalt (II) ion from wastewater using pomegranate peel activated carbon as biosorbent. Journal of the Serbian Chemical Society 90, 529–543. https://doi.org/10.2298/JSC240520084S

Sutirman, Z.A., Sanagi, M.M., Abd Karim, K.J., Wan Ibrahim, W.A., 2016. Preparation of methacrylamide-functionalized crosslinked chitosan by free radical polymerization for the removal of lead ions. Carbohydr. Polym. 151, 1091–1099. https://doi.org/10.1016/J.CARBPOL.2016.06.076

Suzuki, M., Suzuki, M., 1990. Adsorption engineering.

Syeda, H.I., Muthukumaran, S., Baskaran, K., 2025. Dynamic adsorption of heavy metals on functionalized and regeneratable biopolymeric aerogels: Fixed-bed column reactor modelling and dual functionality elution technique. Sep. Purif. Technol. 363, 131861. https://doi.org/10.1016/J.SEPPUR.2025.131861

Syeda, Shan E Zehra, Khan, M.S., Skwierawska, A.M., 2024. Chitosan-based modalities with multifunctional attributes for adsorptive mitigation of hazardous metal contaminants from wastewater. Desalination Water Treat. 100679.

Syeda, Shan E.Zehra, Khan, M.S., Skwierawska, A.M., 2024. Chitosan-based modalities with multifunctional attributes for adsorptive mitigation of hazardous metal contaminants from wastewater. Desalination Water Treat. 320. https://doi.org/10.1016/j.dwt.2024.100679

Taha, A.M., Mustafa, F.H.A., Ibrahim, H.E., Mohamadein, L.I., Anwar, Z.M., Elsharaawy, R.F.M., 2025. Adsorptive removal of heavy metal ions from wastewater using shrimp chitosan-cysteine-glutaraldehyde hydrogel as a sustainable biosorbent. Int. J. Biol. Macromol. 312, 143846. https://doi.org/10.1016/J.IJBIOMAC.2025.143846

Tobiason, J.E., Bazilio, A., Goodwill, J., Mai, X., Nguyen, C., 2016. Manganese Removal from Drinking Water Sources. Curr. Pollut. Rep. 2, 168–177. https://doi.org/10.1007/S40726-016-0036-2

Tofan, L., Teodosiu, C., Paduraru, C., Wenkert, R., 2013. Cobalt (II) removal from aqueous solutions by natural hemp fibers: Batch and fixed-bed column studies. Appl. Surf. Sci. 285, 33–39. https://doi.org/10.1016/J.APSUSC.2013.06.151

Tolesa, L.D., Gupta, B.S., Lee, M.J., 2019. Chitin and chitosan production from shrimp shells using ammonium-based ionic liquids. Int. J. Biol. Macromol. 130, 818–826. https://doi.org/10.1016/j.ijbiomac.2019.03.018

Tran, T.T., Jing, C., Lee, M.S., 2025. Mineral Processing and Extractive Metallurgy Review An International Journal A Review on the Recovery Methods of Lithium Hydroxide from Diverse Lithium-Bearing Resources A Review on the Recovery Methods of Lithium Hydroxide from Diverse Lithium-Bearing R…. Mineral Processing and Extractive Metallurgy Review 46, 980–989. https://doi.org/10.1080/08827508.2025.2486959

Uddin, M.S., Khand, S., Dong, C., 2024. Effect of Crosslinking Agents on Chitosan Hydrogel Carriers for Drug Loading and Release for Targeted Drug Delivery. Gels 10, 421. https://doi.org/10.3390/GELS10070421/S1

Upadhyay, A., Alimohammadi, F., Tehrani, R., 2024. Engineering Porosity-Tuned Chitosan Beads: Balancing Porosity, Kinetics, and Mechanical Integrity. ACS Omega 9, 33857–33867. https://doi.org/10.1021/ACSOMEGA.4C03583

Urias, P.M., Reis Menêzes, L.H. dos, Cardoso, V.L., de Resende, M.M., de Souza Ferreira, J., 2020. Leaching with mixed organic acids and sulfuric acid to recover cobalt and lithium from lithium ion batteries. Environ. Technol. 1–39.

Vakili, M., Deng, S., Cagnetta, G., Wang, W., Meng, P., Liu, D., Yu, G., 2019. Regeneration of chitosan-based adsorbents used in heavy metal adsorption: A review. Sep. Purif. Technol. 224, 373–387. https://doi.org/10.1016/J.SEPPUR.2019.05.040

Vanderbruggen, Anna, Hayagan, N., Bachmann, K., Ferreira, A., Werner, D., Horn, D., Peuker, U., Serna-Guerrero, R., Rudolph, M., 2022. Lithium-Ion Battery Recycling─Influence of Recycling Processes on Component Liberation and Flotation Separation Efficiency. ACS ES and T Engineering 2, 2130–2141. https://doi.org/10.1021/ACSESTENGG.2C00177/ASSET/IMAGES/LARGE/EE2C00177_0012.JPEG

Vanderbruggen, A., Salces, A., Ferreira, A.M.R., Rudolph, M., Serna-Guerrero, R., 2022. Improving Separation Efficiency in End-of-Life Lithium-Ion Batteries Flotation Using Attrition Pre-Treatment.

Vanitha, M., Balasubramanian, N., 2013. Waste minimization and recovery of valuable metals from spent lithium-ion batteries–a review. Environmental Technology Reviews 2, 101–115.

Vaughan, J., Dieters, C., Fu, W., Byrne, K., 2016. Properties of Lewatit® TP272, a commercial solvent impregnated cation exchange resin for cobalt recovery. Miner. Eng. 88, 2–8. https://doi.org/10.1016/J.MINENG.2015.07.005

Velázquez-Martínez, O., Valio, J., Santasalo-Aarnio, A., Reuter, M., Serna-Guerrero, R., 2019. A Critical Review of Lithium-Ion Battery Recycling Processes from a Circular Economy Perspective. Batteries 2019, Vol. 5, Page 68 5, 68. https://doi.org/10.3390/BATTERIES5040068

Verma, A., Kore, R., Corbin, D.R., Shiflett, M.B., 2019. Metal recovery using oxalate chemistry: a technical review. Ind. Eng. Chem. Res. 58, 15381–15393.

Verma, R., Asthana, A., Singh, A.K., Prasad, S., 2017. An arginine functionalized magnetic nano-sorbent for simultaneous removal of three metal ions from water samples. RSC Adv. 7, 51079–51089. https://doi.org/10.1039/c7ra09705k

Vijayaraghavan, K., Jegan, J., Palanivelu, K., Velan, M., 2005. Biosorption of cobalt(II) and nickel(II) by seaweeds: batch and column studies. Sep. Purif. Technol. 44, 53–59. https://doi.org/10.1016/J.SEPPUR.2004.12.003

Wang, B., Lan, J., Bo, C., Gong, B., Ou, J., 2023. Adsorption of heavy metal onto biomass-derived activated carbon: review. RSC Adv. https://doi.org/10.1039/d2ra07911a

Wang, Chongzhi, Ai, T., Gao, X., Lu, J., Liu, J., Zhu, W., Luo, Y., 2024. Effective recycling of critical metals from LiCoO2 batteries by hydrated deep eutectic solvents: Performance, kinetic and mechanism. Journal of Water Process Engineering 59, 105088. https://doi.org/10.1016/J.JWPE.2024.105088

Wang, C., Zhu, J.J., Qiu, Y., Wang, H., Xu, Y., Haghani, H., Er, H., 2025. Protic Ionic Liquids with Chelating Amine. J. Solution Chem. 54, 55–72. https://doi.org/10.1007/S10953-024-01408-1

Wang, Chi, Zhu, J.J., Qiu, Y., Wang, H., Xu, Y., Haghani, H., Er, H., 2024. Protic Ionic Liquids with Chelating Amine. J. Solution Chem. https://doi.org/10.1007/S10953-024-01408-1

Wang, H., Li, F., Zhu, C., Chen, C., Ding, Z., Chen, X., 2025. Chromatographic separation of Li, Ni, Co and Mn by functionalized fiber towards spent lithium-ion battery recycling. Chemical Engineering Journal 505, 159417. https://doi.org/10.1016/J.CEJ.2025.159417

Wang, H., Liu, J., Bai, X., Wang, S., Yang, D., Fu, Y., He, Y., 2019. Separation of the cathode materials from the Al foil in spent lithium-ion batteries by cryogenic grinding. Waste Management 91, 89–98. https://doi.org/10.1016/J.WASMAN.2019.04.058

Wang, K., Zhang, G., Luo, M., Zeng, M., 2022. Separation of Co and Mn from acetic acid leaching solution of spent lithium-ion battery by Cyanex272. J. Environ. Chem. Eng. 10, 108250.

Wang, T., An, Y., Sun, J., Yang, H., Huang, Y., Zheng, H., 2023. Hollow self-floating microspheres capture cobalt (Co2+)/nickel (Ni2+) ions from the acidic leachate of spent

lithium-ion battery cathodes. Chemical Engineering Journal 465, 142950. https://doi.org/10.1016/J.CEJ.2023.142950

Wang, Y., Gan, H., Wei, Q., Wang, S., Ren, X., 2025. Extraction of Chitin from Food Waste Using Recyclable Deep Eutectic Solvents. ACS Food Science and Technology 5, 780–787. https://doi.org/10.1021/ACSFOODSCITECH.4C00981/ASSET/IMAGES/LARGE/FS4C00981_0006.JPEG

Wang, Y., Tu, Y., Xu, Z.Q., Zhang, X., Chen, Y., Yang, E.Z., 2022. A promising method for recovery of graphite and cathode materials from spent lithium-ion batteries. Ionics (Kiel). 28, 2603–2611. https://doi.org/10.1007/S11581-022-04542-2/FIGURES/8

Wang, Z., Liu, W., Sun, X., Zhang, Q., Ji, J., Yan, Y., Sun, J., 2025. Remediation of Hg-Contaminated Groundwater via Adsorption on Supramolecular Polymers in Batch Process and Column Test. Molecules 30, 1406. https://doi.org/10.3390/MOLECULES30071406/S1

Watwe, V., Kulkarni, P., 2021. Evaluation of Cr(VI) adsorption on glutaraldehyde crosslinked chitosan beads using cyclic voltammetry employing gold electrode. J. Anal. Sci. Technol. 12, 1–10. https://doi.org/10.1186/S40543-021-00291-5/FIGURES/7

Wesselborg, T., Asumalahti, S., Virolainen, S., Sainio, T., 2025. Continuous multicolumn ion exchange process for spent lithium-ion battery leachate: Recovery and purification of a Li+Ni+Co mixture. Sep. Purif. Technol. 353, 128351. https://doi.org/10.1016/J.SEPPUR.2024.128351

Windisch-Kern, S., Gerold, E., Nigl, T., Jandric, A., Altendorfer, M., Rutrecht, B., Scherhaufer, S., Raupenstrauch, H., Pomberger, R., Antrekowitsch, H., 2022. Recycling chains for lithium-ion batteries: A critical examination of current challenges, opportunities and process dependencies. Waste Management 138, 125–139.

Wu, Z., Soh, T., Chan, J.J., Meng, S., Meyer, D., Srinivasan, M., Tay, C.Y., 2020. Repurposing of Fruit Peel Waste as a Green Reductant for Recycling of Spent Lithium-Ion Batteries. Environ. Sci. Technol. 54, 9681–9692. https://doi.org/10.1021/ACS.EST.0C02873

Xiao, C., Yan, L., Chen, Y., 2025. Cyanex 272 blended PVDF adsorption beads for cobalt and nickel separation in lithium-ion battery recycling. J. Environ. Chem. Eng. 13, 118135. https://doi.org/10.1016/J.JECE.2025.118135

Xu, L., Chen, C., Fu, M.-L., 2020. Separation of cobalt and lithium from spent lithium-ion battery leach liquors by ionic liquid extraction using Cyphos IL-101. Hydrometallurgy 197, 105439.

Xu, M., Kang, S., Jiang, F., Yan, X., Zhu, Z., Zhao, Q., Teng, Y., Wang, Y., 2021. A process of leaching recovery for cobalt and lithium from spent lithium-ion batteries by citric acid and salicylic acid. RSC Adv. 11, 27689–27700. https://doi.org/10.1039/D1RA04979H

Yamada, S., Tsuchiya, M., Hotta, M., Koga, N., 2025. Kinetic insight into the solid-state thermal degradation of chitin: Multistep kinetics and the effect of particle size. Polym. Degrad. Stab. 239, 111391. https://doi.org/10.1016/J.POLYMDEGRADSTAB.2025.111391

Yang, C., Wang, J., Yang, P., He, Y., Wang, S., Zhao, P., Wang, H., 2022. Recovery of Valuable Metals from Spent LiNi0.8Co0.1Mn0.1O2 Cathode Materials Using Compound Leaching Agents of Sulfuric Acid and Oxalic Acid. Sustainability 2022, Vol. 14, Page 14169 14, 14169. https://doi.org/10.3390/SU142114169

Yang, H., Hu, X., Zhang, G., Dou, B., Cui, G., Yang, Q., Yan, X., 2024. Life cycle assessment of secondary use and physical recycling of lithium-ion batteries retired from electric vehicles in China. Waste Management 178, 168–175. https://doi.org/10.1016/J.WASMAN.2024.02.034

Yang, H., Yuan, L., Yuan, M., Ning, P., 2023. Insight into the Mechanism of Cobalt-Nickel Separation Using DFT Calculations on Ethylenediamine-Modified Silica Gel. Materials 2023, Vol. 16, Page 3445 16, 3445. https://doi.org/10.3390/MA16093445

Yang, L., Feng, Y., Wang, C., Fang, D., Yi, G., Gao, Z., Shao, P., Liu, C., Luo, X., Luo, S., 2022. Closed-loop regeneration of battery-grade FePO4 from lithium extraction slag of spent Li-ion batteries via phosphoric acid mixture selective leaching. Chemical Engineering Journal 431, 133232.

Yang, X., Pan, Q., Ao, Y., Du, J., Dong, Z., Zhai, M., Zhao, L., 2020. Facile preparation of L-cysteine–modified cellulose microspheres as a low-cost adsorbent for selective and efficient adsorption of Au(III) from the aqueous solution. Environmental Science and Pollution Research 27, 38334–38343. https://doi.org/10.1007/s11356-020-09789-8

Yang, X., Wan, Y., Zheng, Y., He, F., Yu, Z., Huang, J., Wang, H., Ok, Y.S., Jiang, Y., Gao, B., 2019. Surface functional groups of carbon-based adsorbents and their roles in the removal of heavy metals from aqueous solutions: A critical review. Chemical Engineering Journal 366, 608–621. https://doi.org/10.1016/J.CEJ.2019.02.119

Yang, X., Zhou, T., Ren, B., Hursthouse, A., Zhang, Y., 2018. Removal of Mn (II) by Sodium Alginate/Graphene Oxide Composite Double-Network Hydrogel Beads from Aqueous Solutions. Scientific Reports 2018 8:1 8, 1–16. https://doi.org/10.1038/s41598-018-29133-y

Yazidi, A., Sellaoui, L., Badawi, M., Dotto, G.L., Bonilla-Petriciolet, A., Lamine, A. Ben, Erto, A., 2020. Ternary adsorption of cobalt, nickel and methylene blue on a modified chitin: Phenomenological modeling and physical interpretation of the adsorption mechanism. Int. J. Biol. Macromol. 158, 595–604. https://doi.org/10.1016/J.IJBIOMAC.2020.05.022

Yu, D., Huang, Z., Makuza, B., Guo, X., Tian, Q., 2021. Pretreatment options for the recycling of spent lithium-ion batteries: A comprehensive review. Miner. Eng. 173, 107218. https://doi.org/10.1016/J.MINENG.2021.107218

Yu, L., Liu, X., Feng, S., Jia, S., Zhang, Y., Zhu, J., Tang, W., Wang, jingkang, Gong, J., 2023. Recent progress on sustainable recycling of spent lithium-ion battery: Efficient and closed-loop regeneration strategies for high-capacity layered NCM cathode materials. Chemical Engineering Journal 476, 146733. https://doi.org/10.1016/J.CEJ.2023.146733

Yu, Y., Liu, W., Zhang, Y., Zhang, B., Jin, Y., Chen, S., Tang, S., Su, Y., Yu, X., Chen, G., 2024. Chitosan/magnetic biochar composite with enhanced reusability: Synergistic effect of functional groups and multilayer structure. Arabian Journal of Chemistry 17, 105746. https://doi.org/10.1016/J.ARABJC.2024.105746

Yuan, Q., Zeng, J., Sui, Q., Wang, Z., Xu, S., … S.M.-J. of, 2023, undefined, n.d. Thermodynamic and experimental analysis of lithium selectively recovery from spent lithium-ion batteries by in-situ carbothermal reduction. Elsevier.

Yücel, A., Yörükoğlu, A., 2024. Use of Lithium Manganese Oxide Ion Sieves in Fixed Bed Columns for Lithium Recovery: A Mini-Review. Mineral Processing and Extractive Metallurgy Review 45, 847–857. https://doi.org/10.1080/08827508.2023.2295849

Zabiszak, M., Nowak, M., Taras-Goslinska, K., Kaczmarek, M.T., Hnatejko, Z., Jastrzab, R., 2018. Carboxyl groups of citric acid in the process of complex formation with bivalent and trivalent metal ions in biological systems. J. Inorg. Biochem. 182, 37–47. https://doi.org/10.1016/J.JINORGBIO.2018.01.017

Zanoletti, A., Carena, E., Ferrara, C., Bontempi, E., 2024. A Review of Lithium-Ion Battery Recycling: Technologies, Sustainability, and Open Issues. Batteries 10, 38. https://doi.org/10.3390/BATTERIES10010038/S1

Zeng, A., Chen, W., Rasmussen, K.D., Zhu, X., Lundhaug, M., Müller, D.B., Tan, J., Keiding, J.K., Liu, L., Dai, T., Wang, A., Liu, G., 2022. Battery technology and recycling alone will not save the electric mobility transition from future cobalt shortages. Nature Communications 2022 13:1 13, 1–11. https://doi.org/10.1038/s41467-022-29022-z

Zeng, G., Yao, J., Liu, C., Luo, X., Ji, H., Mi, X., Deng, C., 2021. Simultaneous Recycling of Critical Metals and Aluminum Foil from Waste LiNi1/3Co1/3Mn1/3O2Cathode via Ethylene Glycol-Citric Acid System. ACS Sustain. Chem. Eng. 9, 16133–16142. https://doi.org/10.1021/ACSSUSCHEMENG.1C04806/ASSET/IMAGES/LARGE/SC1C04806_0008.JPEG

Zhang, G., Ding, L., Yuan, X., He, Y., … H.W.-J. of E., 2021, undefined, n.d. Recycling of electrode materials from spent lithium-ion battery by pyrolysis-assisted flotation. Elsevier.

Zhang, G., Liu, Z., Yuan, X., He, Y., Wei, N., Wang, H., Zhang, B., 2022. Recycling of valuable metals from spent cathode material by organic pyrolysis combined with in-situ thermal reduction. J. Hazard. Mater. 430, 128374. https://doi.org/10.1016/J.JHAZMAT.2022.128374

Zhang, G., Yuan, X., He, Y., Wang, H., Xie, W., Management, T.Z.-W., 2020, undefined, n.d. Organics removal combined with in situ thermal-reduction for enhancing the liberation and metallurgy efficiency of LiCoO2 derived from spent lithium-ion. Elsevier.

Zhang, G., Yuan, X., He, Y., Wang, H., Zhang, T., Xie, W., 2021. Recent advances in pretreating technology for recycling valuable metals from spent lithium-ion batteries. J. Hazard. Mater. 406, 124332.

Zhang, J., Ding, Y., Shi, H., Shao, P., Yuan, X., Hu, X., Zhang, Q., Zhang, H., Luo, D., Wang, C., Yang, L., Luo, X., 2024. Selective recycling of lithium from spent LiNixCoyMn1-x-yO2 cathode via constructing a synergistic leaching environment. J. Environ. Manage. 352, 120021. https://doi.org/10.1016/J.JENVMAN.2024.120021

Zhang, S., Du, Q., Sun, Y., Song, J., Yang, F., Tsang, D.C.W., 2020. Fabrication of L-cysteine stabilized α-FeOOH nanocomposite on porous hydrophilic biochar as an effective adsorbent

for Pb2+ removal. Science of the Total Environment 720. https://doi.org/10.1016/j.scitotenv.2020.137415

Zhang, T., He, Y., Ge, L., Fu, R., Zhang, X., Huang, Y., 2013. Characteristics of wet and dry crushing methods in the recycling process of spent lithium-ion batteries. J. Power Sources 240, 766–771. https://doi.org/10.1016/J.JPOWSOUR.2013.05.009

Zhang, Y., Zhang, Y., Liu, Y., Wu, H., Fullerenes, M.Z.-, Nanotubes, undefined, 2023, undefined, 2023. Chitosan grafted with crown ether with high selectivity and adsorption on lithium-ion. Taylor & Francis 1–11. https://doi.org/10.1080/1536383X.2023.2188201

Zhong, X., Liu, W., Han, J., Jiao, F., Qin, W., Liu, T., 2020a. Pretreatment for the recovery of spent lithium ion batteries: theoretical and practical aspects. J. Clean. Prod. 263, 121439. https://doi.org/10.1016/J.JCLEPRO.2020.121439

Zhong, X., Liu, W., Han, J., Jiao, F., Zhu, H., Qin, W., 2020b. Pneumatic separation for crushed spent lithium-ion batteries. Waste Management 118, 331–340. https://doi.org/10.1016/J.WASMAN.2020.08.053

Zhuang, L., Sun, C., Zhou, T., Li, H., Dai, A., 2019. Recovery of valuable metals from LiNi0. 5Co0. 2Mn0. 3O2 cathode materials of spent Li-ion batteries using mild mixed acid as leachant. Waste management 85, 175–185.

Chapter 12 APPENDICES

12.1. Weights and Mass Balance

After dismantling the collected spent LIBs, the components were weighed to determine the weight percentages of the cathode, anode, and other materials for each type. As shown in Table 12.1, Li-polymer batteries, cellphone batteries, and laptop batteries contained 42.53%, 35.75%, and 29.38% of cathode materials, respectively. Regarding other materials, including casings, plastic covers, and separators, Li-polymer batteries have lower amounts than those in cell phone and laptop batteries. This may be due to the lighter casings of lithium-polymer batteries compared with those of other batteries.

Table 12.1. The weights of different parts of the LIBs

	Li-Polymer		**Cellphone**		**Laptop**			
	g	**%**	**g**	**%**	**g**	**%**	**without plastic case (g)**	**without plastic case (%)**
Other	1033.24	22.86	5577.94	39.20	5433.63	56.36	3165.67	42.94
Cathode	1922.2	42.53	5086.45	35.75	2831.95	29.38	2831.95	38.41
Anode	1564.65	34.62	3564.49	25.05	1374.63	14.26	1374.63	18.65
Total	4520.09		14228.88		9640.21		7372.25	

12.2. TGA Results

To improve the recovery process's efficiency, binder materials must be decomposed. Thermal treatment, or pyrolysis, is an efficient method for this purpose. Different furnace atmospheres, times, and temperatures were studied in this stage. To optimize the temperature, TGA was conducted in simulated air and inert, argon atmospheres in a range of room temperature to 800 °C. In the simulated air environment (20% oxygen + 80% argon), 49.30 mg of cathode material was placed in the furnace, and the temperature was raised from 25 °C to 800 °C. Mass changes were

measured using a computer-controlled balance. Figure 12.1 (a and b) shows the results of TG, DTG, and dTA for mixed battery black mass in the 20% oxygen and 80% argon atmosphere. As shown in the TG figure, there are three stages in the mass changes. Stage 1, from 42 °C to 220 °C, is referred to as the volatilization stage, in which the volatilization of adsorbed water and the electrolyte residue occurs. The mass reduction is 1.74 mg (3.53%). Mass reduction in stage 2, 220 °C to 544 °C, was 2.33 mg (4.73%). In this stage, the binder is decomposed by heating, a process called decomposition. According to the literature, in the temperature range of 260-500 °C, the binder materials (PVDF bonds, or -(CH2CF2)-n) are decomposed to vinylidene fluoride (CH_2-CF_2) (Zhang et al., 2020). Stage 3, during which reactions such as alloying or melting Al might occur, spans 544 °C to 818 °C. The mass reduction was 1.80 mg (3.65%). The DTG results illustrate that in stage 2, there are two peaks that can refer to the combustion PDVF, and in stage 3, there is one peak (about 650 °C), which may refer to Al melting.

Figure 12.2 (a and b) shows the TG, DTG, and dTA results of the mixed battery black powder in an argon atmosphere from 25-800 °C. 49.49 mg of the sample was placed in the furnace. The TG results show the three-stage mass reduction trend. The same results have been shown in three stages: 31 to 177 °C, 177 to 571 °C, and 571 to 821 °C. Mass reductions in stages 1, 2, and 3 were 3.35% (1.66 mg), 3.02% (1.49 mg), and 4.78% (2.33 mg), respectively. The second stage shows the binder decomposition. In this regard, 570 °C has been selected as the optimal temperature for binder removal in an argon atmosphere. Since there was no oxygen in the environment, no combustion peaks were detected in the DTG results. The peaks only show the decomposition of binder materials. In an inert environment, the emitted gas can be captured and recycled. Based on the TGA results in both atmospheres, 570°C is the optimum temperature at which PDVF bonds should decompose.

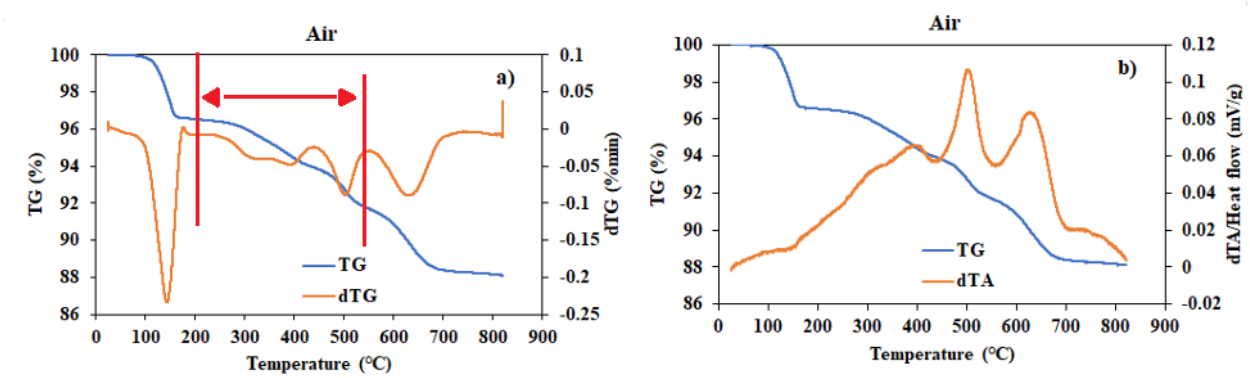

Figure 12.1. a) TG and DTG and b) TG and dTA results of mixed battery black powder in 20% oxygen and 80% argon in a range of 25-800°C.

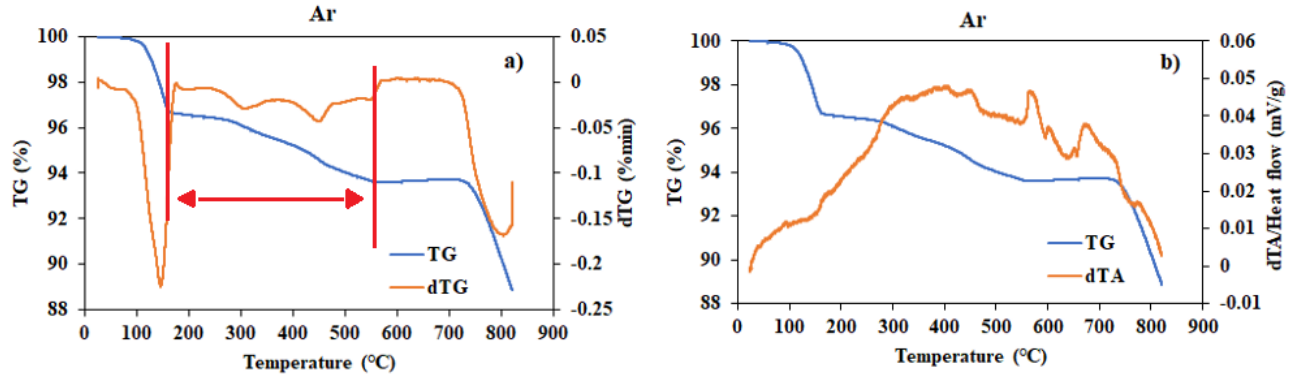

Figure 12.2. a) TG and DTG b) TG and dTA result of mixed battery black powder in argon in a range of 25-800°C.

To confirm the TGA results and further investigate the processing time (30 min, 4 h, and 6 h), different experiments were conducted at 570 °C, 600 °C, and 650 °C in air and argon atmospheres. The results show that higher temperatures, 600 °C and 650 °C, are not suitable to decompose binders and separate Al from the black powder, especially at 650 °C, since the Al foil was brittle, and separation was not efficient. Also, the results show that a process time of 6 h, i.e., beyond 4 h, did not enhance separation, as almost complete separation was achieved in lower times (30 min and 4 h). Therefore, based on TGA and separation results, processing times of 30 min and 4 h at 570 °C were selected for further investigation and application in pyrolysis. Table 12.2 shows the mass balance of the cathode materials at different times and furnace atmospheres at 570 °C. The results show that the black powder content, or lithium metal oxide material, is about 77-82%,

which is in agreement with the literature. Also, the Al contents and binder materials are around 10-14% and 7-10%, respectively. It was found that these processes (air, 570°C for 30 min; air, 570°C for 4 h; and Ar, 570°C for 30 min) were capable of separating Al from black powder and could be further examined to determine whether the binder materials were completely decomposed. In other words, further investigation (XRD and SEM-EDS) is required to determine in which furnace atmosphere binder materials completely decompose, while the compositions of cathode materials remain unchanged. The process time will also be optimized based on the results of XRD and SEM-EDS.

Figure 12.3 (a, b, and c) shows the heat-treated cathode materials (separated Al and black mass) at 600℃ in the air atmosphere for 6h, 650℃ in the air atmosphere for 6h, and 600 ℃ in the air atmosphere for 4h, respectively. Figure 12.4 (a-f) shows heat-treated cathode materials (separated black mass and Al) of different batteries at 570 ℃ in air and argon atmosphere for 30 min.

Table 12.2. Weights of the cathode's parts after heat treatments at different conditions

	570°C-Air- 4h	570°C -Air-30 min	570°C -Ar-30 min
Cellphone			
	%	%	%
Binder	10.00	7.66	8.60
Al	9.57	10.21	13.96
Black Powder	80.43	82.13	77.44
Laptop			
Binder	8.70	7.34	8.03
Al	14.19	12.36	11.47
Black Powder	80.32	80.31	80.50
Li-Polymer			
Binder	7.42	7.47	7.54
Al	12.88	9.54	12.38
Black Powder	79.60	82.99	80.08

Figure 12.3. Heat-treated cathode materials (separated black mass and Al) a) 600℃ in the air atmosphere in 6h b) 650℃ in the air atmosphere in 6h, and c) 600 ℃ in the air atmosphere in 4h.

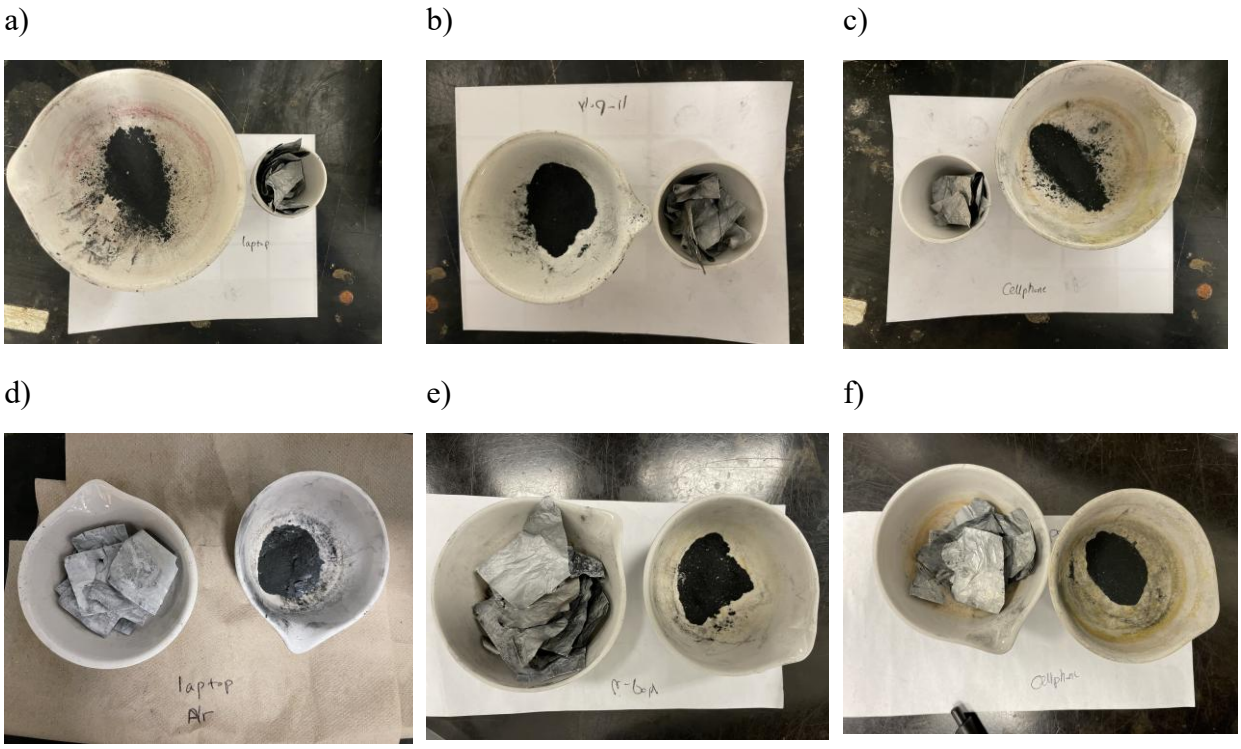

Figure 12.4. Heat-treated cathode materials a) laptop, b) Li-polymer, and c) cellphone batteries at 570℃ in air atmosphere in 30 min, and heat-treated cathode materials d) laptop, e)Li-polymer, and f) cellphone batteries at 570℃ in Ar atmosphere in 30 min.

12.3. XRD Results

An XRD analysis was conducted on raw and heat-treated LIB cathode materials to determine the phase composition of the metals present in the cathode materials, as well as the thermal process conditions that are most efficient. The conditions that cathode materials were analyzed were as follows: raw materials; heating the samples in Argon atmosphere for 30 min and cooling them down in the same environment; heating the samples in the air atmosphere for 30 min and cooling them down in the same environment; heating the samples in the air atmosphere for 4 h and cooling them down in the same environment. XRD results show that all battery types contain lithium cobalt oxide (LCO) as their primary component. Figure 12.5 shows the XRD results of the cellphone batteries. The main peaks of the untreated sample are LCO, Al, and graphite (which can be referred to as carbon in PVDF). Also, some peaks of lithium nickel cobalt manganese oxide (NMC) can be observed. However, the NMC's intensity is low. Therefore, it can be assumed that the quantity is not high. The results show that the treated sample under argon still shows the graphite peak, but the amount of graphite is reduced. Since the graphite peaks are insignificant, the process appears to have successfully decomposed the binder materials. Also, some peaks of cobalt(II,III) oxide (Co3O4) are observed. It means that some LCOs convert to cobalt oxide, which is not a desirable result but is inevitable, and Co (III) is generally not desirable due to its difficulty in leaching. Air samples taken after 30 min and four hours showed the same results as the sample in the argon atmosphere. However, graphite peaks have not been observed. Again, the binder materials were decomposed by the process.

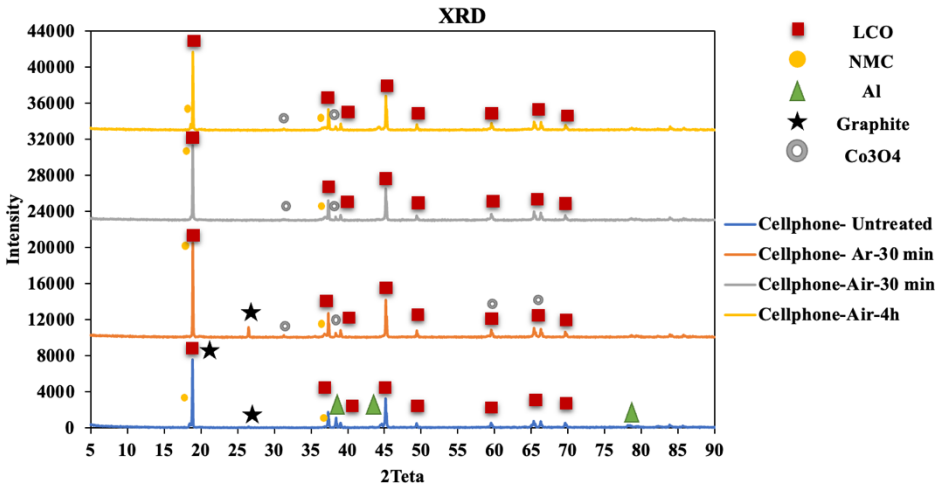

Figure 12.5. XRD results of untreated and treated cellphone batteries.

Figure 12.6 illustrates the XRD results for untreated and treated laptop batteries. The untreated sample's main peak is LCO. Other peaks are the same as the cellphone batteries (Al, graphite, NMC). After the heat treatments, some LCOs convert to Co_3O_4, and the peak intensities are nearly identical across all treatments. As a result of treating the sample in both Ar and air atmospheres for 30 minutes, the binder's carbon can be observed. However, there were no obvious peaks of graphite in 4 h of treatment in the air. Therefore, considering that graphite peaks were not detected, the process was able to decompose the binder materials.

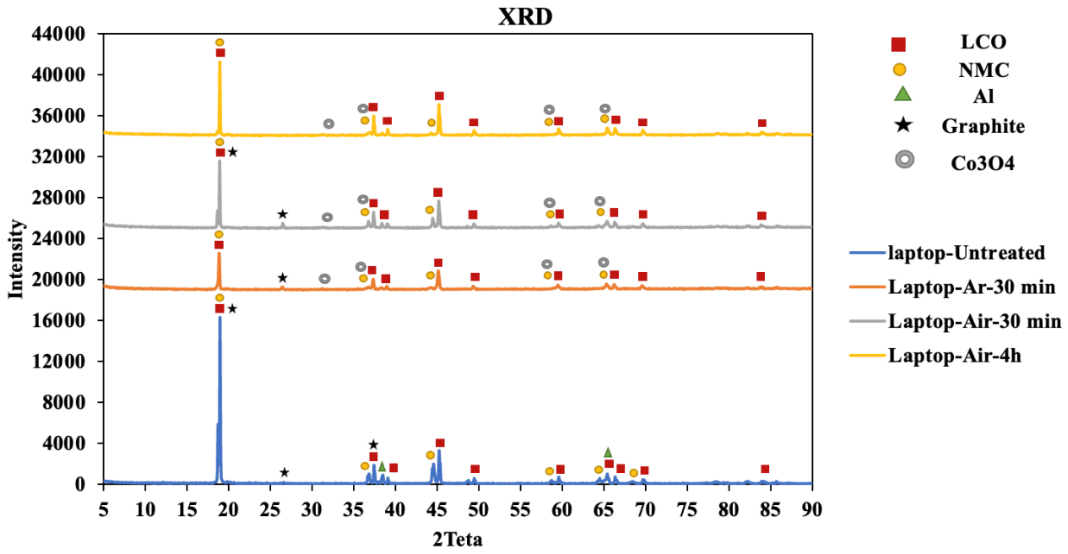

Figure 12.6. XRD results of untreated and treated laptop batteries.

Figure 12.7 shows the XRD results of untreated and treated Li-polymer batteries at different conditions. As can be seen in the untreated sample result, the main components are LCO, lithium manganese oxide (LMO), Al, and graphite. According to the results, Li-polymer batteries contain cathode materials made from LCO and LMO types. All treatments show the conversion of cobalt oxide to $Co3O_4$. Interestingly, none of the treatments shows graphite peaks. It can be a result of the fact that the samples may be heterogeneous.

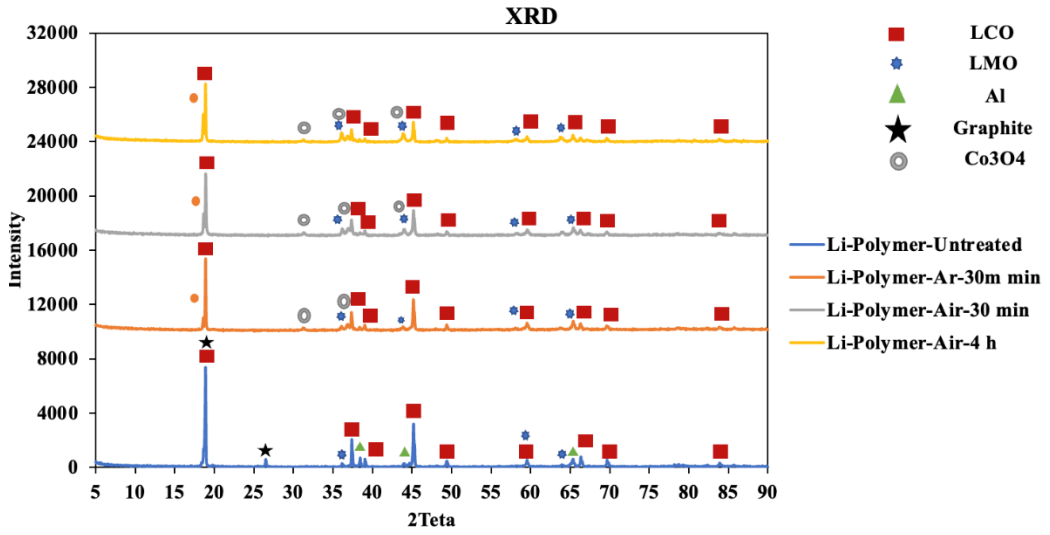

Figure 12.7. XRD results of untreated and treated Li-polymer batteries.

As discussed above, Co and Li are expected to be the principal elements of cathode materials. Ni and Mn are also present in the raw materials but at lower concentrations. The results of the mass balance and XRD analysis indicated that the heat treatment, i.e., pyrolysis, in an air atmosphere and an argon atmosphere, had the same outcome. Considering the cost of argon, the air atmosphere was selected. However, 30 min of the treatment is insufficient to decompose all the binder materials. Therefore, further experiments should be conducted to optimize the time. Table 12.3 shows the results of mass balance for 1 and 2 h of heat treatment at 570°C. Based on the results, 8.5% of the carbon materials decomposed in 1 hour, and 9% in 2 hours. In terms of weight loss, 2 hours of treatment appears to be sufficient, and the majority of carbon materials are removed from the cathode materials as compared to the 4 h treatment. Therefore, 2 h treatment in an air atmosphere in 570°C was selected as the optimum condition.

Table 12.3. Heat treatment at 570°C in 1 and 2 h

	1 h	2 h
	%	%
Binder	8.5	9
Black powder	82	79.5
Al	9.5	11.5

12.4. ICP Results

Table 12.4 shows the concentration of metals in the cathode material of different types of batteries (cellphones, laptops, Li-polymers, and a mixture of all of them). Regarding the untreated cellphone batteries, the main metal was Co with 44.49 wt.%. Li concentration was 5.74 wt.%, and the concentration of Ni and Mn were 2.87 wt.% and 3.67 wt.%, respectively, which was in agreement with the XRD results. XRD results for NMC cathodes showed low-intensity peaks due to the low concentration of Ni and Mn. As can be seen, the thermal treatment in the furnace helped remove Al foil efficiently since the concentration decreased from 9.50 wt.% to 0.28 wt.%. Regarding the Li-polymer batteries, the same as cellphone batteries components, the main metals were Co, Mn, and Li. The concentration of Ni was also considerable. After heat treatment and the separation of Al, the concentration of Mn was 19.30 wt.%, which suggested that these types of batteries should contain LMO cathodes. Considering the results of the ICP, the NMC cathode was expected to be present, but the amount was lower than that of LCO and LMO. In terms of the material composition of the heat-treated laptop batteries, Co and Li were the main metals, and Ni and Mn are also present. The result recommends that the LCO cathode should be the primary cathode type, and NMC may be present in the laptop batteries but in a lower amount. The concentrations of Co, Li, Ni, and Mn in the treated mixed batteries were 50.06 wt.%, 6.28 wt.%, 2.82 wt.%, and 7.99 wt.%, respectively. In the next stages, a mixture of all types of batteries (Cellphone: Laptop: Li-Polymer = 1:1:1) will be used. Table 12.5 shows the proportions of other metals to Li mass.

Table 12.4. ICP results for different battery types before and after the furnace

	Al	Co	Cr	Cu	Fe	Li	Mn	Na	Ni	V	Zn
Cellphone - Average (mg/L)	94973	498875	13	5380	422	57971	2920	342	6162	42	49
% RSD	6.3	0.5	8.3	82.6	10.5	0.5	1.2	10.5	1.0	1.7	4.8
Percentage (wt.%)	9.50	49.89	0.00	0.54	0.04	5.80	0.29	0.03	0.62	0.00	0.00
Heat Treated Cellphone	1178	561592	8	535	-15	67031	17285	1117	35079	25	230
Percentage (wt.%)	0.12	56.16	0.00	0.05	0.00	6.70	1.73	0.11	3.51	0.00	0.02
Li-Polymer - Average (mg/L)	101205	408176	29	295	675	48766	78752	680	13847	43	100
% RSD	8.4	0.5	10.1	5.6	10.5	0.7	2.6	6.2	2.7	7.6	2.0
Percentage (wt.%)	10.12	40.82	0.00	0.03	0.07	4.88	7.88	0.07	1.38	0.00	0.01
Heat Treated Li-polymer	2293	373168	40	253	587	52919	193014	2057	34785	34	225
Percentage (wt.%)	0.23	37.32	0.00	0.03	0.06	5.29	19.30	0.21	3.48	0.00	0.02
Laptop - Average (mg/L)	88427	408637	22	408	321	60298	49676	489	46681	37	297
% RSD	5.7	1.3	4.4	0.7	33.3	0.9	2.0	6.4	1.7	5.2	1.8
Percentage (wt.%)	8.84	40.86	0.00	0.04	0.03	6.03	4.97	0.05	4.67	0.00	0.03
Heat Treated Laptop (mg/L)	5080	577806	6	375	-43	68595	9753	1371	19384	32	136
Percentage (wt.%)	0.51	57.78	0.00	0.04	0.00	6.86	0.98	0.14	1.94	0.00	0.01
Mixed batteries - Average (mg/L)	78754	444936	13	1683	625	57423	36743	657	28740	39	190
% RSD	26.0	2.6	10.7	71.7	24.2	2.7	18.5	57.6	25.9	5.0	24.7
Percentage (wt.%)	7.88	44.49	0.00	0.17	0.06	5.74	3.67	0.07	2.87	0.00	0.02

Heat Treated Mixed batteries (mg/L)	2817	500591	23	360	290	62768	79924	1707	28213	30	186
Percentage (wt.%)	0.28	50.06	0.00	0.04	0.03	6.28	7.99	0.17	2.82	0.00	0.02

Table 12.5. Other metals to Li mass ratio for different battery types before and after the furnace

	Al	Co	Cr	Cu	Fe	Li	Mn	Na	Ni	V	Zn
Cellphone- Average (mg/L)	1.64	8.61	0.00	0.09	0.01	1.00	0.05	0.01	0.11	0.00	0.00
% RSD:	6.4	0.3	8.6	82.6	10.2	0.0	1.4	10.9	1.0	2.1	4.8
Heat Treated Cellphone (mg/L)	0.02	8.38	0.00	0.01	-0.00	1.00	0.26	0.02	0.52	0.00	0.00
Li-Polymer - Average (mg/L)	2.08	8.37	0.00	0.01	0.01	1.00	1.61	0.01	0.28	0.00	0.00
% RSD	8.8	0.7	10.8	5.6	10.9	0.0	2.0	5.8	2.2	7.2	2.0
Heat Treated Li-polymer (mg/L)	0.04	7.05	0.00	0.00	0.01	1.00	3.65	0.04	0.66	0.00	0.00
Laptop - Average (mg/L)	1.47	6.78	0.00	0.01	0.01	1.00	0.82	0.01	0.77	0.00	0.00
% RSD	6.5	0.5	3.5	1.2	33.9	0.0	2.4	5.9	2.0	4.7	2.2
Heat Treated Laptop (mg/L)	0.07	8.42	0.00	0.01	-0.00	1.00	0.14	0.02	0.28	0.00	0.00
Mixed - Average (mg/L)	1.38	7.75	0.00	0.03	0.01	1.00	0.64	0.01	0.50	0.00	0.00
% RSD	28.1	3.1	11.7	68.8	22.7	0.0	18.4	57.6	23.3	6.3	22.0
Heat Treated Mixed	0.04	7.98	0.00	0.01	0.00	1.00	1.27	0.03	0.45	0.00	0.00

12.5. SEM Results

Figure 12.8 shows the results of SEM-EDS on untreated cathode materials. The figures show the surface of cathode materials before the heat treatment. The presence of metals (Li, Co, Ni, and Mn) on the surface was confirmed.

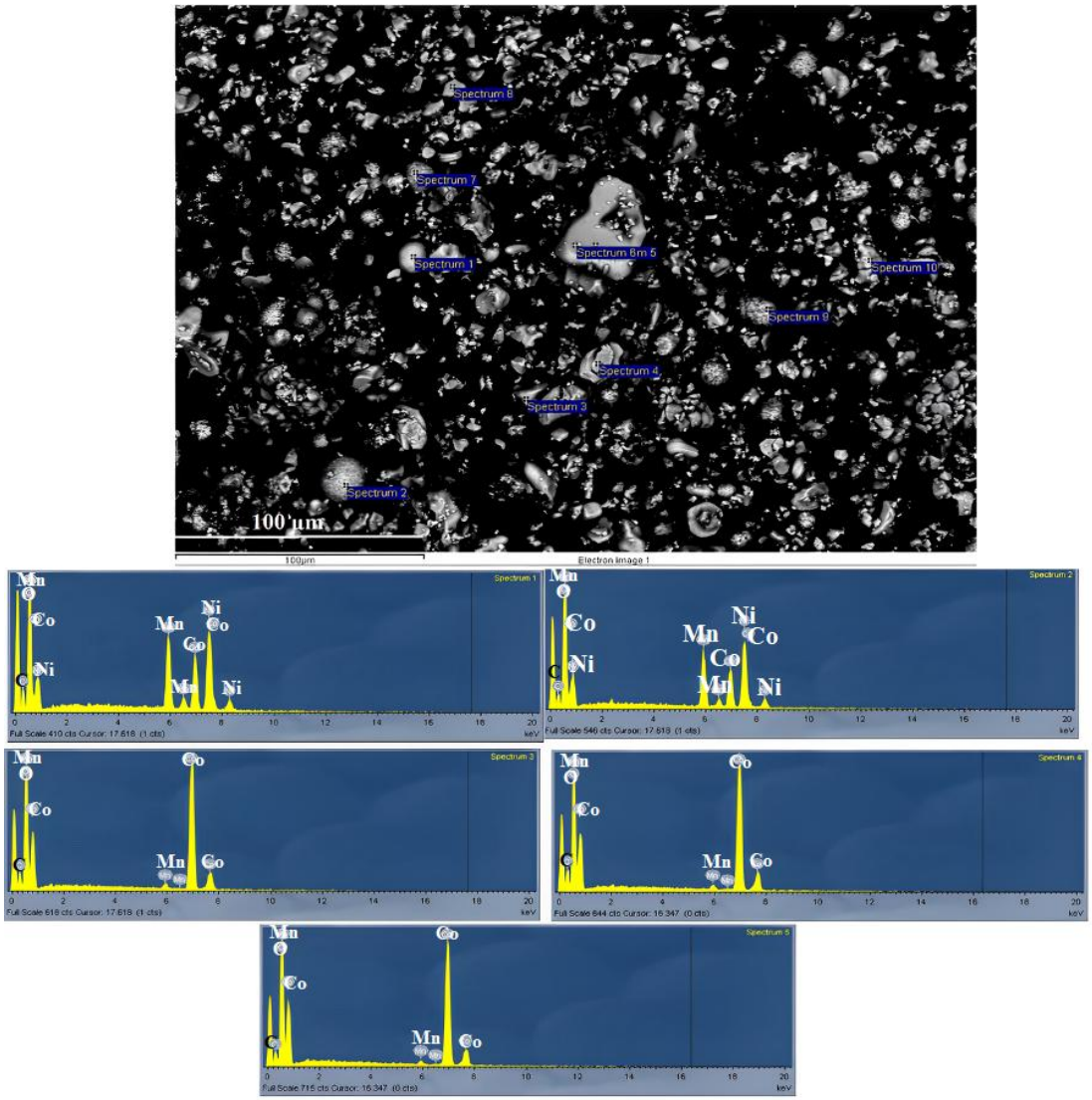

Figure 12.8. SEM-EDS image of cathode materials (a mixture of cellphones, laptops, and Li-polymer).

12.6. Leaching Design of Experiment

The correlation coefficient (R-squared) values are close to 1, indicating that the predicted models can be fitted to the experimental data. Models predicting metal recoveries can be found in the following equations:

$$Li\ recovery = 96.72 + 1.55\ SA + 0.9727\ Org + 0.8835\ AT - 3.44\ SA * Org - 3.98\ SA * AT - 1.28\ Org * AT - 1.41\ SA^2 - 2.69\ Org^2 \quad (12\text{-}1)$$

$$Co\ recovery = 94.14 - 133.51\ SA - 223.17\ Org + 4.92\ AT + 1.75\ SA * Org + 7.81\ SA * AT + 9.9\ Org * AT + 23.83\ SA^2 - 23.36\ Org^2 + 10.8\ SA * Org * AT - 0.3233\ SA^2 * Org + 29.98\ SA^2 * AT - 4.78\ SA * Org^2 - 27.38\ Org^2 * AT + 154.11\ SA^3 + 237.85\ Org^3 \quad (12\text{-}2)$$

$$Ni\ recovery = 99.55 - 40.61\ SA - 33.84\ Org + 0.45\ AT - 1.51\ SA * Org + 0.9278\ SA * AT + 3.14\ Org * AT + 3.17\ SA^2 - 6.46\ Org^2 - 0.8802\ SA * Org * AT + 3.79\ SA^2 * Org + 2.28\ SA^2 * Org + 2.54\ SA * Org^2 - 3.72\ Org^2 * AT + 42.54\ SA^3 + 33.64\ Org^3 \quad (12\text{-}3)$$

$$Mn\ recovery = 99.37 - 36.9\ SA - 36.88\ Org + 0.515\ AT - 1.28\ SA * Org + 0.857\ SA * AT + 3.02\ ORG * AT + 3.19\ SA^2 - 6\ Org^2 - 0.2331\ SA * Org * AT + 4.63\ SA^2 * Org + 235\ SA^2 * AT + 3.05\ SA * Org^2 - 3.17\ Org^2 * AT + 37.45\ SA^3 + 35.91\ Org^3 \quad (12\text{-}4)$$

where SA, Org, and AT represent the coded values of sulfuric acid concentration, organic acid concentration, and acid type (acetic acid and citric acid), respectively.

Table 12.6.R-squared data for metal recoveries

Metal	Li	Co	Ni	Mn
R^2	0.89	0.99	0.95	0.95
P-Value	<0.0001	<0.0001	0.0006	0.0004
F-value	0.0067	120.49	1047	11.32

12.7. Adsorption Selection Results

Adsorption experiments were conducted at room temperature with an initial pH of 7, employing a dilution factor of 100 over 24h. Modified flax, chitosan, and AC were used at a dosage of 10 g/L, and GO at 3.6 g/L. Table 12.7 outlines the adsorption rates of Co(II), Mn(II), Ni(II), and Li onto the modified flax, chitosan, activated carbon, and GO at pH 7 and unadjusted pH (2.5). At pH 7, the recovery rates for Co(II), Mn(II), and Ni(II) were notably low, with Li also being adsorbed (qe = 0.11 mg/g), indicating non-selective adsorption. This behavior could be due to the functional groups of the modified flax (carboxyl (–COOH) and aldehyde (–CHO)) (Fathi et al., 2017). In comparison with chitosan and activated carbon, all divalent metals (Co(II), Mn(II), and Ni(II))

were adsorbed, leaving Li in the solution. Activated carbon exhibited moderate adsorption for Co(II) and Ni(II) and high-capacity adsorption for Mn(II), whereas chitosan showed superior adsorption for Co(II) and Ni(II) and moderate adsorption for Mn(II). The primary functional groups of chitosan are amine and hydroxyl (–OH), while activated carbon's main functional groups are carboxyl and hydroxyl. This could be attributed to the greater tendency of chitosan's amine and hydroxyl groups for Co(II) and Ni(II) adsorption over Mn(II), while activated carbon's carboxyl group favors Mn(II) adsorption (Babakhani and Sartaj, 2023a, 2022a; Bakshi et al., 2020; Mirzaee and Sartaj, 2022). A previous study indicated that AC demonstrates an affinity for Mn removal from both water and wastewater, which aligns with the observed behavior in this study (Tobiason et al., 2016). Concerning GO, the adsorption rates were as follows: Mn(II) exhibited a superior rate (over 65%), Co(II) showed a moderate rate (32%), and Ni(II) had a low rate (7%). Despite this, GO also adsorbed Li (4%), showing a lack of selectivity in the adsorption process. Its strong attraction to Mn(II) could be attributed to its carboxyl and hydroxyl functional groups. Additionally, hydroxyl groups might interact with Co(II), while the carbonyl groups (C=O) could react with Li (Aliyev et al., 2019).

Figure 12.9 (a-c) depicts the equilibrium adsorption capacity of Co(II), Mn(II), and Ni(II) onto modified flax, chitosan, AC, and GO. Notably, chitosan exhibited a substantial equilibrium adsorption capacity of 27.23 mg/g for Co(II) and 1.78 mg/g for Ni(II). Conversely, AC demonstrated an equilibrium adsorption capacity of 1.05 mg/g for Mn(II). Further investigation involved examining the adsorption of metals onto chitosan and AC from the pregnant solution with a dilution factor of 100 and an unadjusted pH (pH=2.5). Table 12.7 and Figure 12.10 illustrate the adsorption rate and equilibrium adsorption capacity for Co(II), Mn(II), and Ni(II) onto chitosan and AC at pH=2.5. The findings indicated that while AC exhibited ineffective metal adsorption, chitosan displayed impressive adsorption rates, adsorbing over 80% of Co(II) and Ni(II) and 15% of Mn(II). This outcome underscores chitosan's suitability as a robust adsorbent for acidic environments, aligning with existing literature (Conte and Gómez, 2024; Das et al., 2022). Consequently, because of higher recovery rates for Co(II) and Ni(II), chitosan was chosen for further investigation.

Table 12.7.Adsorption rate (%±SD) of different adsorbents for Co(II), Mn(II), Ni(II), and Li

Adsorption rate (%±SD)				
pH=7	**Co**	**Mn**	**Ni**	**Li**
Modified Flax	14.57±0.68	15.60±0.58	4.11±1.89	2.93±0.07
Chitosan	86.55±0.00	38.13±0.00	82.56±0.00	-
AC	47.14±3.50	72.10±1,34	55.10±1.01	-
GO	31.83±0.32	65.69±4.98	7.15±1.12	4.01±0.04
pH=2.5	**Co**	**Mn**	**Ni**	**Li**
Chitosan	81.26±0.27	15.18±0.10	81.02±2.60	-
AC	7.49±1.51	0	5.60±2.36	-

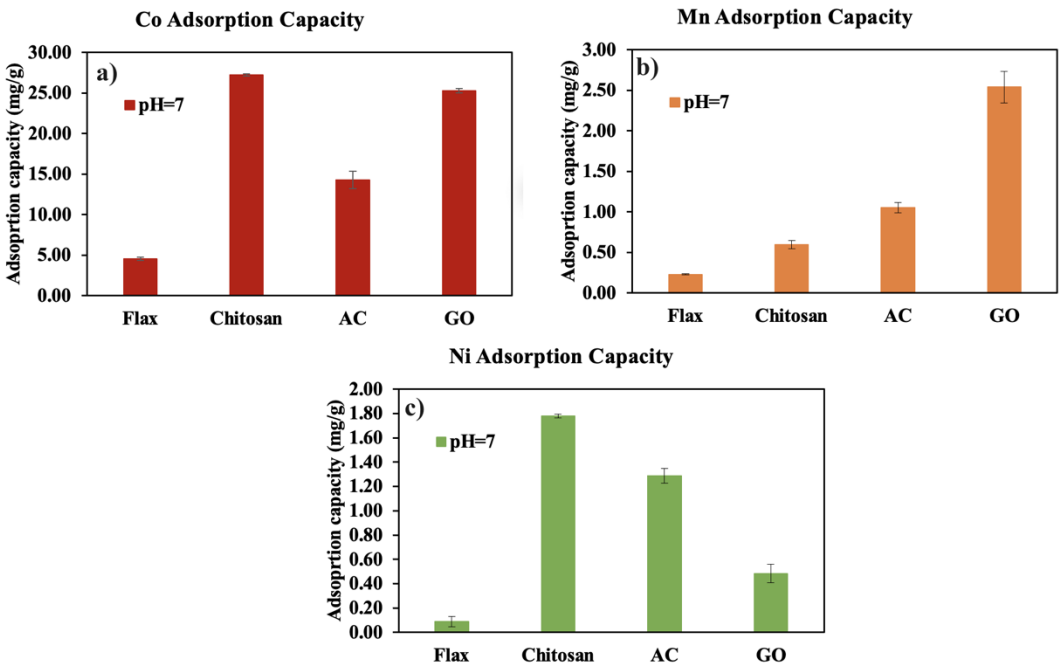

Figure 12.9. The equilibrium adsorption capacity of a) Co(II), b) Mn(II), and c) Ni(II) onto modified flax, chitosan, AC, and GO at a pH of 7, room temperature, adsorbent dosage of 10g/L, and in 24h.

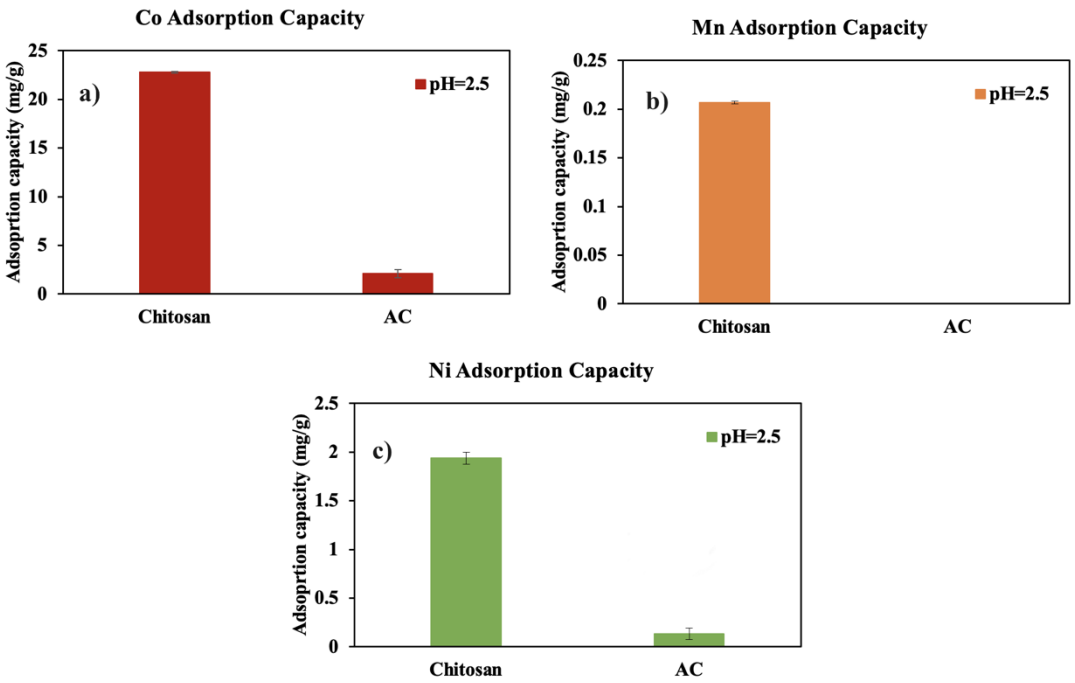

Figure 12.10. The equilibrium adsorption capacity of a) Co(II), b) Mn(II), and c) Ni(II) onto modified flax, chitosan, and AC at a pH of 2.5 (unadjusted pH), room temperature, adsorbent dosage of 10g/L, and in 24h.

12.7.1. Effect of pH

As depicted in Figure 12.11, increasing the pH results in a slight reduction in the adsorption of Co(II) and Ni(II), whereas Mn(II) adsorption increases from 31% to 45%. This indicates that Mn(II) adsorption is more favorable at elevated pH. Since all final pH values are at or below 8, any pH value could be chosen. While elevated pH levels led to increased metal adsorption, it is crucial to admit that higher pH also decreases the solubility of metal ions, leading to their precipitation (Babakhani and Sartaj, 2023a). Therefore, selecting a more acidic environment, such as pH 4 or 5, minimizes Mn(II) adsorption, reduces the need for NaOH to adjust the pH, and prevents metal precipitation.

Table 12.8. The effect of pH on the equilibrium adsorption capacity of metals onto the chitosan

Equilibrium adsorption capacity (qe, mg/g)				
Initial pH	**Final pH**	**Co(II) (mg/g)**	**Mn(II) (mg/g)**	**Ni (II)(mg/g)**
4	7.08	27.52±0.00	0.46±0.00	1.66±0.01
5	7.48	26.21±0.18	0.52±0.05	3.12±0.02
6	7.63	26.72±0.00	0.54±0.03	3.02±0.02
7	7.67	26.64±0.01	0.56±0.04	3.00±0.02
8	8.01	29.02 ±0.19	0.67±0.09	1.97±0.01

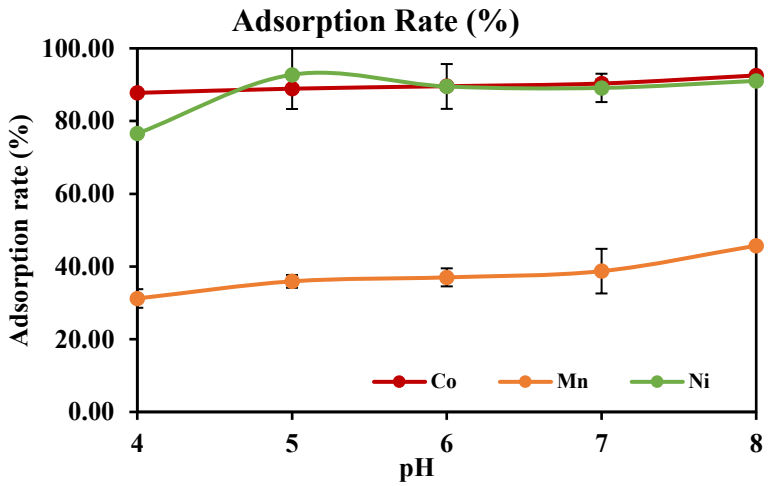

Figure 12.11.The effect of pH on the adsorption rate of Co(II), Mn(II), and Ni(II) at different pH, room temperature, adsorbent dosage of 10g/L, and in 24h.

12.8. Bead Modification

The results in Figures 12.12 and 12.13, as well as in Table 12.9, show that all tested crosslinkers yielded satisfactory adsorption performance for Co(II), Ni(II), and Mn(II), with particularly high uptake values for Co(II) and Ni(II). In contrast, beads prepared with STPP exhibited notably lower adsorption capacity. This reduction can be attributed to STPP's use of the $–NH_2$ groups of chitosan

for ionic crosslinking, thereby reducing the availability of amine functional groups for metal binding. Moreover, STPP-crosslinked beads showed weaker structural stability, as confirmed by the observed mass loss. In comparison, modifiers such as L-cystine preserved chitosan's amine sites by crosslinking through –COOH and –SH groups. This covalent interaction not only maintained active adsorption sites but also enhanced bead stability, as reflected in the minimal mass change after adsorption. Among the different crosslinkers, L-cysteine provided a safe and effective modification, combining strong structural stability with favorable adsorption performance, making it a promising choice for sustainable applications.

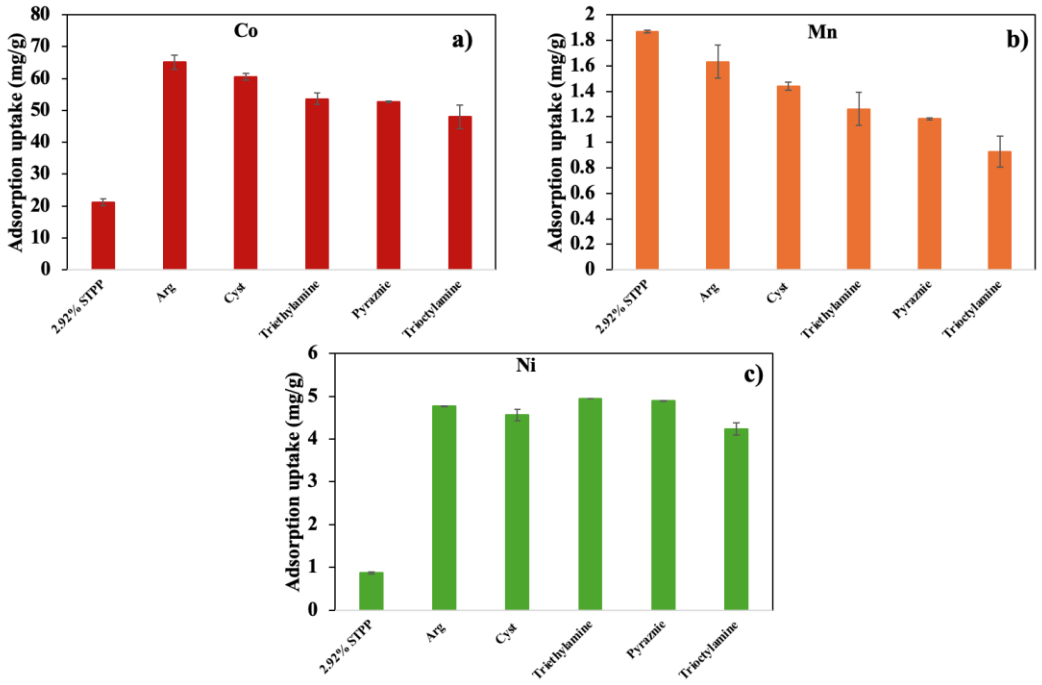

Figure 12.12. Adsorption uptakes using different crosslinkers.

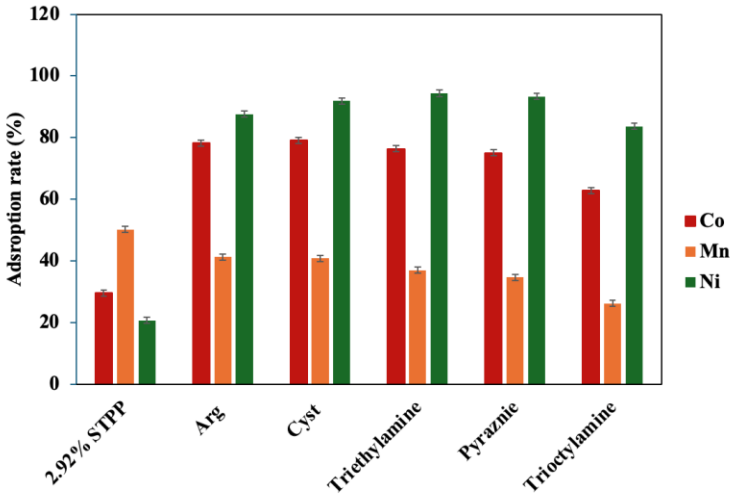

Figure 12.13. Adsorption rates using different crosslinkers.

Table 12.9. Mass balance for the beads using the different crosslinkers

Crosslinker	Initial Mass (g)	Final Mass (g)	Final pH
2.92% STPP	0.5	0.45	4.25
Arg	0.5	0.48	8.13
Cyst	0.5	0.51	7.31
Triethylamine	0.5	0.44	8.24
Pyrazine	0.5	0.47	8.3
Tricotylamine	0.5	0.54	7.77

AC and magnetic iron oxide were added to chitosan to examine possible improvements in metal adsorption. The pH increase was due to basic surface groups on AC (–OH, $–COO^-$, $–O^-$), residual alkaline ash, and deprotonation/restructuring of Fe–OH groups. However, this modification did not enhance the removal of Mn(II) or other metals. The performance of magnetic beads was slightly better than that of AC. While stability was maintained, the higher cost from adding extra components makes the approach less practical, as bead formation alone is sufficient for large-scale separation without requiring magnetic modification.

Table 12.10. Effect of composing CS with AC and magnetic iron oxide

Adsorbent	Co %	Li %	Mn %	Ni %	Mass Loss (%)	pH
CS: AC 1:0.25	70.29	0.92	31.92	81.45	2	8.00
CS: AC 1:0.5	69.62	0.51	41.19	88.51	0	8.18
CS: AC 1:0.75	59.70	0.27	28.02	77.31	0	7.84
CS: Magnet 1:0.25	69.02	0.69	29.53	92.09	0	7.89
CS: Magnet 1:0.5	77.16	0.54	43.01	86.98	0	7.92
CS: Magnet 1:1	59.24	0.38	23.98	85.80	0	8.08

12.9. Comparison CS1%CYS Beads (commercial and [Eth]-extracted)

The adsorption performance of CS1%CYS beads sourced from two different chitosan sources (commercial and [Eth]-extracted) was evaluated for Co(II), Mn(II), and Ni(II) ions. The adsorption rate (%) and uptake (Q, mg/g) were measured at various dilution factors (×10–×40), and the equilibrium data were analyzed using Langmuir and Freundlich isotherm models.

12.9.1. Adsorption Efficiency and Capacity

As shown in Figure 12.14, both adsorbents displayed a high affinity toward Co(II), followed by Ni(II) and Mn(II). For the [Eth]-extracted chitosan beads, the removal efficiency of Co(II) increased from 41.9% at X10 to 77.4% at ×40, with a uptake rise from 56.11 to 121.33 mg/g. A similar upward trend was seen for Ni(II) (from 68.9% to 92.5%) and Mn(II) (from 23.6% to 41.4%). [Eth]-extracted chitosan beads showed a similar trend but with slightly higher percentage removals at higher concentrations. The adsorption uptakes at ×10 were 127.86 mg/g for Co(II), 3.58 mg/g for Mn(II), and 13.84 mg/g for Ni(II). Overall, Co(II) consistently exhibited the highest uptake for both bio-adsorbents, confirming its preferential binding to amino and hydroxyl sites. The [Eth]-extracted chitosan showed marginally better Co(II) removal at lower dilution factors (higher concentrations), suggesting enhanced surface reactivity and easier access to binding sites due to the ionic-liquid-assisted extraction.

12.9.2. Isotherm Modeling

Both data fit the Langmuir and Freundlich models well, with correlation coefficients (R^2) exceeding 0.95. For the commercial chitosan, the Langmuir model showed a good fit with R^2 (0.99), providing maximum monolayer adsorption capacities, q_m for Co(II) (136.14 mg/g) and Mn(II) (3.86 mg/g), while showing a comparable capacity for Ni(II) (15.53 mg/g). However, the Langmuir constant (K_L) and the Freundlich parameters (K_n and n_F) indicate a stronger binding affinity and a more favorable adsorption process, with $K_L = 3.29\times10^{-2}$–1.05×10^{-1} L/mg; n_F 3.45 for Co(II). The lower MSE values also confirm a better model fit for the [Eth]-extracted chitosan, suggesting enhanced homogeneity of active sites after ionic liquid extraction. Therefore, while the commercial chitosan showed slightly higher theoretical capacities, the [Eth]-extracted chitosan demonstrated higher adsorption rates and uptakes. These results suggest that the ionic liquid extraction method effectively improved the functional accessibility and affinity of chitosan without significantly reducing its adsorption capacity. The CS1%CYS beads using [Eth]-extracted chitosan, therefore, provide a greener, equally effective alternative for recovering metal ions from battery leachates.

Table 12.11. The effect of different initial concentrations on the adsorption rate (%) and adsorption uptake (mg/g) of the CS1%CYS beads using [Eth]-extracted chitosan at a pH of 4

$\frac{\textbf{Adsorption rate (\%)}}{\textbf{Adsorption Uptake } (\frac{mg}{g})}$	Co	Mn	Ni
×40	77.43± 1.12	41.38± 0.78	92.48± 1.98
	56.11± 0.81	1.31± 0.02	4.59± 0.10
×30	75.64± 0.32	45.94± 0.69	91.69± 0.34
	73.09± 0.31	1.94± 0.03	6.07± 0.02
×20	63.76± 1.64	32.75± 0.91	86.17± 0.71
	92.41± 2.38	2.08± 0.06	8.56± 0.07
×10	41.86± 0.43	23.61± 20.18	68.92± 1.03
	121.33± 1.24	2.99± 0.02	13.69± 0.21

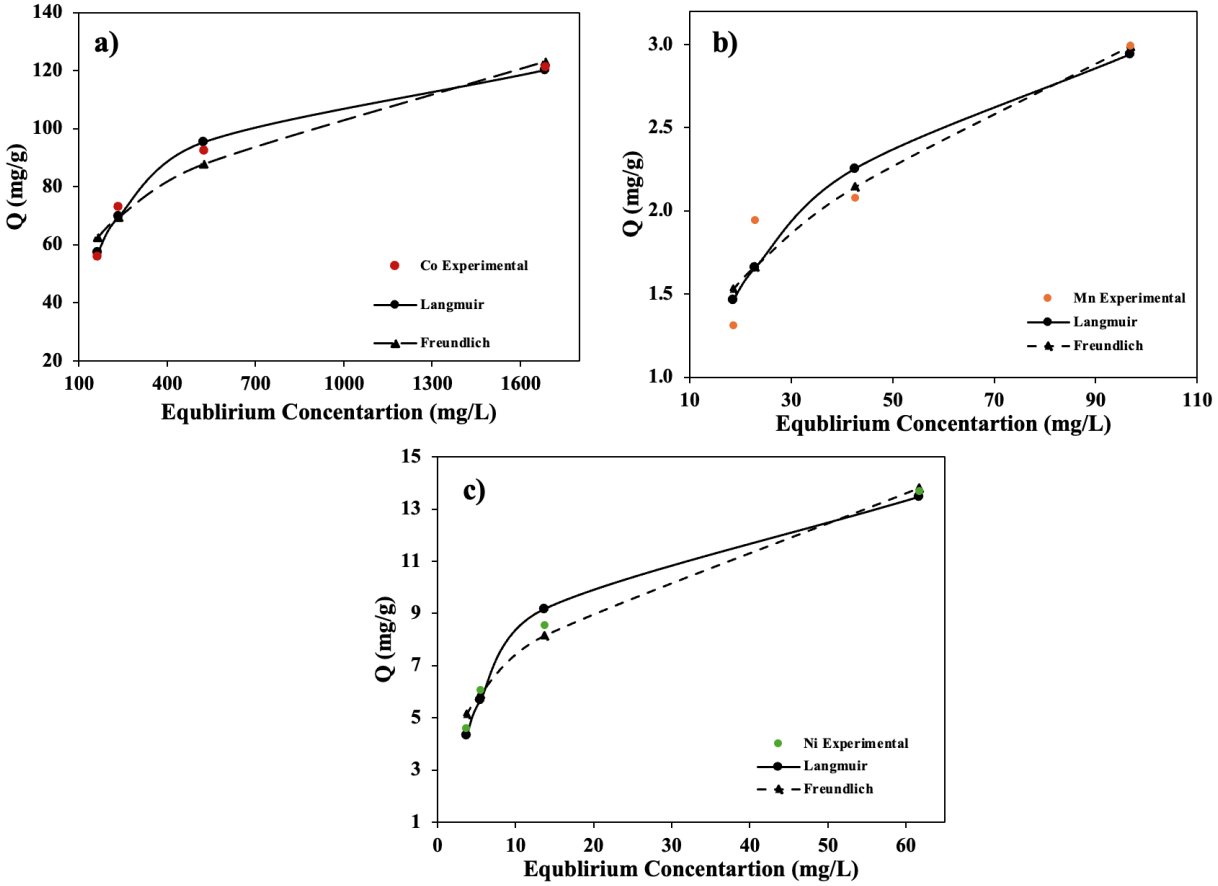

Figure 12.14. Experimental data and adsorption isotherms for a) Co(II), b) Mn(II), and c) Ni(II) for CS1%CYS beads using [Eth]-extracted chitosan.

Table 12.12. Adsorption isotherm parameters

Isotherm model	Parameter	Co (II)	Mn (II)	Ni (II)
Langmuir	K_L (L/mg)	4.47E-03	3.29E-02	1.05E-01
	q_m (mg/g)	136.14	3.86	15.53
	R-squared	0.99	0.95	0.99
	SSR	113.75	0.43	3.88
	MSE	9.48	0.04	0.32
Freundlich	k_F	14.29	0.47	3.24
	n_F	3.45	2.47	2.85
	R-squared	0.98	0.95	0.99
	SSR	272.72	0.40	2.52
	MSE	22.73	0.03	0.21

12.10. Column Study

Figures 12.15 and 12.16 present the experimental setup and breakthrough curve for the column study at a flow rate of 1 mL/min and a bed height of 20 cm. The run was stopped after 12.58 h, treating 785 mL of influent, due to suspected channeling. The setup was subsequently improved by inserting a glass disk between the bead layers to ensure a more uniform flow. However, the results followed the expected trend, confirming the test's reliability.

Figure 12.15. Column study at a flow rate of 1 mL/min with a pH of 4 and a dilution factor of 4.

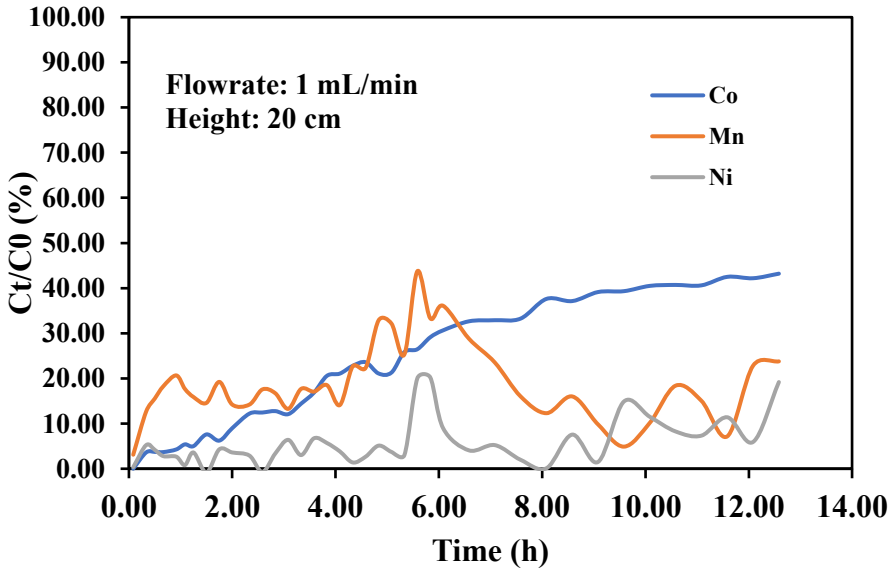

Figure 12.16. Breakthrough curve for the flow rate of 1 mL/min.